# Nanoscale insights on hypoxia radiosensitization with ion beams

**Einblicke in die Hypoxie-Radiosensibilisierung auf Nanometerebene nach Ionenstrahlung**
Vom Fachbereich Physik der Technischen Universität Darmstadt
zur Erlangung des akademischen Grades eines Doktors der Naturwissenschaften (Dr. rer. nat.)
genehmigte Dissertation von Dipl.-Phys. Daria Boscolo aus Cecina, Italien
Tag der Einreichung: 09.04.2018, Tag der Prüfung: 30.05.2018
Darmstadt — D 17

1. Gutachten: Prof. Dr. Marco Durante
2. Gutachten: Prof. Dr. Regine von Klitzing

TECHNISCHE
UNIVERSITÄT
DARMSTADT

GSI

Nanoscale insights on hypoxia radiosensitization with ion beams

Einblicke in die Hypoxie-Radiosensibilisierung auf Nanometerebene nach Ionenstrahlung

Genehmigte Dissertation von Dipl.-Phys. Daria Boscolo aus Cecina, Italien

1. Gutachten: Prof. Dr. Marco Durante
2. Gutachten: Prof. Dr. Regine von Klitzing

Tag der Einreichung: 09.04.2018
Tag der Prüfung: 30.05.2018

Darmstadt — D 17
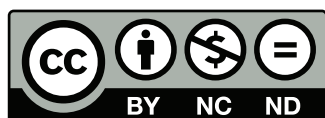
# Abstract

Tumors with a nonuniform oxygen distribution show also an inhomogeneous radiosensitivity. In particular, the hypoxic regions results to be more radioresistant, limiting the efficacy of radiotherapy. It has been observed that high linear energy transfer, LET, radiation can counteract this effect to a certain extent, suggesting ion beam therapy as one of the most promising strategies to treat hypoxic tumors.

On the nanoscale, the oxygen effect is assumed to be related to the indirect action of radiation. Several theories exist that aim to provide an explanation of the nature of this effect and its LET dependence, on the radiation chemistry. However, a mechanistic description is still missing and little is known about the indirect action and the chemical processes taking place along an ion track. In this work, the Monte Carlo particle track structure code TRAX has been extended to the pre-chemical and chemical stage of the radiation effect and is now able to simulate the chemical evolution of the most important products of water radiolysis under different irradiation conditions and target oxygenation levels. The validity of the model has been verified by comparing the calculated time and LET-dependent yields of the different radiolytic species to experimental data and other simulation approaches.

As an example of the application of the newly implemented TRAX-CHEM code, a study on the dose enhancement effect and radical enhancement effect of gold nanoparticles has been performed under varying irradiation conditions and oxygenation levels. This will contribute to the basic understanding of still unsolved mechanisms for nanoparticle sensitization.

# Zusammenfassung

Tumore mit ungleichmäßiger Oxygenierung zeigen auch eine inhomogene Strahlenempfindlichkeit. Insbesondere sind die hypoxischen Regionen strahlenresistenter, was die Wirksamkeit der Strahlentherapie einschränkt. Es wurde beobachtet, dass eine hohe LET-Strahlung diesem Effekt bis zu einem gewissen Grad entgegenwirken kann, was Ionenstrahltherapie eine der vielversprechendsten Strategien zur Behandlung hypoxischer Tumore macht.

Es wird angenommen, dass der Sauerstoffeffekt auf der Nanometerskala mit der indirekten Strahlenwirkung zusammenhängt. Es gibt mehrere Theorien, die eine Erklärung für den Ursprung dieses Effekts und seine LET-Abhängigkeit auf der nanoskopischen und chemischen Ebene liefern. Eine mechanistische Beschreibung fehlt jedoch bislang, und über die indirekte Wirkung und die chemischen Prozesse entlang einer Ionenspur ist wenig bekannt. In dieser Arbeit wurde der Monte-Carlo Code TRAX zur Simulation der Teilchenbahnstruktur um die vorchemische und chemische Stufe des Strahlungseffekts erweitert und ist nun in der Lage, die chemische Entwicklung der wichtigsten Produkte der Wasserradiolyse unter verschiedenen Bestrahlungsbedingungen und Oxygenierungsniveaus des Mediums zu simulieren. Die Gültigkeit des Modells wurde verifiziert, indem die berechneten Zeit- und LET-abhängigen Ergebnisse der verschiedenen radiolytischen Produkte mit experimentellen Daten und anderen Simulationsansätzen verglichen wurden.

Als ein Anwendungsbeispiel der neu implementierten Version des TRAX-CHEM-Codes wurde eine Studie über den Dosisverstärkungseffekt und den Effekt der Radikalverstärkung von Goldnanopartikeln unter verschiedenen Bedingungen durchgeführt. Dies wird das Grundwissen erweitern, das für die biologische Behandlungsplanung für Goldnanopartikel verstärkte Strahlentherapie notwendig ist.

# Contents

# List of Abbreviations

| | |
|---|---|
| **AuNP** | Gold Nanoparticle |
| **BEA** | Binary Encounter Approximation |
| **BEB** | Binary Encounter Bethe |
| **BED** | Binary Encounter Dipole |
| **CSDA** | Continuous Slowing Down Approximation |
| **DEF** | Dose Enhancement Factor |
| **FWHM** | Full With Half Maximum |
| **GSH** | Glutathione |
| **IMRT** | Intensity Modulated Radiation Therapy |
| **IRT** | Independent Reaction Time |
| **LET** | Linear Energy Transfer |
| **MRI** | Magnetic Resonance Imaging |
| **NP** | Nanoparticle |
| **NSCLC** | Non-Small Cell Lung Cancer |
| **OER** | Oxygen Enhancement Ratio |
| **PET** | Positron Emission Thomography |
| **PIDE** | Particle Irradiation Data Ensembles |
| **PTCOG** | Particle Therapy Co-Operative Group |
| **PWA** | Partial Wave Analysis |
| **RBE** | Relative Biological Effectiveness |
| **REF** | Radiolysis Enhancement Factor |
| **RNS** | Reactive Nitrogen Species |
| **ROS** | Reactive Oxygen Species |
| **SER** | Sensitivity Enhancement Ratio |
| **SOD** | Superoxide Dismutases |
| **WNP** | Water Nanoparticle |

# List of Publications

**Peer-reviewed articles**

**Boscolo D.**, Krämer M., Durante M., Fuss M.C., Scifoni, E.. TRAX-CHEM: A pre-chemical and chemical stage extension of the particle track structure code TRAX in water targets. *Chemical Physics Letters* (2018) 698 pp. 11-18.

O'Leary M., **Boscolo D.**, Breslin N., Brown J. M. C., Dolbnya I. P., Emerson C., Figueira C., Fox O. J. L., Grimes D. R., Ivosev V., Kleppe A. K., McCulloch A., Pape I., Polin C., Wardlow N. & Currell F.J.. Observation of dose-rate dependence in a Fricke dosimeter irradiated at low dose rates with monoenergetic X-rays. *Scientific Reports* (2018) Published online.

Sokol, O., Scifoni, E., Tinganelli, W., Kraft-Weyrather, W., Wiedemann, J., Maier, A., **Boscolo, D.**, Friedrich, T., Brons, S., Durante, M. and Krämer, M.. Oxygen beams for therapy: advanced biological treatment planning and experimental verification. *Physics in medicine and biology* (2017) 62(19), pp.7798-7813.

**Boscolo D.**, Scifoni E., Carlino A., La Tessa C., Berger T., Durante M., Rosso V. and Krämer, M.. TLD efficiency calculations for heavy ions: an analytical approach. *The European Physical Journal D*, (2015) 69(12), 286.

**Book chapter**

Ferruz, M. B., Ivosev, V., Haume, K., Ellis-Gibbings, L., Traore, A., Thakare, V., Rosa, S., de Vera, P., Tran, V.-L., Mika, A., **Boscolo D.** et al., (2017). New research in ionizing radiation and nanoparticles: the argent project. In *Nanoscale Insights into Ion-Beam Cancer Therapy,* pages 379 - 434. Springer.

**Scientific reports**

**Boscolo D.**, Krämer M., Durante M., Fuss M.C., Scifoni, E., 2017. Contribution of the molecular oxygen to the chemical track evolution. *GSI Scientific Report 2017.*

**Boscolo D.**, Scifoni, E., Krämer M., Durante M., 2016. TRAX-CHEM. *GSI Scientific Report 2016.*

Bolsa M., **Boscolo D.**, Porcel E., Lacombe S., Sokol O. , Wiedemann J. , Scifoni E., Tinganelli W., Jakob B., Roux S., Jimenez G., Durante M., Krämer M., 2016 Nanoparticles radio-enhancement of ion beams at different oxygenation conditions., 2016. *GSI Scientific Report 2016.*

**Boscolo D.**, Scifoni, E., Krämer M., Durante M., 2015. Chemical stage implementation in TRAX. *GSI Scientific Report 2015.*

**Boscolo D.**, Scifoni, E., Durante M., Rosso V. and Krämer M., 2014.Validity analysis of the single ion approach for TLD efficiency calculations.*GSI Scientific Report 2014.*

**Boscolo D.**, Scifoni, E., Durante M., Rosso V. and Krämer M., 2013.TLD Efficiency calculation for heavy ions: a new approach.*GSI Scientific Report 2013.*

# Introduction

Heterogeneity in tumor oxygenation is considered to be one of the main limiting factors for tumor control in radiotherapy. Based on evidence from *in vitro* experiments (Tinganelli et al., 2015), tissues in hypoxic conditions, or with hypoxic regions, may be up to three times more radioresistant compared to well oxygenated ones (Tinganelli et al., 2015). On the nanoscopic level, the oxygen effect is considered to be strongly related to the indirect damage of radiation (Sonntag, 1987) and, in particular, to the $OH^{\bullet}$ radical (Hirayama et al., 2013). Among the chemical species produced by water radiolysis, $OH^{\bullet}$ radicals are believed to be the most harming; they have, indeed, a very short half-life and can react with almost every molecule, including DNA (Reiter et al., 1995). Generally, the damage induced by radicals on biological systems can be repaired by the action of antioxidants. However, in oxygenated conditions, the molecular oxygen may react with the damaged molecule stabilizing the damage and making it permanent. In addition, in oxygenated media, the radiolytic species produced during the irradiation can interact with the molecular oxygen dissolved in the target, leading to the production of two highly toxic species $O_2^{\bullet-}$ and $HO_2^{\bullet}$, which might be responsible for a part of the oxygen sensitization effect (Colliaux et al., 2011). It has been observed that densely ionizing radiation can mitigate the hypoxia induced radioresistence (Alper, 1956), motivating a growing interest in ion radiation therapy for treating hypoxic tumors. On the clinical level, new optimization techniques accounting for the oxygenation level and ion linear energy transfer have been recently developed for particle therapy.

Additionally to ion irradiation techniques, the possible use of advanced treatment strategies based on nanosensitizers has been recently considered for treating hypoxic tumors (Lacombe et al., 2017). High-Z nanoparticles (NPs) are discussed as possible radiation effect enhancers in order to improve the selectivity and efficacy of radiation therapy. The addition of NPs could, indeed, increase the radiation effects within the tumor, ultimately allowing the reduction of the dose deposited in healthy tissues. This effect has been observed *in vivo* and *in vitro*, and clinical trials with X-ray radiation have been already initiated (Kuncic and Lacombe, 2018). On the nanoscopic scale, the NPs radiosensitization effect is generally explained as a local dose enhancement induced by an increased production of secondary electrons in the vicinity of the NP (McMahon et al., 2011). A significant increase of radical production has also been measured with X-ray radiation and observed by indirect measurements after ion irradiation (Sicard-Roselli et al., 2014; Porcel et al., 2010) and other effects might be involved as well (Lacombe et al., 2017). However, while in the case of photon radiation the radio-enhancement effect induced by metallic nanoparticles is fairly understood, in the case of ion radiation a complete picture of the physical and chemical mechanisms involved in the NP sensitization is not yet clear.

In this context an FP7 European multi-ITN (Marie Curie Action Initial Training Network) project, named "Advanced Radiotherapy, Generated by Exploiting Nanoprocesses and Technologies"(ARGENT) was founded with the aim of understanding and exploiting the nanoscale processes induced by ionizing radiation in the presence of radiosensitizing nanoparticles (Ferruz et al., 2017). The work presented in this thesis formed part of the research carried out in this consortium and focuses on the quantification

and definition of some of the most important nanoscopic mechanisms underlying the indirect effect of radiation under different oxygenation conditions and in presence of nanosensitizers. An explicit and appropriate description of the radiation chemistry initiated by the passage of ion radiation is, indeed, needed to develop a nanoscopic understanding of the oxygen effect and to model the nanoparticle sensitivity enhancement ratio, SER. Having an exhaustive definition of the SER for different irradiation conditions, oxygenation level and nanoparticles concentration will, indeed, help in the development of biologically optimized treatment planning for nanoparticle enhanced radiation therapy.

The thesis is structured in five chapters. In Chapter 1 some of the most important nanoscopic mechanisms underlying the ion induced radiation effect and the indirect damage are presented. A particular focus is given to oxygen sensitization and on the possible use of metallic nanoparticle as radiation sensitizers. In Chapter 2 the Monte Carlo particle track structure code, TRAX, together with the physical models adopted to describe the passage of ion radiation through water and gold material, is introduced. In Chapter 3 the new implementation of the pre-chemical and chemical extension of the TRAX code is described and used to simulate the yield of radiolytic species in water target under different irradiation conditions. Simulation results are crosschecked with experimental data and predictions from other simulation tools. In Chapter 4 the impact of the target oxygenation level on the chemical evolution of the track has been, then, studied for different particle radiation and oxygen concentrations. In the last chapter, an extended analysis of the nanoscopic mechanisms involved in the NP sensitization effect has been carried out with the classical version of the TRAX code and with the chemical extension here implemented, under different oxygenation conditions.

# 1 The role of nanoscale analysis in the understanding of ion beam therapy

## 1.1 Ion beam therapy

Nowadays ion beam therapy is a well-established method to treat cancer: at the moment there are 70 facilities in operation and 42 are under construction worldwide (PTCOG, 2016a,b). Currently, only 0.8% of patients receiving radiation therapy are treated with high-energy charged particle beams but this number is rapidly increasing over the years (Durante and Paganetti, 2016). Patients are mostly treated with proton radiation, however eleven carbon ion beam therapy centers are already in operation and the possibility of using other ions, such as helium and oxygen has been also considered (Krämer et al., 2016; Sokol et al., 2017).

The large success of charged particle therapy comes from an improved conformity and tumor targeting respect to standard X-ray radiation treatment. This is clearly shown in Figure 1.1(a) where treatment plans for a base of skull meningioma, obtained with intensity modulated radiation therapy, IMRT and carbon ions scanned beam therapy are compared.



(a)          (b)
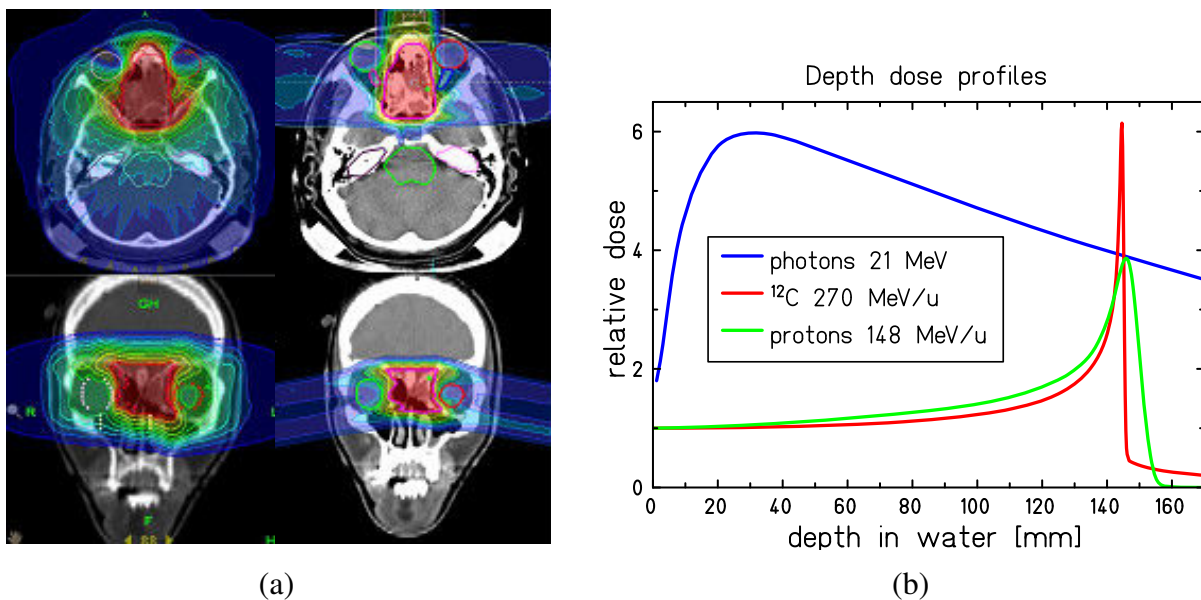
**Figure 1.1.:** Subfigure (a):Treatment planning comparison for a base of skull meningioma: on the left panel IMRT and on the right panel scanned carbon ions, adapted from (Combs et al., 2012). Right panel: depth dose distribution profiles for different radiation types: photons 21 MeV, proton radiation of 148 MeV and carbon ion radiation of 270 MeV, figure from (Krämer and Durante, 2010).

From the physical point of view, the main advantage of ion beam therapy comes from a favorable depth dose distribution[1], as shown in Figure 1.1(b). Different from photon radiation, the energy deposition of charged particles in medium increases with the depth and is characterized by a distinct narrow peak at the end of the particle range, the so called Bragg peak. The position of this peak can precisely be adjusted to the desired depth in tissue by changing the ion beam kinetic energy. Thanks to this inverted depth dose profile it is, thus, possible to deposit most of the ion energy in a certain depth (and thus in the tumor volume), sensibly reducing the unwanted dose deposition in healthy tissues, for example in the beam entrance channel. Additionally, the well defined penetration range and the sharp decrease of the dose after the Bragg peak allow reducing the dose delivered to eventual organs at risk located in the vicinity of the tumor. Ions heavier than protons present also an enhanced relative biological effectiveness (RBE) in the Bragg peak region, with respect to the photon radiation. This latter effect can be explained by an increased complexity of the radiation damage and, thus, to a lower cell repair probability (Schardt et al., 2010).

The physical and radiobiological processes involved in ion radiation therapy have been largely studied in the last 50 years and generally speaking, most of these processes are now fairly understood, even if sometimes not with the desired precision. The most crucial problem addressed by these studies is the prediction of the biological response of the body after receiving the irradiation. The complexity of the problem arises from the many processes involved and the very large temporal and spatial scale covered by radiation effect: from the nanoscopic interaction of radiation with biological material (characterized by time scale in the order of $10^{-17}$ s and spatial scale of the femtometer) to tumor treatment and secondary effects of radiation damage (taking place from minutes to years after the radiation exposure and characterized by spatial scale from 1 millimeter to 10 centimeters). Figure 1.2 shows a schematic representation of the spatiotemporal scale involved in the different stages of ion radiations effect while in Table 1.1 the spatiotemporal scale of the main process and the different disciplines involved is shown.

**Table 1.1.:** Spatiotemporal scales of the different processes and disciplines involved in the radiation effect. Adapted from Surdutovich and Solov'yov (2014).

| Phenomenon | Discipline | Sace scale | Time scale |
|---|---|---|---|
| Primary ionization, transport of secondaries | Atomic/Molecular Physics | 0.1-10 nm | $10^{-17}$-$10^{-14}$s |
| Dissociative electron attachment and other reactions | Quantum Chemistry | Å | $10^{-15}$s |
| Molecular dissociation, relaxation, thermalization | Molecular Physics | 0.1-10 nm | $10^{-15}$-$10^{-12}$s |
| Diffusion and recombination of radicals | Chemistry | 1-10 nm | $10^{-12}$-$10^{-5}$s |
| Local heating, heat transfer, stress | Thermo/hydro-dynamics | 1-10 nm | $10^{-14}$-$10^{-9}$s |
| Initial resulting damage effect | Biochemistry | 0.1-10 nm | $10^{-5}$s |
| Repairing mechanisms | Molecular Biology | 1-100nm | s-min |
| Cellular network and interaction | Cell Biology | $\mu$m | min |
| (Tumour) Cell death | Medicine | mm-cm | min-years |

---

[1] The dose is the most important physical quantity in radiotherapy. It is defined as the average energy $dE$ deposited by the radiation in a mass element $dm$: $D = \frac{dE}{dm}$. It is measured in Gray (Gy) and is defined by the International Commission on Radiation Units (ICRU) (International Commission on Radiation Units and measurements, ICRU, 1998) by the term absorbed dose.
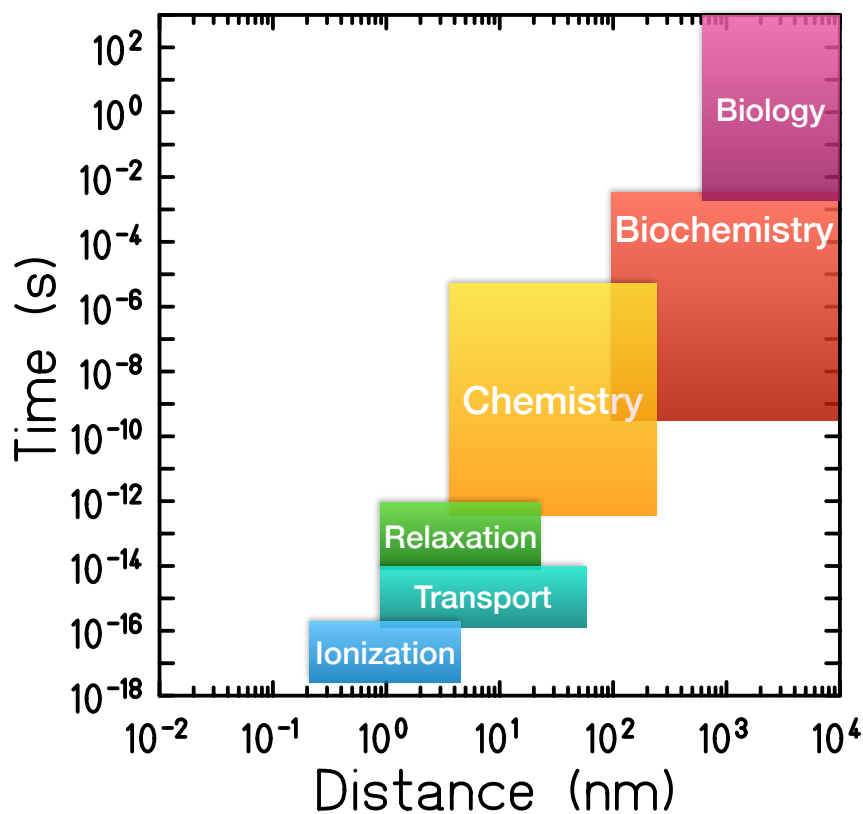
**Figure 1.2.:** Space-time diagram showing the processes and disciplines involved at the different stages of radiation effect from ionization and excitation to the biological effect. Adapted from Surdutovich and Solov'yov (2014).

When modeling the effect of radiation on biological targets, because of the numerous physical, chemical, biological and medical aspects involved on such a wide scale, it is impossible to follow a completely bottom up approach within a reasonable computing time and satisfactory precision. For these reasons more pragmatic semi-empirical approaches have been adopted (Scholz and Kraft, 2004; Wälzlein et al., 2014a). A deep knowledge of the nanoscopic processes involved in the radiation effect is, however, still very important not only for providing a better understanding of the basic principle underlying ion radiation damage, but also to benchmark and improve the precision of input data for the radiobiological models (Scifoni, 2015).

In this chapter some of the most important microscopic characteristics of ion radiation, such as the ion track structure and the microscopic basis of radiation damage, will be introduced as well as their impact on macroscopic quantities like the relative biological effectiveness, RBE, and oxygen enhancement ratio, OER, i.e. the increased radioresistance of tumors in restricted oxygenation conditions. Finally, the possibility to use nanoscopic dose modifiers, like gold nanoparticles, as radiosensitizers in order to enhance the effect of ion beam radiation therapy will be presented.

### 1.2.1 Ion track

The major difference between photon and ion radiation is due to the different nanoscopic interactions they have with matter, resulting in a completely different microscopic spatial dose/energy distribution.

In photon radiation, the energy is transferred to the biological (low atomic number) medium mainly through Compton and photoelectric effects. During these processes, the primary photons get completely absorbed or scattered at a large angle and secondary electrons are produced and might give rise to tertiary and higher order species. On the macroscopic level, this effect will result in an exponential attenuation of the beam intensity as a function of the depth, where the absorption coefficient is directly related to the total cross section for all the possible interaction processes. Since the interaction probabilities for incident photons are rather low, only few ionization events can be registered in a volume comparable with the cellular one (Schardt et al., 2010). Only a few electrons are, thus, generated from the target molecules and, in order to achieve a significant radiation effect, the target volume has to be irradiated with many photons. Since these photons are randomly distributed, the resulting ionization distribution (and more in general the dose distribution) can be assumed to be uniform over the volume.
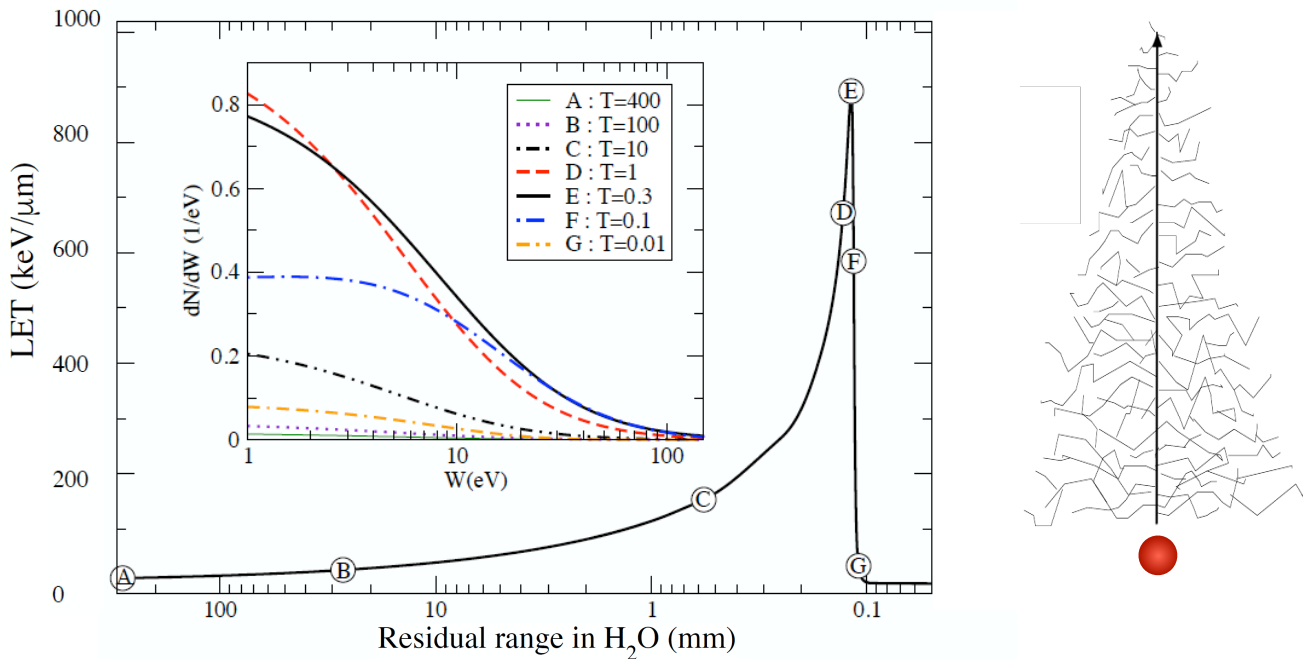


**Figure 1.3.:** Left panel: Secondary electron energy spectra along a carbon ion track (insert) at different depth positions (indicated with letters in the larger plot), in water. Adapted from Scifoni (2015). Each position corresponds to a specific residual energy $T$ (in MeV/u) of the primary ion. Right panel: schematic representation of an ion track including secondary electrons.

The energy deposition process of heavy charged particles is completely different. In this case, thanks to its positive charge, the ion loses most of the kinetic energy through the many Coulomb interactions

with the electrons of the target material, resulting in an almost continuous slowing down. During these many scattering processes, the charged particle can ionize or excite the target material leading to the formation of secondary and eventually higher order electrons. Under normal conditions (as for the case of photon radiation) the major contribution to the energy loss and radiation damage induced by ion radiation comes from the secondary species (Nikjoo et al., 2006). However, in contrast to photons, the primary ion loses a relatively small part of its energy in every collision with the target molecules. The secondary electrons are, thus, generated all along the ion path, resulting in a very localized energy distribution centered along the ion trajectory, reaching doses up to kilo- or even Mega-Grays in the center of the ion track (Wälzlein et al., 2014b). The high ionization and excitation density along a charged particle track can be well justified looking at the energy spectra of the secondary electrons generated at different depth along a carbon ion trajectory in water, left panel of Figure 1.3. Most of the electrons are, indeed, produced with energies lower than 100 eV and, especially in the Bragg peak region, the number of secondary electrons produced at very low the energies (<10 eV) appears to be very peaked, leading to the production of a very narrow track, with an extremely high energy deposition density (Scifoni, 2015).

The lateral size of the ion track is determined by the range of the most energetic secondary electrons, and thus, by the maximum energy which can be transferred by the primary ion: it is larger for more energetic ions. Monte Carlo simulations allowed a parametrization of this maximum range of secondary electrons, $R_{el}$, depending of the kinetic energy of the primary ion, E, and on the target medium density $\rho$ (Scholz, 2003):

$$R_{el} \propto \frac{1}{\rho} \cdot E^{1.7}. \tag{1.1}$$

On the right panel of Figure 1.3 a schematic representation of an ion track is shown.

### 1.2.2  Track structure codes

In the last 20 years, several codes have been developed in order to simulate the ion radiation transport through different media. Monte Carlo codes, in particular, result to be especially suitable thanks to their capability to handle the stochastic nature of radiation interactions with a target material.

Two main approaches have been adopted by these simulation tools, the macroscopic or condensed history transport method and the event by event or track structure approach (Scifoni, 2015). In the first ones particle deflections are sampled according to multiple scattering models and the stopping process is based on the continuous slowing down approximation (CSDA): the computation of the energy losses is based on stopping power tables. These codes received a large success since they are computationally fast and perfectly reliable for high energy and large scales: when the number of collisions required to stop the primary ion is high (Berger et al., 1963). Among the best known macroscopic particle radiation transport model we can find Geant4 and FLUKA.

Track structure codes, instead, describe the three-dimensional radiation passage following ions and electrons event by event, using the interaction cross sections as input parameters. These codes result to be computationally expensive and thus inefficient to simulate the whole ion trajectory. However, they allow describing ion track segments with a nanometric precision following secondary electrons down to
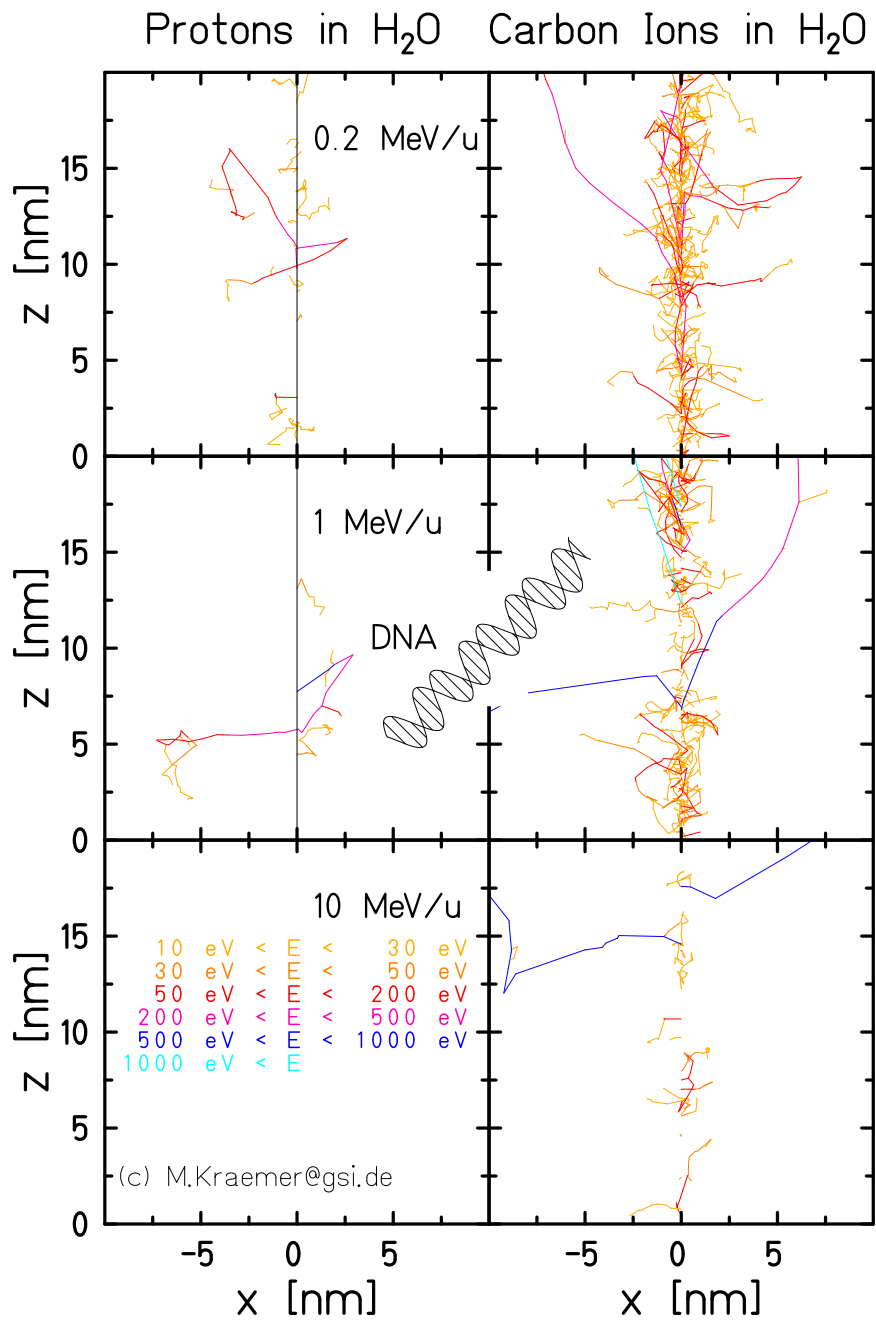
**Figure 1.4.:** Trajectories of secondary and higher order electrons generated along a proton and carbon ion track at different energy. The simulation has been performed by the particle track structure code TRAX. Image from (Krämer and Durante, 2010).

very low energies (1-10 eV). This feature becomes particularly important when it comes to describing the radiation effect on a biological system, as it has been demonstrated that very low energy electron (<10 eV) can still induce severe damages on biomolecules, (Boudaïffa et al., 2000; Scifoni, 2015). Figure 1.4 shows a simulation of the trajectories of secondary and higher order electrons generated along the track of protons and carbon ions of different energy, the calculation has been obtained with the particle track structure code TRAX (Krämer and Kraft, 1994; Wälzlein et al., 2014a).

In the track structure Monte Carlo codes, the particle transport is described as a succession of single interactions. The distance between two consecutive interactions can be derived from the mean free path, $\lambda$, of the particle in a specific target material and depends on the total interaction cross section $\sigma_{tot}$:

$$\lambda = \frac{M_{mol}}{N_A \cdot \rho \cdot \sigma_{tot}} \tag{1.2}$$

with $M_{mol}$ the molar mass (in g) , $\rho$ the target density (in g/cm$^3$) and $N_A$ the Avogadro number. The total cross section can be obtained summing up the contribution of all the possible elastic and inelastic interactions:

$$\sigma_{tot} = \sigma_{elastic} + \sigma_{ionization} + \sigma_{excitation}. \tag{1.3}$$

Once the mean free path is known, the actual distance between two consecutive interactions, $d$, can be sampled using a random number, $R$, between 0 and 1 as follow:

$$d = -\lambda \cdot ln(R). \tag{1.4}$$

The reliability of track structure codes, as well as their spatial resolution, depends on the interaction cross sections sets implemented. In particular, for an accurate description of the radiation effect on biological material, a large interest exists in the establishment of accurate and precise cross sections of electrons in liquid water. Studies have been carried out in order to investigate the propagation of radiation in the liquid phase of water and some sets of inelastic cross sections based on dielectric theory (Dingfelder et al., 1999; Emfietzoglou et al., 2005; Scifoni et al., 2010a,b) or quantum mechanical ab-initio calculations for elastic scattering (Champion et al., 2009) have already been developed and implemented in some Monte Carlo codes like PARTRAC, NOREC (Dingfelder et al., 2008) and Geant4-DNA (Francis et al., 2011). However, these cross sections have not been experimentally validated, and, for this reason, most of the track structure codes still use cross sections for water vapor or for ice and adding, then, some corrections to account for the solid phase effects (Wälzlein et al., 2014; Scifoni, 2015).

In addition, because of the limited information on the low energy electrons interactions, many codes cannot perform reliable simulations for energies below a certain cut-off energy: electrons with an energy below the cut-off will be removed from the simulation. This energy value represents, thus, the spatial and energetic resolution of the simulation and might become very important in order to describe processes characterized by a nanometric scale or depending on shell specific excitation, like molecular dissociation and the formation of radiolytic species.

With the increase of the computational capability and with the necessity of a more accurate description of the nanoscopic processes involved in radiation damage the interest in track structure codes increased

sensibly. Among the most known and advanced track structure codes we can find PARTRAC (Ballarini et al., 2000; Kreipl et al., 2008), KURBUC (Nikjoo et al., 2006; Uehara and Nikjoo, 2006), TRAX (Krämer and Kraft, 1994; Wälzlein et al., 2014a; Boscolo et al., 2018), RITRACKS (Plante, 2011a,b; Plante and Devroye, 2017) and Geant4-DNA (Karamitros et al., 2011). Some of these codes are now able to follow the track evolution up to advanced stages of the radiation effect, including the production and interaction of chemical species generated as a consequence of water radiolysis and simulating complex target material including portions of DNA, up to several hundreds of convolutions (Scifoni, 2015). Some algorithms for accounting also the DNA damage and repair have been developed; however, at the moment only a few DNA damage pathways have been investigated and none of these account for the chemistry involved (Nikjoo et al., 2016). A more detailed description of the track structure code TRAX will be provided in Chapter 2 and in Chapter 3 the implementation of the radical diffusion and interaction in the TRAX code is presented.

## 1.3 Direct and indirect damage of radiation

### 1.3.1 Direct damage

The large difference in the spatial energy deposition between ions and photon radiation is at the basis of the different radiation damage generated by these two different radiation types on biological media. The center of an ion track has a typical extension of few nanometers and the dose deposited in this area can reach kilo or even the Mega Grey. This means that, in this region, ionization and excitations events are taking place in the vicinity of each other, resulting in complex biological damage. Additionally, depending on the ion type and on its velocity the dose deposition along the track changes significantly: it is broader for lighter and faster ions while it becomes extremely narrow for heavy and slow ions.

In contrast, in the case of photon radiation, the energy deposition can be assumed homogeneously distributed over a cellular target leading to a larger separation between neighbouring damage sites. An example of the different microscopic dose distributions obtained with photon and carbon ions radiation of different energy, on a target of 5 $\mu$m side for an average macroscopic dose 2 Gy is shown in Figure 1.5

Since the cellular repair capability decreases with the damage complexity, ion radiation damage results to be biologically more effective than the one induced by photon radiation. Moreover, the ions capability of inducing lethal damage changes depending on the ion type and on the ion energy and, as it will be discussed in Section 1.4, for successfully treating a tumor it is necessary to take this effect into account.

### 1.3.2 Indirect damage

The biological damage induced by radiations through direct ionizations represents only one part of the biological effect of radiation. To have a comprehensive description of the radiation damage, it is, indeed, necessary to consider also the damage induced indirectly by highly reactive chemical species produced by the molecular dissociation of ionized and excited target molecules.
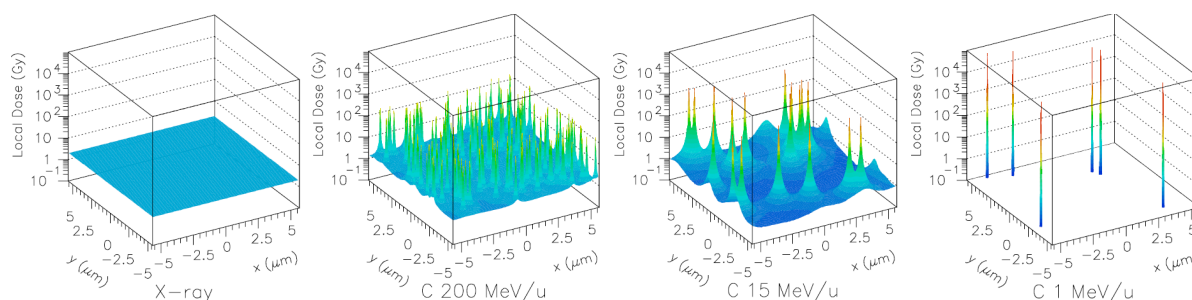
**Figure 1.5.:** Microscopic dose distributions for photon and carbon ion radiation of different energy, on a target of 5 $\mu$m size, resembling cell nucleus dimensions, for an average macroscopic dose of 2 Gy. While in the case of photon radiation the dose results to be uniformly distributed over the target, for carbon ion radiation sharp spikes of dose can be observed especially for the lower ion energies. Figure from Scholz (2003).

Among these species, the so called reactive oxygen species (ROS) are assumed to be the main responsible for the biological damage. The collective term ROS refers to the chemical species derived from oxygen molecules including free oxygen radicals[2] and non-radical molecules which can be either oxidizing agents or easily converted into radicals. Among them, we can find hydrogen peroxide ($H_2O_2$), the hydroxyl radical ($OH^\bullet$), the superoxide anion ($O_2^{\bullet-}$) and its protonated form, the perhydroxyle radical ($HO_2^\bullet$). These species are commonly produced in living organisms as a result of the oxygen metabolism and have an important role in cell signaling and homeostasis. However, they can also react rapidly with lipids, proteins, carbohydrates, and nucleic acids leading to significant damage to cell structures (Reczek and Chandel, 2017). In case of environmental stress, as in the case of exposition to radiation, their levels can increase dramatically and the biological system might not be able to detoxify and repair the resulting damage. This condition is known as oxidative stress and is thought to be implicated in a very large number of pathologies and major disorders including aging, inflammatory and cardiovascular pathology, cancer and degenerative diseases (Winterbourn, 2008).

In order to quantify and characterize the impact of the indirect damage, it is convenient to analyze the yield of production and diffusion of the different radiolytic species generated in a target solution at different time points after the irradiation. In radiation chemistry, the quantity generally used to evaluate the yield of free radical production is the G value, defined as the number of a specific chemical species generated per 100 eV of energy deposited by radiation in the target medium.

This quantity can be measured, with a high temporal resolution (few picoseconds) by means of pulse radiolysis experiments. This technique allows performing direct spectroscopic measurements of the time evolution by a chemical species by coupling a pulsed radiation source (with pulse length ranging from the nanosecond to the femtosecond) to a laser probe. Alternatively, indirect methods, such as the Laplace transformation technique (Monchick, 1956), allow to estimate the temporal evolution of chemical species based on a series of not temporally resolved measurements in presence of a scavengers (chemical substances added to a mixture in order to remove or de-activate impurities and unwanted

---

[2]  free radicals are atoms, ions or molecules with an unpaired valence electron. This characteristic makes these species highly chemically reactive.

reaction products), compounds able to react with the molecule of interest. The use of scavenger molecule can be applied also to directly evaluate the impact of the indirect damage in biological systems. As an example, a significant decrease of the indirect effect (and in particular of the $OH^\bullet$ radical action) for high linear energy transfer, LET [3], radiation has been observed *in vitro*, by the use of Dimethylsulfoxide (DMSO), a powerful scavenger of $OH^\bullet$ radical (Hirayama et al., 2013).

In the following some of the main reactive oxygen species involved in the indirect effect of radiation damage will be briefly discussed.

---

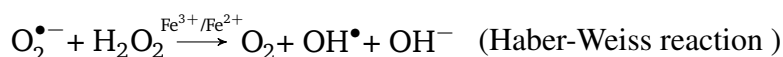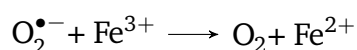Reactive oxygen species and their biochemical role under irradiation and in normal conditions

---

**Superoxide anion $O_2^{\bullet-}$**

The Superoxide ion is one of the most common ROS in aerobic organisms. In normal conditions, it is produced mainly by the reaction of molecular oxygen with electrons leaking from the mitochondrial respiratory chain and rapidly dismutates into $H_2O_2$ through the enzymatic action of the superoxide dismutases SOD (Winterbourn, 2008; Balagopalakrishna et al., 1996).

Despite its low reactivity, it is considered to be an important mediator for a large number of cellular effects and to be involved in cellular signaling processes (Keyer et al., 1995; Fridovich, 1997; Buetler et al., 2004; Chen et al., 2009). It can interact with Fe/S clusters releasing iron, inactivate proteins containing iron-sulfur clusters and subtract hydrogen atoms from many biological molecules including DNA, RNA and fatty acids (Winterbourn, 2008; Buetler et al., 2004). Additionally, it is involved in the production of highly damaging species such as hydroxyl radicals $OH^\bullet$ and peroxinitrite ions $ONOO^-$, a species particularly deleterious for DNA, protein, and lipids.

Hydroxyl radicals can be generated, starting from the $O_2^{\bullet-}$, trough the Haber-Weiss reaction (Haber and Weiss, 1932), catalyzed by the presence of transition metals such as $Fe^{2+}$ (or $Cu^{1+}$):

$$O_2^{\bullet-} + Fe^{3+} \longrightarrow O_2 + Fe^{2+}$$

$$Fe^{2+} + H_2O_2 \longrightarrow Fe^{3+} + OH^\bullet + OH^- \quad \text{(Fenton reaction)}$$

$$O_2^{\bullet-} + H_2O_2 \xrightarrow{Fe^{3+}/Fe^{2+}} O_2 + OH^\bullet + OH^- \quad \text{(Haber-Weiss reaction)}$$

Peroxinitrite ions ($ONOO^-$) can be produced by the interaction of superoxide ions with nitrogen monoxide ($NO^\bullet$), which is regularly present in living organisms (Hall and Garthwaite, 2009):

$$O_2^{\bullet-} + NO^\bullet \longrightarrow ONOO^-.$$

Under irradiation conditions, the superoxide anion production yield increases significantly thanks to the rapid reaction of the many electrons generated by the interaction of radiation with the biological matter and the molecular oxygen dissolved in the cell. Being created by the interaction of molecular oxygen instead of being a product of water radiolysis, the superoxide ion is not produced in hypoxic conditions (see also Chapter 4).

---

[3]    In this work, with the term Linear Energy Transfer (LET), we refer to the unrestricted linear energy transfer which corresponds to the amount of energy transferred, $dE$, by a particle traversing a medium per unit path length $dx$. The SI unit for the LET is $Jm^{-1}$, but it is generally expressed in keV/$\mu m$.

**Perhydroxyle radical** $HO_2^\bullet$

The perhydroxyle radical or hydroperoxyl radical $HO_2^\bullet$ is the protonated form of the superoxide anion. This radical can be formed by the transfer of a proton to the superoxide anion or by the transfer of an hydrogen atom (or ion) to the molecular oxygen:

$$H^+ + O_2^{\bullet-} \longrightarrow HO_2^\bullet$$

$$H^\bullet + O_2 \longrightarrow HO_2^\bullet$$
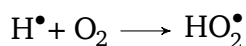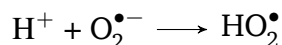
Even though very little is known on this oxygen species, it plays an important role in the lipid peroxidation reactions chain (Aikens, 1991) (see Section 1.5.2) and, in analogy with the superoxide anion, it can react with a nitrogen monoxide leading to the formation of peroxynitrous acid, which is also toxic (Goldstein and Czapski, 1995):

$$HO_2^\bullet + NO^\bullet \longrightarrow ONOOH.$$

Additionally, thanks to its high reactivity with biomolecules and its membrane permeance, it is thought to be a mediator of toxic side effect in the aerobic respiration (de Grey., 2004). As for the superoxide anion, this ROS can be found only in oxygenated conditions and its yield of production increases significantly in case of exposition to low LET radiation.

**Hydrogen peroxide** $H_2O_2$

The hydrogen peroxide is a neutral molecule and is not a radical species. Under normal conditions of temperature and pH, and in absence of metal ions, $H_2O_2$ is stable and it can easily diffuse through membranes (Reczek and Chandel, 2017). However, despite its low reactivity with most biological compounds, it is accounted among the ROS because of its important role in cell signaling and its implication in the chain of production of hydroxyl radicals through the Fenton reaction (Winterbourn, 2008).

The main production channel for $H_2O_2$ is the dismutation of $O_2^{\bullet-}$ through the enzymatic activity of the superoxide dismutases (SOD). However, to keep the $H_2O_2$ concentration within the optimal range for cellular signaling and to limit its cellular toxicity, a series of antioxidative enzymes exist, including peroxiredoxins, glutathione peroxidases, and catalase. Their function is to metabolize the hydrogen peroxide and convert it into water molecules ($H_2O$).

Under irradiation conditions the yield of $H_2O_2$ increases (especially for high LET radiation) because of the recombination reactions between two newly produced hydroxyl radicals.

$$OH^\bullet + OH^\bullet \longrightarrow H_2O_2.$$
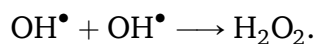
This reaction, highly improbable under normal conditions, becomes more probable in case of ion irradiation, when the yield of $OH^\bullet$ radicals increases significantly in a very localized area (along the ion track).

**Hydroxyl radical** $OH^\bullet$

The hydroxyl radical is considered to be the most dangerous and reactive radical species. Thanks to its large size and the large electroreactivity it can react with any molecule it encounters, including

**Table 1.2.:** Estimated half lives of some of the major reactive oxygen species and radical species in absence of radiation. Table adapted from (SIES, 1993).

| Species | Half life (s)) |
|---|---|
| OH$^\bullet$  Hydroxyl radical | $10^{-9}$ |
| RO$^\bullet$  Alkoxyl radical | $10^{-6}$ |
| ROO$^\bullet$  Peroxyl radical | 7 |
| $H_2O_2$  Hydrogen peroxide | - enzymic |
| $O_2^{\bullet-}$  Superoxyde | - enzymic |
| NO$^\bullet$  Nitric oxyde radical | $1 - 10$ |
| NOO$^-$  Peroxinitrite | $0.05 - 1$ |

macromolecules such as nucleic acids, proteins, carbohydrates and lipids (Reiter et al., 1995). Due to its high reactivity, the hydroxyl radical is characterized by a very short in vivo half-life, $\sim 10^{-9}s$ (SIES, 1993). It will, then, react in the very close vicinity of its formation site and this makes it a very dangerous compound extremely difficult to scavenge by the organism. In Table 1.2 the estimated half life of some of the major radical species and reactive oxygen species are reported.

In normal conditions, hydroxyl radicals can be formed, in presence of transition metals $Fe^{2+}$ or $Cu^{1+}$, by the breakage of the hydrogen peroxide via the Fenton reaction (Reiter et al., 1995). A schematic representation showing the most common production channels for the hydroxyl radical and the other ROS, in normal condition (Not after irradiation) is shown in 1.6.

In case of exposition to ionizing radiation a significant increase in the yield of formation of OH$^\bullet$ radical can be observed. As it will be largely discussed in Chapter 3, this radical species is, indeed, one of the main products of water radiolysis and is generated by the dissociation of both ionized and excited water molecules. A significative yield of production, up to 5-6 molecules per 100 eV of energy deposited have been observed and predicted in the case of low LET radiation and several studies pointed to this radical species as the main responsible of the indirect effect of radiations (Hirayama et al., 2013).
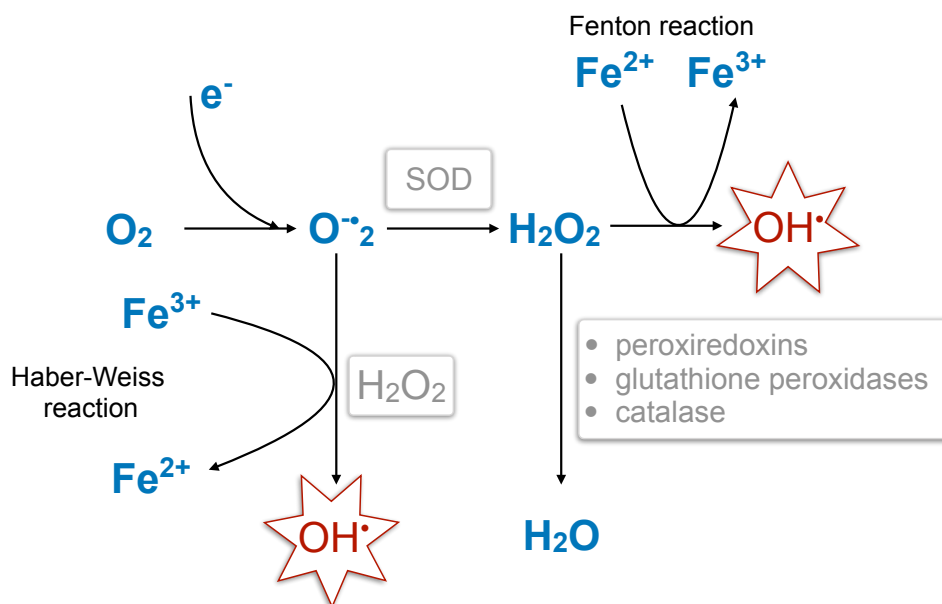
**Figure 1.6.:** Schematic representation of the ROS generating process in absence of irradiation. The super-oxide anion $O_2^{\bullet-}$ can be formed by the interaction of dissolved molecular oxygen with electrons leaking from the mitochondrial respiratory chain. The $O_2^{\bullet-}$ can be reduced to hydrogen per-oxide ($H_2O_2$) via the catalytic action of the enzymes superoxide dismutases (SODs). The hydrogen peroxide $H_2O_2$ can be detoxified by the action of various antioxidative enzymes, including peroxiredoxins, glutathione peroxidases, and catalase or it can be reduced to highly damaging hydroxyl radicals, $OH^{\bullet}$( by reacting with a transition metal $Fe^{2+}$ via the Fenton re-action). When not scavenged by the SODs, the superoxide anion can interact with iron $Fe^{3+}$ generating $Fe^{2+}$ which can further form $OH^{\bullet}$ through the Fenton reaction interacting with a $H_2O_2$. The network of these two reactions is known as the Haber-Weiss reaction.

## 1.4 Relative Biological Effectiveness

The biological response of a system exposed to radiation can vary sensibly depending on a complex combination of biological and physical effects including the cell type and their repair capability as well as the absorbed dose and the radiation quality. As a consequence, at a fixed dose, different radiation types will lead to different biological endpoints (Schardt et al., 2010).

Densely ionizing radiation (such as ion radiations) can, indeed, induce complex localized damages to biomolecules, which are difficult to repair and in many cases lethal for the cells. In contrast, for the same amount of delivered dose, biological damages induced by sparsely ionizing radiation, as photon radiation, are less localized and, thus, easier to repair.

According to the linear quadratic model varying the absorbed dose $D$, the fraction of cell surviving $S$ can be expressed as

$$S(D) = e^{-\alpha D - \beta D^2},$$ \hfill (1.5)

where $\alpha$ and $\beta$ are specific parameters accounting the different cell types, radiation qualities etc. These survival curves show a typical shoulder shape determined by the ratio between $\alpha$ and $\beta$. This ratio is a very important quantity in radiobiology and radiotherapy applications because it is linked to the cell repair capability. A smaller value of $\alpha/\beta$ corresponds to a more pronounced shoulder of the dose response curve that means a larger repair capability (Schardt et al., 2010).

The left panel of Figure 1.7 shows two typical survival curves obtained with photon and ion radiations. It is clearly visible from the figure that for ion radiation not only the $\alpha/\beta$ is larger (indicating a lower repair probability) but also that, in order to get a fixed survival level, it is always needed a lower dose by ions compared to the case of photon radiation.
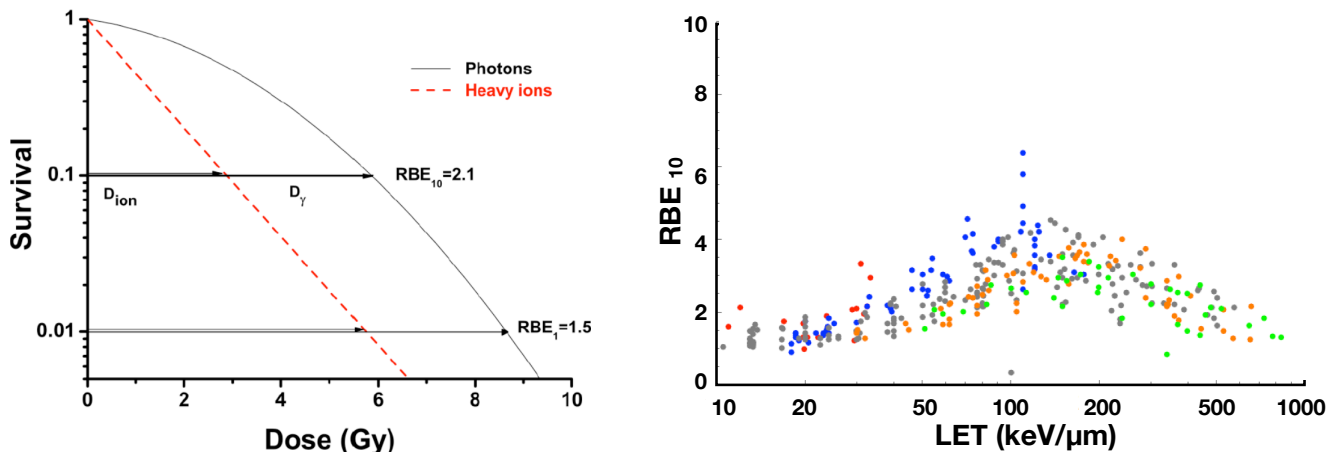


**Figure 1.7.:** Left panel: Graphical representation of the RBE definition for cell inactivation at two different survival levels 1% and 10% (Schardt et al., 2010). Right panel: a collection of *in vitro* data for the RBE, at 10% survival, as a function of the LET (Friedrich et al., 2012)

In order to characterize the different biological effectiveness of different radiation types, a powerful and versatile quantity is the relative biological effectiveness, RBE. The latter is defined, for a specific survival fraction, as the ratio between the values of two different radiation types leading to a same effect:

$$RBE_S(Z, LET) = \left.\frac{D_{\text{ref}}}{D_{\text{ion}}(Z, LET)}\right|_{\text{same effect}}, \tag{1.6}$$

where $D_{\text{ref}}$ is the dose for a reference radiation (generally X-ray) and $D_{\text{ion}}(Z, LET)$ is the dose for ion radiation with a charge Z at a given LET. In the left panel of Figure 1.7, RBE values for cell inactivation are indicated for two significative effect levels 1% and 10%.

A collection of RBE values for different radiation quality, different biological target, and different delivery techniques can be found on the PIDE (particle irradiation data ensembles) database (Friedrich et al., 2012). In the right panel of Figure 1.7, RBE in-vitro data as a function of the LET are shown for 10% survival fraction.

In the case of ion radiation the RBE values can be very significant (RBE $\gg 1$) and, for this reason, in ion therapy treatment planning applications it is one of the most important quantities. The RBE allows, indeed, to calculate the so called biological RBE-weighted dose and optimize the treatment plans in

order to guarantee a uniform biological effect over the tumor minimizing the damage to the surrounding healthy tissues.

However, because of the large variability of the RBE and the large number of effects contributing to it, finding a model able to predict the RBE with a good accuracy for all tissue types is a difficult task. Several approaches have been developed over the years to calculate the RBE but at the moment only the LEM (Scholz and Kraft, 1996), based on an amorphous track structure approach, and the MKM (Hawkins, 2003), based on a microdosimetric approach, have been adopted for clinical application (Scifoni, 2015).

## 1.5 Oxygen effect

The oxygenation level significantly affects the radiosensitivity of a tissue. Tissues characterized by a restricted oxygenation condition result to be more radioresistant in comparison with well oxygenated ones. This effect has been observed for the first time by Holthusen (1921) but a complete description and quantification of the oxygen effect under low LET radiation arrived only 30 years later with the work of Gray et al. (1953).

Unfortunately, it is not unfrequent to find tumors presenting regions with reduced oxygenation: due to the rapid proliferation of cancer cells and their high metabolic consumption tumors are often not sufficiently vascularized, limiting the oxygen supply to the cells. As an example, Figure 1.8 shows a PET image of a NSCLC (non-small cell lung cancer) where a strong oxygenation heterogeneity can be observed.

Clinically, the difficulties in treating tumors in hypoxic conditions, or with hypoxic regions, are considered to be one of the main limiting factors for the tumor control in radiotherapy (Fyles et al., 2002; Tinganelli et al., 2015). On the left panel of Figure 1.9 the progression free survival from a prospective program evaluating the impact of hypoxia in patients with cervix cancer is presented (Fyles et al., 2002). Patients with large hypoxic tumors show a significantly reduced disease-free survival curve compared to these with better oxygenated tumors. In analogy, on the cellular level, the pronounced radioresistance of CHO cells in hypoxic conditions is clearly visible on the right panel of Figure 1.9.

In radiation biology the increased radioresistance in reduced oxygenation conditions is quantified by the oxygen enhanced ratio, OER, defined, for a given biological effect, as the ratio between the dose values in hypoxic and in fully oxygenated conditions

$$OER(pO_2) = \frac{D_{pO_2}}{D_{\text{normoxic}}}\bigg|_{\text{same effect}}, \tag{1.7}$$

where $pO_2$ is the partial oxygen pressure, $D_{normoxic}$ is the dose in fully oxygenated condition (in air $pO_{2_{\text{air}}} = 21\%$) and $D(pO_2)$ is the dose needed to get the same effect under hypoxia ($pO_2 < pO_{2_{\text{air}}}$).
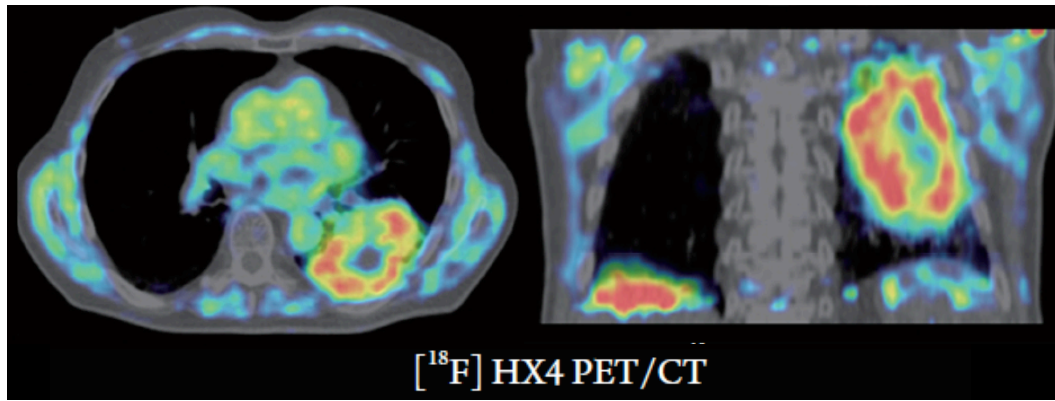
**Figure 1.8.:** Example of a clinical PET image of an NSCLC (non-small cell lung cancer) showing a strong oxygenation heterogeneity with a hypoxia [$^{18}$F]HX4-PET/CT scan (van Elmpt et al., 2013).
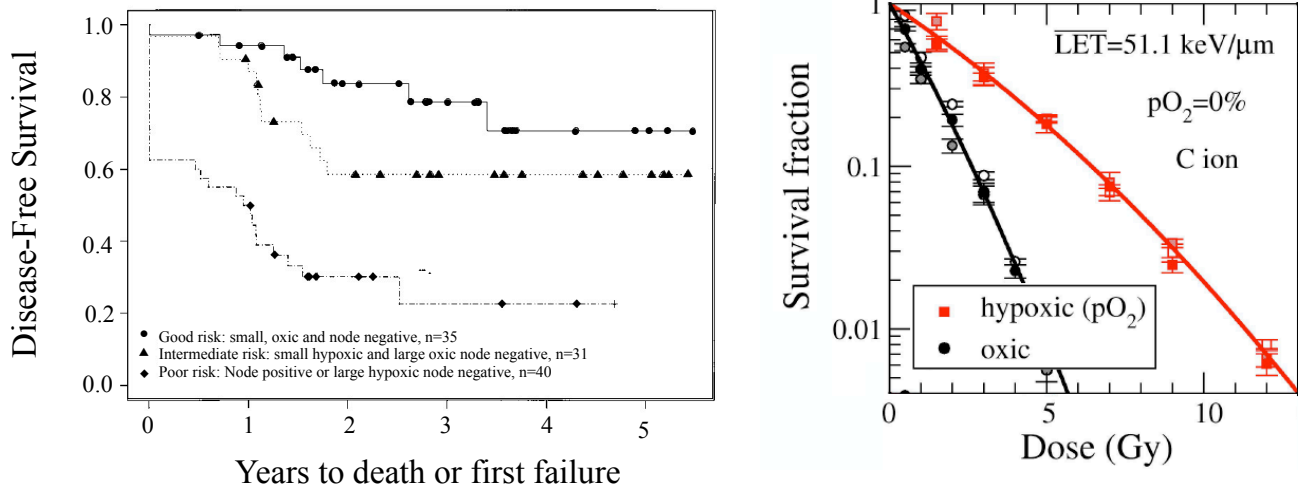


**Figure 1.9.:** Left panel: results from a prospective program for evaluating the impact of hypoxia in patients with cervix cancer (Fyles et al., 2002). Right panel: *in vitro* survival rate measurements on CHO cells irradiated with carbon ion radiation in oxic and hypoxic conditions (Tinganelli et al., 2015).

### 1.5.1 Dependences of the OER on the oxygen concentration and LET

In case of low LET radiation, the OER shows its maximum value of $\sim 3$ in anoxia ($pO_2 = 0\%$) and decrease when increasing the oxygen concentration until reaching unity in fully oxygenated conditions. At a fixed LET value, the dependence of the OER on the oxygen concentration can be expressed empirically according to Carlson et al. (2006) as:

$$OER(pO_2) = \frac{MK + pO_2}{K + pO_2} \tag{1.8}$$

with $M$ the maximum value of the OER and $K$ the oxygen concentration corresponding to the half maximum sensitization, i.e. $((M-1)/2)$. Figure 1.10 shows the evolution of the OER as a function of the $O_2$ concentration for V79 Chinese hamster cells irradiated with low LET radiation at different oxygenation conditions (Carlson et al., 2006).
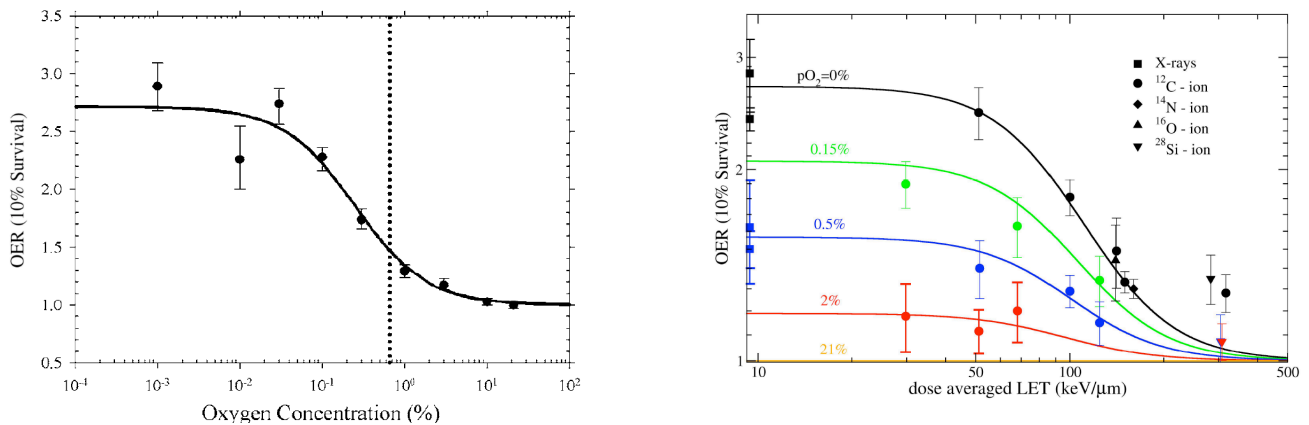


**Figure 1.10.:** Left panel: OER dependence on the oxygen concentration: experimental data are obtained from survival data of V79 cells irradiated with low-LET radiation while the curve is calculated with Equation 1.8 with $M = 2.7$ and $K = 0.25$ (Carlson et al., 2006). Right panel: OER dependence on the LET for different oxygen concentration. Experimental data are obtained from survival data of CHO cells irradiated with different radiation types (Tinganelli et al., 2015)

The oxygenation level, however, is not the only parameter affecting the OER: the oxygen effect results, indeed, to be less pronounced for high LET radiation and approaches unity for radiation with LET larger than $\sim 200 \mathrm{keV}/\mu\mathrm{m}$, as shown in the right panel of Figure 1.10. This latter behavior strongly motivated the growing interest in ion radiation therapy for treating hypoxic tumors and, for this purpose, new optimization techniques accounting for both LET and $\mathrm{pO_2}$ have been recently developed (Scifoni et al., 2013; Tinganelli et al., 2015; Sokol et al., 2017).

On the nanoscopic level, a complete description of the basic mechanisms underlying the oxygen effect is still missing. In the following, a brief description of the main processes which are supposed to be involved in the oxygen effect and its dependency on the LET is presented.

## 1.5.2 Nanoscopic processes underlying the Oxygen effect

On the nanoscopic level the oxygen effect is considered to be strongly related to the indirect effect of radiation (Sonntag, 1987) and in particular to the effect of the $\mathrm{OH}^\bullet$ radical (Hirayama et al., 2013). Generally it is described as a combination of two main phenomena: the first one related to the capability of the molecular oxygen to fix the cellular damage (known as the oxygen fixation hypothesis) while the second one relates to the toxic effect of the superoxide radical $\mathrm{O_2^{\bullet-}}$ and its protonated form $\mathrm{HO_2^\bullet}$, both produced as a result of water radiolysis (Colliaux et al., 2011).

The oxygen fixation hypothesis identifies the capability of molecular oxygen to chemically stabilize the radiation damage as one of the of the main processes involved in the oxygenation effect (Johansen and Howard-Flanders, 1965; Liu et al., 2015a).

Figure 1.11 shows a schematic representation of this process assuming the DNA as the target molecule. After the passage of radiation, the DNA can be damaged via the indirect action of radiation and become DNA-derived free radical, $DNA^\bullet$. This damage can generally be repaired by the action of antioxidants, such as glutathione antioxidant (GSH), and the biological molecule may revert to its original state (Beuve et al., 2015). However, in presence of molecular oxygen, the $DNA^\bullet$ can also react with the $O_2$ producing a peroxide radical $DNAOO^\bullet$. In this case, the action of an antioxidant fixes the damage by the formation of a hydroperoxide, DNA-OOH, which is a stable molecule (Beuve et al., 2015).
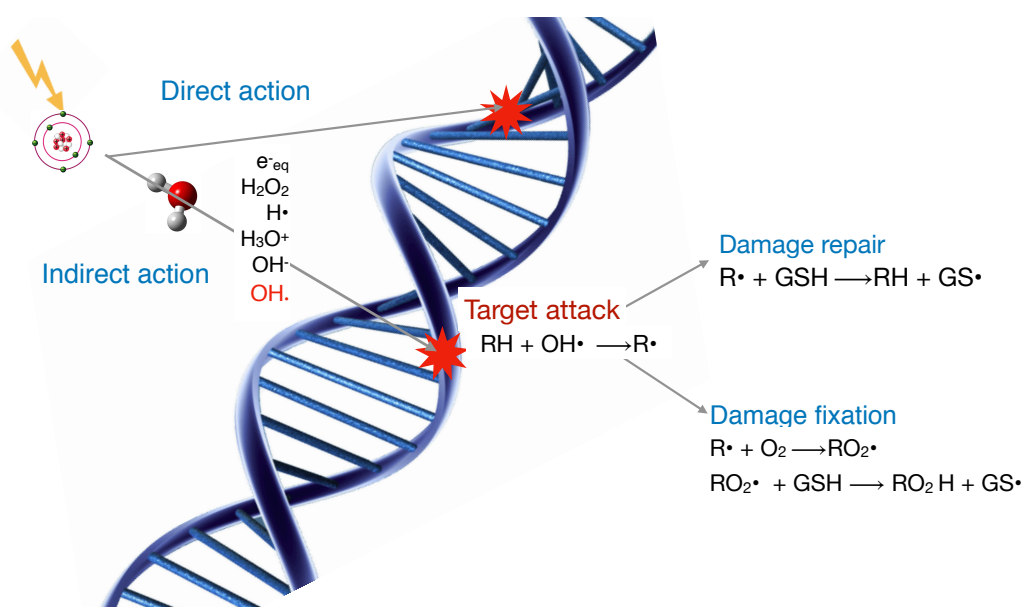


**Figure 1.11.:** Schematic representation of the action of the indirect damage on the target molecule R (in the figure represented by the DNA) and on how it can be fixed by the action of molecular oxygen is presented.

In hypoxic condition, due to the lack of molecular oxygen, the process of damage fixation will be less important and the radiation induced damage will be more efficiently repaired.

DNA, however, is not the only target of radiation effect, other biological molecules can be severely damaged as well. Another important scenario triggered by the presence of dissolved molecular oxygen is the peroxidation process of fatty acid, LH. Lipids are the main constituent of the cellular membrane and, in presence of a damage induced by a radical species $R^\bullet$, a complex chain of peroxidation reactions can take place leading to the destruction of the cellular membrane, (Repetto et al., 2012):

$$\text{Initialization:} \quad LH + R^\bullet \longrightarrow L^\bullet + RH$$

$$\text{Propagation:} \quad L^\bullet + O_2 \longrightarrow LO_2{}^\bullet$$

$$LO_2{}^\bullet + LH \longrightarrow L^\bullet + LOOH$$

$$\text{Secondary initialization:} \quad LOOH \longrightarrow LO^\bullet + OH^\bullet$$

$$LOOH \longrightarrow L^\bullet + HO_2^\bullet$$

$$\text{Termination:} \quad LO_2{}^\bullet + LO_2{}^\bullet \longrightarrow LOOL + O_2$$

$$LO_2{}^\bullet + R^\bullet \longrightarrow LOOR.$$

---
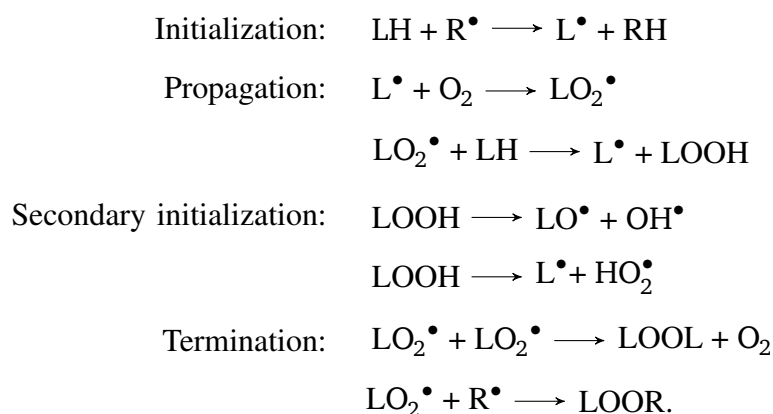
### Toxicity of $O_2^{\bullet-}$ and $HO_2^\bullet$

During the process of radiolysis of aqueous solutions, solvated electrons, $e_{aq}^-$, and hydrogen atoms, $H^\bullet$, are generated in a large amount. In presence of molecular oxygen dissolved in the water solution, these species can interact with the $O_2$ leading to the production of the superoxide anion, $O_2^{\bullet-}$, and its protonated form $HO_2^\bullet$:

$$e_{aq}^- + O_2 \longrightarrow O_2^{\bullet-}$$

$$H^\bullet + O_2 \longrightarrow HO_2^\bullet.$$
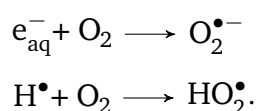
As described in Section 1.3.2 both these species belong to the so called reactive oxygen species and their toxicity is mainly due to their involvement in the lipid peroxidation chain and to their role in the production of highly toxic species, such as hydroxyl radicals $OH^\bullet$ and peroxynitrite ions $ONOO^-$.

Since the yield of the production of $e_{aq}^-$ and $H^\bullet$, and consequently the yield of $O_2^{\bullet-}$ and $HO_2^\bullet$, is larger for lower LET while it decreases with increasing the LET (see Section 1.5.3) these two ROS are suspected to mediate the oxygen effect by increasing the toxicity of radiation in living organisms (Colliaux et al., 2011). This hypothesis is supported by theoretical and experimental studies (Tomita et al., 1997; Watanabe and Saito, 2001; Goldstein and Czapski, 1995; Mikkelsen and Wardman, 2003; de Grey., 2004; Aikens, 1991). In particular, the work of Kuninaka et al. (2000) showed that an increased concentration in the mitochondria of $O_2^{\bullet-}$ (induced by suppression of the mitochondrial manganese SOD, Mn-SOD) correlates with an increased cell apoptosis after irradiation, confirming the theory that superoxide radicals might act as mediators of apoptosis.

A detailed study on the yield of production of these species in water radiolysis under different oxygen concentration and irradiation condition will be presented in Chapter 4.

---

### 1.5.3 Nanoscopic processes underlying the LET dependence of the Oxygen effect

Currently, a complete mechanistic description of the nanoscopic processes underlying the OER dependence on the LET is still missing. However, the problem has been widely investigated and several possible scenarios, not necessarily mutually exclusive, have been proposed.

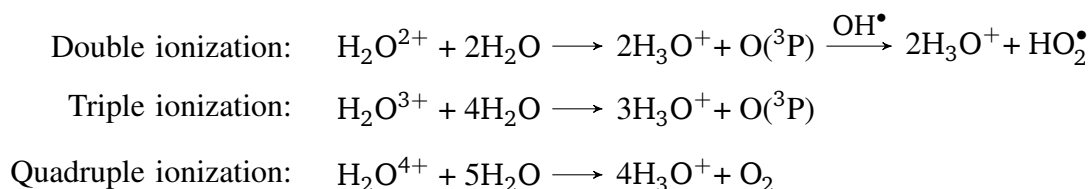The first one, presented for the first time by Alper (1956), is based on the ratio between the direct/indirect contribution of the radiation damage and is generally addressed as the "interacting radical hypothesis ". For high LET radiation, when the particle track is denser, there is a high probability of recombination between the radiolytic species which will lead to a reduced impact of the indirect radiation damage. Additionally, the radical-radical recombination competes also with the interaction between the radiolytic species and the molecular oxygen dissolved in the target, limiting also the yield of production of $O_2^{\bullet-}$ and $HO_2^{\bullet}$ (Colliaux et al., 2011). This interacting radical hypothesis is supported by both theoretical and experimental studies showing, for high LET irradiation, a decreased yield of some of the most dangerous radiolytic species, such as $OH^{\bullet}$ and $e_{aq}^{-}$ and, in oxygenated media, $O_2^{\bullet-}$ and $HO_2^{\bullet}$ (Hill and Smith, 1994; Naleway et al., 1979; Burns and Sims, 1981; Michael, 1996; Tomita et al., 1997; Ballarini et al., 2000; Ito et al., 2006; Colliaux et al., 2011). This scenario, where the decrease of the oxygen effect when increasing the LET is interpreted as a result of a reduced impact of the radical damage, seems to be confirmed by *in vitro* studies aimed at the evaluation of the contribution of the indirect/direct damage for different LET radiation (Hirayama et al., 2009; Ito et al., 2006).

This latter findings can be justified, also, by an increased impact of the direct damage of radiation. In case of densely ionizing radiation, the complexity and localization of the damage can become so important and so difficult to repair that the biological endpoint is not affected by the target oxygenation level. This theory has been generally identified as the lesion multiplicity model and has been supported by numerous groups (Ward, 1994; Michael, 1996).

An alternative scenario is the so called "oxygen in the track". This hypothesis was developed for the first time by Neary (1965) and is based on the hypothesis that $O_2$ can be generated in the center of high LET ion tracks, locally restoring a normoxic condition.

This theory has been supported by the experimental observation of molecular oxygen formation in the inner part of ion tracks (Sauer Jr et al., 1978; Baverstock and Burns, 1981) and recently advanced Monte Carlo track structure codes (Meesungnoen and Jay-Gerin, 2005, 2009; Meesungnoen et al., 2003; Gervais et al., 2006, 2005) estimated the production yields of $O_2^{\bullet-}/HO_2^{\bullet}$ for different LET radiations. In their work, Meesungnoen and Jay-Gerin (2005, 2009) and Gervais et al. (2006, 2005), suggested that multiple ionization processes of water molecules could explain, at least in part, the oxygen effect. The basic principle is that multiple ionization of water molecule can generate oxygen atoms O, which, in a second step, can produce $HO_2^{\bullet}$ by reacting with the $OH^{\bullet}$ radicals formed along the track by water radiolysis and $O_2$ interacting between themselves (Meesungnoen and Jay-Gerin, 2005):

$$\text{Double ionization:} \quad H_2O^{2+} + 2H_2O \longrightarrow 2H_3O^+ + O(^3P) \xrightarrow{OH^{\bullet}} 2H_3O^+ + HO_2^{\bullet}$$

$$\text{Triple ionization:} \quad H_2O^{3+} + 4H_2O \longrightarrow 3H_3O^+ + O(^3P)$$

$$\text{Quadruple ionization:} \quad H_2O^{4+} + 5H_2O \longrightarrow 4H_3O^+ + O_2$$

However, even if this theory got a lot of success and has been largely investigated during the last ten years, the exact mechanisms and the cross sections for multiple ionization and the dissociation channels for multiply ionized water molecules, are still not completely established. Additionally, the oxygen concentration in the track produced by multiple ionization seems to be solely insufficient to explain the oxygen effect (Colliaux, 2009).

## 1.6 Nanoparticles as radiation sensitizers

Given the broad success of charged particle therapy, the possibility to develop new advanced techniques to further improve the efficacy and range of applicability is raising a great interest in the scientific community. One of the most studied aspects is the possibility to improve the tumor targeting, maximizing the so called peak-to-base ratio, i.e. the ratio between the dose delivered to the tumor (which has to be maximized) and the dose delivered the healthy tissue seated in the entrance channel of the ion beam (which has to be minimized). In this direction, in the last ten years, a large number of studies were oriented towards a combined treatment including radiosensitizers.

Among these compounds, a large interest has been raised by high atomic number (Z) nanoparticles (NPs). Additionally to their capability to enhance the radiation effect, NPs result to be particularly advantageous because, thanks to their small size (diameter < 200nm), they tend to accumulate in tumor tissue while being secreted from normal tissues: this phenomenon, facilitated by the porous blood vessels near the tumor, is called enhanced permeability and retention effect (EPR) and is at the basis of many passive tumor targeting techniques (Peer et al., 2007; Conde et al., 2014; Haume et al., 2016; Lacombe et al., 2017). The high absorption coefficient for X-rays and the possible application of some of these nanoparticles as a contrast agent in clinical exams, e.g. gadolinium NPs for MRI, make these NPs particularly suitable for *theranostic* applications: the simultaneous use of NPs for therapy and diagnosis.

The first study demonstrating the radiosensitization efficacy of nanoparticles was carried out using 1.9 nm gold nanoparticles (AuNPs) delivered to mice exhibiting mammary carcinoma prior to X-ray irradiation (Hainfeld et al., 2004). In their work, the authors showed a 1 year survival of 86% in mice treated with NPs versus 20% in mice irradiated without the NP injections, Figure 1.12. After this first success, a long series of *in vitro* and *in vivo* experiments confirmed the large efficacy of AuNPs with X-ray radiation. Other nanoparticle types have been investigated as well. Among these only two NPs have been already transferred to the clinic: AGuIX, based on ultrasmall gadolinium NPs (produced by NH TherAguix, Lyon, France) and hafnium NPs NBTXR3 (produced by Nanobiotix, Paris, France) (Lacombe et al., 2017). An extensive overview of the major progress to date from the experimental, modeling and simulation studies on the radio enhancement effect of NPs with both photon and ion radiation can be found in (Kuncic and Lacombe, 2018)

### 1.6.1 Physical processes underlying NPs sensitization effect

On the nanoscale, the observed radiosensitization effect of NPs is generally explained as a localized dose enhancement effect due to an increased production of secondary electrons in the vicinity of the NP (McMahon et al., 2011). Low to medium energy photon radiations as well as charged particle radiations have, indeed, a larger interaction cross section for high Z material with respect to biological tissues; resulting in a larger density of ionization and excitation processes within the NP (Haume et al., 2016). Additionally, ionized and excited NP molecules undergo a series of process of recombination resulting in the production of fluorescent photons and Auger electrons. All these secondary species can be produced in a very broad energy range (between few eV and few MeV in case of delta electrons) and they can either deposit their energy in the surrounding medium, increasing the dose deposition around the NP,
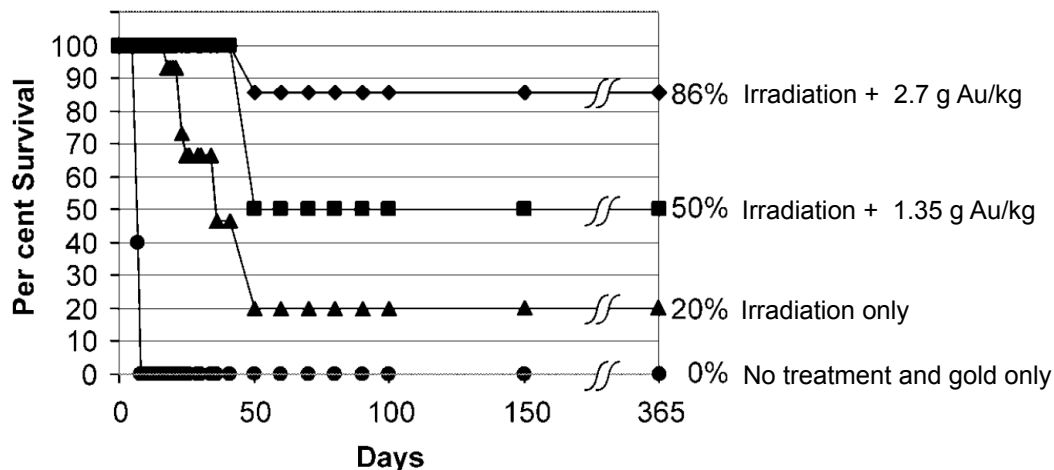
**Figure 1.12.:** Survival fraction of mice exhibiting mammary carcinoma after different treatment strategies. Circles: no treatment or gold only treatment without irradiation. Triangles: Irradiation only with 26 Gy 250 kVp X-ray. Square: X-ray irradiation after i.v. injection of 1.35 g Au/kg gold nanoparticles. Diamonds: X-ray irradiation after i.v. injection of 2.7 g Au/kg gold nanoparticles. A significant sensitization effect of gold nanoparticles is observed. Adapted from (Hainfeld et al., 2004).

or interact with neighboring NPs (Kuncic and Lacombe, 2018). In particular, while delta electrons and fluorescent photons are generally produced with high energies and their penetration depth can be in the order of cm in tissue, Auger electrons are generally stopped within the first 100 nm and are considered the main responsible of a localized dose enhancement in the close vicinity of the NP (Kuncic and Lacombe, 2018).

In the case of photon radiation the microscopic processes underlying nanoparticle sensitization are fairly understood, a large number of experimental studies have been carried out and simulation studies demonstrated that a significant sensitization effect can be achieved simply including the enhanced local dose deposition due to the increased Auger electrons production (McMahon et al., 2011).

A different scenario emerges, instead, for ion radiation. In this case, the local dose enhancement induced by secondary electrons can not justify the radiosensitization evidence found both in molecular scale processes (Usami et al., 2005, 2007; Porcel et al., 2010, 2012, 2014; Schlathölter et al., 2016), *in vitro* (Usami et al., 2008; Polf et al., 2011; Kim et al., 2010; Li et al., 2016; Liu et al., 2015b, 2016) and *in vivo* (Kim et al., 2010, 2012). A complete overview of all the experimental results of NP sensitization under ion radiation has been proposed by Lacombe et al. (2017).

### NP sensitization effect with ion radiation

For ion radiation, the dose deposition is very localized along the track and the interaction probability between the ion, or the secondary electrons, with the NPs, is small. For therapeutic proton fluences Lacombe et al. (2017) estimated the direct hit probability to be between $10^{-3} - 10^{-4}$. In addition, because of the very dense dose deposition along the ion track, an extremely high dose has to be induced by the NP in order to give a significant biological effect (Lacombe et al., 2017; Cho et al., 2016).
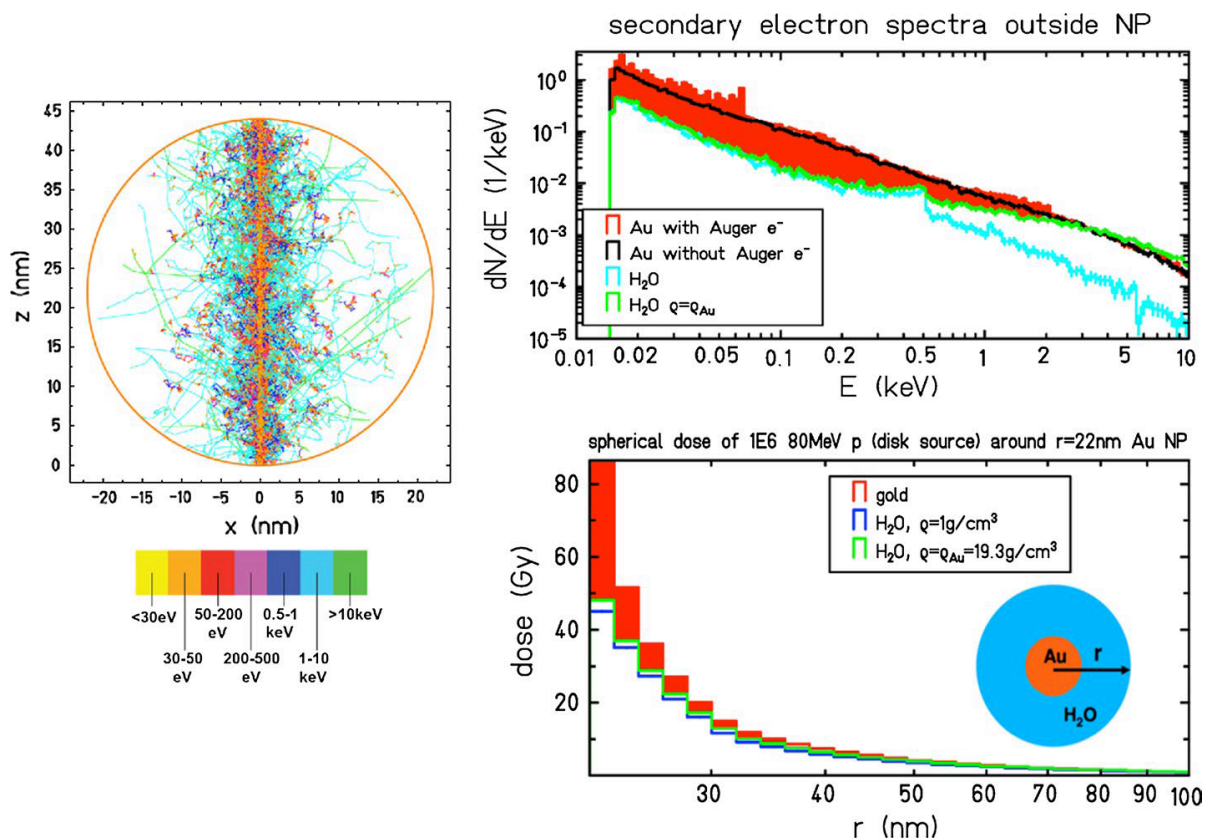
**Figure 1.13.:** TRAX simulations of gold nanoparticle sensitization for a 22 nm NP irradiated with 80 MeV proton radiation, adapted from Wälzlein et al. (2014). Left panel: simulation of a proton track structure within the NP. Right upper panel: simulated spectra of secondary electron escaping from the nanoparticle in case of a gold nanoparticle, water nanoparticle and a dense water nanoparticle (composed by water but with the density of gold). A significant contribution of low energy Auger electrons can be observed. Right-lower panel: dose deposition in the water sphere surrounding the NP in case of AuNP, water NP, and dense water NP.

Wälzlein et al. (2014) were the firsts to approach the problem of NP sensitization in ion radiation. In their work, the authors estimated the local dose enhancement effect for proton radiation traversing NPs of different materials with the Monte Carlo code TRAX. As shown in Figure 1.13, a significant contribution of Auger electron to the local dose deposited in the vicinity of the NP has been observed. However, the calculated dose enhancement is not sufficient to justify the large biological effect experimentally observed (Wälzlein et al., 2014). These findings have been later on confirmed by the study of Ahmad et al. (2016) and an additional support came from Lin et al. (2015), who showed that, in case of proton irradiation, the NPs uptake and their localization inside the cell is much more crucial than with photon radiation. With photons, the large production of long range photoelectron and the abundance of radical species generated, allow the nanoparticles located in the cytoplasm to contribute to the DNA damage (Haume et al., 2016; Gao and Zheng, 2014). In the ion case, instead, the range of secondary electrons is shorter and the resulting indirect damage contribution is smaller. Thus, in order to observe an

enhancement effect comparable to the one obtained with photons, it is necessary to increase significantly the NPs uptake (Lin et al., 2015).

Alternative sensitization channels have, then, to be considered. Verkhovtsev et al. (2015a,b) suggested that, in case of ion radiation, an additional significant increase of secondary electrons can be emitted via collective excitation channels such as surface plasmon excitations. In their work, the authors demonstrated that, including this effect, the number of low energy electrons generated by the NP can be up to an order of magnitude larger compared to the one produced by direct ionization (Verkhovtsev et al., 2015a,b).

Mechanisms on the biological and chemical pathway might also be important: Kobayashi et al. (2010) and Porcel et al. (2010) envisaged that charged NPs (after the emission of photoelectrons and Auger electrons) can generate an instability in the surrounding medium, facilitating the water molecule dissociation and increasing the radical yield. This hypothesis is in accord with the observations of Sicard-Roselli et al. (2014) and Paudel et al. (2015), in low LET radiation field. In both these works an OH$^\bullet$ radical production, not compatible with the radical production induced only by secondary electrons, has been measured. In addition, Paudel et al. (2015) pointed out that this effect is more important for larger surface-to-volume ratio nanoparticles, confirming the hypothesis that surface effects might play an important role in the NP sensitization effect.

Even though a thorough theoretical description of the enhanced radical production in presence of high Z material is not available and this effect has still to be deeply investigated, these observations are very promising, especially in the context of using the NPs in conditions where, as in the case of hypoxia, the reduction of the indirect damage by radicals is supposed to be the main responsible of tumor radioresistance. In this thesis, the radical production in the vicinity of NP under different oxygenation condition will be studied in Chapter 5.

Figure 1.14 shows a schematic representation of the main physical and chemical processes assumed to be at the basis of nanoparticle sensitization from ion beam radiation.
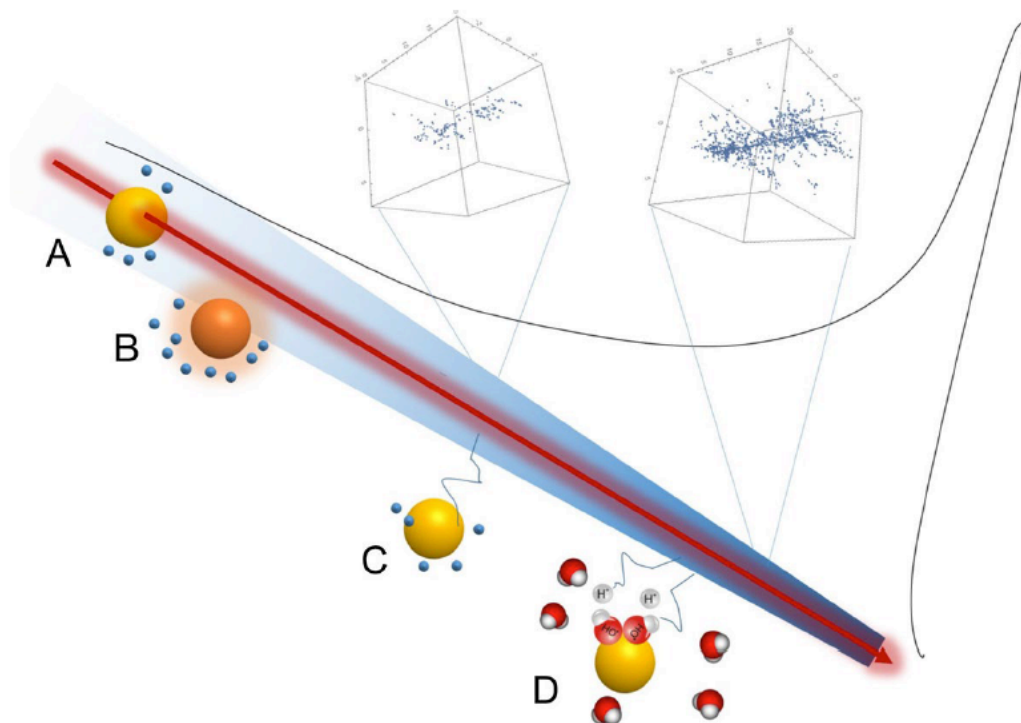
**Figure 1.14.:** Schematic representation of the main physical and chemical processes argued to be involved in the nanoparticle radiosensitization for ion beam radiation (Lacombe et al., 2017). A) Enhanced production of secondary electrons, Auger electrons, and Auger cascades. B) Plasmon surface excitations followed by an increased production of secondary electrons. C) electrons produced in the primary track interacting with the nanoparticle. D) Enhancement of the radiolytic species production via processes catalyzed by the nanoparticle presence and surface effects.

# 2 The TRAX code

TRAX is a Monte Carlo particle track structure code constantly developed during the last twenty years at GSI Helmholtzzentrum für Schwerionenforschung GmbH, Darmstadt (Krämer and Kraft, 1994; Wälzlein et al., 2014a). This program is designed to describe the passage of electrons and ions (in all the possible charge states) through different materials. The trajectories are followed interaction by interaction and all the positions and energy depositions are evaluated event by event.

The code allows the evaluation of the most important physical endpoint like electron backscattering and transmission coefficients, electron spectra (energy and angular resolved) and ionization distributions. In addition, many relevant radiation quantities like radial and depth dose distributions, W-values, microdosimetric quantities such as the lineal and specific energy transfer can be calculated as well.

The energy range covered by TRAX goes from a maximum energy of few hundred MeV/u for ions and few MeV for electrons to a lower threshold of between 10 to 1 eV. These characteristics make the code particularly suitable for describing the passage of radiation through dosimetric devices and radiation damage in a biological system.

Thanks to its modular structure, it is particularly suitable to be extended in different directions such as the implementation of new interaction processes or, as it will be shown in the next chapter, the extension at more advanced stages of radiation effect. Additionally, all the input parameter such as projectile, source and target characterization and the interaction models are loaded from external files collected in specific databases. Thus, they might be revised, updated and extended without modifying the code.

Simulated geometry has to be defined and loaded from an external file. The simulated volumes can be cylinders, spheres or boxes or a combination of them and can consist of all the possible material supported by TRAX. The target material can be atomic or molecular or a mixture of atomic and molecular. For simulations in living systems, water is considered as a tissue equivalent material. The different targets are described by the physical properties of the medium, like the density and shell structure information (including binding energies, number of electrons in a specific shell and their kinetic energy). As far as possible, parameters are taken from experimental values.

As in all the track structure codes, the reliability and the accuracy of the simulations crucially depend on the available cross sections. These cross sections can be either calculated from semi-empirical and analytical formula, either read from external cross section tables. Recently the whole set of available cross sections has been updated and, in the next sections, a brief summary of the interaction models implemented in TRAX will be presented.

## 2.1 Cross sections

In a track structure code, the availability of robust and trustable cross section tables is of primary importance. The reliability and the accuracy of the whole simulation depend on the capability of reproducing, as precisely as possible, all the possible interaction events, thus on the selection of the cross sections set.

In particular, cross sections for electron interaction play a very important role: while the cross sections for ions are needed only to describe the interaction of the primary projectile, the electron cross sections are used also to simulate all the interaction of the secondary and higher order electrons generated along the primary radiation trajectory, which make up most of the energy loss process.

In TRAX the interactions considered, for electron radiation, are electronic excitation, ionization, elastic scattering, Auger electrons production and plasmon excitation. For many target materials, the used cross sections allow the differentiation between ionization of certain sub-shells and handle excitation as a separate interaction rather than using a complete description for inelastic scattering. This feature is, however, fundamental to follow radicals production; in this case, the shell specific excitation cross sections are, indeed, necessary.

For ion projectiles, the ionization cross sections are computed internally to the code, while excitation cross sections are calculated by scaling the cross sections for electrons traveling at the same velocity. This latter approach is, however, valid only for high-energy ions: in the case of protons for energies larger than 500 keV (Nikjoo et al., 2012; Dingfelder et al., 2000). In the low energy regions different approaches, such as the semiempirical model developed by Miller and Green (1973) based on the electron impact excitation, might yield more accurate results. However, at the current state, the TRAX code still does not account this possible extension.

Energy losses due to bremsstrahlung and nuclear fragmentation are also neglected. However, concerning the nuclear fragmentation, the neglection can be justified considering that the cross sections for this process are several orders of magnitude smaller than excitation, ionization, and elastic scattering.

Recently a large part of the implemented cross section in TRAX have been revised and extended (Wälzlein, 2013; Wälzlein et al., 2014; Wälzlein et al., 2014a,b).

In this section, a brief overview of all the cross section sets used in this work will be presented with a particular focus on the cross section for water and gold target materials. A more extended description of all the cross section implemented in TRAX can be found in Wälzlein (2013).

### 2.1.1 Ionization

#### Ion ionization

The standard cross sections implemented on TRAX for ion induced ionization rely on the Binary Encounter Approximation (BEA).

This approach treats the interaction of an incident, light and structureless, ion and the electron as a binary encounter between two free classical particles of velocity respectively $v_p$ and $v_e$ (Krämer and Kraft, 1994). This condition is well met for small impact parameters between the incident and the target electron.

The electron is assumed to be free but the potential of the target nucleus is implicitly included in the momentum distribution of the electron and in the ionization potential. The calculation yields a triple differential cross sections: differential in the energy transfer and on the electron ejection angle. The energy and angular distribution of the ejected electron can be determined integrating over the initial velocity distribution of the target electron.

The mean kinetic energy of secondary electrons predicted by the BEA method is in the order of 100 eV with a maximum energy transferred in the case of forward scattering (Krämer and Kraft, 1994). In this case, because of classical kinematics, the secondary electron obtains twice the velocity of the projectile ion: for an ion projectile with an energy of 10 MeV/u, the maximum energy transferred to a secondary electron is 20 keV (Krämer and Kraft, 1994). The approach allows the calculation of the ionization cross section for all the possible combination of target and projectile but its range of application is restricted to light and structureless ions and is known to underestimate the backward emission at high energy, (Krämer and Kraft, 1994).

In addition to the BEA, for several materials, the Rudd model for the calculation of the ion induced ionization cross section is implemented as well. This approach allows the calculation of improved ionization cross sections applying shell dependent empirical corrections and it relies on parameters fitted to experimental data. However, being dependent on measurements, this model can be used only for specific target materials where these data are available (He, Ne, Ar, Kr, $H_2$, $N_2$, $O_2$, $H_2O$, $CO_2$, $CH_4$, $C_3H_8$, $C_2H_4$ and C).

For heavy projectiles with nuclear charge $Z_0$ interacting with a medium at a given energy, an effective charge $Z_{eff}$ is assumed according to Barkas (1963) , in order to account for the effect of electron capture at low energy:

$$Z_{eff} = Z_0 \big[ 1 - exp\big( -125\beta Z_0^{-2/3} \big) \big]; \qquad (2.1)$$

with $\beta = v/c$ where v is the ion velocity and c is the speed of light.

In all the simulations presented in the present work the ion induced ionization in water have been always calculated with the empirical Rudd model while in gold target the cross sections have been computed with the BEA approach.

---

### Electron ionization

---

The total electron induced ionization cross sections, in TRAX, are computed for all the atomic and molecular target material using the binary encounter Bethe (BEB) model (Kim and Rudd, 1994).

This approach is based on a combination between the Mott theory, for hard collision processes, with the dipole interaction between the incident particle and the target electrons, for soft collisions (Kim and Rudd, 1994). This method provides shell specific electronic cross section without the need of empirical or fitting parameter (Kim and Rudd, 1994). The information needed to calculate the cross sections are easily available for a large range of atomic materials, and, besides the electron shell occupation $N$, necessary parameters are: accurate experimental or theoretical data on shell specific values for the binding energy $B$ and kinetic energy of each bound electron $U$. The formula to obtain the contribution of a specific shell to the total cross section is (Kim and Rudd, 1994):

$$\sigma(T) = \frac{S}{t + (u+1)/n} \left[ \frac{\ln(t)}{2} \left( 1 - \frac{1}{t^2} \right) + \left( 1 - \frac{1}{t} - \frac{\ln(t)}{t+1} \right) \right] \qquad (2.2)$$

where T is the energy of the incident electron, $t = T/B$, $u = U/B$ and, considering the Bohr constant $a_0$=0.52918 Å and the Rydberg constant R=13.6057 eV, $S = 4\pi a_0^2 N (R/B)^2$. TRAX also considers a relativistic version of the BEB model, derived by (Kim et al., 2000).
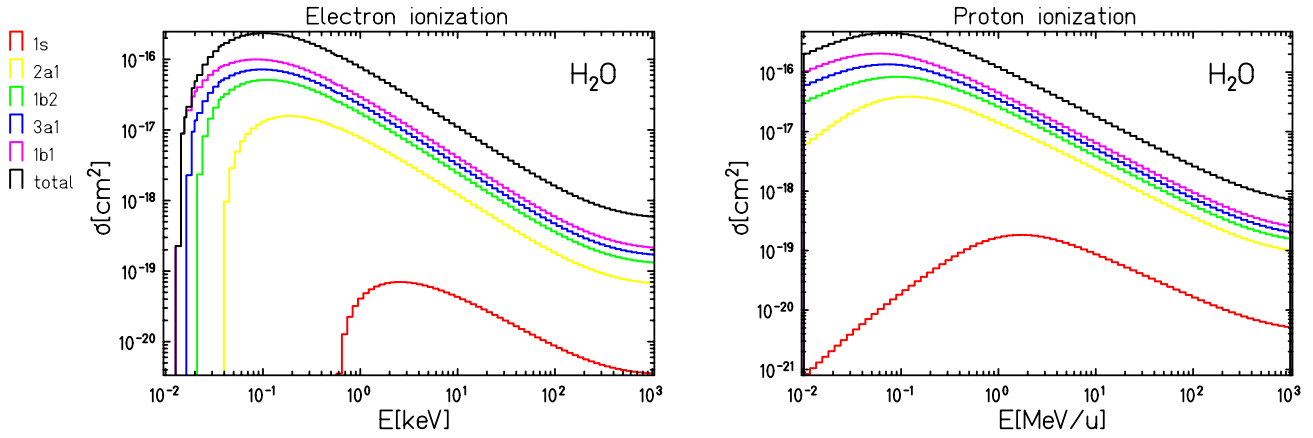
**Figure 2.1.:** Individual electron ionization cross sections for water target implemented in TRAX. Left panel: electron ionization cross section. Right panel: proton ionization cross sections.
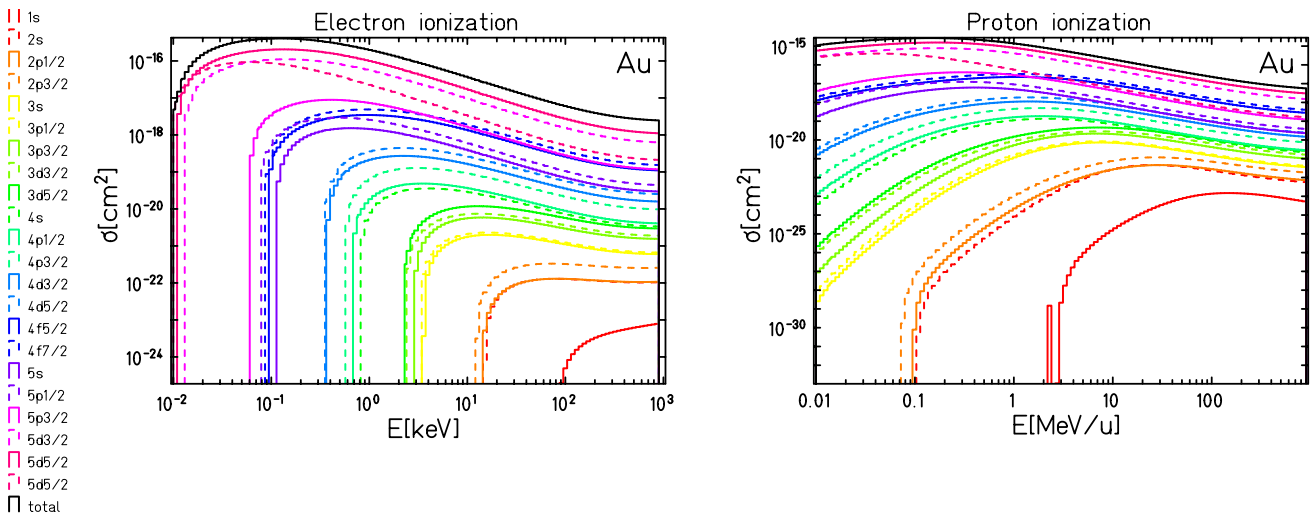


**Figure 2.2.:** Individual electron ionization cross sections for gold target implemented in TRAX. Left panel: electron ionization cross section. Right panel: proton ionization cross sections.

In TRAX the required input parameters have been recently revised and, as far as possible, parameters taken from experimental data have been selected (Wälzlein, 2013). For binding energies, experimental values proposed by Winter (2012); Williams (2000); Thomas (1997) have been adopted. Total cross sections strongly depend on the value adopted for the binding energy of the outermost shell: the larger contribution to the cross sections comes from the more external orbital since the cross section increases for loosely bounded electrons (lower binding energy values). Experimental data adopted for the outermost orbital binding energy have been taken from Kramida et al. (2013), when experimental values were not available, calculated binding energies have been taken from Perkins et al. (1991). In particular, concerning the two main target material considered within this thesis: the water binding energy values have been taken from Kramida et al. (2013) while for gold the values proposed by Perkins et al. (1991) have been adopted (Wälzlein, 2013). In Figure 2.1 and 2.2 electron induced and proton induced ionization cross sections have been reported for water and gold target material, which are the two material used in the framework of this thesis. The secondary electron emission angle is sampled according to Grosswendt and Waibel (1978).

## 2.1.2 Auger electrons

Auger electrons are electrons which can be emitted during the relaxation process taking place after an ionization event. After an ionization of an inner shell, a secondary electron is emitted leading to the formation of a vacancy. This vacancy is filled by an outer shell electron and, in this process, the excess energy can be transferred to a fluorescence photon or to another electron. This electron, called Auger electron, has a discrete energy corresponding to the difference between the binding energies of the involved shells and is isotropically emitted. The fluorescence photon emission is a competing process to the formation of Auger electron. The fluorescence probability depends on the atomic number and for a K-shell ionization is approximately proportional to $Z^4$. For low Z material, the photon production can be almost neglected while for gold atom the probability fluorescence emission after an ionization process in the K-shell reaches the 97%.

For high Z material there is also the possibility of emission of Auger electron cascades: if an inner shell of these materials gets ionized Auger electrons are emitted until the vacancy has moved to the outermost shell.

In TRAX the production of Auger electron, as well as cascades of Auger electron have been implemented by Wälzlein et al. (2014). The probability for different Auger transitions and fluorescent photons for atomic targets are taken from the Livermore Evaluated Atomic Data Library (Perkins et al., 1991), for water target, instead, Auger emission probabilities have been included according to experimental data from Siegbahn et al. (1975).

## 2.1.3 Electronic excitation

Electron induced excitations play a major role in energy losses for electrons at energies lower than 100 eV and, thus, in the transport of secondary electrons. Recently the set of TRAX electronic excitation cross sections have been updated by the implementation of new cross sections for a broader range of target materials and low energy electron excitations cross sections able to handle individually different

electronic transitions (Wälzlein, 2013). This is important when one is interested in sampling events dependent on the excitation channel, like different molecular dissociation processes and radical production, which is one of the crucial points of this work.

In a system with n possible electronic excitation transitions, the sum of the contribution of each excitation channel, $\sigma_i(T)$, gives the total electronic excitation cross section, $\sigma_{tot}(T)$; the different excitation channel differ only in the amount of energy needed in order to make the excitation. The mean energy loss can be calculated from the specific energy loss of each channel, $\Delta E_i(T)$, according to Equation 2.3, as a function of the kinetic energy $T$ of the projectile:

$$\sigma_{tot}(T) = \sum_{i=1}^{n} \sigma_i(T) \qquad \Delta E_{average}(T) = \sum_{i=1}^{n} \frac{\Delta E_i(T) \cdot \sigma_i(T)}{\sigma_{tot}(T)} \tag{2.3}$$

In TRAX the electron angular deflection after an electronic excitation process is considered to be negligible. The excitation is thus considered to be an interaction where only an energy loss occurs, and the projectile electrons stay on their propagation direction. The justification for this assumption comes from experimental results for electronic excitation in $N_2$, where a strongly forward peaked distribution of the electrons exciting molecular levels has been shown (Trajmar et al., 1983; Krämer and Kraft, 1994). Ion excitation cross section are obtained by scaling the cross sections for electrons traveling at the same velocity.

## Water

Excitation cross sections for electrons incident on water have been recently updated by Wälzlein (2013) according to Paretzke (1988); Green and Stolarski (1972); Nikjoo et al. (2006). This new set of cross sections distinguish between single excited states. In particular the 8 major excitation modes of $H_2O$ are considered: five molecular excitations ($A^1B_1$, $B^1A_1$, Rydberg A+B, Rydberg C+D and diffuse bands) and three dissociative excitations (H* Lyman $\alpha$, H* Balmer $\alpha$ and OH*). The energy losses required to reach these excited states range from 7.4 eV to 21.0 eV. In Table 2.1, the eight excitation states with the corresponding transition energies are reported.

The total excitation cross section can be obtained, according to Equation 2.3, summing up the contribution of all the individual cross sections of the single excitation levels. The capability of distinguishing between shell specific excitation is fundamental to follow radical production; in this case, indeed, the shell specific electronic excitation cross sections are necessary.

In order to describe the transport of sub-excitation electrons, i.e. electrons having kinetic energies below the first excitation level of water, a set of cross sections down to the very low energies have been included in the TRAX cross section database, according to measurements in amorphous ice (Michaud et al., 2003). The cross section data for amorphous ice are considered to have an uncertainty of 30-40% (Nikjoo et al., 2006; Michaud et al., 2003). These cross sections include 9 possible channels of excitation leading to a certain vibrational, librational, translational, bending or stretching modes of the molecule and allow to reduce the cut off for electrons to 1.7 eV. In the new extension of the TRAX code, this cross sections can be added to the electron excitation cross sections as an additional excitation channel.

In Figure 2.4 a complete set of electronic excitation cross sections for water and the mean energy loss are shown as a function of the incident electron energy. The contribution of the sub-excitation electrons

**Table 2.1.:** Excitation states for water implemented on TRAX with the corresponding transition energy, adapted fromNikjoo et al. (2006)

| Excitation state | Energy(eV) |
|---|---|
| $A^1B_1$ | 7.4 |
| $B^1A_1$ | 9.7 |
| Rydberg (A+B) | 10.0 |
| Rydberg (C+D) | 11.0 |
| diffuse bands | 13.3 |
| H* Lymann $\alpha$ | 21.0 |
| H* Balmer $\alpha$ | 21.0 |
| OH* | 9.5 |
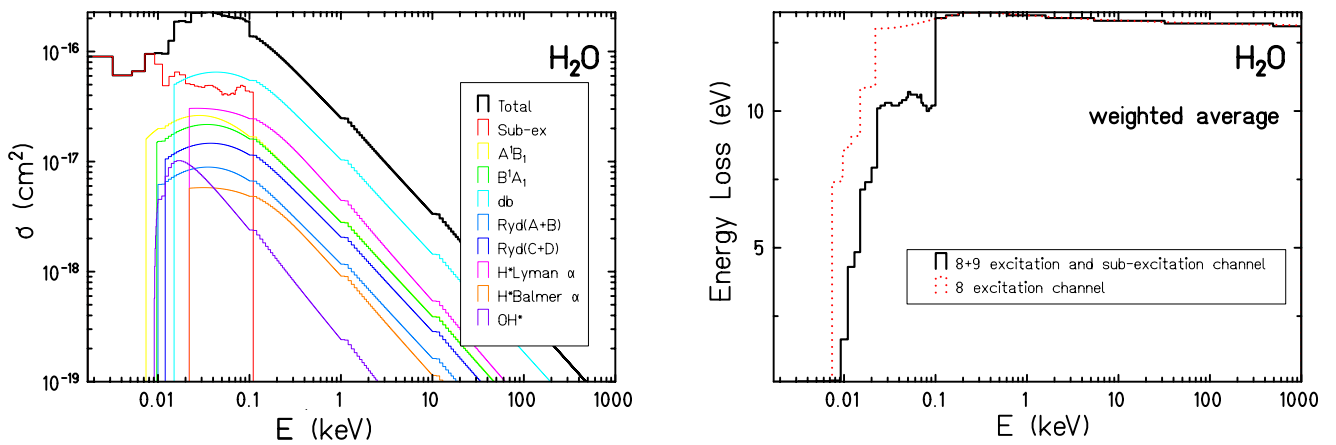


**Figure 2.3.:** In the left panel the total cross sections and individual excitation cross sections, for all the 8 excitation channel considered in TRAX, are shown as a function of the incident electron energy in water. On the right panel the mean energy loss, calculated as the average of all the contributions from the different transitions weighted by the cross sections of the individual channel, is represented including or not the contribution of sub-excitation channels.

to the total cross section is significant up to 100 eV. However, while the total cross section increase with the contribution of sub-excitation electrons, the mean energy loss, calculated as the average of all the contributions from the different transitions weighted by the cross sections, decrease correspondingly. This is because these excitation modes lead to very low energy losses, between 0.01 eV and 0.835 eV (Michaud et al., 2003).

Even though the contribution of the sub-excitation cross sections to the total stopping power is very small, the introduction of this additional channel results to be important for the implementation of the chemical extension of the code. It provides, indeed, information on the displacement of the sub-excitation electrons, when they are very close to the thermalization.

## Gold

The electronic excitation cross sections for gold targets implemented in TRAX are obtained by experimentally measured collision strengths for the three most important electron transitions: from the ground state to the $(5d^{10}6p)^2P_{1/2}$ state with an energy transfer of 4.6 eV, from the ground state to the $(5d^{10}6p)^2P_{3/2}$ state ($E= 5.1$ eV) and from the ground state to the $(5d^96s^2)^2D_{3/2}$ state with an energy loss of 2.7 eV (Maslov et al., 2008; Zatsarinny et al., 2008).

Since experimental data are available only up to certain energies, for higher energies the cross sections are extrapolated according to the Bethe-Born approximation (Wälzlein et al., 2014).

Theoretical approaches exist to calculate the contribution of further transitions, however, it has been shown that these methods are able to reproduce the measured energy dependency but not the absolute cross section value: theoretical cross sections are larger than the measured values by approximately a factor two (Maslov et al., 2008). Thus, considering also that the higher lying electron shells are not expected to contribute significantly to the total excitation cross section, further transitions are neglected (Wälzlein et al., 2014).

Validation for the used cross section has been performed indirectly by reproducing experimental data e.g. the stopping power of electron in gold (Wälzlein et al., 2014), and backscattered electron emission after proton impact on gold films, Figure 2.5 (Hespeels et al., 2017). A further validation of the gold cross sections implemented in TRAX will be presented in Chapter 5 where simulations and measurements of secondary electron transmission spectra after layers of gold of different thickness will be compared.

## 2.1.4 Elastic scattering

During elastic scattering processes, ions and electrons do not lose their energy. However, even though these processes do not contribute to the dose deposition and to the radiation damage, they define the spatial distribution of the secondary species around the ion trajectory and in the low energy region, elastic scattering in the dominant interaction (Krämer and Kraft, 1994). A reliable sampling of the elastic processes is, thus, extremely important when it comes to introduce or analyze processes strongly dependent on the positions of all the secondary and higher order particles, i.e. compute the transmission and backscattering coefficient or to follow the radical production and recombination, as it will be shown in Chapter 3.
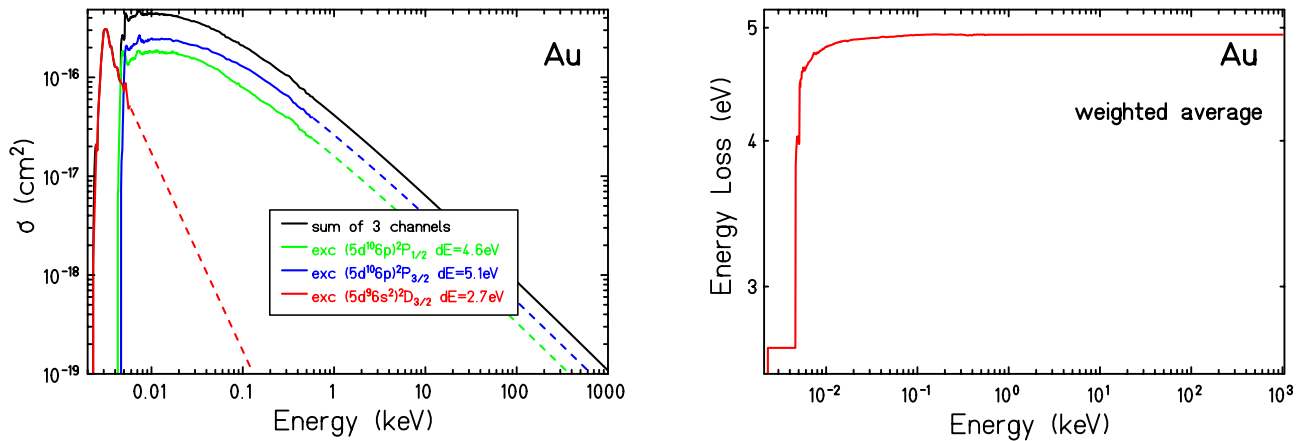
**Figure 2.4.:** On the left panel the total cross section and individual electron excitation cross sections, for the three excitation channel considered in TRAX, are shown as a function of the incident electron energy in gold. The cross section represented by a solid line corresponds to the measured value of Maslov et al. (2008), while the cross sections represented with a dotted line are extrapolated. On the right panel the mean energy loss due to electronic excitations, calculated as the average of all the contributions from the different transitions weighted by the cross sections of the individual channel, is represented.
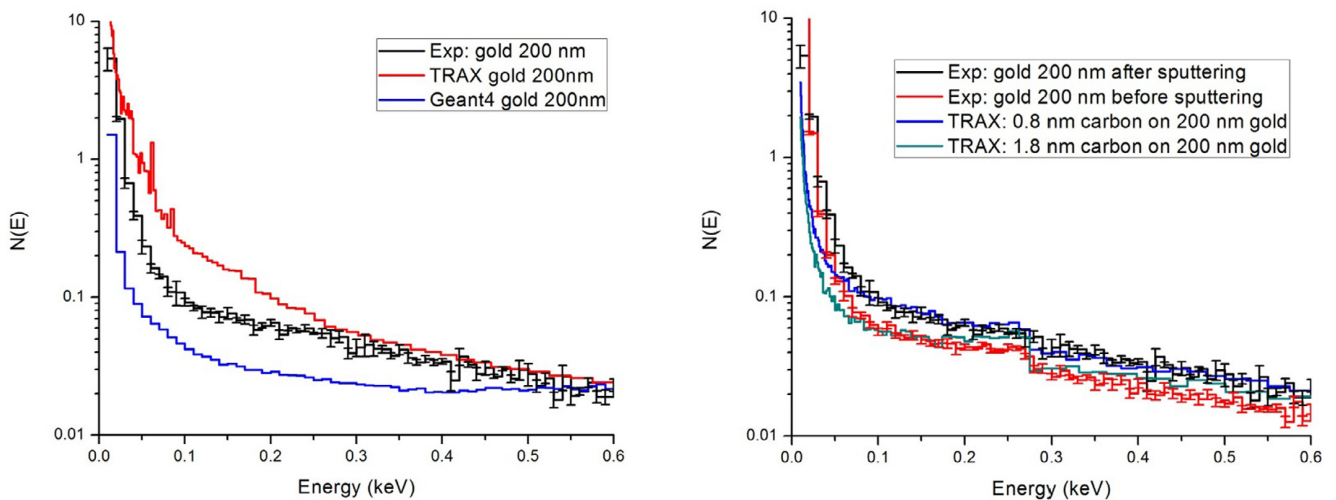


**Figure 2.5.:** Left panel: backscattering spectra of secondary electrons (from $0°$ to $80°$ with respect to the surface normal) generated by a 200 nm thick gold film irradiated with 2 MeV proton beam. Experimental data are compared with TRAX and Geant4 simulations. For energies lower than 300 eV TRAX simulation overestimate the experimental spectrum.Two reasons have been pointed out by the author of this work to justify this observation: pollution of the gold surface and underestimation of the very low energy electron ionization cross sections (Hespeels et al., 2017). Right panel: TRAX simulations repeated adding a thin film of carbon contamination (estimated by the authors to be respectively 1.8 nm and 0.8 nm thick before and after removing the pollutant material with a sputtering method) placed above the gold thin film (Hespeels et al., 2017).

In TRAX, for high and medium projectile energies, the elastic cross sections are calculated with the screened Rutherford approximation. In the low energy range and for high Z materials, cross sections from the ELAST database, relying on partial wave analysis (PWA), are adopted.

Screened Rutherford cross sections are easy and fast to calculate, the differential cross section can be computed, for a nucleus of charge $Z \cdot e$, with the well known formula (Berger et al., 1963):

$$\frac{d\sigma}{d\Omega}(E, \theta) = \frac{Z^2 \cdot e^4}{4E^2(1 - cos\theta + 2\eta)^2}. \tag{2.4}$$

The screening parameter, $\eta$, accounts for the screening of the nuclear charge by the orbital electrons and can be calculated as suggested by Berger et al. (1963) : $\eta = Z^{2/3} \cdot 1.7 \times 10^{-5} \eta_c(1/\beta^2 - 1)$, where $\eta_c$[1] is a semi-empiric screening parameter (Uehara et al., 1993; Wälzlein, 2013).

However, the range of validity of the screened Rutherford cross sections is restricted by the Born approximation ($v/c >> Z/137$, with $v$ the particle velocity and $Z$ the atomic number of the target), thus, for high projectile energy and low Z target material.

In water, these cross sections reproduce accurately the elastic scattering for electrons with energies larger than 500 eV. For lower energy electrons this approach underestimates significantly the large-angle scattering (Krämer and Kraft, 1994). For water target experimental elastic cross sections are used, when experimental data for water when experimental data were not available data for $H_2$ and $O_2$ have been used ($\sigma_{H_2O} = \sigma_{H_2} + 1/2\sigma_{O_2}$).

For high Z material, e.g. gold, and low energy region, cross sections calculated with more elaborate approaches like PWA provide much more correct results. PWA cross sections, often denoted as Mott cross sections, should provide the correct description of the elastic scattering but are difficult to calculate because of the need of a correct description of the scattering potential and the summation of terms up to infinity. For these reasons, in the latest version of TRAX single differential cross sections from the ELAST database, relying on PWA are implemented only for the low energy region (in gold targets for energies lower than 20 keV) (Wälzlein et al., 2014).

---

[1] the formulation of the semi empirical screening parameter, $\eta_c$, in the original version of the code was incorrect, with little impact on the simulation results. However, recently the correct formulation of the $\eta_c$ parameter has been implemented and, in the present work, all the calculation have been performed with the revised elastic cross sections.

# 3 Chemical extension of the TRAX code

According to the standard paradigm of radiation damage, the evolution of a particle track is assumed to be complete only when the track reaches the chemical equilibrium and can be described as a three stage process, where the different stages are characterized by a typical time scale: the physical, the pre-chemical and the chemical stage; schematically represented in figure: 3.1.

The physical stage is supposed to be complete $10^{-15}$s after the particles passage through medium and corresponds to the direct effect of radiation.

The pre-chemical stage (from $10^{-15}$s to $10^{-12}$s after the irradiation) consists in the production of chemical species by the relaxation, auto-ionization or dissociation of the ionized and excited water molecules. This stage is assumed to be concluded when all the chemical species and the sub-excitation electrons thermalize.

The chemical stage includes the Brownian diffusion and the reactions between all the chemical species generated during the pre-chemical stage. This stage is the longest and lasts up to $10^{-6}$ s; after that time the chemical development of the track is supposed to be over and the radical yields are assumed to be constant.

Most of the particle track structure codes are limited to the description of the so called physical stage of radiation effect, i.e. the first $10^{-15}$s after the irradiation. These standard codes are able to calculate the physical dose deposition in a medium through a complete description of all the excitation and ionization processes induced by both the primary and secondary particles on the target material. However, when describing the effect of radiation on biological media it has to be considered that up to 70% of the radiation effect on biological systems is induced indirectly by the action of water-derived free radicals. Water radiolysis, indeed, produces highly reactive free radicals able to inflict severe damages on biological medium. These are mostly: $OH^\bullet$, $H^\bullet$, $H_2$, $H_2O_2$, $OH^-$, $H_3O^+$ and $e_{aq}^-$.

Although the importance of the indirect effect of radiation on biological systems is well known and several dosimetric techniques are based on the detection of chemical reactions with radiation-induced free radicals, there are some gaps of knowledge on ion beam induced water radiolysis and on radical diffusion along a particle track. Very few experimental data are available for ion irradiation and many theories are not completely proven. In addition, a mechanistic description of the indirect effect of radiation in different irradiation condition is still missing. In this direction, many groups attempt to develop models of diffusion and interaction of chemical species. The first codes have been developed in the 1980s (Turner et al., 1983; Clifford et al., 1985, 1986; Turner et al., 1988; Terrissol and Beaudré, 1990; Pimblott et al., 1991; Hill and Smith, 1994) and progressively refined over the years. Among the more recent one can mention PARTRAC (Ballarini et al., 2000; Kreipl et al., 2008), CHEMKURBUK (Nikjoo et al., 2006; Uehara and Nikjoo, 2006), IONLYS-IRT (Meesungnoen and Jay-Gerin, 2005, 2009) Geant4-DNA (Karamitros et al., 2011), and RITRACKS (Plante, 2011a,b; Plante and Devroye, 2017).

Two main approaches have been adopted in order to follow chemical species: the so called independent reaction time (IRT) technique and the step by step approach.
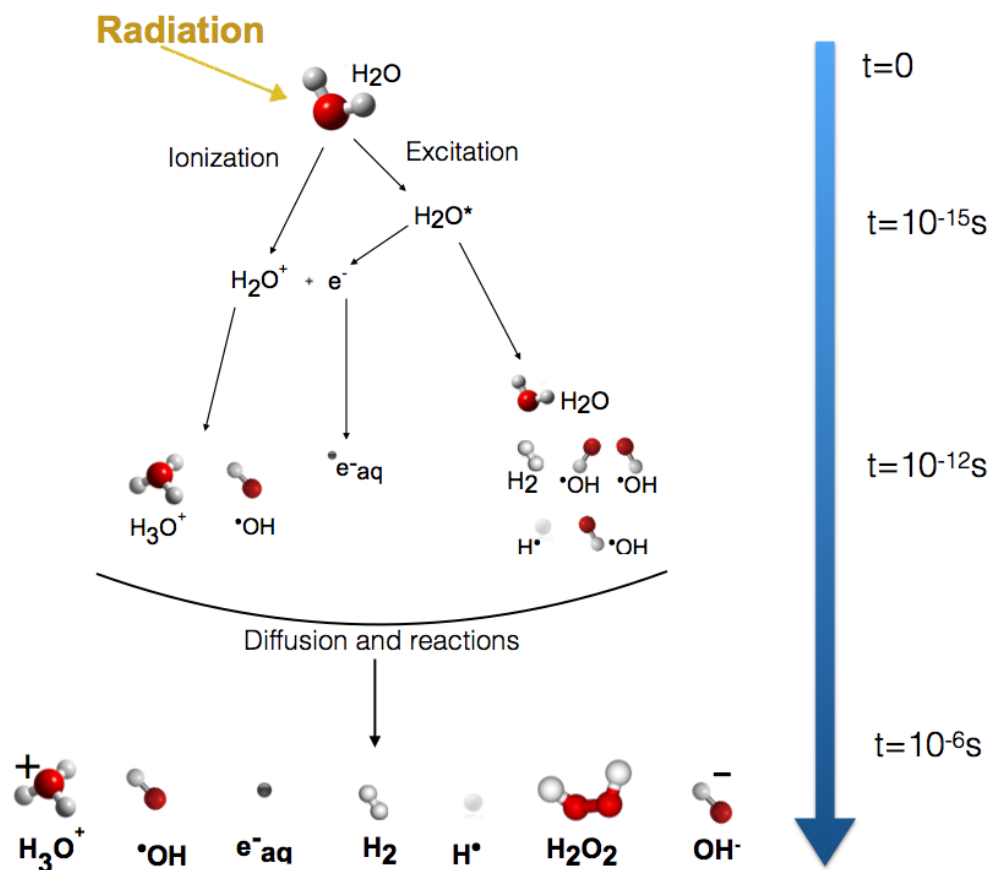
**Figure 3.1.:** Schematic representation of the time scale of events in water radiolysis leading to the primary products: $OH^\bullet$, $H^\bullet$, $H_2$, $H_2O_2$, $OH^-$, $H_3O^+$ and $e_{aq}^-$.

The first one is based on an approximate Monte Carlo method used to simulate reaction times. The main assumption is that the whole distribution of species can be modeled as a list of independent reactant pairs: the interaction time between two chemical species is independent of the presence of other molecules. Depending on the initial separation, for each pair, a reaction time is computed according to a time-dependent survival probability (Frongillo et al., 1998). Once all the reaction times are sampled, the reactions are realized in an ascending temporal order: every time a reaction takes place the reactants are removed from the list of possible reactions and new interaction time are computed for the reaction products. This method is computationally fast but it does not provide directly the position of the reactive species as a function of the time.

In the step by step approach, instead, the position of all the species is known at each time step of the simulation and it is possible to monitor every reaction. The diffusion of each molecule is followed with a resolution defined by the simulation time step, generally chosen in the order of picoseconds. For every time step, the reactive species diffuse randomly with a step size dependent on their diffusion coefficient. The reactions between reactants are defined via a proximity parameter generally indicated as the reaction radius. This method is more accurate than the IRT approach, however, it is up to few hundred times computationally slower (Frongillo et al., 1998).
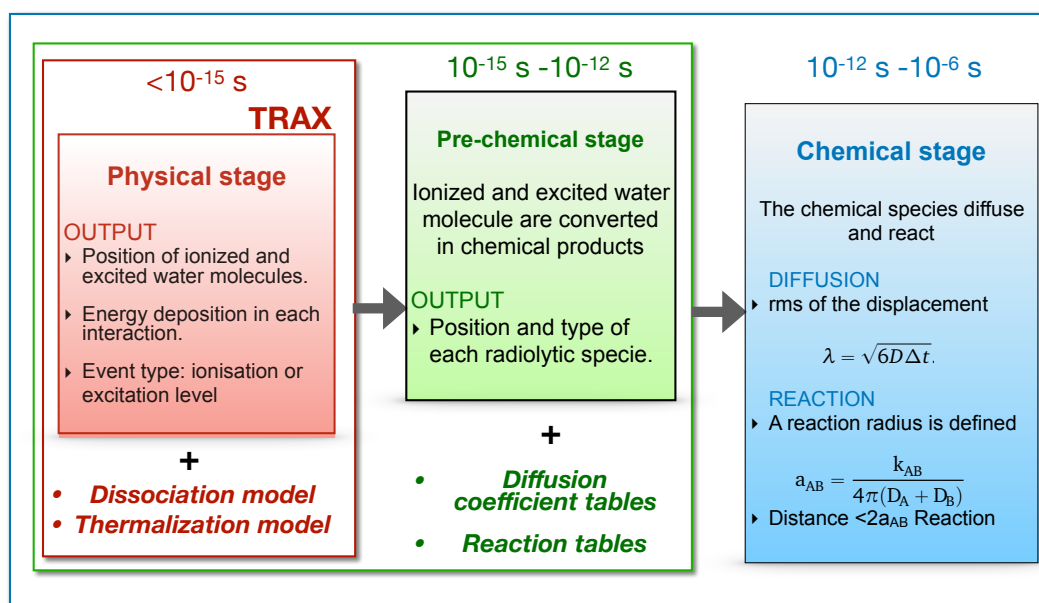
**Figure 3.2.:** Schematic view of the approach followed for the implementation of the pre-chemical and chemical stage of radiation damage in the track structure code TRAX.

In this chapter the development of the pre-chemical and chemical module of TRAX, following a step by step approach, will be presented. The TRAX code is particularly suitable for an extension to the chemical stage of radiation, thanks to the capability of following secondary electrons down to the nanometer scale and the possibility to distinguish between shell specific excitation channels. As it will be discussed in the following sections, these characteristic are indeed, extremely important in order to define the proper dissociation model and the original position of the chemical species at the beginning of the chemical stage. A schematic view of the approach followed in the implementation is shown in Figure 3.2. A complete description of the pre-chemical and chemical stage implemented in TRAX as well as of the resulting radiolytical yields presented in this chapter can be found in Boscolo et al. (2018)

## 3.1 Pre-chemical Stage

After the initial ionization or excitation of the water molecule, types and positions of the the products generated during the physical stage of radiation ($H_2O^+$, $H_2O^*$, $e^-_{sub}$) are passed to the subsequent pre-chemical stage. During this stage these species can dissociate, leading to the formation of new molecular products, or relax to ground state. In case of dissociation, the new species will need to thermalize and get in equilibrium with the medium before starting to behave as chemical species and enter in the chemical stage of radiation. This process will be completed approximately $10^{-12}$s after the irradiation. This is the time of the longitudinal relaxation of water and approximately corresponds to the time required for the

hydration of an electron in the lower sub excitation energy range (Turner et al., 1983). The new species generated during this phase are $H_3O^+$, $e_{aq}^-$, $H^\bullet$, $H_2$, $OH^\bullet$.

Very little is known about the processes involved in the formation of this species in liquid water and on their position on the picosecond scale. For this reason, a series of parameters not completely known have to be assumed.

The effect of these uncertainties significantly affects the time-resolved evolution of the chemical species. In particular, while the uncertainties in branching ratio and dissociation processes affect the initial yield of radicals the lack of knowledge in the thermalization length and direction heavily affects the evolution of the radical species over the time (Kreipl et al., 2008).

### 3.1.1 Molecular dissociation

#### Ionization products

The probability to undergo a specific dissociation process is different depending on whether the water molecule is ionized or excited and, if it is excited, on the specific excitation level.

Two possible models exist in order to describe the dissociation process of ionized water and, since they lead to the formation of the same products and are both very fast processes, $\sim 50$ fs, it is not easy to experimentally determine which is the actual process involved in the dissociation of ionized water,(Barnett and Landman, 1995). One possibility is that the ionized water molecule dissociates to $OH^\bullet$ and $H^+$, and, immediately after this dissociation process, the hot $H^+$ atom interact with a water molecule of the medium leading to the formation of the $H_3O^+$. Alternatively, the other possible process involves a proton transfer from ionized water molecule to the solvent yielding $H_3O^+$ (Thomsen et al., 1999).

$$H_2O^+ \xrightarrow{+H_2O} H_3O^+ + OH^\bullet \quad (a)$$
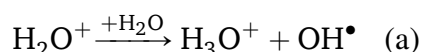
Multiple ionization processes are still not accounted in TRAX and this can represent a possible outlook for a future extension of the code. Some simulation codes, indeed, showed that they might have a significant role in the chemical evolution of high LET radiation (Gervais et al., 2006; Meesungnoen and Jay-Gerin, 2009), however both the cross sections as well as the dissociation channels for these processes in liquid water are still not completely known.

#### Dissociation of excited water molecules

In case of an excited liquid water molecule, instead, little is known about the quantitative and qualitative production of chemical species starting from each possible excited state in liquid water. As shown in Table 3.1 different groups use very different sets of decay probabilities, with differences ranging from 0% to 100% (Ballarini et al., 2000). This is motivated by the necessity of matching the picosecond yield of the different chemical species to experimental evidences. As the inelastic cross sections adopted in the different codes are not the same, the authors were forced to adapt the individual excitation branching ratio in order to reproduce the expected radical yield. The total yield of production of a particular species

is, indeed, strongly dependent on the cross section used to model the physical stage: partial cross sections essentially determine the probability of the respective ionization or excitation types.

In the present work, four possible dissociation patterns have been considered: auto-ionization (b), two dissociative decays (c)(d) and relaxation to the ground state (e).

$$H_2O^* \xrightarrow{+H_2O} H_3O^+ + OH^\bullet + e_{aq}^- \quad (b)$$

$$\longrightarrow OH^\bullet + H^\bullet \qquad\qquad (c)$$

$$\xrightarrow{+H_2O} H_2 + H_2O_2 \qquad\quad (d)$$

$$\longrightarrow H_2O + \Delta E \qquad\qquad (e)$$
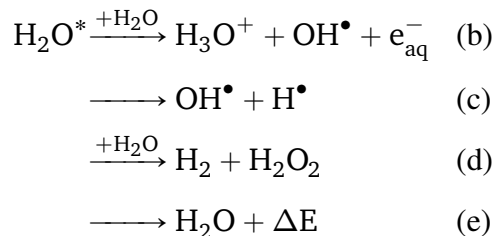
The auto-ionization, process (b), is an indirect ionization which can be produced when an electronic excitation of the water molecule produces excited states above the first ionization threshold. In this case, the water molecule can decay by auto-ionization ejecting an electron. In liquid water, photolysis measurements showed the production of solvated electrons already at excitation energies of c.a. 6.5eV (Boyle et al., 1969). Since this energy is not sufficient for a vertical ionization, this observation is considered to be the proof that, thanks to the liquid structure of the water, indirect ionization processes can appear even at low excitation energies (Thomsen et al., 1999; Han and Bartels, 1990).

In our model, we assumed the auto-ionization as a unique dissociation channel for the diffuse bands excitation and the two dissociative excitations $H^*Lyman\alpha$ and $H^*Balmer\alpha$. A probability of respectively 57% and 30% are assumed for the two Rydberg series and for the $B^1A_1$ molecular excitation state.

Also the relaxation to the ground state, process (e) has a lower probability to occur in the gas phase, when water molecules are farther to each other, compared to the liquid phase. This process can be originated when an excited molecule transfers the excess energy to the surrounding medium or by an immediate recombination between the dissociation products.

A complete description of the dissociation scheme with the relative branching ratios adopted in this work is shown in Table 3.1. However, since the dissociation model is imported from an external file, it is possible to change it at any time, this follows the general idea of TRAX of having a modular structure.

**Table 3.1.:** Collection of different dissociation schemes adopted by different research groups. Adapted and extended from Ballarini et al. (2000).

| Dissociation channel | | Probability(%) | | | | | | | |
|---|---|---|---|---|---|---|---|---|---|
| | | Turner et al. (1983) | Meesungnoen and Jay-Gerin (2005) | Tomita et al. (1997) | Ballarini et al. (2000) | Kreipl et al. (2008); Karamitros et al. (2011) | Nikjoo et al. (2006) | Gervais et al. (2006) | This work |
| **Ionization** | $H_3O^+ + OH^\bullet + e_{aq}^-$ | 100 | 100 | 100 | 100 | 100 | 100 | 100 | 100 |
| **Excitation** $A^1B_1$ | $H_2O$ | - | 45 | - | 35 | 35 | - | 30 | 25 |
| | $OH^\bullet + H^\bullet$ | 100 | 55 | 75 | 65 | 65 | 75 | 70 | 75 |
| | $H_2 + O^{\bullet\bullet}$ | - | - | 25 | - | - | 25 | - | - |
| $B^1A_1$ | $H_2O$ | - | 22.5 | - | 23 | 30 | 45 | 22.5 | 15 |
| | $H_3O^+ + OH^\bullet + e_{aq}^-$ | - | 50 | - | 50 | 55 | - | 25 | 55 |
| | $OH^\bullet + H^\bullet$ | - | 21.7 | - | 20 | - | - | 40.95 | - |
| | $H^\bullet + H^\bullet + O^{\bullet\bullet}$ | - | 2.2 | - | 3.9 | - | - | 6.30 | - |
| | $H_2 + O^{\bullet\bullet}$ | 100 | 3.6 | 100 | - | 15 | - | 5.25 | - |
| | $H_2 + H_2O_2$ | - | - | - | 3.2 | - | 55 | - | 30 |
| Ryd(A+B), Ryd(C+D) | $H_2O$ | - | - | - | 50 | 50 | 23 | - | 23 |
| | $OH^\bullet + H^\bullet$ | - | - | - | - | 50 | 20 | - | 20 |
| | $H_3O^+ + OH^\bullet + e_{aq}^-$ | 100 | - | 100 | 50 | - | 57 | - | 57 |
| Diffuse bands | $H_2O$ | - | - | - | 50 | 50 | 23 | - | - |
| | $OH^\bullet + H^\bullet$ | - | - | - | - | 50 | 20 | - | - |
| | $H_3O^+ + OH^\bullet + e_{aq}^-$ | 100 | - | 100 | 50 | - | 57 | - | 100 |
| Collective excitations | $H_2O$ | - | - | 70 | - | - | - | - | - |
| | $OH^\bullet + H^\bullet$ | - | - | 30 | - | - | - | - | - |
| H* Lyman $\alpha$ H* Balmer $\alpha$ | $H_2O$ | - | - | - | - | 50 | 23 | - | - |
| | $OH^\bullet + H^\bullet$ | - | - | - | - | 50 | 20 | - | - |
| | $H_3O^+ + OH^\bullet + e_{aq}^-$ | 100 | - | - | - | - | 57 | - | 100 |
| OH* | $H_2O$ | - | - | - | - | - | 23 | - | - |
| | $OH^\bullet + H^\bullet$ | - | - | - | - | - | 20 | - | - |
| | $H_3O^+ + OH^\bullet + e_{aq}^-$ | - | - | - | - | - | 57 | - | 100 |
| $e_{sub}^-$ | $e_{aq}^-$ | 100 | 100 | 100 | 100 | 100 | 100 | 100 | 100 |

### 3.1.2 Thermalization and displacement of hot fragments

During the dissociation process a small amount of energy is released. The dissociation fragments will, then, have a certain kinetic energy at the moment of their production. Only after releasing this energy and getting thermalized with the surrounding medium these fragments start to behave as chemical species and interact with each other. This step determines the end of the pre-chemical stage and is supposed to be concluded $10^{-12}$ s after the irradiation.

In the simulation, the multi-step thermalization process is described as a single step relocation of the dissociation fragment at a certain thermalization distance in a random direction, with respect to the original position of the ionized or excited water. Unfortunately, at the moment, there are no theoretical models or experimental observations able to provide quantitative information on the spatial distribution of the chemical products at the end of the pre-chemical stage. As a consequence, thermalization distances often have to be estimated and are usually validated by comparison to the experimental yield of species at later moments (Turner et al., 1983). A large part of the authors (Hill and Smith, 1994; Tomita et al., 1997; Nikjoo et al., 2006) adopted the values for thermalization distances proposed by Turner et al. (1983) and adjusted them depending on the dissociation scheme implemented in their model. An additional set of thermalization distances have been proposed by Kreipl et al. (2008) and adopted by Karamitros et al. (2011), but, also in this case, the values are assumed and adjusted based on the resulting yields of species (Kreipl et al., 2008).

In this work, an attempt to give an estimation of the thermalization distances has been made. Thermalization distances have been calculated based on experimental measurements of the translational energy transferred to the hot fragments in the dissociation process (Kawazumi and Ogawa, 1987; Kurawaki et al., 1983). To our knowledge, however, this quantity is known only for few dissociation processes. So, in order to estimate an approximative value for the kinetic energy transferred in the channels which are not documented, assumptions have to be made.

The average distance made by the different species during the first $10^{-12}$ s is computed treating the excess energy of the fragment as a thermal equivalent energy, represented as a local increase of the system temperature. A local variation in the temperature will affect the diffusion coefficient and, consequently, the mean free path of a certain species in a specific time interval. According to the Stokes-Einstein relationship

$$\frac{D}{T} = \mu k_B \qquad (3.1)$$

where $\mu$ is the particle mobility in water, $k_B$ is the Boltzmann constant and T is the absolute temperature. The diffusion coefficient, $D'$, for a different system temperature, $T'$, can be calculated from the relation

$$\frac{D'}{T'} = \frac{D}{T} \qquad (3.2)$$

where D and T are respectively the diffusion coefficient and the absolute temperature.

**Table 3.2.:** List of all the chemical species used in this work and their respective diffusion coefficients, **D**.

| Species | $D$ $(m^2 s^{-1})$ |
|---------|---------|
| $OH^\bullet$ | $2.8 \times 10^{-9}$ |
| $H_3O^+$ | $9.0 \times 10^{-9}$ |
| $H^\bullet$ | $7.0 \times 10^{-9}$ |
| $e_{aq}^-$ | $4.5 \times 10^{-9}$ |
| $H_2$ | $4.8 \times 10^{-9}$ |
| $OH^-$ | $5.0 \times 10^{-9}$ |
| $H_2O_2$ | $2.3 \times 10^{-9}$ |

Under the assumption of a local heating, the equivalent temperature $\tau$ can be calculated from the mean kinetic energy, $E_k$, of the hot dissociation fragment through the relation $E_k = 3/2 k_B \tau$. The diffusion coefficient, $D_\tau$, in a system at a temperature $\tau$ according to Equation 3.2 will than result in:

$$D_\tau = \frac{D E_k}{\frac{3}{2} k_B T}.$$  (3.3)

At the room temperature $k_B T = 25 \times 10^{-3}$ eV, then, expressing $E_k$ in eV, it will be

$$D_\tau = \frac{1}{0.038} D E_k.$$  (3.4)

Given the diffusion coefficient, $D_\tau$ for the hot fragment the root mean square displacement, $\lambda_\tau$ of a species after a time interval, $\Delta t$, can be calculated with the Einstein-Smoluchowski equation for three-dimensional system (see Appendix A)(Berg, 1993):

$$\lambda_\tau = \sqrt{6 D_\tau \Delta t}.$$  (3.5)

In the following, a brief description of the thermalization model applied for all the dissociation processes will be presented. In Table 3.2 the diffusion coefficient adopted for the different species are shown.

**(a) Ionization**

After an ionization process, the ionized water molecule, $H_2O^+$ is assumed to undergo a series of fast charge transfers which will result in a shift of the dissociation position respect to the original $H_2O^+$ production position. The displacement of $H_2O^+$, at the time of the dissociation process, is sampled from a three-dimensional Gaussian distribution with a mean displacement of 1.5 nm (Turner et al., 1983). In the new position, the $H_2O^+$ interacts with another water molecule of the medium leading to the formation of $H_3O^+$ and $OH^\bullet$ (Eigen and de Maeyer, 1958). The two fragments are assumed to

be ejected in opposite directions. The mean free paths are computed, depending on their kinetic energy, according to Equation 3.4 and the direction is randomly selected from a uniform distribution.

For one of the majors dissociation processes of $H_2O^+$, a total translational energy of $E_{tot} = 4.23 - 7.41$ eV has been measured with laser-fluorescence techniques (Kawazumi and Ogawa, 1987). In the original work this energy is associated to a slightly different process: $H_2O^+ \longrightarrow H^+ + OH^\bullet$, where the two fragment gain a kinetic energy respectively $E_{H+} = 4 - 7$ eV and $E_{OH^\bullet} = 0.23 - 0.41$ eV. Assuming that the proton is immediately transferred to a solvent water molecule leading to the formation of $H_3O^+$ and imposing the momentum conservation, we distribute the kinetic energy between the two fragment as follow

$$E_{H_3O+} = \tfrac{17}{36}E_{tot} = 2 - 3.5 \text{ eV} \qquad\qquad E_{OH^\bullet} = \tfrac{19}{36}E_{tot} = 2.23 - 3.91 \text{ eV}.$$

Since the measurements provide an interval of translational energies the mean free path for the two fragments is computed according to Equation 3.4 taking, as kinetic energy the average between the two values proposed.

$$\bar{\lambda}_{H_3O^+} = 1.96 \text{ nm} \qquad\qquad \bar{\lambda}_{OH^\bullet} = 1.16 \text{ nm}$$

**(b) Auto-ionization**

The auto-ionization process is described following the same scheme of the ionization. The emerging electron is assumed to be produced with an energy of $\sim 1.7$ eV (Han and Bartels, 1990) and thermalized following the scheme of the the sub-excitation electrons (as described below).

**(c) Dissociation** $H_2O^* \longrightarrow OH^\bullet + H^\bullet$

The translational kinetic energy transferred to the fragment produced in this dissociation channel has been measured by (Kawazumi and Ogawa, 1987). The $H^\bullet$ and $OH^\bullet$ are assumed to receive translational energy of respectively:

$$E_{H^\bullet} = 1.25 - 2.91 \text{ eV} \qquad\qquad E_{OH^\bullet} = 0.073 - 0.171 \text{ eV}.$$

The position of the two fragment at the end of the pre-chemical stage is sampled as a jump of the two fragments in opposite directions. The mean free path of the $OH^\bullet$ and $H^\bullet$ is calculated with the same method as for the ionization.

$$\bar{\lambda}_{H^\bullet} = 1.51 \text{ nm} \qquad\qquad \lambda_{OH^\bullet} = 0.23 \text{ nm}$$

**(d) Dissociation** $H_2O^* + H_2O \longrightarrow H_2 + H_2O_2$

In this case the dissociation is assumed to be a two step process: at first the water molecules dissociate leading to the production of $H_2$ and $O^{\bullet\bullet}$. The $O^{\bullet\bullet}$ is then supposed to react immediately with a target water molecule forming the $H_2O_2$.

$$H_2O^* \longrightarrow H_2 + O^{\bullet\bullet} \xrightarrow{+H_2O} H_2 + H_2O_2$$
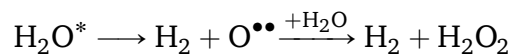
This dissociation channel is much less probable compared to all the processes described up to now. For this reason, very little is known and, to our knowledge, the kinetic energy transferred to the fragments is not known for this process. In order to give an estimation, we assumed that the total kinetic energy

transferred is the same as the one released in the process (c). The kinetic energy to the $H_2$ fragment is computed imposing the momentum conservation while the $O^{\bullet\bullet}$ fragment is assumed to react rapidly with a water molecule leading to the formation of $H_2O_2$, (Cobut et al., 1998). In this case, the $H_2O_2$ is supposed to stay in the interaction position. The kinetic energy transferred to the $H_2$ and the computed mean free path are respectively.

$$E_{H_2} = 1.95 \text{ eV} \qquad \bar{\lambda}_{H_2} = 1.23 \text{ nm}$$

### 3.1.3 Sub excitation electrons

Sub-excitation electrons, referring to electrons with a kinetic energy lower than the first electronic excitation potential of water (7.4 eV), deposit their excess energy through a series of vibrational (bending or stretching), librational and translational modes until they reach the thermal equilibrium with the surrounding medium ($\sim 25$ meV at room temperature).

Because of its negative charge, the thermalized electron in aqueous solutions forms a cluster by attaching to the surrounding molecules. At this stage, the electron starts to behave as a chemical species and is named hydrated electron, aqueous electron or solvated electron. The thermalization process of the sub-excitation electron can last up to 1ps and determines the end of the pre-chemical stage of radiation. The distance travelled by a sub-excitation electron before thermalizing depends on the electron energy and is known as a thermalization distance.

This quantity plays a fundamental role in the simulation of the dynamic of chemical species along an ion track and extensive studies have been carried on using theoretical, stochastic and experimental approaches (Meesungnoen et al., 2002; Zaider et al., 1994; Terrissol and Beaudré, 1990). However, because of the complexity of the problem, there is no agreement between the different methods (Ballarini et al., 2000).

Many track structure codes describe this process as a single step in a random direction sampling the mean free path of the sub-excitation electron depending on its energy according to tables of thermalization distance (Kreipl et al., 2008; Nikjoo et al., 2006; Ballarini et al., 2000; Tomita et al., 1997). In the chemical version of TRAX the thermalization scheme for condensed water, proposed by Zaider et al. (1994), has been implemented, Figure 3.3. According to the electron energy the thermalization distance is sampled from a gaussian distribution with mean value and FWHM respectively equal to the peak and to the width of the range distribution proposed by Zaider et al. (1994).

In the more recent version of TRAX, it is also possible to use cross sections for sub-excitation electrons able to follow secondary electrons down to 1.7 eV (see Section 2.1.3). This approach is more accurate, however it is also more sensitive to uncertainties on the cross section tables and results to be computationally more expensive. In Section 3.3.6 the impact of the choice of different thermalization approaches on the calculation of the radical yield along the particle track will be shown.

## 3.2 Chemical stage

The chemical stage is the last and longest stage of the track structure development. In this stage, the chemical species generated during the pre-chemical phase, diffuse and interact between themselves and
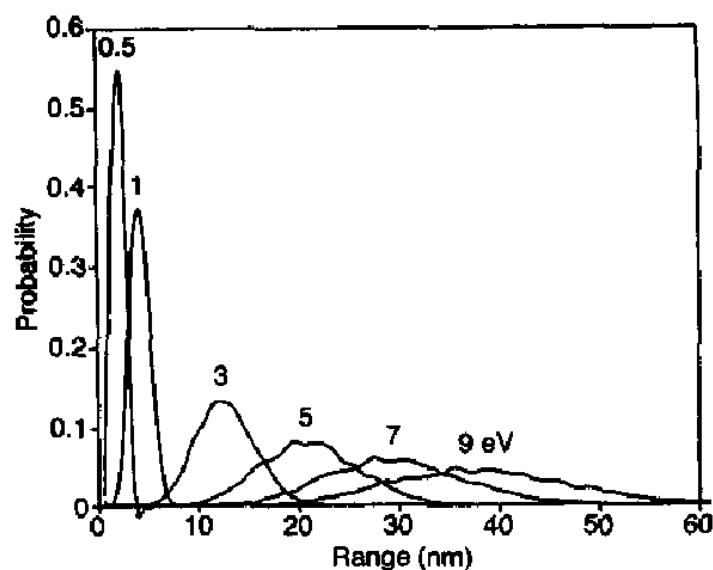
**Figure 3.3.:** Range distribution for sub-excitation electron for indicated energies at 1 ps after the irradiation, (Zaider et al., 1994).

with the water molecules of the medium. This phase is considered to be completed within $1\mu s$, at this time the track evolution is assumed to be over and the radical yield is supposed to be constant.

The reaction kinetics during the whole chemical evolution of the track can be very complex. The time-dependent concentration of the chemical species is, also, strongly affected by the initial position of the radiolysis products. In the case of high-LET radiation the track is dense, the radiolytic species are produced close to each other and the probability that a chemical reaction will take place between them is high. For sparsely ionizing radiation, on the other hand, the distance between the radiation-induced water free radical is larger, decreasing the interaction probability.

Because of the kinetic complexity, it can be difficult to study a particular process accounting for all the secondary and concurrent reactions. For this reason, the possibility to perform simulations, in this context, represents a powerful support to experimental measurement. In TRAX the track evolution is followed by a step by step algorithm and allows to determine the position of each chemical species at every step of the simulation. Since the time lapse of the entire simulation is very large (it spans 6 orders of magnitude) the time step changes gradually during the simulation, as shown in Table 3.3, to speed up the calculation. In such a way the track evolution is sampled accurately during the first moments, when the species are close to each other and many reactions occur, while a larger time step is used for the last part of the track evolution, when the species are already diffused and the reaction rate is much lower. A similar approach has been implemented in the PARTRAC code (Kreipl et al., 2008). However, the suggested time interval resulted to be too gross for the chemical evaluation of high LET track and discontinuities in the time evolution where observed. For this reason in TRAX a more fine time step in the evolution interval between 0.1 ns and $1\mu s$ has been adopted.

During each time step, $\Delta t$, all the water free radicals and their reaction products undergo two main processes: the radical diffusion and the chemical reactions. The diffusion process is modeled as a jump

**Table 3.3.:** List of all the time steps, $\Delta t$, used for all the calculations in this work.

| Time interval (s) | $\Delta t$ (s) |
|---|---|
| $10^{-12} < t < 10^{-10}$ | $10^{-13}$ |
| $10^{-10} < t < 5 \times 10^{-9}$ | $10^{-12}$ |
| $5 \times 10^{-9} < t < 10^{-8}$ | $2 \times 10^{-12}$ |
| $10^{-8} < t < 5 \times 10^{-7}$ | $5 \times 10^{-12}$ |
| $t > 5 \times 10^{-7}$ | $10^{-11}$ |

**Table 3.4.:** List of all the reactions and reaction rate constants, k, used in this work.

| Reaction | | Products | $k(10^{10} \text{dm}^3 \text{mol}^{-1} \text{s}^{-1})$ |
|---|---|---|---|
| $OH^{\bullet} + OH^{\bullet}$ | $\longrightarrow$ | $H_2O_2$ | 0.6 |
| $OH^{\bullet} + e_{aq}^-$ | $\longrightarrow$ | $OH^-$ | 2.2 |
| $OH^{\bullet} + H^{\bullet}$ | $\longrightarrow$ | $H_2O$ | 2.0 |
| $OH^{\bullet} + H_2$ | $\longrightarrow$ | $H^{\bullet} + H_2O$ | 0.0045 |
| $OH^{\bullet} + H_2O_2$ | $\longrightarrow$ | $HO_2^{\bullet} + H_2O$ | 0.0023 |
| $e_{aq}^- + e_{aq}^- + H_2O + H_2O$ | $\longrightarrow$ | $H_2 + OH^- + OH^-$ | 0.55 |
| $e_{aq}^- + H^{\bullet} + H_2O$ | $\longrightarrow$ | $H_2 + OH^-$ | 2.5 |
| $e_{aq}^- + H_3O^+$ | $\longrightarrow$ | $H^{\bullet} + H_2O$ | 1.7 |
| $e_{aq}^- + H_2O_2$ | $\longrightarrow$ | $OH^{\bullet} + OH^-$ | 1.0 |
| $H^{\bullet} + H^{\bullet}$ | $\longrightarrow$ | $H_2$ | 1.0 |
| $H^{\bullet} + H_2O_2$ | $\longrightarrow$ | $OH^{\bullet} + H_2O$ | 0.01 |
| $H^{\bullet} + OH^-$ | $\longrightarrow$ | $e_{aq}^- + H_2O$ | 0.002 |
| $H_3O^+ + OH^-$ | $\longrightarrow$ | $H_2O + H_2O$ | 10.0 |

of the chemical species in a random direction. The step is sampled from a 3D Gaussian distribution with root mean square displacement given by the Einstein Smoluchowski equation, as introduced for the above mentioned process, for the three-dimensional system (see Appendix A) (Berg, 1993):

$$\lambda = \sqrt{6D\Delta t}. \tag{3.6}$$

A list of the diffusion coefficients adopted in this work is shown in Table 3.2.

After the diffusion step is concluded the radicals can start to react between themselves. The reaction process is described through a proximity parameter called the reaction radius, a. For diffusion controlled reactions between two species, A and B, with diffusion coefficient and reaction radius respectively $D_A$, $D_B$ and $a_{AB}$, the reaction radius is defined as

$$a_{AB} = \frac{k_{AB}}{4\pi(D_A + D_B)}. \tag{3.7}$$

If the distance between two radicals is smaller than the reaction radius then the reaction is supposed to take place. The two reacting species are removed from the simulation and replaced by the reaction products.

The reaction considered and their respective reaction rate constants are loaded from an external chemical file and can easily be modified at any time. In this work we included 13 reactions within 8 chemical species. For almost all the reactions we adopted the reaction rate constants suggested by Nikjoo et al. (2006) except for the reaction $OH^{\bullet} + e^{-}_{aq} \rightarrow OH^{-}$, where we chose a reaction rate constant of $2.2 \times 10^{10} dm^{3}mol^{-1}s^{-1}$ instead of $2.5 \times 10^{10} dm^{3}mol^{-1}s^{-1}$, and the reaction $e^{-}_{aq} + H_2O_2 \rightarrow OH^{\bullet} + OH^{-}$, where we adopted a reaction rate constant of $1.0 \times 10^{10} dm^{3}mol^{-1}s^{-1}$ instead of $1.3 \times 10^{10} dm^{3}mol^{-1}s^{-1}$.

A list of all the reactions included and the reaction rate constants adopted is shown in Table 3.4; all the reactions and the reaction rate constants are reported for pure water under normal conditions (neutral pH and 25°C).

## 3.3 Results

### 3.3.1 Calculation

At the current stage, the chemical extension of TRAX is able to perform simulations of the chemical dynamics induced by electron and ion radiation in water. In Figure 3.4 and 3.5 the simulated chemical evolution in the beam eye view and lateral profile of a track of one 8 MeV/u carbon ion is shown in the time interval $10^{-12} to 10^{-6}$ s.

Differently from the physical stage, where all the information of the track evolution is stored in a binary, external LISTMODE file, in the chemical stage the evaluation is done on the fly.

The dissociation tables, diffusion coefficient, and reaction tables are loaded from an external file and can be easily modified without code changes.

The simulations are performed in a cube of water with size $5 \times 5 \times 5 \mu m^3$ for low-LET radiation. For high-LET radiations a geometry of $5 \times 5 \times 0.5 \mu m^3$ (thinner in the beam direction) is preferred in order to guarantee the track segment condition, i.e. that the linear energy transfer of the primary radiation can be assumed constant in the target geometry.

For each simulation, a series of parallel calculation, completely independent of each other, has been performed. Thus, no inter-track interaction have been included. The number of primary particles simulated for each condition was chosen high enough to reduce statistical fluctuation: the total energy deposited by all the primary ion tracks in the target was at least 2.5 MeV.

The yield of the different chemical products are described in terms of the G-values, this is one of the most common quantities used in radiation chemistry and is defined as the number of molecules produced per 100 eV of energy deposited.

### 3.3.2 Calculated Yield at one picosecond

After the completion of the water dissociation process, the species generated are $H_3O^+$, $OH^{\bullet}$, $e^{-}_{aq}$, $H^{\bullet}$, $H_2$, and $H_2O_2$. The type of chemicals produced during the pre-chemical stage is exclusively determined by the dissociation tables while the yield of production of the different species strongly depends also
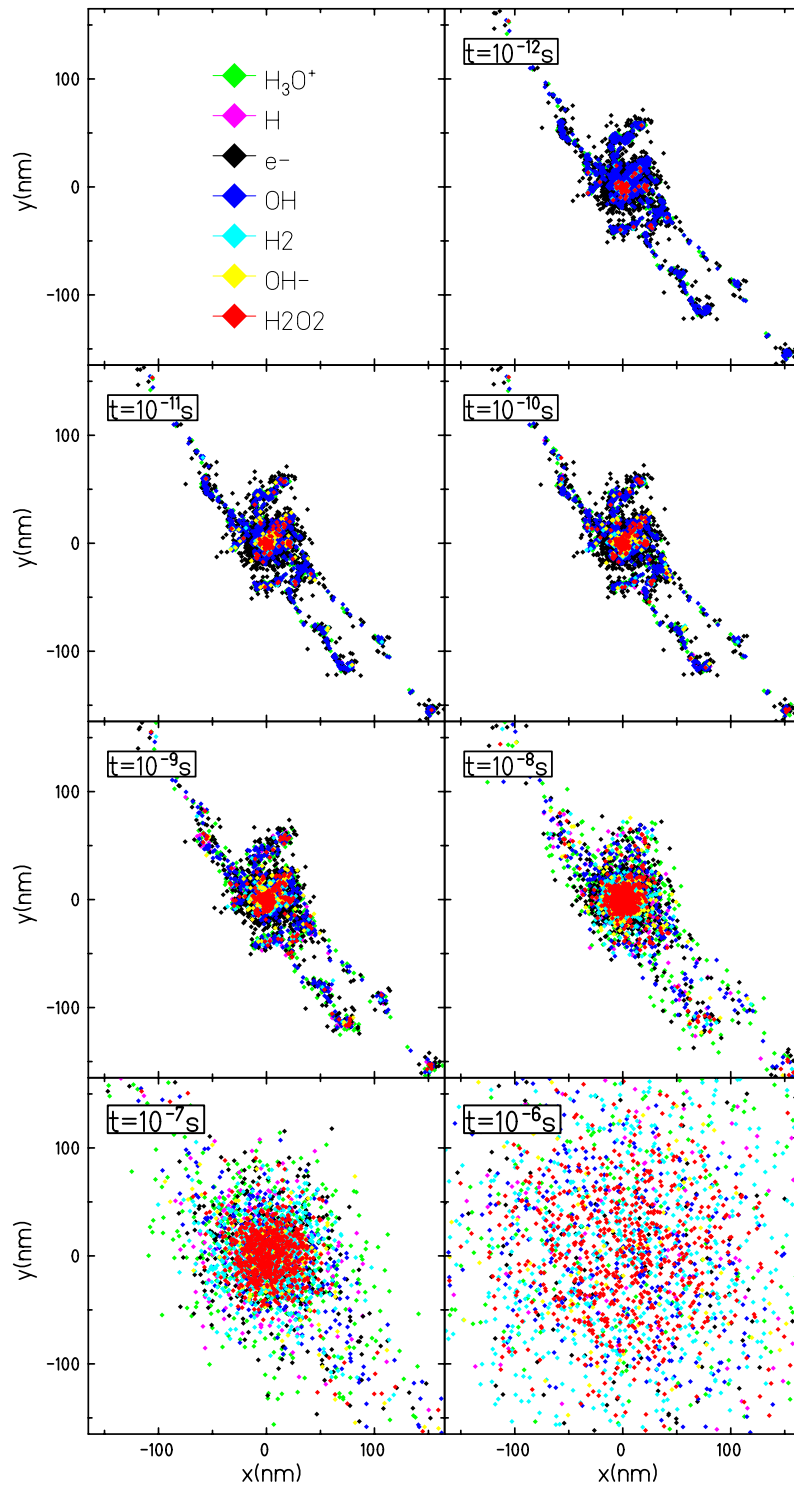
**Figure 3.4.:** Chemical evolution of a 8 MeV/u carbon ion track in water in the time interval $10^{-12} - 10^{-6}$ s, as computed with the present work, shown in beam eye view.
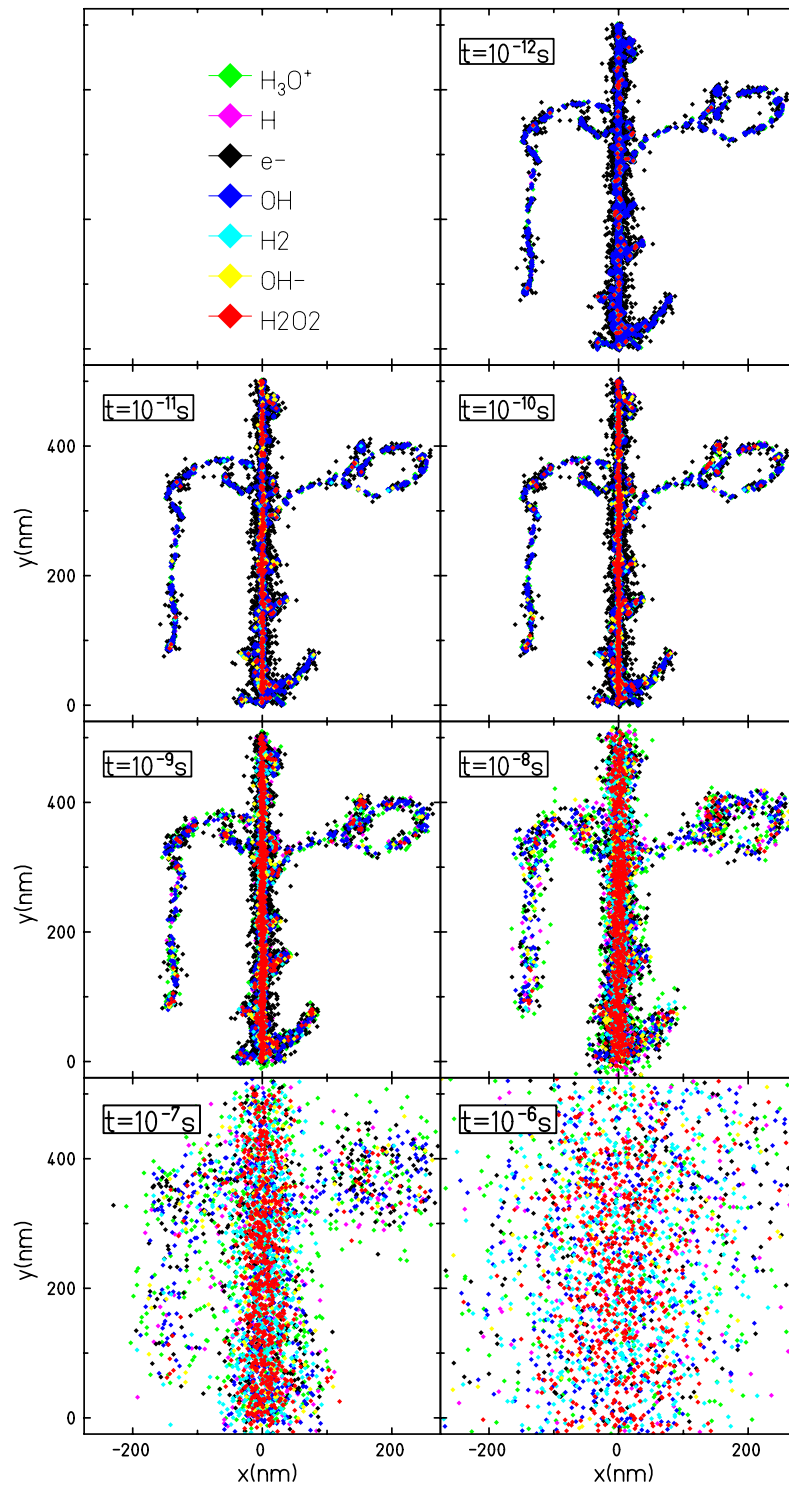
**Figure 3.5.:** Chemical evolution of a 8 MeV/u carbon ion track in water in the time interval $10^{-12} - 10^{-6}$ s, as computed with the present work, shown in top view.

on the cross sections used during the physical stage: the partial cross sections, indeed, determine the probability for the different ionization or excitation types.

In TRAX shell specific ionization and excitation cross sections are implemented. In particular the cross sections include five ionization shells (1s, 2a1, 1b2, 3a1 and 1b1) and eight excitation states: five molecular excitations ($A^1B_1$, $B^1A_1$, Rydberg A+B, Rydberg C+D and diffuse bands) and three dissociative excitations ($H^*$ Lyman $\alpha$, $H^*$ Balmer $\alpha$ and $OH^*$).

The yield of the products after the completion of the physical stage for ionization sub-excitation electrons and all the different excitation states obtained with TRAX are reported in Table 3.5 for electron and proton radiation of different energies. The yield of the different physical processes do not significantly depend on the radiation quality: electron and proton radiation show differences smaller than 3%, while no significant differences have been obtained between the same radiation type at different energy. Even if the cross sections for the different ionization and excitation processes strongly depend on the radiation energy, for electron and ion radiation most of the energy is, indeed, deposited through secondary and higher order electrons, which are emitted with broad energy spectra.

In Table 3.6 the results of our calculations at the completion of the physical stage in liquid water irradiated with 1 MeV electron radiation are compared with the ones of PARTRAC (Ballarini et al., 2000) and CHEMKURBUC (Uehara and Nikjoo, 2006). The difference between our calculation and the yield proposed by the other codes is small for $H_2O^+$ and $e^-_{sub}$: only 1.8% of difference with CHEMKURBUC and 1.4% with PARTRAC. In the contribution to the different shell specific excitations, no significant difference (<2.5%) between TRAX and CHEMKURBUC calculations appears; the two codes use indeed very similar cross sections. In contrast, the PARTRAC code shows a difference up to 7.4% in the partitioning between the different excitation processes.

Depending on the ionization or excitation state the water molecule dissociates during the pre-chemical phase according to the dissociation scheme shown in Table 3.1. The recombination process between hot dissociation fragments is in competition with the thermalization, many of these fragments will, then, recombine immediately after their production. The number of radicals undergoing an immediate recombination process depends on the proximity between the fragments along the track. For low-LET radiation around 4% of the fragment recombine at the very beginning of the chemical stage while for high-LET radiation this number increases up to 13%.

The resulting yield represents the production rate of the chemical species at the end of the pre-chemical stage (1 ps after the irradiation). In Table 3.7 the computed yield of TRAX are compared with literature data compiled in Kreipl et al. (2008).

The values reported are obtained averaging over the G-value of all the radiation type. At the end of the pre-chemical stage, the G-values are only weakly dependent on the primary radiation quality since, as shown in Table 3.5, the branching ratio for the different physical process are nearly independent of the LET and radiation type. As underlined by Kreipl et al. (2008), it is important to notice that at the moment there are no experimental data available for these quantities and all the values reported are model parameters or result from theoretical considerations.

**Table 3.5.:** Products' yield after the completion of the physical stage for ionization, sub-excitation electrons and all the different excitation states obtained with TRAX, for electron and proton radiation of different energies.

| | | $H_2O^+$ (%) | $e_{sub}^-$ (%) | $H_2O^*$ (%) | | | | | | | |
|---|---|---|---|---|---|---|---|---|---|---|---|
| | | | | $A^1B_1$ | $B^1A_1$ | Ryd A+B | Ryd C+D | db | $H^*Ly\alpha$ | $H^*Bal\alpha$ | $OH^*$ |
| **Electron** | 1MeV | 35.77 | 35.83 | 8.67 | 4.37 | 1.57 | 2.19 | 7.19 | 2.18 | 0.43 | 1.80 |
| | 750 keV | 35.12 | 35.17 | 8.62 | 4.59 | 1.63 | 2.35 | 7.77 | 2.49 | 0.48 | 1.79 |
| | 100 keV | 34.26 | 34.29 | 8.72 | 4.74 | 1.74 | 2.53 | 8.65 | 2.77 | 0.54 | 1.76 |
| **Proton** | 200 MeV | 37.08 | 37.14 | 8.93 | 4.47 | 1.70 | 2.39 | 7.77 | 2.43 | 0.48 | 1.91 |
| | 90 MeV | 37.25 | 37.31 | 8.89 | 4.59 | 1.66 | 2.37 | 7.63 | 2.40 | 0.48 | 1.92 |
| | 50 MeV | 37.31 | 37.36 | 8.82 | 4.62 | 1.67 | 2.35 | 7.61 | 2.4 0 | 0.46 | 1.88 |
| | 3 MeV | 37.10 | 37.11 | 8.98 | 4.67 | 1.70 | 2.42 | 7.78 | 2.44 | 0.47 | 1.92 |

**Table 3.6.:** Comparison between the yield of products after completion of the physical stage (sub-excitation electrons; ionized water molecules; excitations: $A^1B_1$, $B^1A_1$, Rydberg states, diffuse bands, dissociative excitations) with 1MeV electron tracks as obtained with theTRAX-CHEM code, PARTRAC (Ballarini et al., 2000) code and the CHEMKURBUC code (Uehara and Nikjoo, 2006).

| | $H_2O^+$ (%) | $e_{sub}^-$ (%) | $H_2O^*$ (%) | | |
|---|---|---|---|---|---|
| | | | $A^1B_1$ | $B^1A_1$ | Ryd(A+B), Ryd(C+D), db and de |
| TRAX | 35.77 | 35.83 | 8.67 | 4.37 | 15.36 |
| CHEMKURBUC | 33.9 | 33.9 | 11.1 | 3.6 | 17.5 |
| PARTRAC | 37.1 | 37.1 | 8.7 | 9.7 | 7.5 |

**Table 3.7.:** G-value calculated at 1 ps after the irradiation.Adapted from Kreipl et al. (2008).

| $e_{aq}^-$ | $OH^\bullet$ | $H^\bullet$ | $H_3O^+$ | $H_2$ | Ref |
|------|------|------|------|------|------|
| 4.88 | 5.89 | 0.96 | - | - | Tomita et al. (1997) |
| 5.30 | 6.05 | 0.72 | 5.38 | 0.13 | Cobut et al. (1998) |
| 4.78 | 5.70 | 0.62 | 4.78 | 0.15 | Bisby et al. (1977) |
| 4.7 | 6.0 | 0.8 | 4.7 | 0.25 | Trumbore et al. (1978) |
| 4.78 | 5.40 | 0.62 | 4.78 | - | Naleway et al. (1979) |
| 6.3 | 8.4 | 2.1 | 6.3 | 0.3 | Turner et al. (1983) |
| - | 6.82 | 0.84 | 4.8 | 0.62 | Kaplan et al. (1990) |
| 4.78 | 5.50 | 0.42 | 4.78 | 0.15 | Pimblott and LaVerne (1994) |
| 4.93 | 5.37 | 0.45 | 4.93 | 0.16 | Pimblott and LaVerne (1997) |
| - | 5.6 | - | - | - | LaVerne (2000) |
| 4.83 | 5.78 | 0.63 | 4.83 | 0.16 | Kreipl et al. (2008) |
| 4.84 | 5.71 | 0.91 | 4.84 | 0.13 | This work |

### 3.3.3 Time dependence of the calculated yield

The temporal evolution of the chemical species generated by the irradiation of a water target has been studied in the time interval $10^{-12} - 10^{-6}$ s for different primary radiation and compared, where possible, with experimental data.

In Figure 3.6, time-dependent radiolytic yields for all the radiolytic species generated by incident 20 MeV/u carbon ion radiation in a water cube of $5 \times 5 \times 0.5 \mu m^3$ are presented. The average radiolytic yields have been obtained averaging over 400 independent parallel calculations. For each species, the standard deviation on its yield is shown. The statistical error on the G-values computation span between 1.3% and 20% depending on the time and on the species. However, to keep clean and easy to read the figures in the rest of the manuscript the error bars are not shown.

Figure 3.7 shows the calculated time-dependent yield for all the chemical species generated by 1 MeV electron radiation in a water cube of $5 \times 5 \times 5 \mu m^3$. The curves represented are obtained averaging over 5000 electron tracks, the average energy lost in the water target is 0.64 keV and the average number of radiolytic species per track segment at $10^{-12}$ s is $\sim 105$.

The yields of $OH^\bullet$, $H_3O^+$ and $e_{aq}^-$, the three main species generated by water radiolysis, decrease with time. These species are, indeed, involved in many reaction processes and get consumed during the chemical stage. On the other hand the yields of species generated mainly as reaction products ($H_2O_2$, $H_2$ and $OH^-$) increase while the track evolution proceeds. It is important to notice that, at the end of the calculation ($10^{-6}$ s after the irradiation), the species reach a plateau indicating a chemical equilibrium within the track and the conclusion of the chemical stage of radiation effect.

The calculated curves for some of the more significative species have been compared with experimental data and literature values in Figure 3.8. On the left panel, the time-dependent yield for $OH^\bullet$ (blue
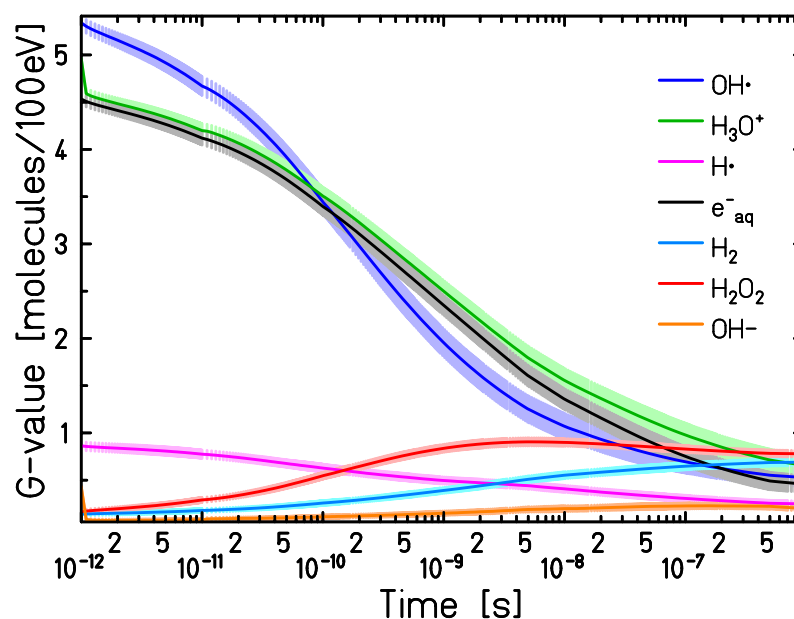
**Figure 3.6.:** Calculated time-dependent yield for all the species produced by a 20 MeV/u carbon ion in a water cube of $5 \times 5 \times 0.5 \mu m^3$. The transparent bars represent a full uncertainties calculation indicating the statistical error for each specie during the whole chemical track evolution.

curve) and $H_2O_2$ (red curve) is reported, while in the right panel the yield of hydrated electrons (black curve) and $H_2$ molecules (light blue curve) are shown.

The OH$^\bullet$ yield shows a good agreement with data from the literature. The obtained G-value for the OH$^\bullet$ at the conclusion of the chemical phase $G_{OH^\bullet}(1\mu s) = 2.75$ matches the standard value of $G_{OH^\bullet}(1\mu s) = 2.8$ (Ferradini and Jay-Gerin, 1999). In addition, our calculations are in good agreement with the recent experimental data measured by El Omar et al. (2011) and with the computed values proposed by Jay-Gerin and Ferradini (2000) and by LaVerne and Pimblott (1991). On the other hand, the simulations from Tomita et al. (1997) yield to slightly higher values and the steep slope predicted in the interval from 0.1 to 10 ns through the inverse Laplace transformation from LaVerne (2000) can not be reproduced with our model, a similar disagreement has been reported also by Kreipl et al. (2008). The measurements obtained with direct optical experiments from Jonah and Miller (1977) have been excluded from this data collection. These data have been, indeed, recently revised by Bartels et al. (2000) and resulted to be overestimated: they rely on an estimation of the initial yield of hydrated electrons which appeared to be too high and had to be rescaled. According to this observation, Bartels suggests that the measured value for OH$^\bullet$ radical at 200 ps $G_{OH^\bullet} = 5.9$ proposed by Jonah and Miller (1977) should be reduced to $G_{OH^\bullet}(200ps) = 5.1$ (Bartels et al., 2000). This value, however, results to be still overestimated respect to the more recent experimental measures $G_{OH^\bullet}(10ps) = 4.8$ and $G_{OH^\bullet}(200ps) = 4.3$ from El Omar et al. (2011).

The computed time-dependent yield for the solvated electron, $e_{aq}^-$, appears to be in general slightly underestimated compared to the literature data. The electron yield at the asymptotic limit of $1\mu s$ results indeed to be $G_{e_{aq}^-}(1\mu s) = 2.56$ while the standard value is $G_{e_{aq}^-}(1\mu s) = 2.65$ (Ferradini and Jay-Gerin, 1999). No clear consensus exists instead on the initial yield of the solvated electrons. Accepted values
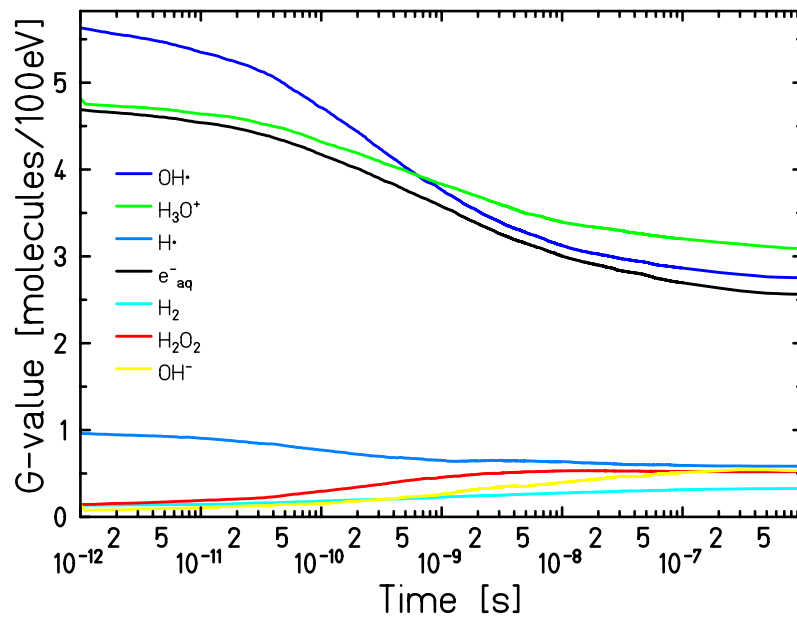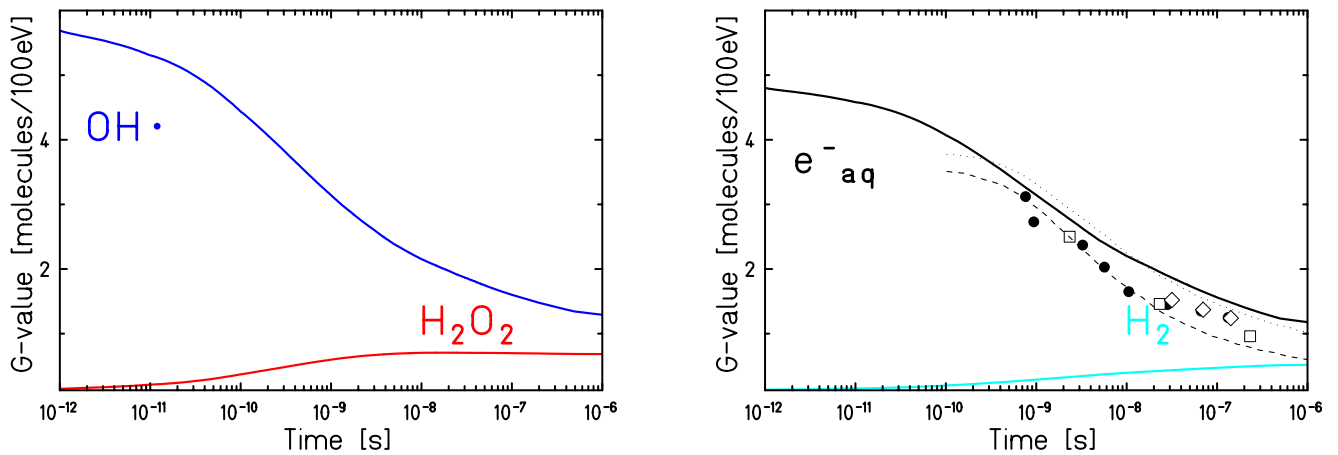
**Figure 3.7.:** Time-dependent radiolytic yields for 1 MeV electron in a water cube of 0.5 $\mu$m sides.
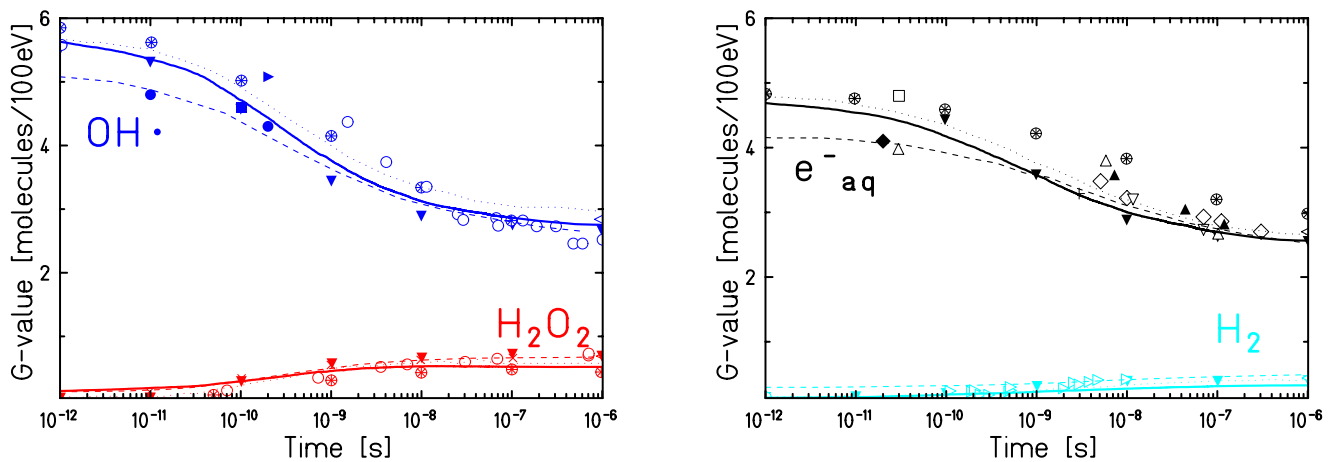


**Figure 3.8.:** Time-dependent radiolytic yields for 1 MeV electrons in a water volume of $5 \times 5 \times 5 \mu m^3$ for the species $OH^{\bullet}$ and $H_2O_2$ (top panel) and $e^-_{aq}$ and $H_2$ (bottom panel). Simulations: solid lines TRAX-CHEM, dashed lines Plante (2011a), dotted lines Kreipl et al. (2008). Experiment: ▼ LaVerne and Pimblott (1991), ⊛ Tomita et al. (1997), ▶ Bartels et al. (2000), ◁ Elliot et al. (1993), ■ Jay-Gerin and Ferradini (2000), ● El Omar et al. (2011), ○ LaVerne (2000) for $OH^{\bullet}$. ▼ LaVerne and Pimblott (1991), × Pimblott and LaVerne (1997), ◁ Elliot et al. (1993), ⊛ Tomita et al. (1997), ○ LaVerne (2000) ◇ Shiraishi et al. (1988), ▲ Buxton (1972), ▼ LaVerne and Pimblott (1991), ◆ Muroya et al. (2005), ⊛ Tomita et al. (1997), × Pimblott and LaVerne (1997), □ Takashi and Meiseki (1982), △ Wolff et al. (1973), ▽, Thomas and Bensasson (1967), + Belloni et al. (1983), ◁ Elliot et al. (1993) for $e^-_{aq}$. ▼ LaVerne and Pimblott (1991), ▷ Draganić and Draganić (1975), ◁ Elliot et al. (1993), ⊕ Schwarz (1969) for $H_2$.

3. Chemical extension of the TRAX code
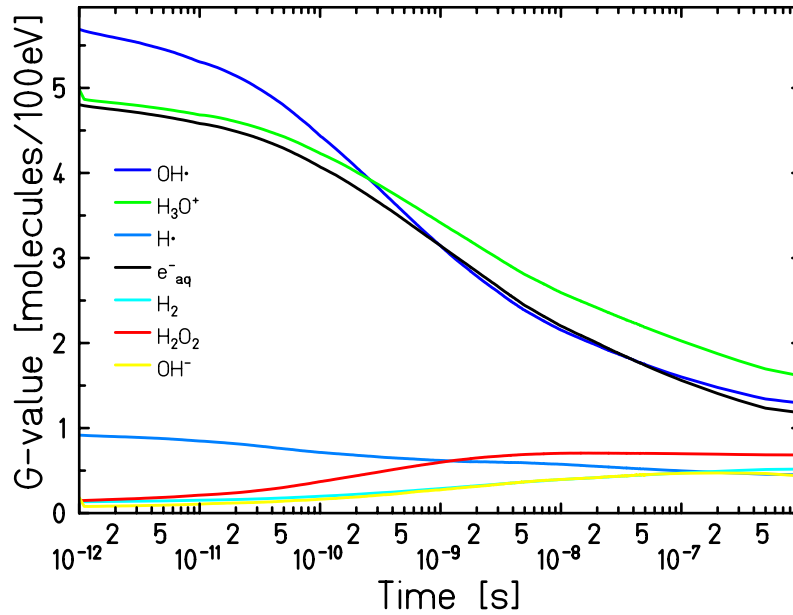
**Figure 3.9.:** Time-dependent radiolytic yields for 3 MeV proton in a water cube of 5 $\mu$m side.



**Figure 3.10.:** Time-dependent radiolytic yields for 3 MeV protons in a water cube of $5 \times 5 \times 5\mu\text{m}^3$ for the species $\text{OH}^\bullet$ and $\text{H}_2\text{O}_2$ (upper panel) and $\text{e}_{\text{aq}}^-$ and $\text{H}_2$ (lower panel). Solid lines TRAX-CHEM simulations, dashed and dotted lines simulations under respectively track average and track segment conditions (LaVerne et al., 2005). Experiments: $\diamond$ LaVerne et al. (2005), $\square$ Burns et al. (1981), $\bullet$ Rice et al. (1982)

range between $G_{e_{aq}^-} = 4.8$ as suggested by Pimblott et al. (1996) and $G_{e_{aq}^-} = 4.0$ as proposed by Bartels et al. (2000). This latter value seems to be slightly underestimated but it appear to be consistent with yield measured by Wolff et al. (1973), $G_{e_{aq}^-}(30ps) = 4.0$, and with the recent measurement from Muroya et al. (2005), $G_{e_{aq}^-}(20ps) = 4.1$.

The calculation for $H_2O_2$ and $H_2$ are in good agreement with the experimental data. The yield of the hydrogen peroxide, $H_2O_2$, however, stabilizes for times larger than $10^{-8}$ s. The final yield at the end of the chemical phase results to be, then, a bit underestimated with respect to the standard values: $G_{H_2O_2}(1\mu s) = 0.5$ instead of $G_{H_2O_2}(1\mu s) = 0.68$ (Ferradini and Jay-Gerin, 1999). This behavior has been observed also in the CHEMKURBUC code (Uehara and Nikjoo, 2006). Since the reaction table implemented in TRAX are very similar to the ones proposed in CHEMKURBUC and both the codes are based on diffusion-controlled reaction, this behavior appears to be determined by the reaction model adopted.

For high-LET proton radiation, the reaction kinetics is much faster: the ion track is denser resulting in an increased reaction rate between the species generated during the water radiolysis. Calculated time-dependent yields for 3 MeV proton radiation are shown in Figure 3.9, corresponding to an LET of $\sim$ 11.5 keV/$\mu$m. The simulation was performed on a water cube of 5 $\mu$m size and the curves presented have been obtained averaging over 80 proton track. The average energy lost in the geometry is $\sim$57 keV and the average number of radiolytic species generated is $\sim$9600.

The time-dependent yield for solvated electron, $e_{aq}^-$, has been compared with experimental data collected by LaVerne et al. (2005) and is shown in Figure 3.10. The calculated yield slightly overestimate the experimental data, however, it is important to notice that the experimental data of Burns et al. (1981) have been taken averaging over the full ion track, thus, the track segment condition is not satisfied.

### 3.3.4 Time and energy dependence of yields

The reaction kinetics, and thus the time-dependent radical yield during the chemical stage of the track evolution, are strongly dependent on the quality of the primary ion. This pronounced dependence has been shown by experimental data and predicted by theoretical models. As already mentioned, indeed, for high-LET radiation the track density is higher and the chemical species are produced close to each other. This, then, results in an accelerated reaction kinetic.

In Figure 3.11 the time-dependent yield of the molecules is shown for different quality of the primary radiation. In Table 3.8 the characteristics of the radiation used for every curve are reported.

Not all the radiolytic species follow the same trend when the LET of the incident radiation is varied. In general, at the microsecond, the G-values of all the more abundant species generated during the water radiolysis ($e_{aq}^-$, $OH^\bullet$, $H_3O^+$ and $H^\bullet$) tend to decrease with increasing LET. The behavior of the other species, instead, change from species to species: while the $H_2$ and $H_2O_2$ increase their yield with the LET, the $OH^-$ production at the end of the chemical stage decrease with increasing LET. Additionally, it can be observed that chemicals involved in many reactions, both as reactant and products, show non-monotone time-dependent yield, among these species we can distinguish $H^\bullet$, $OH^-$ and $H_2O_2$. In particular, the yield of the $H_2O_2$ largely increases at the early stage of the track chemical evolution until reaching a constant value (for high LET a maximum) around 1 ns after the irradiation, long before the

**Table 3.8.:** LET particle type and energy of the radiation used in Figure 3.11

| LET (keV/$\mu$m ) | Particle | Energy |
|---|---|---|
| 0.64 | $^1$H | 90 MeV |
| 1.06 | $^1$H | 50 MeV |
| 2.31 | $^1$H | 20 MeV |
| 4.4 | $^1$H | 10 MeV |
| 8.4 | $^4$He | 20 MeV |
| 11.4 | $^1$H | 3 MeV |
| 15.83 | $^1$H | 2 MeV |

real conclusion of the chemical evolution, at $\sim 1\mu$s. This can be explained as a result of two competing processes playing a role at two different time scales:

$$OH^\bullet + OH^\bullet \longrightarrow H_2O_2$$

$$e_{aq}^- + H_2O_2 \longrightarrow OH^\bullet + OH^-.$$
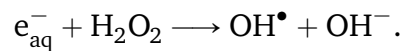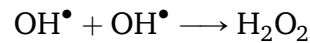
The steep growth at the beginning of the chemical phase of the $H_2O_2$ is mainly due to the reaction between two $OH^\bullet$ radicals, which are very abundant at the first steps of the chemical evolution. At larger times, the number of $OH^\bullet$ radicals decrease and, with it decreases the rate of production of $H_2O_2$. At this stage the second process becomes more important and the yield of $H_2O_2$ stops growing (for high LET, starts decreasing).

A similar trend of the chemical yield for different radiation energies has been shown for Geant4-DNA by Karamitros et al. (2011). However, while the G-value curves of the more abundant and investigated species ($e_{aq}^-$, $OH^\bullet$, $H_2O_2$ and $H_3O^+$) are consistent with our calculations, the yields of $H^\bullet$ sensibly differ at intermediate times. The two codes indeed have different reaction and dissociation models: the yield at the picosecond of $H^\bullet$ radical is $G_{H^\bullet}(1ps) = 0.05$ for Geant4-DNA and $G_{H^\bullet}(1ps) = 0.77$ in TRAX. At the moment because of the lack of experimental data, it is very difficult to establish the correct kinetic for all the radical species, and the yield at the end of the chemical stage is generally used to validate the different models.
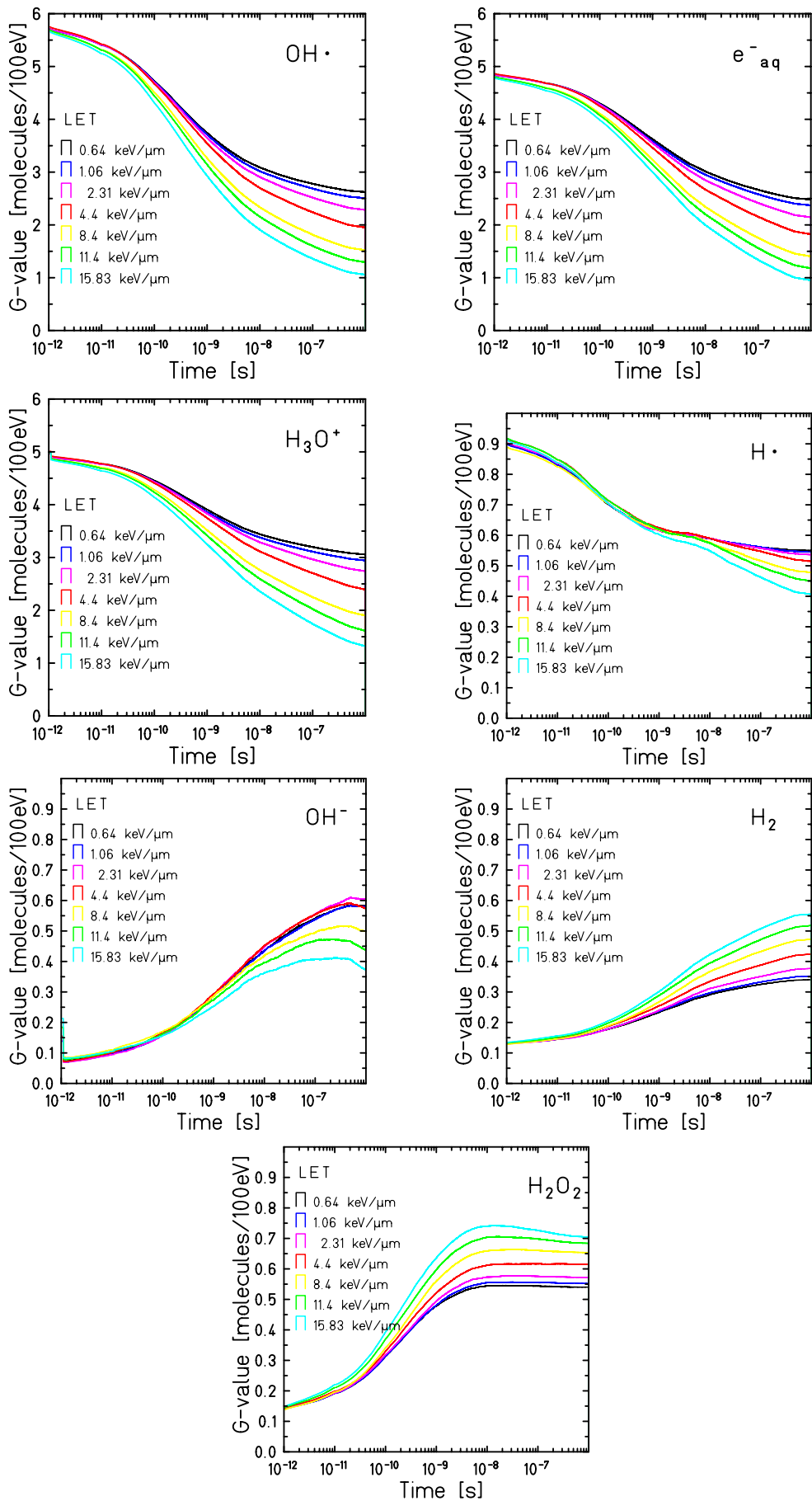
**Figure 3.11.:** calculated time-dependent radiolytic yield for different LET radiation in pure water.

### 3.3.5 LET and radiation type dependence of yields

The LET dependence of the G-values has been evaluated for different radiation energies and different ion types, based on the (time-dependent) yield of the different species. Figure 3.12 shows the G-value dependence on the mean LET for proton, helium and carbon ion radiation, with LET values ranging between 0.14 - 232 keV/$\mu$m. Calculations are presented with experimental values from literature where the different radical yields at the end of the chemical stage of radiation have been measured with: $^{60}$Co $\gamma$-rays (Appleby and Schwarz, 1969; Burns and Sims, 1981), $^{137}$Cs $\gamma$-rays (Wasselin-Trupin et al., 2002), electrons (Elliot et al., 1993), protons (Burns and Sims, 1981; Pastina and LaVerne, 1999; Wasselin-Trupin et al., 2002), deuterons (Appleby and Schwarz, 1969; Naleway et al., 1979), helium ions (Naleway et al., 1979; Appleby and Schwarz, 1969; Pastina and LaVerne, 1999), carbon ions (Pastina and LaVerne, 1999; Wasselin-Trupin et al., 2002), and nitrogen and neon ions (Burns and Sims, 1981).

The overall agreement with the experimental data is good. Radical yields for OH$^\bullet$ and H$^\bullet$ are well reproduced along the whole LET range, while the H$_2$ and H$_2$O$_2$ results slightly underestimated respect to the measurements but the general trend is well reproduced. The e$_{aq}^-$ yield, instead, for LET values larger than 100 keV/$\mu$m overestimate the helium data of Naleway et al. (1979) but matches perfectly the measurements reported by Appleby and Schwarz (1969). At low LET values, instead, our calculations are unable to reproduce the measured value from Appleby and Schwarz (1969) for solvated electrons yield. However, this underestimation is consistent with what is observed in the time-dependent yield for 1MeV electron radiation.

The discontinuities in the LET-dependent curves showed in Figure 3.12 are due to the different velocity of different ions at the same LET.

LET, indeed, is not a unique parameter affecting the radiation chemical effects. Analysis on the dependences of the yield of radiation-induced free radicals showed that G-values are also influenced by the radiation type, especially for heavy ion radiation, (Sauer Jr et al., 1977; Christman and Appleby, 1981; Pimblott and LaVerne, 2002; LaVerne et al., 2005). Different ion radiations with the same LET will lead, then, to different chemical yields. This effect is a result of changes in the track structure due to the velocity and the charge of the primary radiation (Christman and Appleby, 1981). Because of kinematic reasons, at a fixed LET, faster ions (and thus the more highly charged) can transfer larger maximum energy to the secondary electron. This will result in an increased penetration depth for the secondary electrons and in a broader radial dose distribution along the ion path. For two ions with the same LET, the track of the faster ion will result to be less dense, the radicals will be produced at a larger distance and the recombination probability between two radicals will decrease.
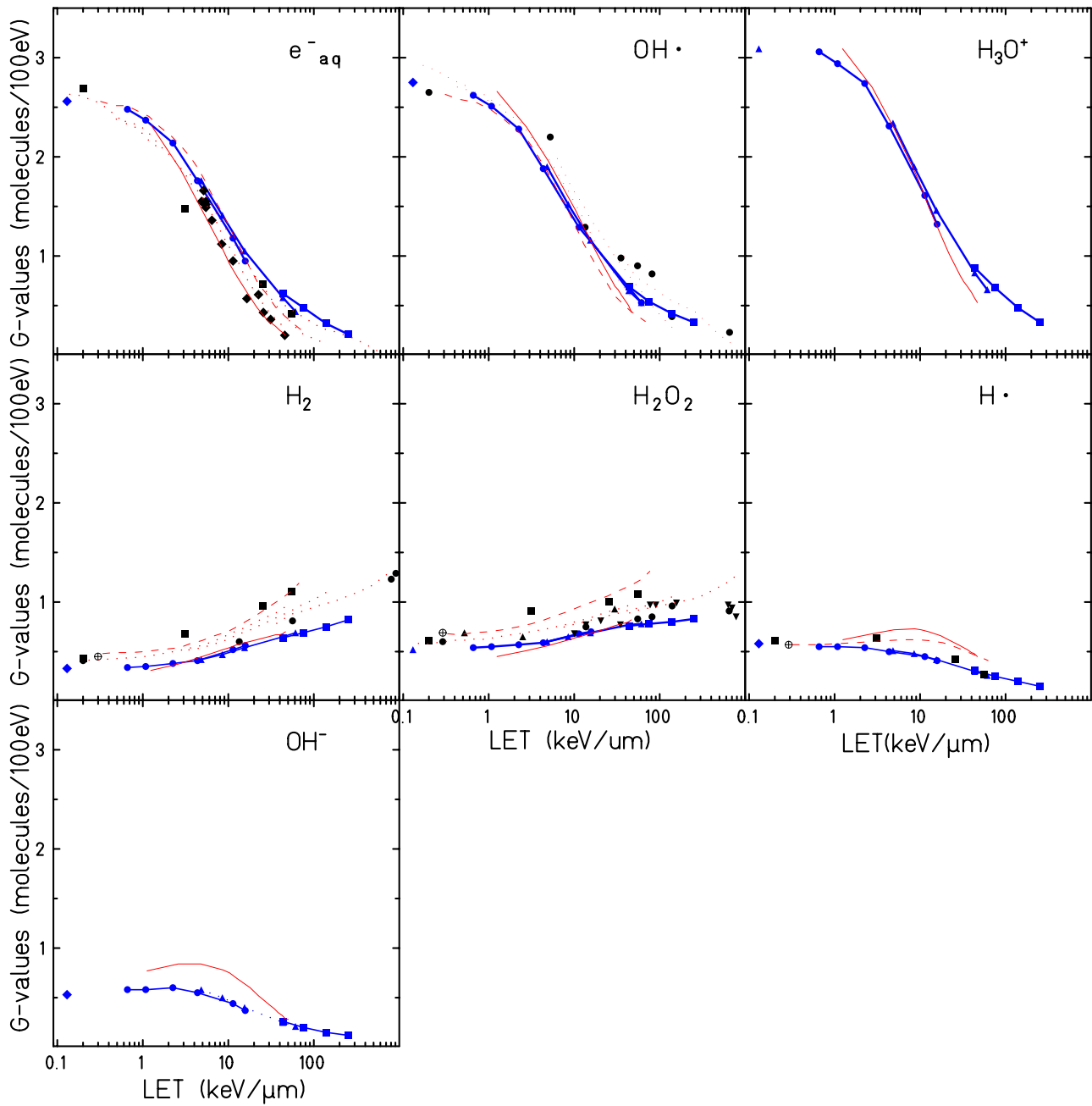
**Figure 3.12.:** LET dependent G-value at $1\mu$s after the irradiation of a water target with different radiation type. TRAX-CHEM calculations: blue solid symbols (bullet) protons, (triangle up) helium ions, (square) carbon ions). Simulations by other codes: red dotted lines Kreipl et al. (2008), red solid lines Plante (2011a), red dashed lines Kreipl et al. (2008). Ex:perimental values ◆ deuterum and helium ions Naleway et al. (1979), ⊛ electrons Elliot et al. (1993), ■ [60]Co $\gamma$-rays, proton, helium, nitrogen and neon ions Burns and Sims (1981), ● [60]Co $\gamma$-rays, proton and helium ions Appleby and Schwarz (1969), ▲ [137]Cs $\gamma$-rays, proton and carbon ions Wasselin-Trupin et al. (2002), ▾ proton, helium and carbon ions Pastina and LaVerne (1999).

The model adopted to describe the thermalization process of sub excitation electrons impacts extensively the simulation of the whole chemical evolution.

In the TRAX-CHEM code, electrons are followed with a step by step approach down to 7.4 eV while the final thermalization stage is described as a single step in a random direction with a step size sampled from a 3D Gaussian distribution. The mean value and the FWHM of this gaussian distribution is determined, depending on the initial energy of the sub-excitation electron, according to the thermalization scheme proposed by Zaider et al. (1994) (see Section 3.1.3).

In Figure 3.13 the time dependent yield $OH^\bullet$ and $H_2O_2$ (left panel) and $e^-_{aq}$ and $H_2$ (right panel) have been calculated with different electron thermalization models for a 90 MeV proton radiation in the time interval $10^{-12}$ to $10^{-6}$ s.

In particular the simulations have been performed substituting the thermalization tables from Zaider (in black) with the ones proposed by Terrissol and Beaudré (1990) (in light blue). This latter method is the one adopted in the CHEMKURBUC code (Nikjoo et al., 2006).

Additionally, in the original version of the TRAX code, it is also possible to load sub-excitation electrons cross sections able to follow electrons with a step by step approach, down to 1.7 eV, based on the measurements of Michaud et al. (2003). The time dependent G-values curves have been calculated also following this method and, in Figure 3.13, are shown in red. In this case, however, since the cutoff energy for the Michaud cross section is still larger than the thermal energy of the system ($\sim 25$ meV), an additional step in a random direction is, then, included in the simulation in order to account the slowing down of the electron to the thermal equilibrium. The step size is sampled from a Gaussian distribution with a mean value of 3 nm and FWHM of 1nm according to the thermalization table proposed by Zaider et al. (1994).

This method is more accurate with respect to the adoption of tabled energy dependent thermalization distances, however, it is also computationally more expensive and more sensible on uncertainties in the cross section tables. Calculating the mean free path and sampling the direction of each the sub-excitation electron at each events, small error on the cross sections will, indeed, propagate during every interaction. The time dependent G-values computed adopting this latter approach, are also shown in Figure 3.13. In this case the radical recombination on the picosecond scale results to be larger compared to the other two models adopted, and it leads to lower chemical yield during the whole track evolution. This observation seems to be supported by the finding of Meesungnoen and Jay-Gerin (2009). In his work, the author, used the cross section table proposed by Michaud et al. (2003) to calculate the energy dependent thermalization length for sub-excitation electron and compared the results with different thermalization models, including the ones used in this work. Form this study it results, that the thermalization distance predicted according to the cross section proposed by Michaud et al. (2003) are shorter compared to the one proposed by Zaider et al. (1994) and by Terrissol and Beaudré (1990) resulting in a denser track, and thus in a higher recombination probability, Figure 3.14.

The impact of the choice of the different thermalization methods on the LET dependent calculated yield at 1 $\mu$s after the irradiation has been also studied and is presented in Figure 3.15. The yield of the more abundant species is significantly different for the low LET range (LET < 10 keV/$\mu$m)

while it is less important in the high LET region. In the low LET region the track is less dense and the chemical evolution is more sensitive to the initial radical position. The yield of the recombination products ($H_2, H_2O_2, OH^- H^\bullet$) is only slightly affected over the whole LET range by the sub excitation model adopted.
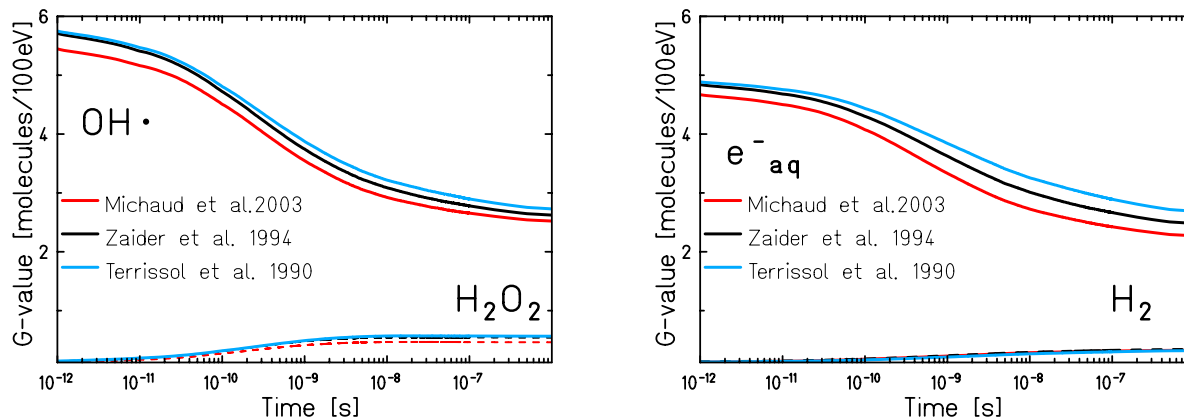


**Figure 3.13.:** Time-dependent radiolytic yields for 90 MeV proton in a water cube of 5 $\mu$m side for the species $OH^\bullet$ and $H_2O_2$ (left panel) and $e_{aq}^-$ and $H_2$ (right panel). For each species the yield have been calculated by using values for the electron thermalization distance as proposed in Zaider et al. (1994) (black curve), Terrissol and Beaudré (1990) (light blue curve) and following the sub-excitation electrons with a step by step approach, down to 1.7 eV, implementing the cross section tables proposed by Michaud et al. (2003) (red curve).
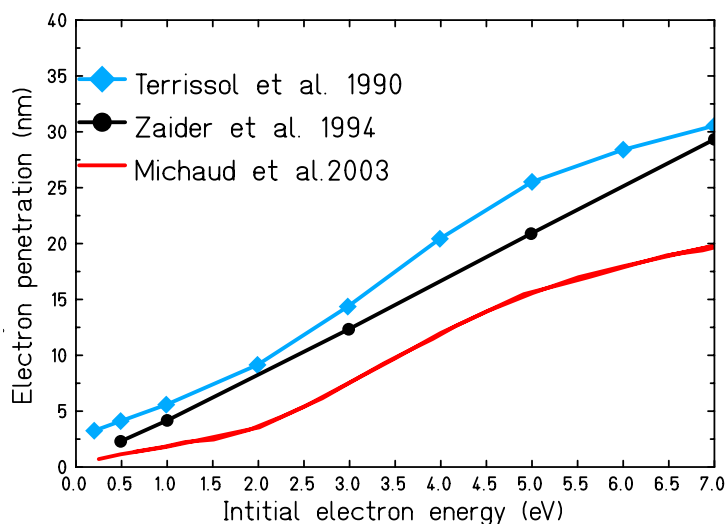


**Figure 3.14.:** Sub-excitation thermalization distances as a function of the initial energy of the sub-excitation electron (0.2-7 eV) in liquid water at room temperature: red curve Meesungnoen and Jay-Gerin (2009), black curve Zaider et al. (1994), light blue curve Terrissol and Beaudré (1990).
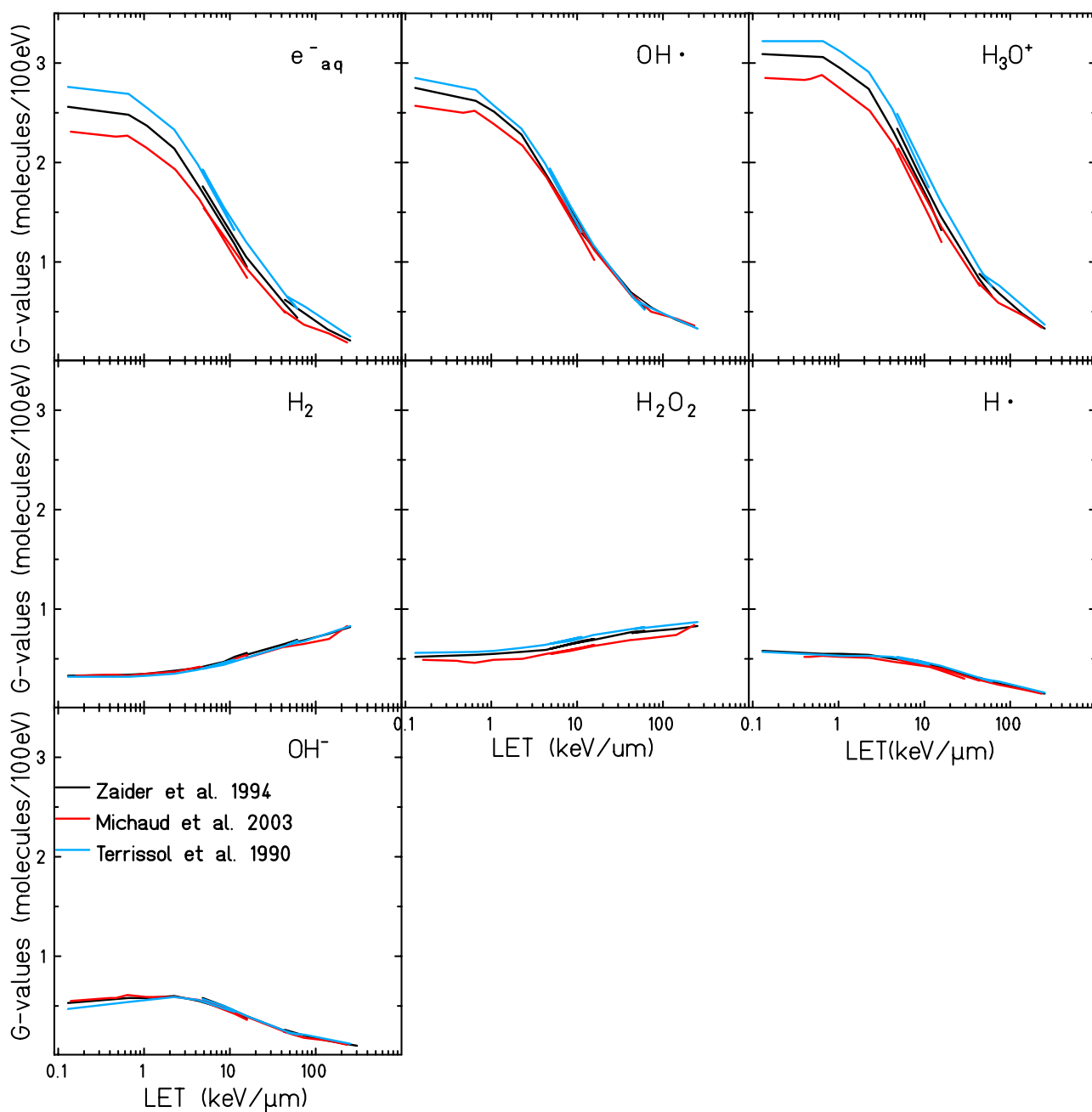
**Figure 3.15.:** LET-dependent radiolytic yields in the LET range 0.14-232 keV$\mu$m for all the chemical species generated by water radiolysis. For each species the yield have been calculated by using values for the electron thermalization distance as proposed in Zaider et al. (1994) (black curve), Terrissol and Beaudré (1990) (light blue curve) and following the sub-excitation electrons with a step by step approach, down to 1.7 eV, implementing the cross section tables proposed by Michaud et al. (2003) (red curve).

# 4 Impact of the water oxygenation level on radical diffusion and on the radiation chemistry of ion tracks

In most of the track structure codes including the chemical stage of radiation effect, the chemical evolution of a particle track is described in pure water, thus, in completely anoxic conditions. However, when it comes to study the impact of radiation in a living organism, this assumption is not realistic and dissolved molecular oxygen has to be considered as well. The implementation of target oxygenation results to be especially important when considering that the dissolved molecular oxygen, $O_2$, strongly increases the radiosensitivity of biological material. The effect of radiation on well oxygenated biological system results to be larger up to a factor three compared to the respective hypoxic condition (Tinganelli et al., 2015).

On the macroscopic scale the oxygen radiosensitization effect is quantified by the oxygen enhancement factor, OER: defined as the ratio of the dose required at a certain oxygenation conditions, $D_{pO_2}$ to the dose required at a normal pressure of oxygen, $D_{normoxic}$, in order to induce the same biological effect. This quantity is extremely important for radiation therapy applications since in many clinical cases the tumor oxygenation level is not uniform and, especially in the centre of large tumors, hypoxic regions might be present.

The increased radioresistance of hypoxic tumors seems to be strongly related to the indirect effect of radiation (Sonntag, 1987), and is generally explained as a combination of two main phenomena. On one hand, molecular oxygen can fix the radical induced DNA damage, making it permanent. On the other hand, the dissolved oxygen can interact with the radiation induced free radicals and increase the yield of production of superoxide anion, $O_2^{\bullet-}$ and of his protonated form $HO_2^{\bullet}$ (Beuve et al., 2015). Oxygen is, indeed, a strong scavenger for $e_{aq}^-$ and $H^{\bullet}$, and $O_2^{\bullet-}$ and $H^{\bullet}$ are mainly produced during the reactions:

$$e_{aq}^- + O_2 \rightarrow O_2^{\bullet-} \tag{4.1}$$

$$H^{\bullet} + O_2 \rightarrow HO_2^{\bullet}. \tag{4.2}$$

This latter theory is supported by both theoretical approaches (Turner et al., 1983; Klassen and Ross, 1997; Tomita et al., 1997; Watanabe and Saito, 2001; Colliaux et al., 2011) and chemical and biological experimental observations (Goldstein and Czapski, 1995; Mikkelsen and Wardman, 2003; de Grey., 2004; Aikens, 1991) mainly based on studies on the Fenton reaction and on the relation with superoxide dismutase enzymes.

It is known that the impact of the medium oxygenation on the radiosensitivity strongly depends on the LET. For low LET radiation, the value of OER can reach a maximum value of 3 and decreases

when increasing the LET down to a minimum asymptotic value of 1, when LET becomes greater than $\sim 100 - 200\text{keV}/\mu\text{m}$. This implies that, when irradiating with ion radiation, in the Bragg peak region there is, basically, no more impact of the tissue oxygenation on the radiation effect. On the microscopic scale, this effect can be explained as a track density effect. As shown in Figure 3.12, the recombination probability of water induced free radicals increases for high LET values, resulting in a lower contribution of the indirect effect of radiation damage and, thus, decreasing the impact of the target oxygenation condition (Colliaux et al., 2011).

However, this is not a unique explanation, many other processes might be involved as well and several additional theories have been developed. One of the most believed, the so-called "oxygen in the track hypothesis", suggests that the production of $O_2$ molecule via multiple ionization processes in the track of densely ionizing radiation can cause locally a partial oxyc response (Meesungnoen and Jay-Gerin, 2009; Gervais et al., 2006; Baverstock and Burns, 1981). Other possible hypotheses are the interacting radical theory (Alper, 1956), the oxygen depletion in the heavy ions tracks (Stuglik, 1995), the lesion complexity hypothesis (Ward, 1994), and the radical multiplicity (Michael, 1996).

In this chapter, the implementation of dissolved oxygen in the chemical module of TRAX will be presented, and its impact on the production and diffusion of chemical species will be studied for different irradiation conditions: different LET, different oxygenation level, and different particles type.

## 4.1 Implementation of dissolved oxygen in TRAX

### 4.1.1 Interaction of the dissolved molecular oxygen with radiation induced water free radicals

The addition of a certain concentration of the molecular oxygen to the target material affects the reaction network. In this case, new species, generated by the interaction of $O_2$ with the radiation induced water free radical, have to be implemented and accounted during all the track chemical evolution. This new species and their diffusion coefficients are presented in Table 4.1. A list describing the new reactions implemented involving this new species is showed in Table 4.2.

### 4.1.2 Dissolved oxygen implementation in TRAX

The presence of dissolved oxygen has been implemented following a similar approach to the one proposed in Pimblott et al. (1991); Green et al. (1990). The molecular oxygen is assumed to be homogeneously distributed and is treated as a continuum. This approximation has been adopted also by other authors (Cobut et al., 1998; Watanabe and Saito, 2001; Colliaux et al., 2011; Tomita et al., 1997).

The explicit introduction of the oxygen in the simulation would, indeed, dramatically increase the computing time even for very dilute solutions. In a system with $n_c$ particles for each time step it is necessary to consider up to $n_c(n_c - 1)/2$ possible combinations of reactants. When a solute is explicitly accounted it is also necessary to include $n_s$ solute molecules. The number of possible reactant combination will then be $n_c((n_c - 1)/2 + n_s)$ and can become excessive for very low oxygen concentration (Pimblott et al., 1991). Just as an example: the chemical species generated by a 10 MeV proton on a water cubic volume with 5 $\mu m$ side is $n_c \sim 10^3$, thus the number of possible reactant combinations would

**Table 4.1.:** List of all the chemical species, and their diffusion coefficients D, added to the chemical species list of TRAX in order to describe the impact of dissolved molecular oxygen in the water target .

| **Species** | **D** $(\mathrm{m^2 s^{-1}})$ |
|---|---|
| $O_2$ | $2.1 \times 10^{-9}$ |
| $HO_2^{\bullet}$ | $2.0 \times 10^{-9}$ |
| $HO_2^{-}$ | $2.0 \times 10^{-9}$ |
| $O_2^{\bullet -}$ | $2.1 \times 10^{-9}$ |

**Table 4.2.:** List of all the reactions and reaction rate constants, k, added to the standard reaction list of TRAX Table 3.4, in order to describe the chemical reaction taking place in presence of dissolved molecular oxygen in the water target.

| **Reaction** | | **Products** | $k(10^{10} \mathrm{dm^3 mol^{-1} s^{-1}})$ |
|---|---|---|---|
| $e_{aq}^{-} + O_2$ | $\longrightarrow$ | $O_2^{\bullet -}$ | 1.9 |
| $H^{\bullet} + O_2$ | $\longrightarrow$ | $HO_2^{\bullet}$ | 2.0 |
| $OH^{\bullet} + HO_2^{\bullet}$ | $\longrightarrow$ | $O_2$ | 1.0 |
| $OH^{\bullet} + O_2^{\bullet -}$ | $\longrightarrow$ | $O_2 + OH^{-}$ | 0.9 |
| $OH^{\bullet} + HO_2^{-}$ | $\longrightarrow$ | $HO_2^{\bullet} + OH^{-}$ | 0.5 |
| $e_{aq}^{-} + HO_2^{\bullet}$ | $\longrightarrow$ | $HO_2^{-}$ | 2.0 |
| $e_{aq}^{-} + O_2^{\bullet -}$ | $\longrightarrow$ | $OH^{-} + HO_2^{-}$ | 1.3 |
| $H^{\bullet} + HO_2^{\bullet}$ | $\longrightarrow$ | $H_2O_2$ | 2.0 |
| $H^{\bullet} + O_2^{\bullet -}$ | $\longrightarrow$ | $HO_2^{-}$ | 2.0 |
| $H_3O^{+} + O_2^{\bullet -}$ | $\longrightarrow$ | $HO_2^{\bullet}$ | 3 |
| $H_3O^{+} + HO_2^{-}$ | $\longrightarrow$ | $H_2O_2$ | 2.0 |
| $HO_2^{\bullet} + HO_2^{\bullet}$ | $\longrightarrow$ | $H_2O_2 + O_2$ | 0.000076 |
| $HO_2^{\bullet} + O_2^{\bullet -}$ | $\longrightarrow$ | $O_2 + HO_2^{-}$ | 0.0085 |

be $\sim 5 \times 10^5$. Assuming an oxygen concentration of $10^{-5}$ mol/l, the number of dissolved molecules to be added in the target geometry will be $n_s \sim 7 \times 10^5$ and the possible number of reactant combination would, then, become $\sim 7 \times 10^7$.

Under the approximation of a continuum distribution of oxygen the probability for a radiolytic species to interact with an oxygen molecule of the target is determined by the rate equation

$$\frac{d\Omega}{dt} = k(t)c_s\Omega(t) \tag{4.3}$$

where $\Omega(t)$ is the time dependent survival probability of the molecule of interest and $c_s$ is the oxygen concentration. k(t) is the time dependent rate coefficient for the reaction of interest and it is defined according to the Noyes theory, (Noyes, 1961), as:

$$k(t) = 4\pi D'R_{reac}\left(1 + \frac{R_{reac}}{\sqrt{\pi D't}}\right) \tag{4.4}$$

where $R_{reac}$ is the reaction radius calculated according to Equation 3.7 and $D'$ is the relative diffusion coefficient (considering the two species A and B, $D' = D_A + D_B$). The probability, $W(t)$, for a species to react with a molecule of dissolved oxygen during a period of time t is then given by:

$$W(t) = 1 - \Omega(t) = 1 - e^{-4\pi D'R_{reac}c_s\left(t + 2R_{reac}\sqrt{\frac{t}{\pi D'}}\right)} \tag{4.5}$$

In the code, the probability that a species will interact with an oxygen species is computed every time step $t$, and is sampled according to the probability distribution P(x) defined as following

$$P(x) = \begin{cases} 1 & \text{if } x \leqslant W(t) \\ 0 & \text{otherwise} \end{cases} \tag{4.6}$$

where $x \in [0:1]$ is a random variable selected by a uniform distribution. When a reaction occurs the reacting product is removed from the list of radicals and the reaction products are added according to the model followed during the chemical stage in TRAX-CHEM.

### 4.1.3 Calculation of oxygen concentration

In order to define a range of oxygen concentrations consistent with the condition of a biological system, it is convenient to relate the concentration of oxygen dissolved in water to the partial pressure of oxygen in the air within standard conditions of pressure.

Given the partial pressure of a gas, $p_{gas}$ (generally in atmospheres), the solubility of the gas at a fixed temperature in a particular solvent, $c_s$ (generally in mol per liter), can be computed through Henry's law:

$$c_s = K_H \times P_{gas} \tag{4.7}$$

where $K_H$ is Henry's constant and corresponds to the gas solubility in water. For $O_2$ at a temperature of 20°C, Henry's constant is $K_H = 1.3 \times 10^{-3}$ mol/(l atm). Hence, for a partial oxygen pressure $P_{O_2} = 21\%$ the oxygen concentration is 0.27 mmol/l

**Table 4.3.:** List of values for atmospheric partial oxygen pressure at the water surface used in the following calculations and respective oxygen concentration in water. Calculated according to Equation 4.7.

| pO2 | Oxygen concentration (mmol/l) |
|------|------------------------------|
| 21%   | 0.273   |
| 10%   | 0.13    |
| 5%    | 0.065   |
| 2.5%  | 0.0325  |
| 1%    | 0.013   |
| 0.5%  | 0.0065  |
| 0.15% | 0.00195 |

## 4.2 Results

### 4.2.1 Radiolysis of oxygenated water

Chemical yields for the different species have been evaluated for different oxygen concentration and different radiation quality.

Figure 4.1 shows the impact of the target oxygenation level on the time dependent evolution of the radiolytic yields for 40 MeV/u helium radiation. On the upper left panel, G-values as a function of the time are reported in the case of hypoxic water target, while in the upper right and bottom panel the chemical yield has been reported for an oxygenated water target, with an atmospheric partial oxygen pressure at the water surface of respectively 1.5% and 21%. In the early stages of the chemical evolution of the track, the yield of radicals is not significantly affected by the presence of dissolved oxygen molecule in the target. At more advanced times, $\sim 0.1$ ns after the passage of radiation, the chemicals are more diffused and all the $e_{aq}^-$ and $H^\bullet$ radicals start to interact with the oxygen leading to the production of $O_2^{\bullet-}$ and $HO_2^\bullet$. In the case of oxygen concentration at the water surface of 1.5%, a sensible reduction in the yield of $e_{aq}^-$ and $H^\bullet$ can be observed, while in the case of $pO_2 = 21\%$, a complete consumption of all the $e_{aq}^-$ and $H^\bullet$ can be observed at 0.2 $\mu s$. The yield of formation of $HO_2^-$ is negligible for the whole time scanned by our calculations for all the oxygen concentrations analyzed.

The presence of $O_2^{\bullet-}$ and $HO_2^\bullet$ is the major effect of dissolved oxygen in the target during the process of water radiolysis. At 1 microsecond after the irradiation the yield of the $O_2^{\bullet-}$ nearly matches the one of the solvated electrons in hypoxic conditions: $G_{O_2^-}(1\mu s, pO_2 = 21\%) = 1.88$ and $G_{e_{aq}^-}(1\mu s, pO_2 = 0\%) = 1.93$. The yield of the $HO_2^\bullet$, $G_{HO_2^\bullet}(1\mu s, pO_2 = 21\%) = 0.70$, is, instead, higher compared to the one of $H^\bullet$, $G_{H^\bullet}(1\mu s, pO_2 = 21\%) = 0.51$. Additionally to the reaction channel showed in Equation 4.2, the $HO_2^\bullet$ radical can be, indeed, also produced by the interaction between one $O_2^{\bullet-}$ and one $H_3O^+$, with a reaction rate of $3 \times 10^{10} dm^3 mol^{-1} s^{-1}$ (see Table 4.2)

$$H_3O^+ + O_2^- \longrightarrow HO_2^\bullet. \tag{4.8}$$
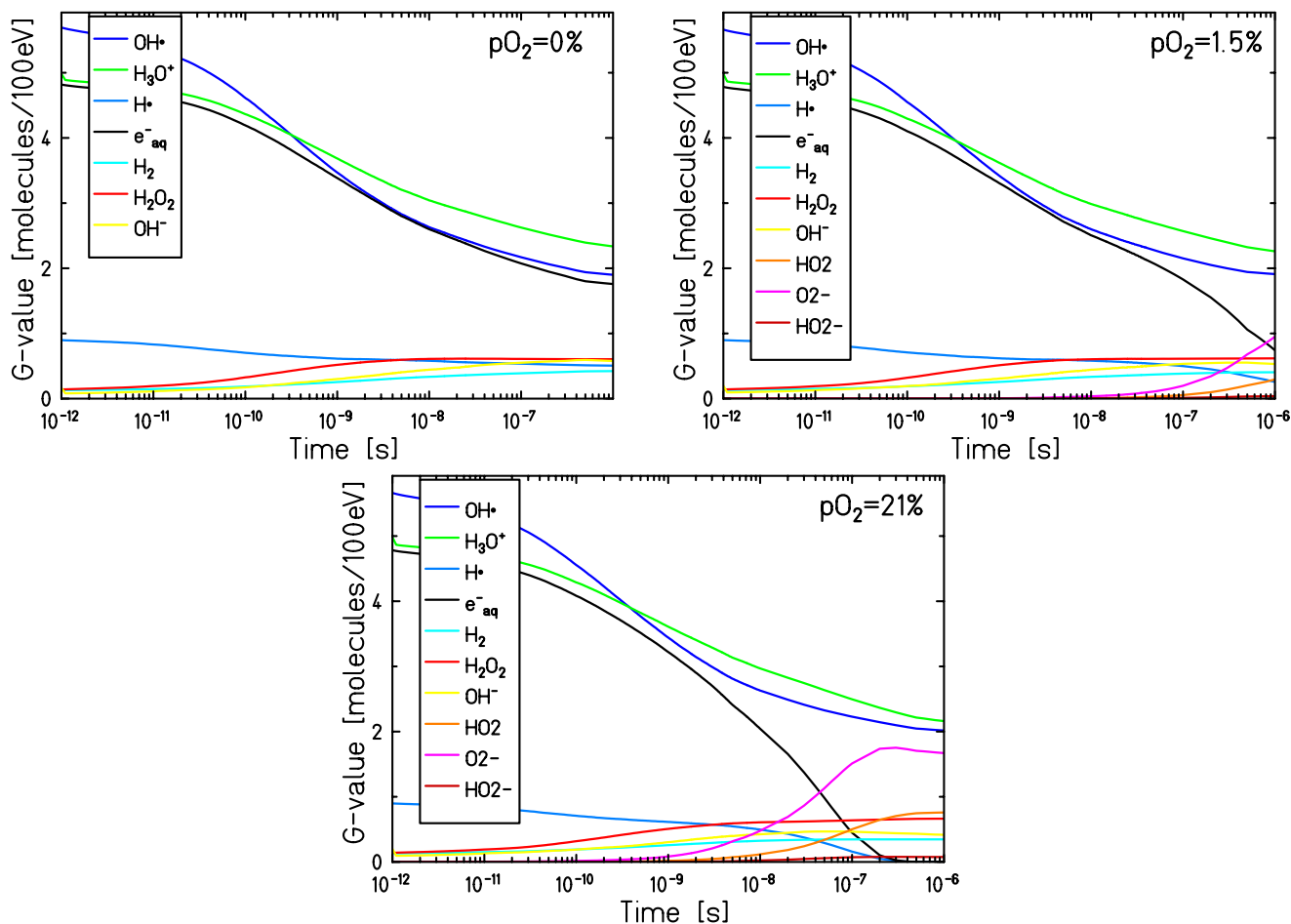
**Figure 4.1.:** Time dependent yield of the chemical species generated by a 40 MeV/u helium track in a hypoxic target (upper left panel) and in an oxygenated water target, with an atmospheric partial oxygen pressure at the surface of the water of the 1.5% (upper right panel) and 21% (bottom panel).

### 4.2.2 Time dependent radiolytic yield for different oxygen concentrations

Figure 4.2 shows the time dependent yield for $e_{aq}^-$, $H^\bullet$, $HO_2^\bullet$ and $O_2^{\bullet -}$, in an oxygenated water target, with oxygen concentration on the water surface between $pO_2 = 0\%$ and $pO_2 = 21\%$, for 500 keV electron irradiation. A strong increase of the yield of $O_2^{\bullet -}$ and $HO_2^\bullet$ (and a decrease of the yield of $e_{aq}^-$ and $H^\bullet$) can be observed for oxygen pressure at the water surface up to $pO_2 = 5\%$ while at larger oxygen concentration a saturation level is reached.

This saturation limit is reached when all the $e_{aq}^-$ and $H^\bullet$ are completely consumed and the yield of $O_2^{\bullet -}$ and $H_2O$ stops growing. At intermediate oxygen pressure many $e_{aq}^-$ and $H^\bullet$ were not completely scavenged by the dissolved oxygen within 1 microsecond. As expected, the higher the oxygen pressure is the faster the $e_{aq}^-$ and $H^\bullet$ consumption is. For intermediate time, indeed, the simulation time stops before the radicals yield reaches an equilibrium. The choice of the simulation time, 1 $\mu$s, is in fact
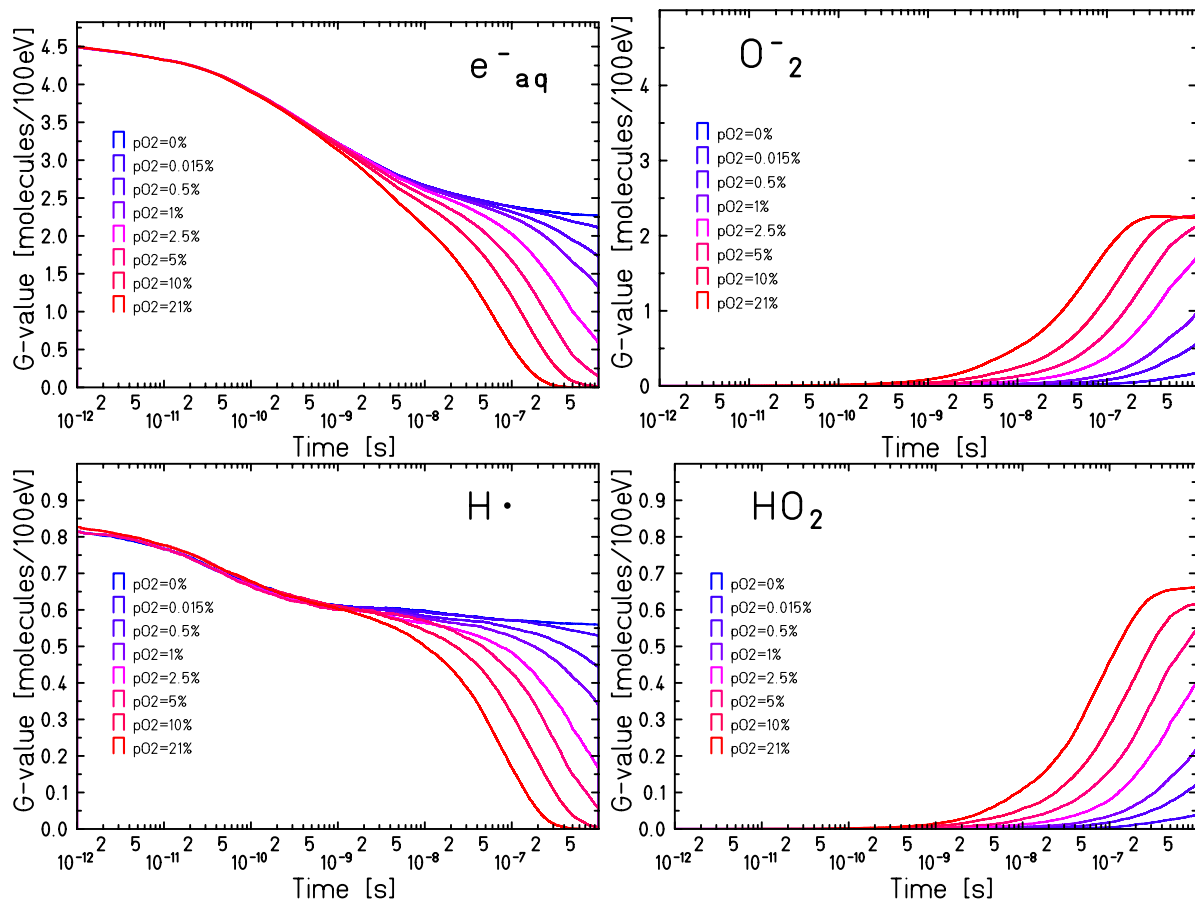
**Figure 4.2.:** Time dependent yield for $e_{aq}^-$ (top left panel), $H^\bullet$ (bottom left panel), $O_2^{\bullet-}$ (top right), $HO_2^\bullet$ (bottom right panel) and in an oxygenated water target, with oxygen concentration on the water surface between $pO_2 = 0\%$ and $pO_2 = 21\%$, for 500 keV electron irradiation.

somehow arbitrary. In the hypoxic case, it corresponds to a time at which a constant yield of the different species is being reached and the chemical interaction rates between the radiation induced water free radicals are supposed to be very low. However, when considering also the interactions with the target material, especially in the case of biological system, there is no reason to define a specific conclusive time and the chemical kinetic can proceed in a complex way for very long time (Colliaux et al., 2011). It has been, thus, decided to keep the timeframe adopted for the hypoxic condition, limiting the study to the track evolution and terminating it when the the track structure is completely lost, i.e., the reaction process is determined only by the reactant concentration and not by their spatial distribution. In the case of oxygenated water, according to our model (Table 4.2), the only species able to interact with the dissolved oxygen are the $e_{aq}^-$ and $H^\bullet$. We can, thus, expect that the reaction kinetics of the whole track will be limited to the lifetime of these two species in the target material.

The dependence of the G-values at $1\mu s$ on the oxygen concentration of the target material is shown in Figure 4.3 for all the chemical species generated by the water radiolysis, the water target was irradiated by 500 keV electrons. As expected, the impact of the dissolved oxygen is mainly affecting the yield of $O_2^{\bullet-}$, $H_2O$, $e_{aq}^-$ and $H^\bullet$. The yield of production and the whole chemical evolution of the other chemical species is not significantly affected by the oxygenation level of the water. In general, a small increase of
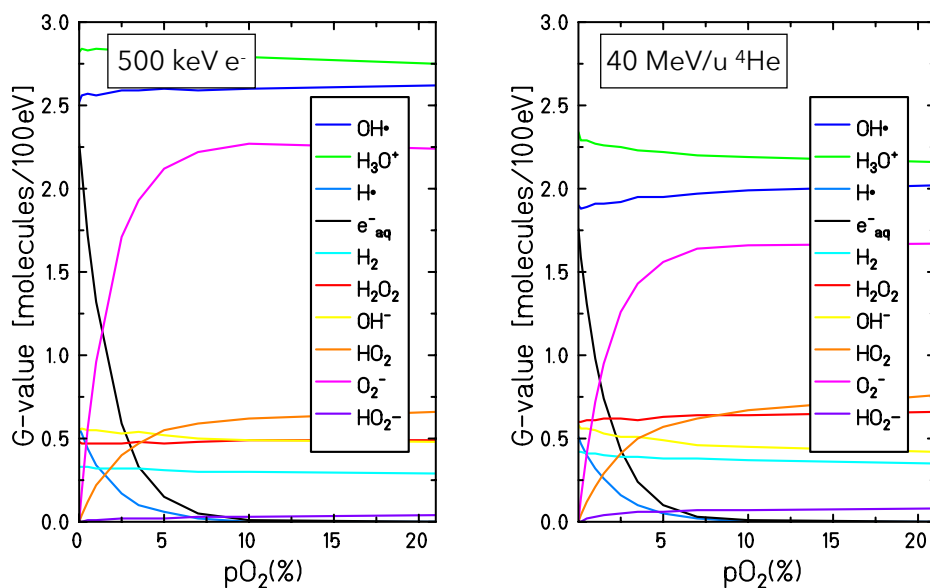
**Figure 4.3.:** Radiolytic yields, at 1 $\mu$s, for all the different chemical species generated by the water radiolysis at different oxygenation conditions by 500 keV electron irradiation (left panel) and 40 MeV/u helium radiation (right panel).

the OH$^{\bullet}$, H$_2$O$_2$ radical yield and a small decrease of the H$_3$O$^+$, H$_2$ and OH$^-$ yield can be observed, but in these cases, changes in the yield of production at the microsecond are lower than 10%.

### 4.2.3 Radiolytic yield for different energy and type of radiation in oxygenated water

*In vitro* experiments have shown that the oxygen effect in biological systems has a pronounced dependence on the radiation LET (Hirayama et al., 2009; Tinganelli et al., 2015). When irradiating with high LET the impact of the target oxygenation becomes less important. Radiolytic yields in oxygenated water with an oxygen pressure of 21% in air have been, then, evaluated for different radiation energies and particle types. In Figure 4.4 the LET dependent yields at one microsecond are presented for pure and oxygenated water.

As expected from what has been discussed in the previous section and observed in Figure 4.3 and Figure 4.2, the solvated electrons and the atomic hydrogen (e$^-_{aq}$ and H$^{\bullet}$) are completely consumed at the microsecond in oxygenated water. For all the range of LET analyzed, their G-value at one microsecond was always zero.

The yield of O$_2^{\bullet-}$ and HO$_2^{\bullet}$, which are the two main indicators of the presence of molecular oxygen, is maximum for low LET radiation and decrease for higher LET values in the oxygenated case. This strong dependence on the LET can be justified as a track structure effect: for high LET the ion track is denser and radicals are produced in close proximity. The radiation induced water radicals will then recombine reacting with each other before any significant oxygen scavenging effect.

Minor effects of the target oxygenation are, instead, observed for the other chemical species generated by water radiolysis. The scavenging effect of the solvated electrons and atomic hydrogen radicals lead to a general decrease of the $H_2$ molecule which is mainly generated as a product of the recombination processes

$$e_{aq}^- + e_{aq}^- \longrightarrow H_2 + OH^- OH^-$$

$$H^\bullet + H^\bullet \longrightarrow H_2.$$
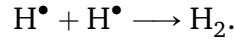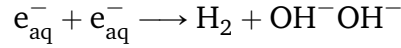
Similarly the yield of the $OH^-$ decrease for all the LET range. According to the reaction model in Table 3.4, this chemical is principally produced by the recombination of $e_{aq}^-$ with many of the water induced radicals ($OH^\bullet$, $e_{aq}^-$, $H^\bullet$ and $H_2O_2$) and competes with the electron scavenging effect.

The yield of the $OH^\bullet$ radical results to be slightly higher in an oxygenated target for low LET, while at high LET no difference between oxygenated and hypoxic target is being observed. One of the main processes consuming the $OH^\bullet$ radical is by its interaction with a solvated electron. In case of an oxygenated target, this reaction is directly competing with the interaction of the $e_{aq}^-$ with the $O_2^{\bullet-}$ and result in a lower amount of scavenged $OH^\bullet$. For high LET, however the track kinetic is faster and the $OH^\bullet$ react with the $e_{aq}^-$ before the interactions with the dissolved oxygen become dominant.

An increase of almost the 20% is observed for $H_2O_2$ at high LET, while no significative oxygen effect is observed at low LET. As discussed in Section 3.3.4, the time dependent yield of the $H_2O_2$ is the result of two main processes:

$$OH^\bullet + OH^\bullet \longrightarrow H_2O_2$$

$$e_{aq}^- + H_2O_2 \longrightarrow OH^\bullet + OH^-.$$
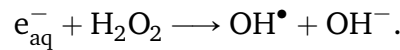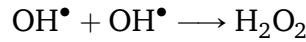
The first one is dominating at the early steps of the chemical track evolution and is the main channel of production of the $H_2O_2$ while the second one becomes significative after 1 ns and removes $H_2O_2$ from the target. The contribution of this second process is more pronounced in the case of high LET radiation. In case of oxygenated water, this reaction channel competes with the molecular oxygen scavenging effect, resulting in a larger yield of $H_2O_2$ at 1 $\mu$s after the irradiation.

Three different radiation types have been used to calculate the chemical yields showed in Figure 4.4 for pure and oxygenated water: proton (circles), helium ions (triangles) and carbon ions (squares). However, the dependence on the radiation type seems to be not significantly dependent on the oxygenation level of the target.

Similar results have been obtained by Colliaux et al. (2011), where the yield $HO_2^\bullet$ and $O_2^{\bullet-}$ have been calculated for different LET and radiation type in a water target with an oxygen pressure at the water surface of $pO_2 = 21\%$ and a glutathione (one of the most important antioxidant present in the cell) concentration of 1mmol/l. As in our calculations, a pronounced decrease in the yield of ($O_2^{\bullet-} + HO_2^\bullet$) with LET has been found. Considering the correlation between the production yield of $O_2^{\bullet-}$ and $HO_2^\bullet$ at different LET, particle type, and dissolved oxygen concentration, the author suggested that the interaction of $e_{aq}^-$ and $H^\bullet$ with the molecular oxygen might lead directly or indirectly to the production of toxic species able to damage the cell structure or altering the cell signaling. However, because of the presence of the dissolved antioxidant, it is impossible to directly compare the results of the two calculations.
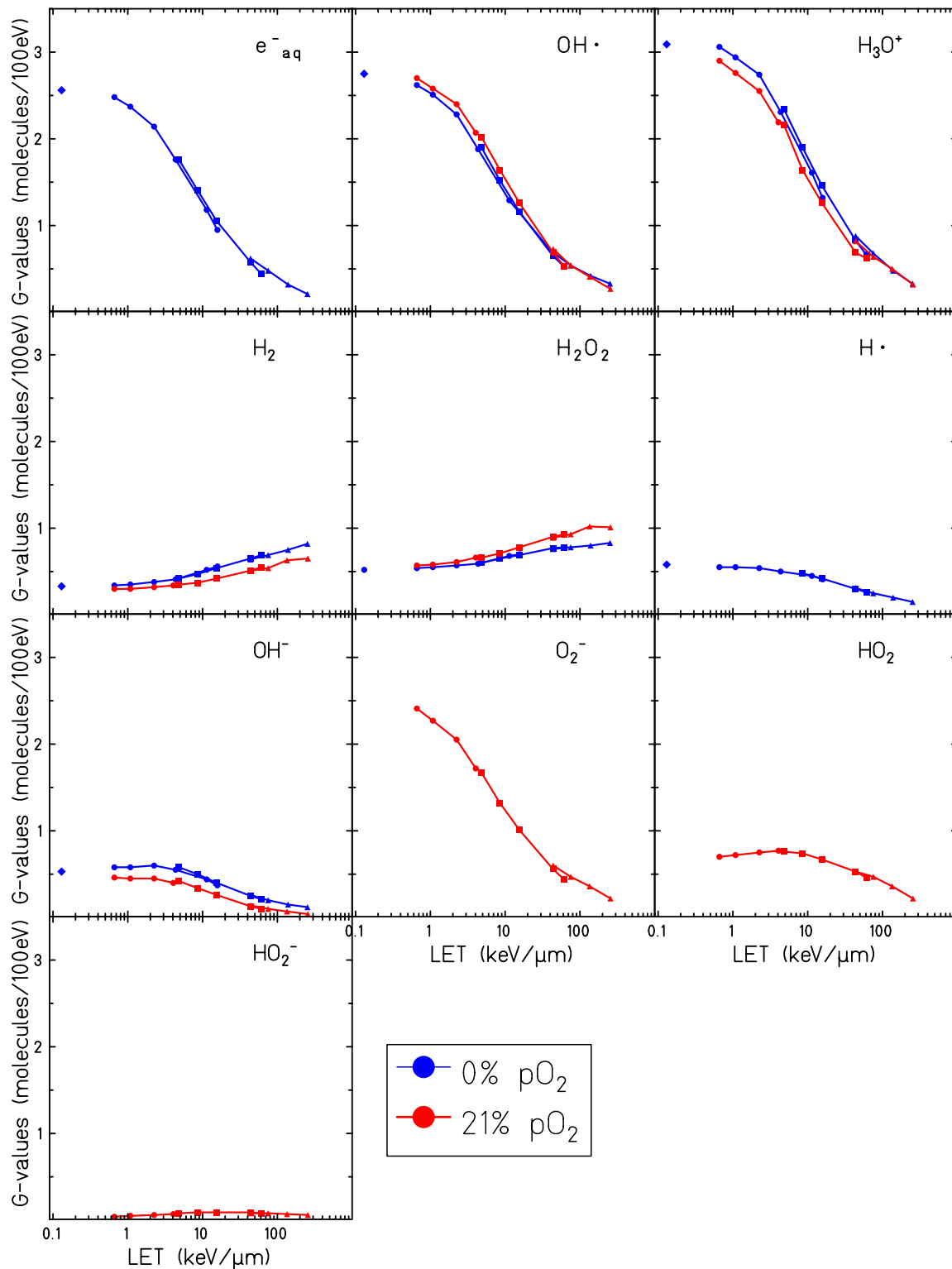
**Figure 4.4.:** Radiolytic yields for all the different chemical species generated by the water radiolysis in hypoxic condition (blue curves) and an oxygen pressure of 21% in air (red curves) for different radiation energy and particle type: proton (bullets), helium ions (triangles) and carbon ions (squares), one microsecond after the irradiation.

# 5 Simulation of metallic nanoparticle

Metallic nanoparticles, NPs, are a promising tool for improving the selectivity and efficacy of radiation therapy. Thanks to their property as radiation dose enhancers, they raised a big interest and inspired several research lines. The efficacy of NPs as radiosensitizers with X-ray and ion radiation has been proven in both *in vivo* and *in vitro* and predicted by theoretical models (Hainfeld et al., 2008; Polf et al., 2011; Butterworth et al., 2012; Porcel et al., 2012; Kwatra et al., 2013; Wälzlein et al., 2014; Lin et al., 2015). In addition some types of NPs can be used as a contrast agent in clinical exams, e.g. gadolinium NPs for MRI, resulting than particularly suitable for theranostic applications: the simultaneous use of NPs for therapy and diagnosis.

Gold NPs (AuNPs) in particular, are especially promising: in addition to their large interaction cross section for X-ray radiation as well as for ion radiation, AuNPs have a good biocompatibility, are relatively simple to synthesize in a wide range of sizes and their surface can easily be functionalized (Haume et al., 2016).

One of the main processes involved in the nanoparticle radiosensitization is the increased dose deposition localized in the vicinity of the NP, induced by an enhanced production of secondary electrons emitted by the NP, see Section 1.6.1. An increased number of ionization events is, indeed, expected to take place in gold when compared to an equivalent volume of water: this is because the number of interaction per energy deposited is larger in gold with respect to water and the gold density (19.3 $g/cm^3$) is also larger than the density of water (1 $g/cm^3$). In addition, it has been demonstrated that an important contribution to the local dose deposited around the NP comes from the emission of Auger electrons and Auger electron cascades (Wälzlein et al., 2014). Generally the increased dose deposition in presence of NPs is quantified by the dose enhancement factor, DEF, defined as the ratio between the average absorbed dose in the tumor region in the presence of AuNPs and dose absorbed, in an equivalent volume, in absence of AuNPs (after performing the same irradiation protocol) (Muddineti et al., 2015).

A significant increase in radical production has been observed in the presence of gold and platinum NPs (Porcel et al., 2010; Sicard-Roselli et al., 2014; Paudel et al., 2015). This phenomenon could be related to surface effects such as a high concentration of low-energy electrons due to the surface plasmon effect (Zhang et al., 2009), catalytic interactions between the metal surface and the water dipole (Paudel et al., 2015), or geometrical factors like the surface volume ratio for high-Z materials (Porcel et al., 2010; Paudel et al., 2015). Recent Monte Carlo simulations calculated the number of radicals generated by the secondary electron coming out from a gold nanoparticle of 50 nm size irradiated with proton radiation (Tran et al., 2016). The radical yield was found to be up to 10 times larger compared to the case of irradiation without NPs.

Thanks to the the possibility of using relatively complex geometries and to the possibility to follow the secondary electrons in gold with a nanometric resolution, Wälzlein et al. (2014) were able, for the first time, to study the radiosensitizing effect of AuNPs in water solutions. In their work, the authors focused

on the study of the secondary electron emission, Auger electron spectra and the radial dose distribution in the vicinity of 2 and 22 nm NPs of different high-Z metal irradiated with 80 MeV protons.

In the present chapter, in order to characterize the physical dose enhancement factor for different irradiation conditions, this study will be extended to different ion and different LET radiations and different NP sizes. Thanks to the new TRAX-CHEM extension, the enhanced production of radiolytic species will be for the first time studied for different ion radiations and different oxygenation conditions. Additionally, the gold cross sections implemented in TRAX have been further validated by comparing the calculated transmission spectra, obtained with different gold absorbers for electron radiation emitted by thallium-204 (Tl-204), with experimental results as well as with different track structure codes.

## 5.1 Energy deposition model for thallium-204 (Tl-204) electron and photon radiation in gold

The physical model for gold targets adopted in TRAX allows preforming simulations on the nanoscopic scale with an almost unique precision. The gold cross section implemented in TRAX allow describing the secondary electron transport interaction by interaction down to 2.7 eV accounting also for the production of Auger electrons and the consequent Auger cascade (for a more extended description see Chapter 2). The reliability of these cross sections has been indirectly validated by comparing simulation results with experimental data, e.g. the stopping power of electrons in gold (Wälzlein et al., 2014), and backscattered electrons emission after proton impact on gold films (Hespeels et al., 2017).

Here we present a further validation test where TRAX simulations of electrons transmission after gold layers of different thickness are compared with experimental results as well as with other simulation tools. This work has been carried out at CSIC in Madrid in collaboration with the group of Prof. Gustavo Garcia (CSIC, Madrid, Spain) and a paper presenting the results shown in this section has been submitted (Williart et al., 2018).

### 5.1.1 Experimental setup and thallium emission spectra

Electron transmission spectra after gold absorbers of different thickness have been measured by Prof. Amalia Williart (UNED, Madrid, Spain). A schematic representation of the experimental geometry is shown in the left panel of Figure 5.1.1. Gold absorbers of 20 $\mu$m, 40 $\mu$m, and 60 $\mu$m have been irradiated with a thallium-204 (Tl-204) disc source.

Tl-204 is a $\beta$-emitter with a half life of $T_{1/2} = 3.83$ years. It decays into Pb-204 with an endpoint energy of 763.76 keV. Additionally, to the $\beta$-decay, the Tl-204 has a probability of 2.92% to decay into Hg-204 through an electron capture process followed by the emission of X-rays at energies defined by the spectral Hg emission lines (Deslattes et al., 2005). The right panel of Figure 5.1 shows the experimental spectrum of the Tl-204 source obtained without any absorber.

Transmission spectra have been measured with a Silicon Lithium, Si(Li), detector for X-ray spectroscopy and beta decay exploration. The detector adopted had a sensitive diameter of 10 mm and 5.27 mm thickness and was placed at 9 mm distance from the gold layer. In the energy range of interest (from 20 keV to 2 MeV) the detector intrinsic efficiency for electrons is 100%.
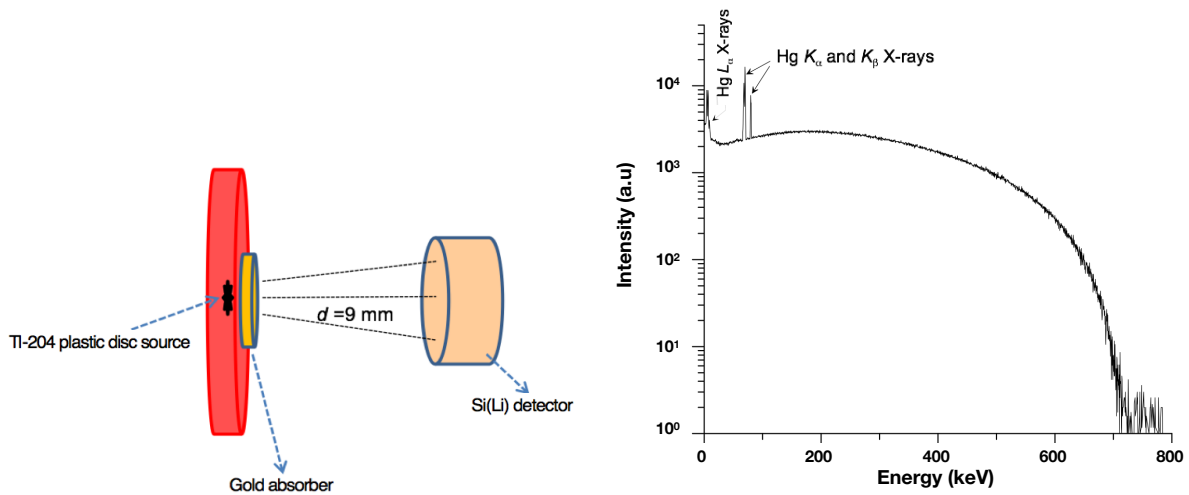
**Figure 5.1.:** Right panel: schematic representation of the experimental setup geometry. Left panel: emission spectrum of Tl-204 source employed in this study. Beta radiation produced during Tl-204/Pb-204 decay as well as the most intense Hg X-ray emissions.

### 5.1.2 Simulated spectra

TRAX simulations for all the different absorbers investigated have been compared with the measured spectra as well as with different simulation tools. In particular, the other codes investigated are Geant4 (Agostinelli et al., 2003), in the framework of GAMOS(v 5.0.0) and PENELOPE (only for the 60 $\mu$m absorber) (Baro et al., 1995; Salvat et al., 2006). The GAMOS and PENELOPE simulations have been performed by Antonio Muñoz (CIEMAT, Madrid, Spain).

For all the simulations, the experimental spectrum obtained without gold absorbers (right panel of Figure 5.1.1) has been used as the incident radiation spectrum. The presence of X-rays and $\beta$-emissions, is generally considered an advantage for these kind of applications since it allows studying photon and electron interactions simultaneously. However, since photon radiation is not yet implemented in the TRAX code, the photon contribution was excluded from the source spectrum used for the TRAX simulations. In this case, the electron spectra were obtained suppressing the photon contribution and extrapolating the electron spectra for energies lower than 100 keV.

Geant4 simulations have instead been performed accounting for two possible cases (with and without photons contribution in the source spectra), in order to better compare the simulation with both experimental and TRAX results.

Simulated and measured spectra for 20 $\mu$m, 40 $\mu$m and 60 $\mu$m gold absorbers are shown in figures 5.2 and 5.3. For the high energy range (E > 400 keV), both codes, TRAX and Geant4, can reproduce the experimental data with a good agreement. The two codes are very consistent in this energy range and can reproduce the measured endpoint energy for all the selected absorbers.

A different scenario is instead appearing in the low energy region: below 200 keV. In this case, discrepancies, between the two codes and between the codes and the experimental data, are clearly visible.

The main difference between TRAX and measured spectra is clearly related to the missing contribution of the photon radiation in TRAX, which is not limited to the missing contribution of photons in the source spectra but also in the bremsstrahlung and secondary photo-electrons.

However, evident differences at low energies are shown also between the TRAX calculations and the ones obtained with Geant4 not including photons. A possible explanation for this discrepancy is the different electron transport model; while TRAX is an event by event code Geant4 simulates the electron transport through condensed history methods. This method consists in the approximation of the cumulative effects of multiple electron collisions in a single step with a specified step length. Often this step is chosen to be several mean free paths and represents the distance traveled by each electron between two collisions (Larsen and Tolar, 2001). This approach speeds up the simulation but results to be less accurate compared to an event by event simulation method, especially for low energies. On the other hand, event by event approaches are very sensitive to the cross sections uncertainties.

In order to clarify this aspect an additional comparison with the Monte Carlo track structure code PENELOPE has been performed for the 60 $\mu$m absorber, the result is presented in Figure 5.3. PENE-LOPE is a radiation transport Monte Carlo code using a mixed stepping procedure: events with deflection angle and energy loss larger than pre-selected cutoffs are simulated in detail, while interactions with smaller angles and/or energy loss are calculated from multiple scattering approaches. In this context, both the parameter for controlling the energy and the angle have been set so that the calculation is performed in an almost event by event way. As it can be noticed in Figure 5.3 the simulated spectra obtained with both TRAX and PENELOPE are very similar, confirming the hypothesis of a possible contribution of the different electron transport model adopted by TRAX and Geant4.
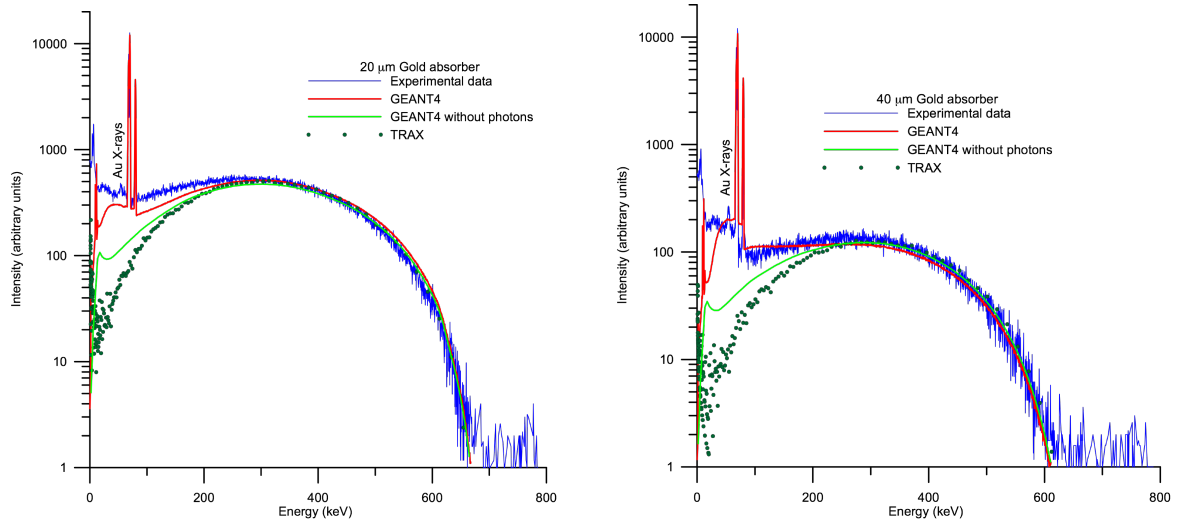
**Figure 5.2.:** Comparison between experimental and simulated spectra obtained with 20 $\mu$m and 40 $\mu$m of gold absorber.
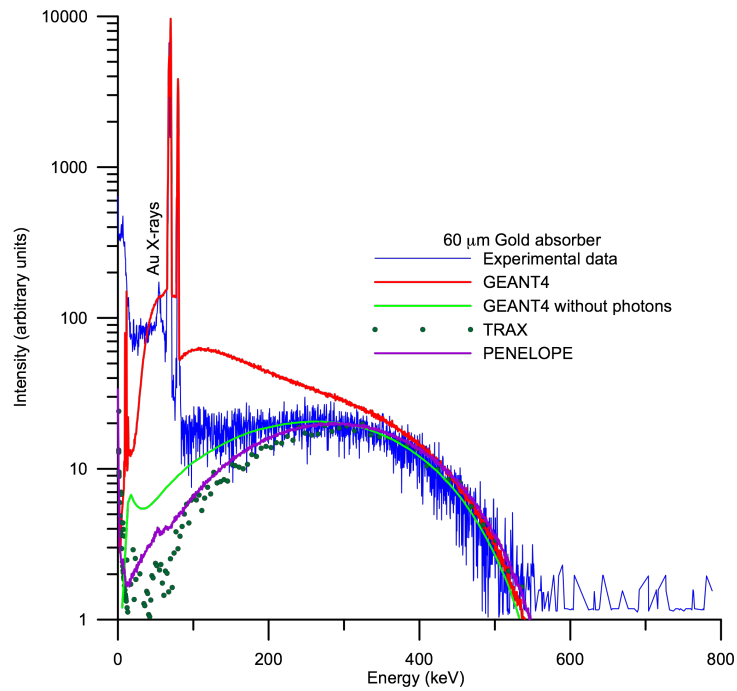


**Figure 5.3.:** Comparison between measured and simulated spectra obtained with 60 $\mu$m of gold absorber.

## 5.2 Gold nanoparticles dose enhancement effect calculations

The enhanced emission of secondary electrons in the vicinity of a gold nanoparticle has been studied for monoenergetic ion irradiation with protons of 80, 20,15 and 10 MeV, carbon ion radiation of 60, 40, 25 and 17 MeV/u and oxygen ion radiation at 100, 51, 26 and 10 MeV/u. Ions and energies have been chosen in a range that allows to scan different possible therapeutical irradiation conditions. Although oxygen ions are still not used for clinical applications, this particle radiation represents one of the most promising candidates for future prospectives of ion beam therapy (Sokol et al., 2017). The nanoparticles used in the simulation have a radius of 2, 7 and 22 nm and are described as a sphere surrounded by a large spherical water halo of 5 $\mu$m radius. NP of 2 nm and 22 nm radius are the more used in literature for both theoretical (Wälzlein et al., 2014; Tran et al., 2016; Lin et al., 2015) and experimental studies (Polf et al., 2011), while the choice of 7nm NP has been taken in order to have an intermediate size for better comparing and understanding the impact of the NP volume on the radiosensitization effect.

Since the TRAX code does not yet handle overlapping volumes: the inner NP sphere and the outer water sphere are separated by a vacuum layer of 0.1 nm thickness. To evaluate the pure effect of ion irradiation in the nanoparticles, a point ion source has been placed in this vacuum layer and the ion is directed in a straightforward direction centrally through the NP volume. To avoid the influence of energy deposition by ions in the scoring water spherical volume the ions are removed as soon as they exit the nanoparticle. In Figure 5.4 a sketch of the geometry used in this thesis work is shown.
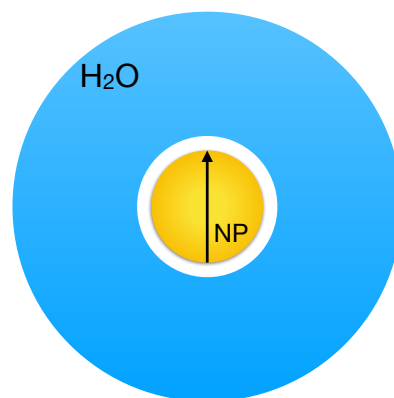


**Figure 5.4.:** Schematic representation of the geometry adopted for analyzing the physical and chemical sensitization effect of AuNP.

### 5.2.1 Dose distributions

To study the dose enhancement effect of gold nanoparticles, the dose distribution for secondary electrons escaping the NPs has been calculated in the external water sphere and compared with the one obtained when replacing the gold nanoparticles with a water nanoparticle of the same dimensions, WNP. As an example, Figure 5.5 shows the 2D dose map and the 2D DEF map around 7 nm AuNP and WNP irradiated with carbon ions of 44 MeV/u . The DEF is calculated as the ratio between the dose deposited

in the water sphere surrounding the NP by secondary electrons escaping from an AuNP over the dose deposited, in the same volume, by secondary electrons escaping from a WNP.
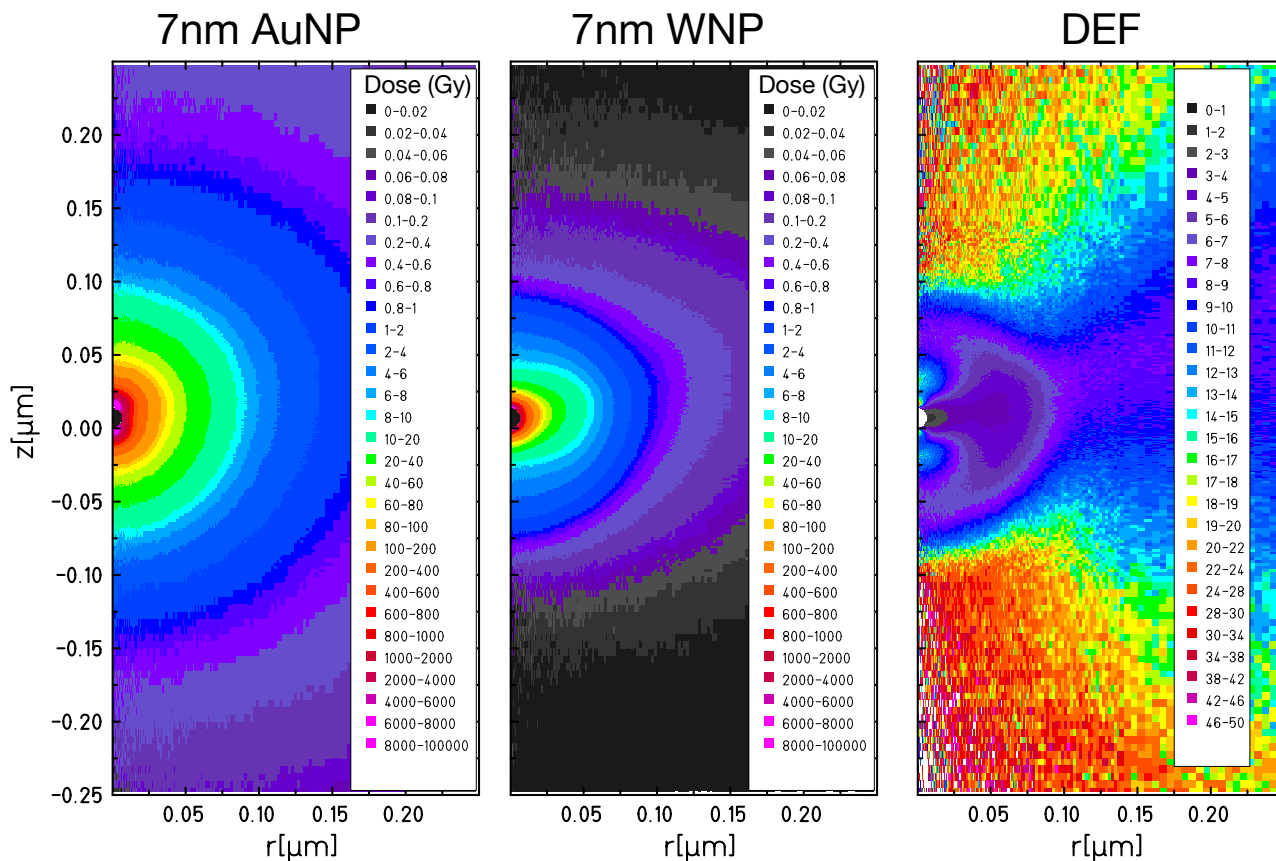


**Figure 5.5.:** Left and central panel: 2D maps of the dose distribution in the water sphere surrounding a 7nm AuNP and a 7 nm WNP traversed by a carbon ion of 44 MeV/u. Right panel: 2D map of the DEF around the NP, calculated as the ratio between the dose deposited by the AuNP and the one deposited by the WNP in each point of the sensitive volume. Courtesy of Dr. M.Fuss (GSI).

Only for the simulations presented in Figure 5.5 a different simulation geometry has been adopted: the nanoparticle was surrounded by a water cylinder with a small central cavity, with 0.1 nm diameter, in the correspondence of the ion track. In these scenarios, the ion is not depositing any energy in the water cylinder and only the contribution of secondary electrons escaping from the NP is recorded. However, the simulation results should not differ from the one we would obtain with the standard geometry, except for the introduction of a small noise contribution in the proximity of the ion cavity.

As it is clearly shown in Figure 5.5, both the dose and DEF distribution around the NP present a complex symmetry, resulting from the mix of a spherical symmetry of the NP and the cylindrical symmetry of the ion track. Therefore it is difficult to define quantities and parametrization able to describe and quantify the dose enhancement effect of NPs. This problem represents one of the main limitations in

describing the NP effect and in the interpretation of the simulation results. In this thesis, for consistency and for having a direct comparison with previous works (Wälzlein et al., 2014; Tran et al., 2016), the NPs dose enhancement effect is studied by analyzing the radial dose distribution for secondary electrons escaping the nanoparticle in a spherical geometry: scoring the deposited dose in spherical shell centered in the center of the NP.

To follow the secondary electrons down to very low energy (1.7 eV) and, thus, with a nanometric spatial resolution, the calculations presented in this section are performed implementing the sub-excitation cross sections for electrons in water target from Michaud et al. (2003) (see Section 2.1.3).

The impact of statistical fluctuations on each calculation is reduced by averaging the result over many independent simulations. The number of primary events simulated vary between $5 \times 10^6$ and $10^9$ depending on the NP size and material. Since in the case of smaller NPs a smaller number of events is scored during each single simulation (the path of the ion within the nanoparticle is shorter), a larger number of primary events is needed to limit the statistical fluctuations. In analogy, since the number of events in gold is much larger than the one scored in the same volume of water, a larger number of primary events is needed in the case of WNP compared to AuNP.

## 5.2.2 Radial dose calculations
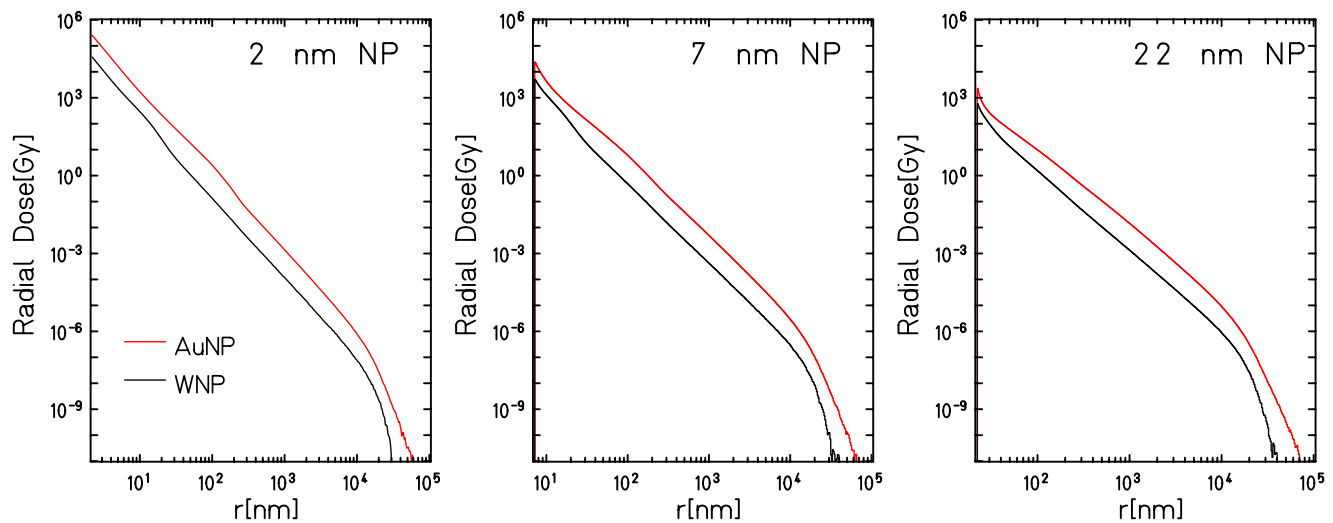


**Figure 5.6.:** Comparison of radial absorbed dose distribution for AuNP (full black lines) and WNP (red lines) of different sizes (2, 7 nm and 22 nm) for 17 MeV/u incident carbon ions.

Figure 5.6 shows the radially absorbed dose in the water around gold and water nanoparticles with 22, 7 and 2 nm radius traversed by 17 MeV/u carbon ions. In all these cases, a steep decrease of the dose can be observed as a function of the distance from the NP and, for a fixed ion energy, the dose deposited around a AuNP results to be always larger compared to the one around the WNP. Additionally, the maximum dose deposited is larger in the vicinity of smaller NPs: up to $\sim 10^5$ Gy at the NP surface in the case of a 2 nm radius AuNP compared to $\sim 10^3$ Gy around a 22 nm radius AuNP. In the case of large NPs, indeed, a significant amount of dose is deposited inside the NP bulk, while, for smaller

volumes, the secondary electrons produced inside the NPs can easily escape the NP and deposit a large part of their energy in the surrounding water volume.

Figure 5.7 shows the radial dose deposition in the water surrounding a 2 nm AuNP, traversed by oxygen ions at different energies (100, 51, 26 and 10 MeV/u ). The dose deposited decreases with increasing distance from the NP, with the same slope for all the oxygen energies and is slightly larger for ions with a lower kinetic energy. For decreasing ion energy, the LET increases and, with that, the number of secondary electrons produced in the nanoparticle. The lateral extension of the radial dose distribution is, instead, larger for ions with a larger kinetic energy, i.e. the range of secondary electrons increases with increasing kinetic energy of the primary ion. This behavior is justified for kinematic reasons: more energetic ions can transfer a larger amount of energy to the secondary electrons, increasing their penetration depth and, consequently, the size of the radial dose distribution.
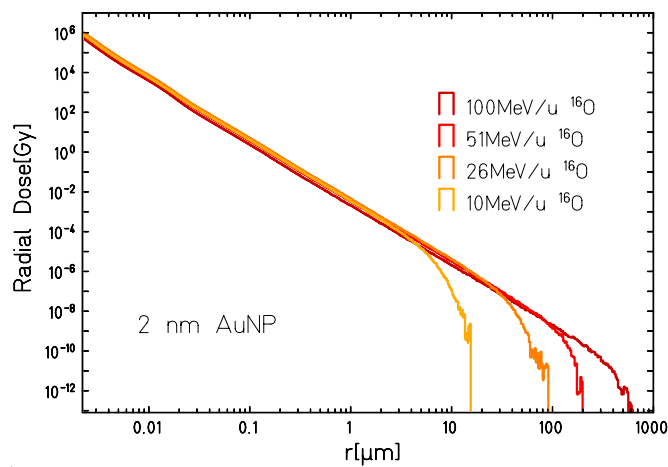


**Figure 5.7.:** Comparison of radial absorbed dose distribution for AuNP of 2nm radius for incident oxygen ions of respectively 100 MeV/u, 51 MeV/u, 26 MeV/u and 10 MeV/u.

### 5.2.3 Dose enhancement factors

The dose enhancement factor DEF(r), as a function of the distance from the NP surface, $r$, has been calculated according to the DEF definition, i.e., the ratio, at fixed irradiation conditions, between the dose deposited at a certain distance, $r$, from the surface of a gold NP, $D(r)_{\text{AuNP}}$, over the dose deposited, at the same distance, from a water NP of the same size, $D(r)_{\text{WNP}}$ :

$$\text{DEF}(r) = \frac{D(r)_{\text{AuNP}}}{D(r)_{\text{WNP}}}\bigg|_{\text{Same irradiation conditions}} . \tag{5.1}$$

The computed DEF(r) for a 22 nm AuNP traversed by an 80 MeV proton is shown in Figure 5.8 and has been compared with the value obtained by Tran et al. (2016) using the Geant4-DNA platform. It has to be noticed that the two simulation conditions are not exactly the same, the Geant4-DNA simulation reported is, indeed, performed for a 25 nm radius NP irradiated by a 75 MeV proton. However, since the LET and the NP size differences between the two simulations are small, we do not expect a significant impact on the calculations of the dose enhancement factor. Both models show a similar trend and the
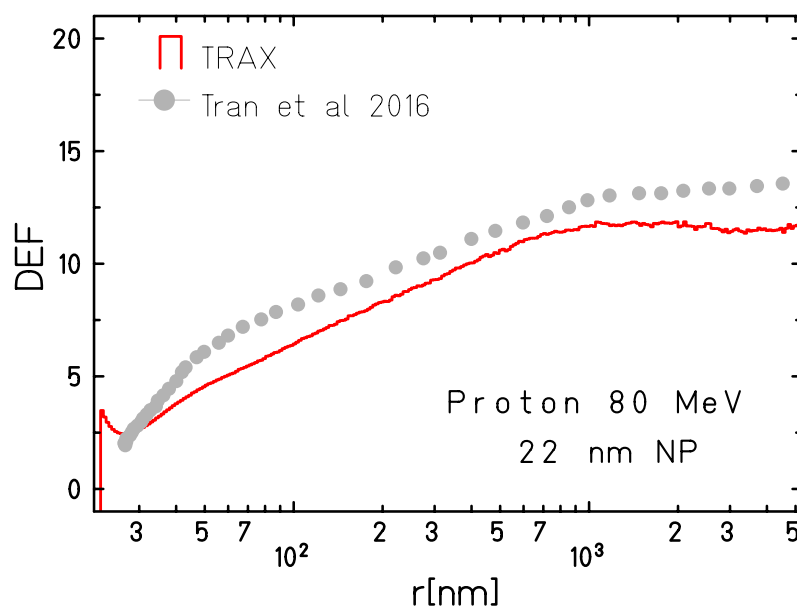
**Figure 5.8.:** TRAX calculation for the DEF of 22 nm traversed by a 80 MeV proton is plotted as a function of the distance from the center of the NP and compared with the simulation results obtained by Tran et al. (2016) with the Geant4-DNA platform.

agreement between the two calculations is reasonably good. However, the Geant4-DNA predicted values result to be slightly larger than the ones obtained with the TRAX code. Several possible factors might justify this small mismatch. At first, the two approaches have a significantly different method to treat the production of secondary particles in the nanoparticle, which might affect significantly the resulting dose deposition, especially in the first 100 nm from the NP surface. The Geant4-DNA platform is, indeed, implemented only for liquid water. Thus, the simulations presented by Tran et al. (2016) have been performed using the standard Geant4 extension to simulate the NPs while the secondary electron transport in the water sphere surrounding the NP has been simulated with the more accurate Geant4-DNA software. The standard Geant4 extension used has, however, a secondary particle production threshold at 13.6 eV (Tran et al., 2016) while TRAX can follow interaction by interaction secondary electrons down to few eV, even in the NP bulk. On the other side, the simulations presented by Tran et al. (2016) include the photon contribution, which is not accounted for in the TRAX code. Another important difference, which might have an important role is the slightly different geometry adopted: in the TRAX simulation, the ion source is a point-like source with ion traversing the NP passing through the NP center, while Geant4-DNA simulation adopted a disc source of 25 nm radius placed in front of the NP.

In Figure 5.9, TRAX calculations of DEF values for all the primary radiation and all the particle sizes investigated are presented. In particular, results obtained for proton radiation are shown in Figure 5.9(a), the ones for carbon ions in Figure 5.9(b) and the ones for oxygen ions in Figure 5.9(c).

In all the cases, the DEF(r) results always to be larger than one, indicating an enhanced dose deposition of AuNPs for all the irradiation conditions at all the radial distances from the NP. In particular, the dose in the vicinity of a AuNP results to be between a factor 2.5 and 20 larger with respect to the case of a WNP of the same size. Additionally, for all the analyzed irradiation conditions a strong dependence of

the DEF on the NP size can be observed while it shows a less strong dependence on the primary radiation quality. In the following, we will analyze both these two aspects separately.

## DEF dependence on the NPs size

The impact of the NP size on the radio-sensitization effect has been studied for 2, 7 and 22 nm radius NPs. The spectra of secondary electrons escaping gold and water NPs and the DEF curve for all the analyzed NP sizes are shown in Figure 5.10 for 60 MeV/u carbon ions traversing the NPs.

Smaller NPs show larger DEF, especially in the first 300 nm from the NP center. This corresponds to the region with the highest absolute dose deposition and an enhanced dose effect in this region might lead to a significative enhancement of the biological response. As the AuNP become larger, the DEF decreases. In this case, indeed, more secondary energy depositions take place within the NP bulk reducing the dose deposited in the water sphere surrounding the NP. Since the gold density is larger than the one of water, this absorption effect results to be more pronounced in the AuNP and leads to a decrease in the DEF. Absorption effects are clearly visible from the secondary electron spectra shown in the panel of Figure 5.10: in case of larger NPs, a significant reduction of the number of secondary electrons escaping the NP can be observed, especially in the low electron energy range (between 5 eV and 1 keV).

This dependence on the NP size is in agreement with the findings of Carter et al. (2007) who observed a larger emission of secondary electrons for 3 nm NPs with respect to 6 nm NPs and of Lin et al. (2015) who predicted a larger cell killing for 2 nm AuNPs respect to 50 nm AuNPs.

For all the analyzed sizes, a local maximum in the DEF can be observed at the NP surface, this peak corresponds to dose deposition events induced by the large number of electrons escaping from the NP in the ion direction. Low energy secondary electrons emitted in the entrance and exit position of the ion have less probability to be absorbed by the NP since they need to cross a smaller thickness of absorber material (see the right panel of Figure 5.5). This first local maximum is successively followed by a minimum and rise again, approaching a constant value of approximately 12 at $\geqslant$300 nm of distance from the NP center. However, the total dose deposited in the water surrounding the NP rapidly decreases with the distance from the NPs surface, and a dose enhancement effect at distances larger than few hundreds nanometer does not necessarily lead to a significant enhancement of the biological effect.

In contrast to the 22 nm nanoparticle, both the 2 and 7 nm NPs show an absolute maximum in the DEF at $\sim$ 100 nm of distance from the NPs center. This maximum results to be more pronounced for the 2 nm and is less important for the 7 nm NP. The nature of this peak is not entirely understood since a series of different effects contribute to it. In this work, we investigated the role of Auger electrons generated both in the NP and in the water sphere surrounding it. For this purpose simulations for 20 MeV proton radiation, excluding the contribution of Auger electrons, have been performed for all the different NP sizes analyzed. The results are presented in Figure 5.11. When the production of the Auger electrons is excluded from the simulation, a sensible decrease in the peak height can be observed for the 2 nm NP and it almost disappears for the 7 nm NP. This allows us to conclude that Auger electrons are responsible for a large part of the increased dose enhancement effect observed for the smaller NP at $r \sim$100 nm. As also suggested by Tran et al. (2016), an additional contribution might come from electrons produced by gold ionizations: electrons with a kinetic energy similar to the mean ionization potential of gold ($\sim$790 eV) have, indeed, a mean free path in water of approximately 100 nm which corresponds to the peak
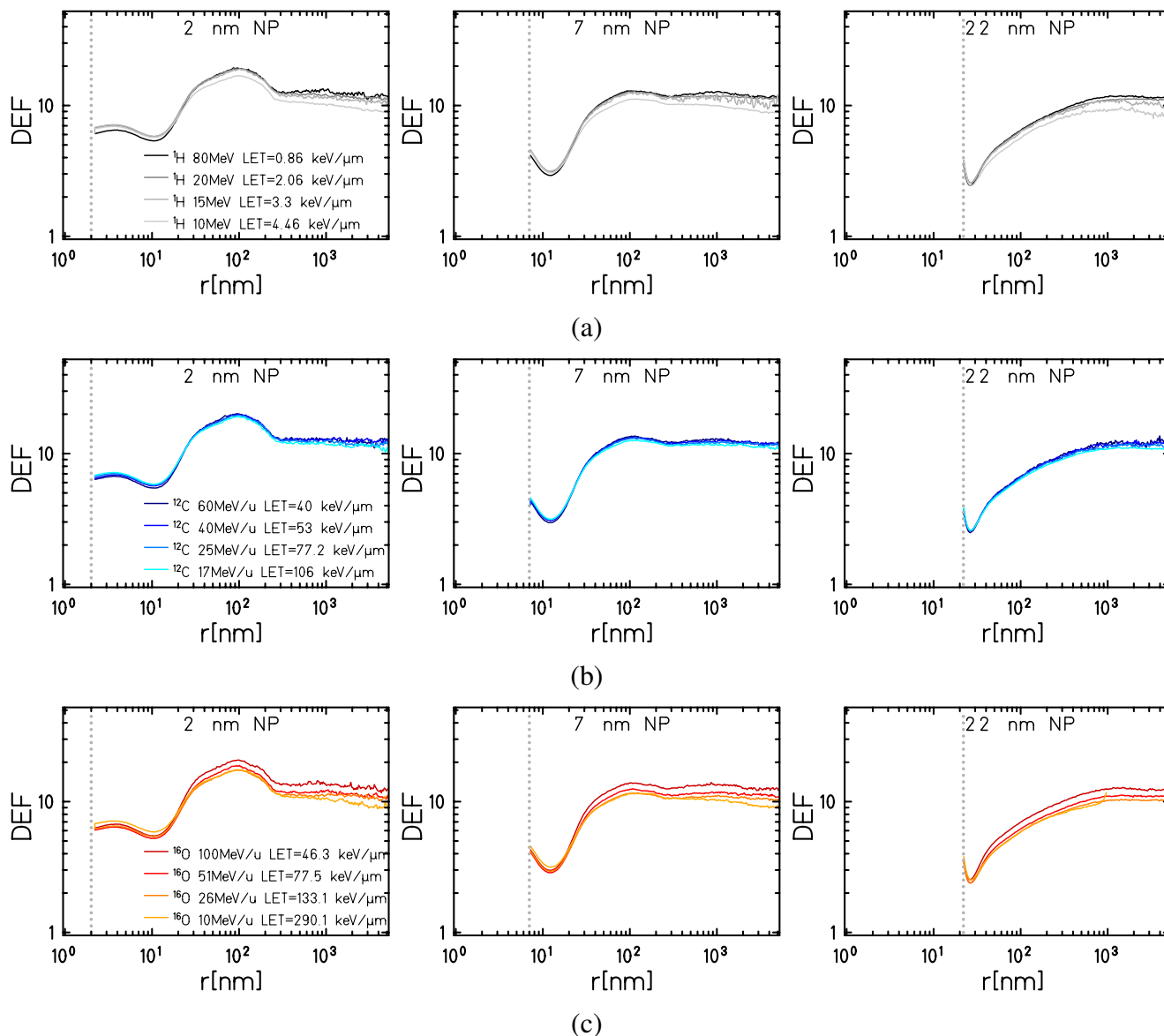
**Figure 5.9.:** DEF as a function of the radial distance from the NP center for different monoenergetic ion radiation and different NP sizes. The vertical dashed line represents the position of the NP surface. Subfigure (a): dose enhancement factor for NP of 2 nm (left panel), 7 nm (central panel) and 22 nm (right panel) irradiated with proton radiation of 80 MeV, 20 MeV, 15 MeV and 10 MeV. Subfigure (b): dose enhancement factor for NP of 2 nm (left panel), 7 nm (central panel) and 22 nm (right panel) irradiated with carbon ion radiation of 60 MeV/u, 40 MeV/u, 25 MeV/u and 17 MeV/u. Subfigure (c): dose enhancement factor for NP of 2 nm (left panel), 7 nm (central panel) and 22 nm (right panel) irradiated with oxygen ion radiation of 100 MeV/u, 51 MeV/u, 26 MeV/u and 10 MeV/u.
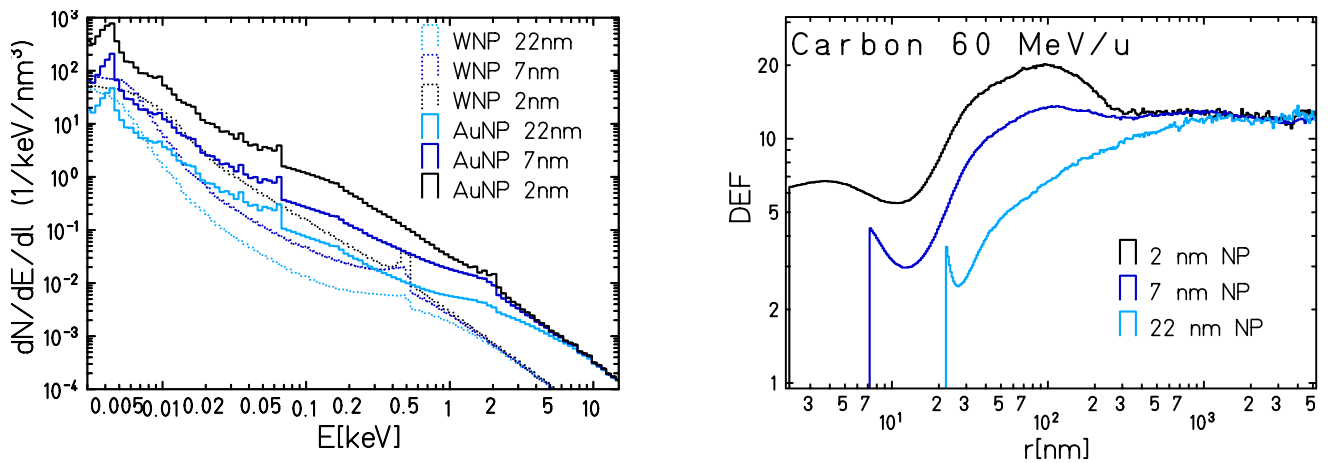
**Figure 5.10.:** Left panel: secondary electron spectra for gold (solid line) and water (dashed lines) NPs of 2, 7 and 22 nm radius traversed by 60 MeV/u carbon ion, normalized for the absorber thickness. Right panel: radial distribution of the DEF produced by 60 MeV/u carbon ions traversing 2, 7 and 22 nm NPs.

positions (Tran et al., 2016). This is consistent also with the different secondary electron production yield in different energy regions shown in the spectra for water and gold NPs, Figure 5.10. In both cases, this effect is more pronounced for smaller nanoparticles because there the impact of the absorption in the bulk of the NP is smaller.

---

### DEF dependence on radiation quality

---

The dependence of the DEF on the radiation quality has been studied analyzing the DEF value at 100 nm and at 1 $\mu$m from the NP center, for all the different ions and all the different energies used in this work. These two radial distances have been chosen to represent two representative radial positions in the DEF(r) curve: the 100 nm distance corresponds to the peak position, where there is the largest DEF difference for the different NP sizes. The 1 $\mu$m radial distance corresponds, instead, to a radial distance where the DEF has reached the plateau and the impact of the NP size is minimum. In Figure 5.12 the DEF dependence, as a function of some of the most common quantities used to describe track effects is reported for the two selected radial distances. In particular Figure 5.12(a) shows the dependence of calculated DEF as a function of the ion kinetic energy per unit mass (expressed in MeV/u), Figure 5.12(b) as a function of the LET and Figure 5.12(c) as a function of $Z^2\beta^{-2}$, where $Z$ is the effective charge of the ion and $\beta$ is the ion velocity relative to the one of the light . The latter parameter is used to describe the stopping power when the sensitive volume is smaller than the maximum radius of $\delta$-electrons (Katz, 1970), and sometimes is more suitable than the LET for describing track effects. As mentioned in Section 3.3.5, LET is, indeed, not a unique parameter to describe ion tracks: different ion species with the same LET have a different kinetic energy, and thus, a different track structure.

In all the analyzed cases, the DEF shows only a moderate dependence on the radiation quality. From the simulation results, the DEF tends to decrease when increasing the LET and the $Z^2\beta^{-2}$, and, consequently, when decreasing the ion kinetic energy. This observation seems to be supported by the work
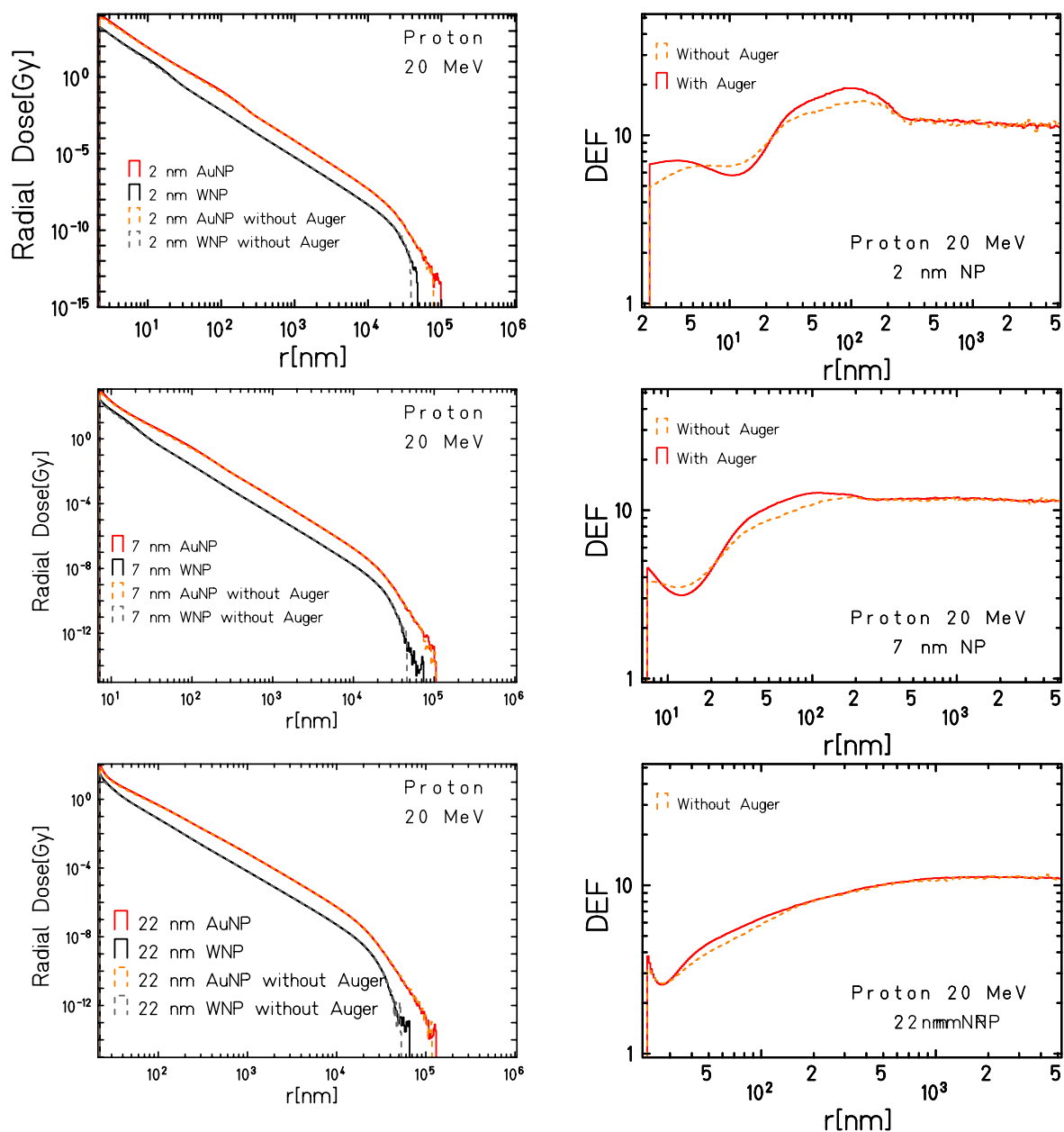
**Figure 5.11.:** Impact of Auger electrons on the radial dose distribution (on the left) and radial DEF distribution (on the right) for 2, 7 and 22 nm NP irradiated with 20 MeV proton radiation. Calculation performed including the contribution of Auger electrons are represented with solid lines, while dashed lines show the result of the same simulation excluding the Auger electron production from both, water and gold, target materials.

of Tran et al. (2016), who noticed a small energy dependence on the DEF for 22.5 nm NP traversed by proton radiation at different energies. However, even though this behavior is not completely understood and a series of other not obvious effects might be involved, a possible explanation is an increased absorption effect for slower ions. The maximum energy transfer to the secondary electrons depends on the ion kinetic energy: it is smaller for slower ions. In this case, the track results to be narrower and a larger number of secondary electrons might be stopped or slowed down by the interaction occurring within the NP.
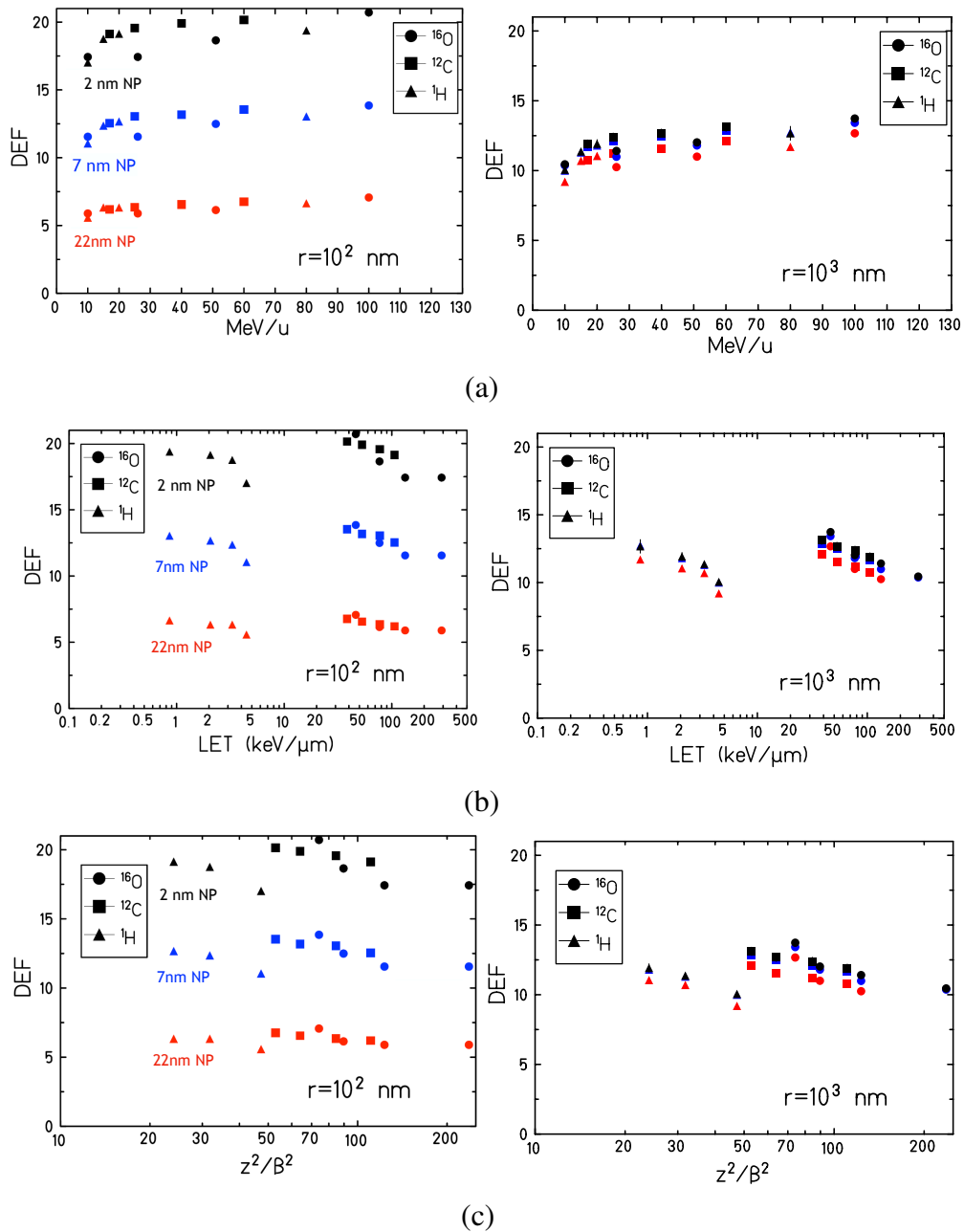


**Figure 5.12.:** DEF dependence on the ion kinetic energy (Subfigure (a)), LET (Subfigure (b)) and $Z^2\beta^{-2}$ (Subfigure(c)) at a radial distance of 100 nm and 1 $\mu$m from the NP center. Calculated values are reported for all the radiation qualities and NP sizes analyzed in this work.
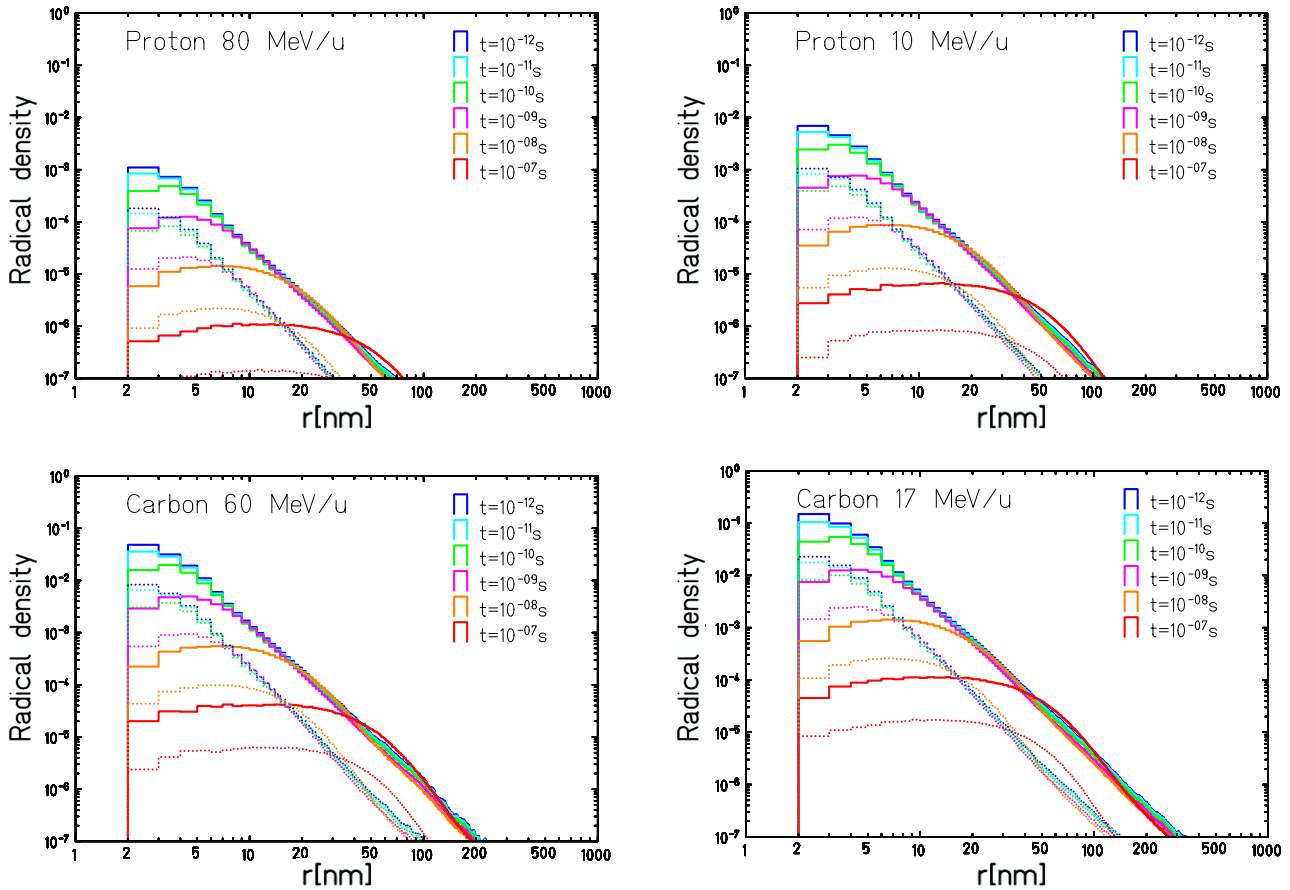
**Figure 5.13.:** Radial density distribution of the chemical species generated per ion by water radiolysis for WNPs (dashed lines) and AuNPs (solid lines) at different points in time after the irradiation. Results presented for different ions traversing the NP: 80 MeV proton (upper left panel), 10 MeV proton (upper right panel), 60 MeV/u carbon ion (bottom left panel) and 17 MeV/u carbon ion (bottom right panel).

## 5.3 Radical enhancement effect

Thanks to the new TRAX-CHEM extension, it is now possible to evaluate the enhanced production of radiolytic species in the proximity of AuNP. The increased number of ionization and excitation events in the vicinity of the NP leads, indeed, to a larger production of chemical species generated by the water radiolysis in the water surrounding the NP.

In analogy to the dose enhancement effect of AuNP, the radical yield as a function of the distance from the center of the NP has been analyzed in a geometry consisting of spherical shells of 1 nm thickness around the center of the NP. The size of the NP was sett to 2 nm since the physical calculation showed a larger effect for smaller NPs.

For each simulation, a series of parallel calculations, completely independent of each other, has been performed. In order to obtain a significant statistic with a reasonable computational time, the number of primary particles simulated varied between $10^5$ and $10^7$, depending on the primary ion energy and

on the NP material: in case of WNP, when the number of interaction is lower, the number of primaries chosen is ten times larger than for AuNP.

For consistency with the calculations performed to evaluate the dose enhancement effect and to be able to follow secondary electron interactions in water, down to the minimum energy of 1.7 eV, sub-excitation cross sections from Michaud et al. (2003) have been adopted.

Figure 5.13 shows the radial density distribution of the number of radiolytic species produced in the surrounding of a AuNP (solid lines) and of a WNP (dashed lines) traversed by protons of 10 and 80 MeV/u and by carbon ions of 17 and 60 MeV/u. Simulation results are shown at six different time points after the irradiation spanning a range between 1 ps and 0.1 $\mu$s. In all these cases an enhanced production of chemical species can be observed for AuNP compared to WNP. The total number of radiolytic products is larger for the 17 MeV/u carbon ion and smaller for the 80 MeV proton and, in general, tends to increase with the LET. The number of radiolytic species is, indeed, proportional to the number of ionization and excitation events taking place in the water target, and, thus, is larger for higher LET radiations.

The radial density distribution at different time points for all the different chemical species is shown for 17 MeV/u carbon ion and 80 MeV protons in Figure 5.14 and Figure 5.15. During the early stages of the chemical evolution (for the first $10^{-10}$ s) the radial radical density distribution does not change significantly, while at larger time scale (from 10 ns to 0.1 $\mu$s) diffusion and recombination effects contribute to a significant modification in the radiolytic radial distribution especially in the close vicinity of the NP: where the dose deposited is higher and the number of produced radicals is larger. A similar trend over the time has been also noticed with 22 nm NPs traversed by proton radiation by Tran et al. (2016).

The total effect of the radiolytic recombination has been analyzed plotting the total number of chemicals as a function of the time. Figure 5.16 shows the yield of $e_{aq}^-$, OH$^\bullet$, H$^\bullet$ and H$_2$O$_2$ for 80 MeV proton and 17MeV/u carbon ion, in case of WNP (dashed lines) and AuNP (solid lines). In both cases, the radiolytic production around the AuNP results to be larger respect to the WNP over the whole chemical evolution. Recombination effects can be observed for both the ions with a decrease of the $e_{aq}^-$ and OH$^\bullet$ while the yield of production of H$_2$O$_2$ and H$^\bullet$ tend to increase over the time. However, the average number of chemical species produced per ion traversing the NP in the case of the 80 MeV proton radiation is relatively low: at 1 ps after the irradiation, the average number of OH$^\bullet$ produced is $\sim 1$ in the case of a AuNP and $\sim 0.1$ for the WNP. This is because the interaction probability of an 80 MeV proton in a 2 nm Au target is low and the probability that the proton can traverse the NP without making any interaction with it is not negligible.

### 5.3.1 Radiolysis enhancement factor

In order to quantify the increased production of radiolytic species, Tran et al. (2016) defined the radiolysis enhancement factor, REF. In analogy to the dose enhancement factor, this quantity is defined, for a given shell, as the ratio between the number of radiolytic species produced around a AuNP and the one around a WNP:

$$\text{REF}(r) = \frac{\text{Radiolytical Species}(r)_{\text{AuNP}}}{\text{Radiolytical Species}(r)_{\text{WNP}}}\Bigg|_{\text{Same irradiation conditions}}. \tag{5.2}$$

Since radiolytic species are produced as a consequence of molecular dissociation processes induced by ionization and excitation events, in the early stages of the chemical evolution the REF follows the same trend as the DEF. Figure 5.17 shows a comparison between the DEF and the REF curve at 1 ps after the irradiation the case of a 17 MeV carbon ion traversing the NP. As expected, the two curves are very similar. However, since during the pre-chemical stage the thermalization process leads to a small dislocation of the molecular dissociation fragments, the REF distribution results to be more smooth compared to the DEF radial distribution.

Figure 5.18 shows the REF value as a function of the radial distance from the NP center in case of protons of 10 and 80 MeV/u and by carbon ions of 17 and 60 MeV/u traversing the NP. Simulations are presented at the same time points as in Figure 5.13. The REF value varies between a factor 5 and a factor 20 for all the ion investigated. As already noticed in the radial radical distribution, at larger time scale recombination processes take place especially in the region where there is a larger concentration of reactive chemical species leading to a significant decrease of the REF for radial distances between 10 and 200 nm from the NP center.

The REF for each specific species produced during water radiolysis is presented for 80 MeV proton and 17 MeV carbon ions respectively in Figure 5.19 and 5.20. Note that the large noise shown in the plots, especially for the less abundant species is an artifact introduced by statistical fluctuation on the radial radical distribution and is amplified by the division (operation) needed to calculate the REF.

Figure 5.21 shows the time evolution of the radiolytic enhancement factor for the total number of some significative species under different irradiation conditions. The species analyzed are $e_{aq}^-$, $H^\bullet$, $H_2$, $OH^\bullet$ and $H_2O_2$. In all the cases the REF values span between 8.5 and 11.5, showing a small, and non trivial, dependence on the radiation quality and on the radiolytic species. However, recombination effects can be observed in the temporal evolution of $H^\bullet$, $H_2$, and $H_2O_2$. These species, mainly generated as reaction products show, indeed, a monotonic increase of the REF over the time while the time dependence of $e_{aq}^-$ and $OH^\bullet$ (which are more reactive species) is less pronounced.
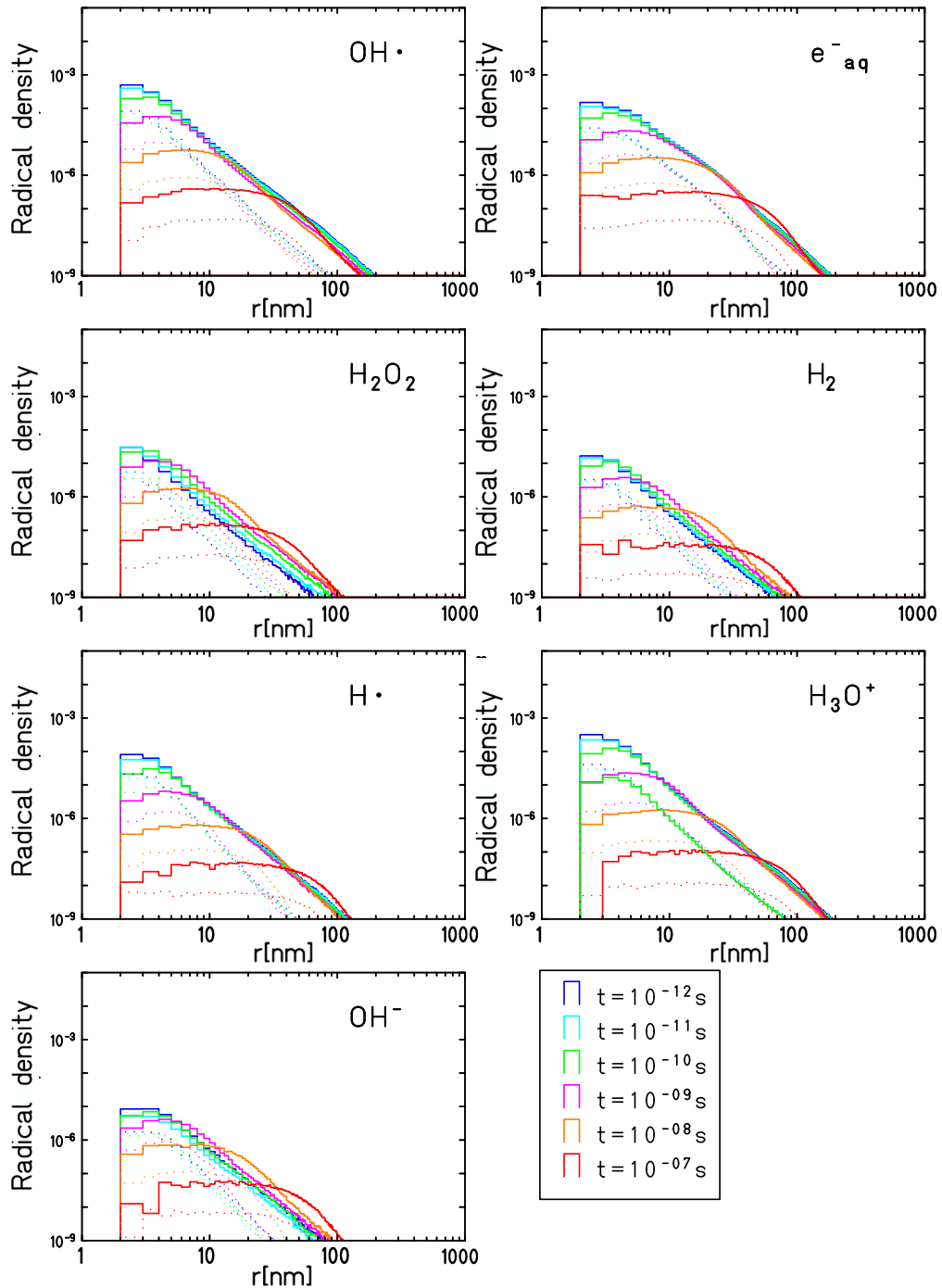
**Figure 5.14.:** Radial density distribution for all the chemical species generated by water radiolysis for WNPs (dashed lines) and AuNPs (solid line) traversed by a proton of 80 MeV. Simulation results are presented for different time points after the irradiation.
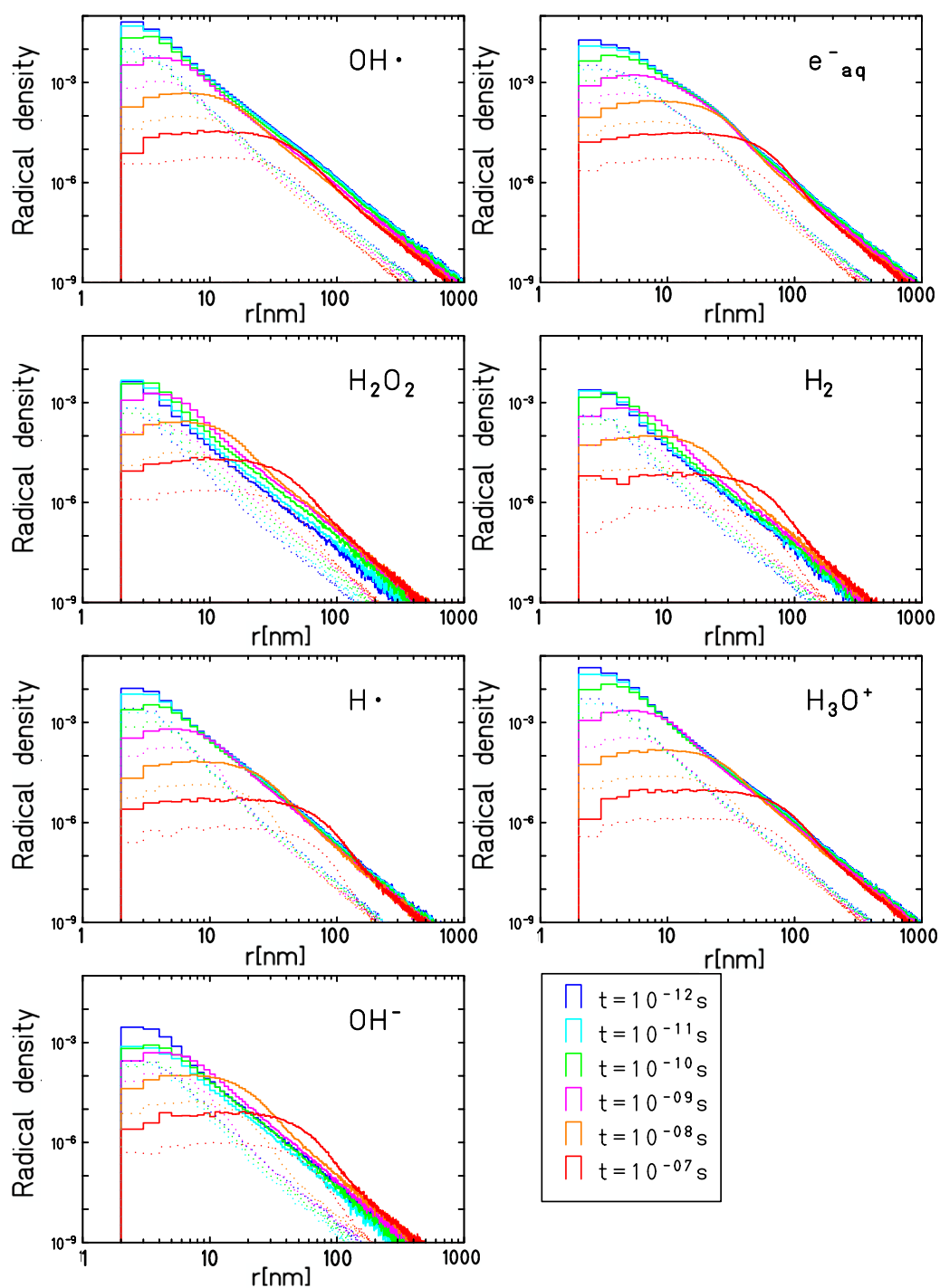
**Figure 5.15.:** Radial density distribution for all the chemical species generated by water radiolysis for WNPs (dashed lines) and AuNPs (solid line) traversed by a carbon ion of 17 MeV/u. Simulation results are presented for different time points after the irradiation.
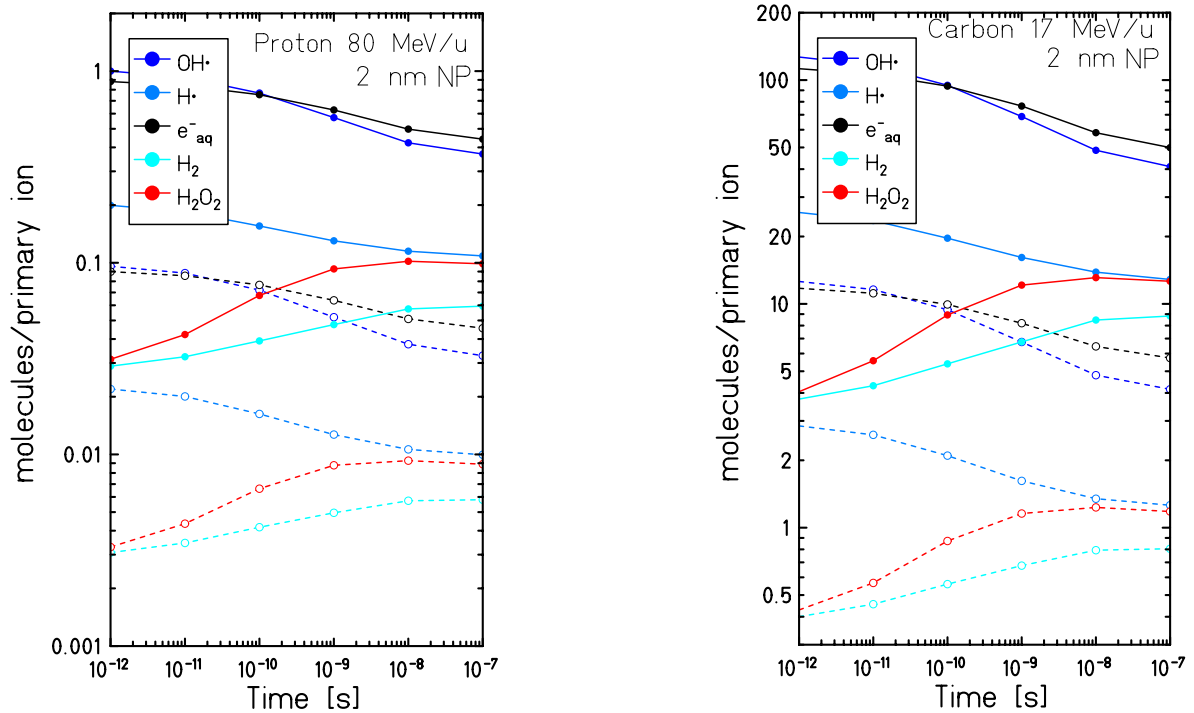
**Figure 5.16.:** Total yield as a function of the time of $e_{aq}^{-}$, $OH^{\bullet}$, $H^{\bullet}$ and $H_2O_2$ around a AuNP (solid lines) and a WNP (dashed line). Left panel: calculation results for an 80 MeV proton traversing the NP. Right panel: calculation results for a 17 MeV/u carbon ion traversing the NP.
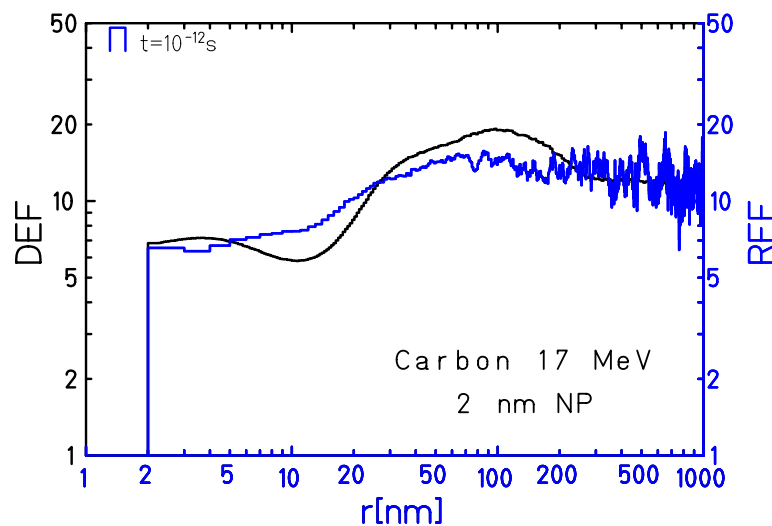


**Figure 5.17.:** Dose enhancement factor (in black) and radiolysis enhancement factor at 1 ps after the irradiation (in blue) for AuNP traversed by a 17 MeV/u carbon ion.
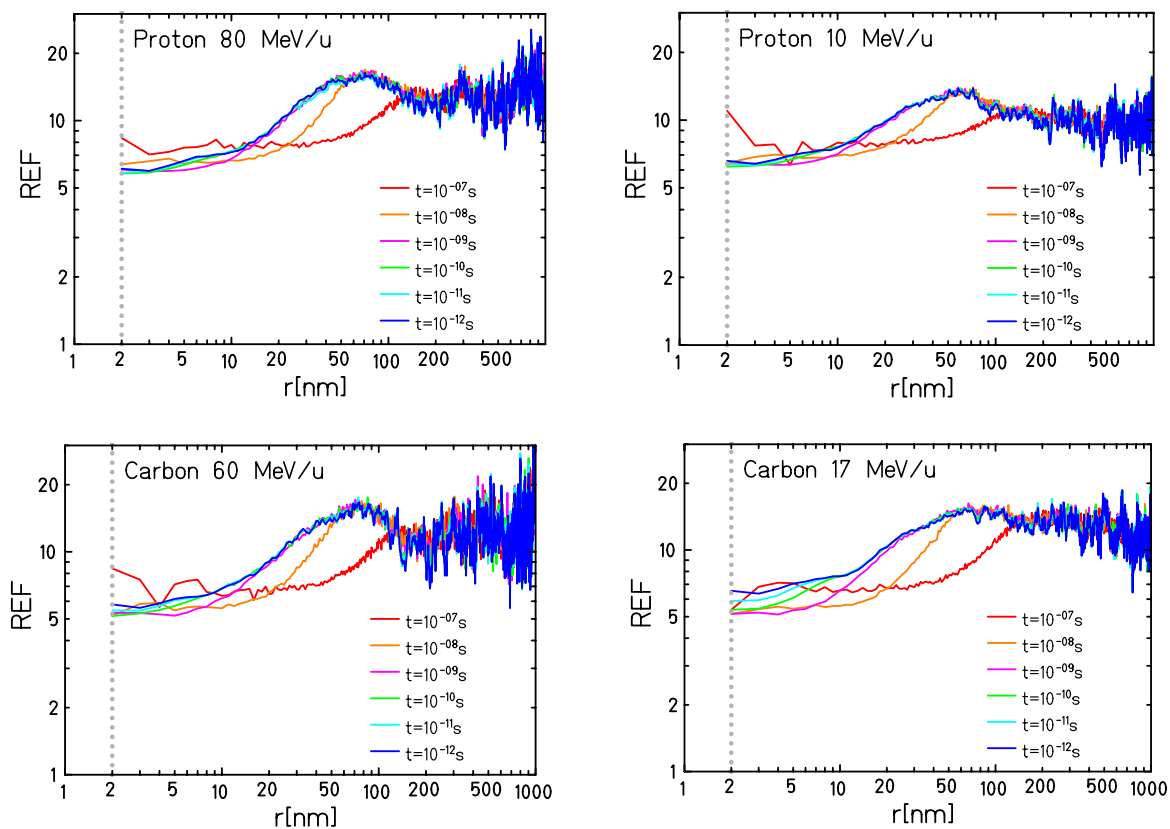
**Figure 5.18.:** Radiolysis enhancement factor as a function of the distance from the NP centre at different time points after the irradiation. Results presented for different ions traversing the NP: 80 MeV proton (upper left panel), 10 MeV proton (upper right panel), 60 MeV/u carbon ion (bottom left panel) and 17 MeV/u carbon ion (bottom right panel). The vertical grey dashed line indicates the position of the NP surface (i.e., the radius).
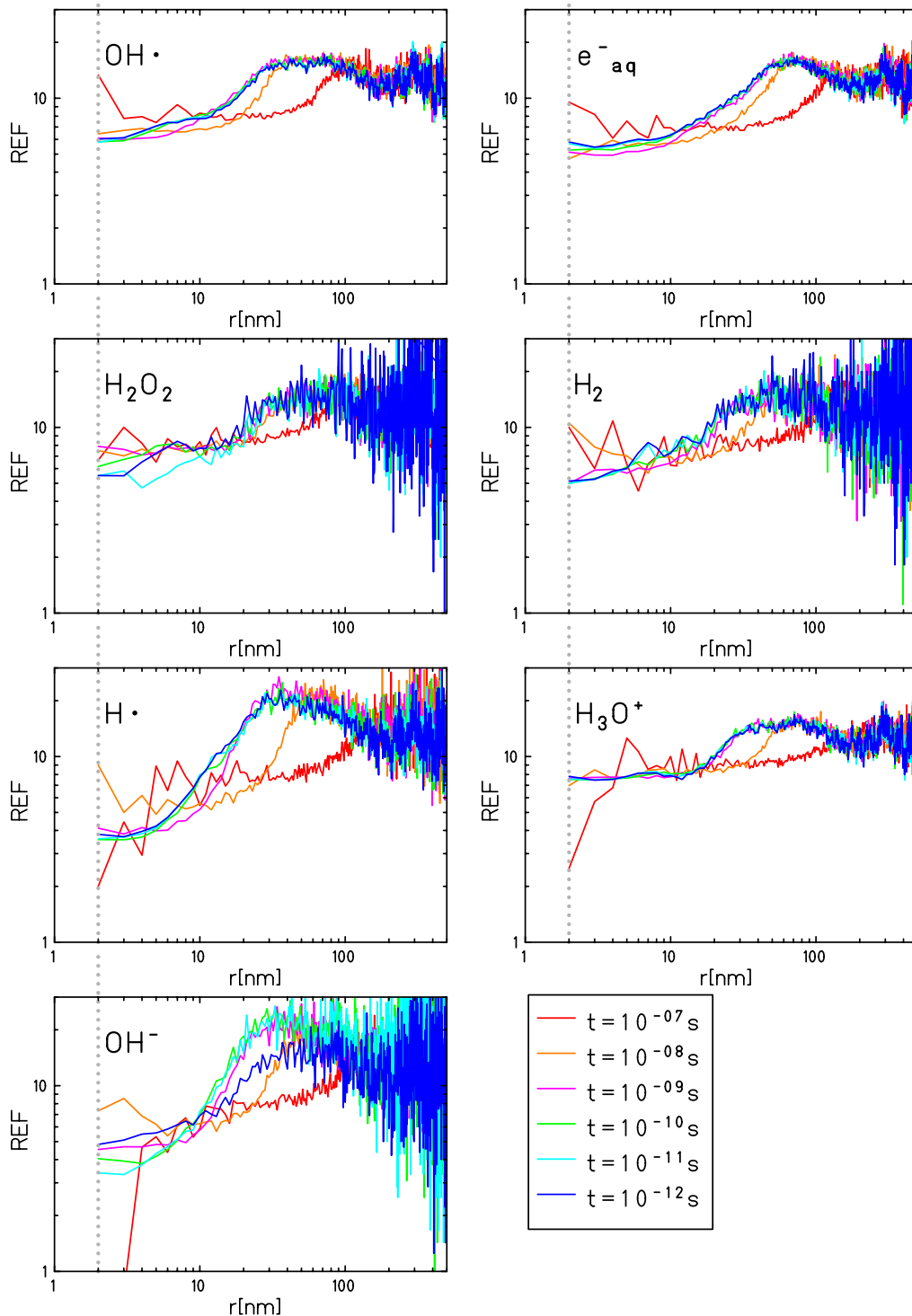
**Figure 5.19.:** Radiolysis enhancement factor as a function of the distance from the NP centre for an 80 MeV proton traversing the NP. Simulation results are presented for different time points after the irradiation.
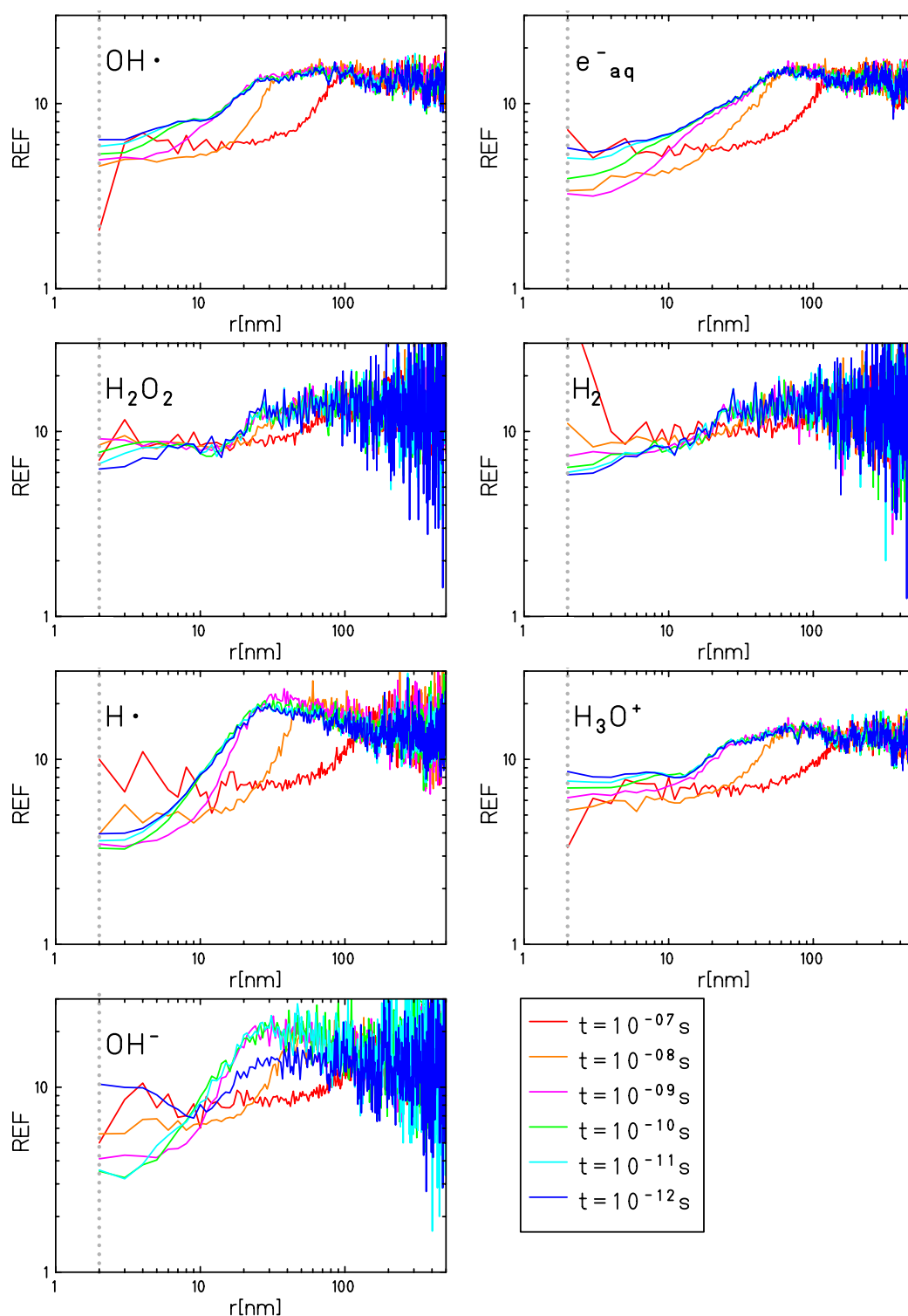
**Figure 5.20.:** Radiolysis enhancement factor as a function of the distance from the NP center for a 17 MeV/u carbon ion traversing the NP. Simulation results are presented for different time points after the irradiation.
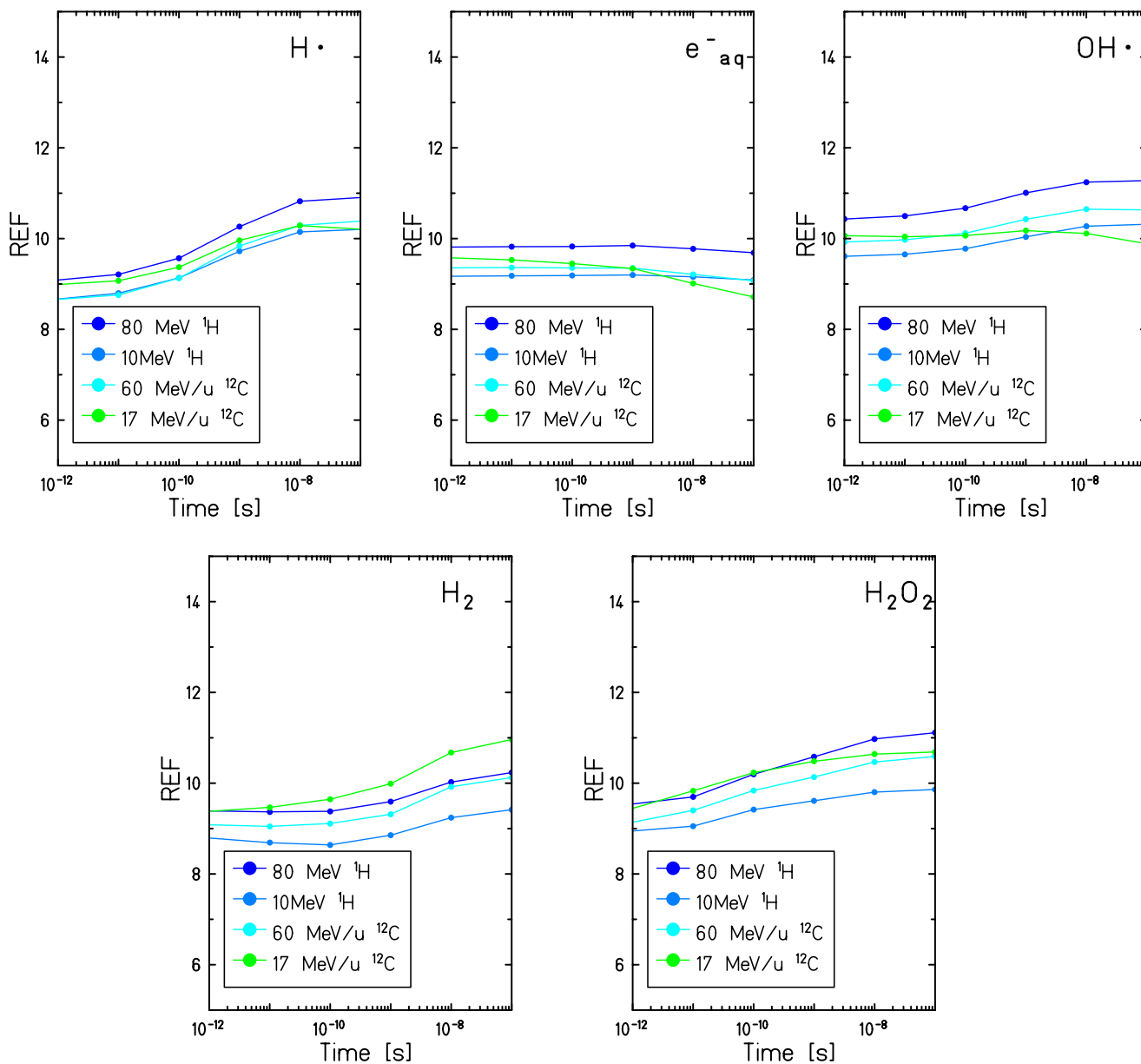
**Figure 5.21.:** Time evolution of the REF for the total number of some significative species under different irradiation conditions. $H^\bullet$ (upper left panel), $e^-_{aq}$ (upper central panel), $OH^\bullet$ (upper right panel), $H_2$ (bottom left panel) and $H_2O_2$ (bottom right panel). Simulations have been performed for 10 MeV and 80 MeV protons and 17 MeV/u and 60 MeV/u carbon ions traversing the NP.

### 5.3.2 Nanoparticle enhancement effect in oxygenated solutions

The impact of the oxygenation level on the radical enhancement effect in presence of gold NP has been studied for the first time ever introducing molecular oxygen in the water target surrounding the NP, as described in Chapter 4. Simulations have been performed for an oxygen concentration at the water surface of 21% for a 2 nm NP traversed by 80 MeV proton and 17 MeV/u carbon ion.

Figure 5.22 shows the radial distribution of the total number of radiolytic species for different time points, in case of oxygenated water solutions (solid lines) and hypoxic water (dotted lines). The impact of the oxygenation level on the total number of radiolytic species produced in the water surrounding the NP is not significant and only a little effect can be observed for advanced stages of the chemical evolution ($t > 10^{-8}$ s).



**Figure 5.22.:** Radial density distribution, from the center of a 2 nm AuNP, of the chemical species generated by water radiolysis in hypoxic condition (dashed line) and for a water target in equilibrium with a gas with an oxygen partial pressure of the 21% (solid line). Results presented 80 MeV proton (left panel) and 17 MeV/u carbon ion (right panel). The simulation results are presented at different time points ranging between $10^{-12}$ s and $10^{-7}$s after the irradiation.

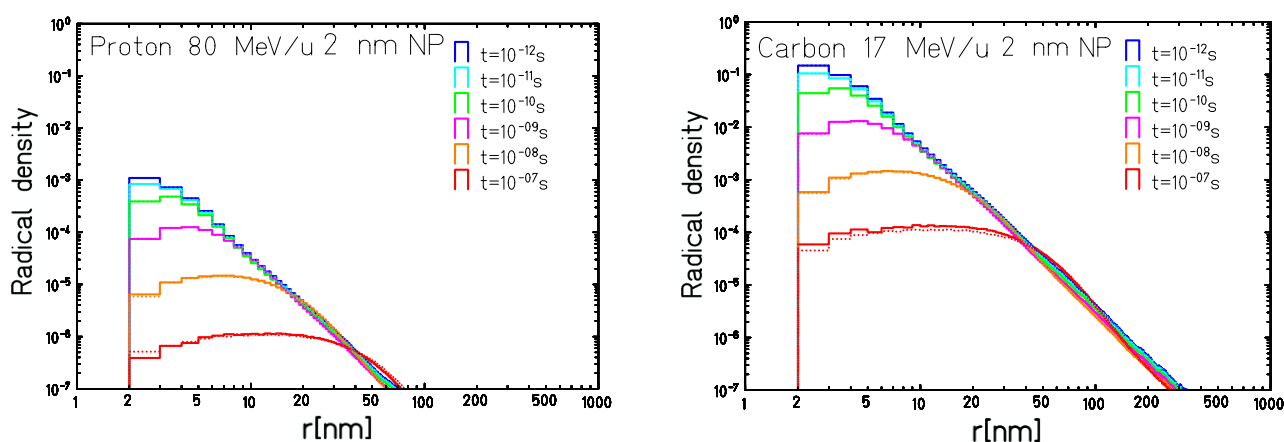The presence of $O_2$ dissolved in the target affects, however, the chemical network and the yield of the different species. Figure 5.23 and Figure 5.24 show the radial concentration of the different radiolytic products in the water sphere surrounding AuNP in oxic (solid lines) and hypoxic conditions (dashed lines). Being the molecular oxygen a strong scavenger for $e_{aq}^-$ and $H^\bullet$ (see Chapter 4), a decrease in the yield of these two species can be observed especially for times larger than 10 ns. The initial stages of the chemical evolution are, indeed, dominated by the interaction among the chemical products generated by water radiolysis along secondary electron tracks. Consistent with a reduction of the $e_{aq}^-$ and $H^\bullet$, a growing production of $O_2^{\bullet-}$ and $HO_2^\bullet$ can be observed over the time until reaching a level comparable with the one of the more abundant species.

As for the case of hypoxic targets, the total number of some of the most important species ($e_{aq}^-$, $H^\bullet$, $OH^\bullet$, $H_2O_2$, $H_2$, $HO_2^\bullet$ and $O_2^{\bullet-}$) has been plotted as a function of time for AuNP (solid lines) and WNP (dashed lines), Figure 5.25. The calculations are presented for an 80 MeV proton (left panel) and for a 17 MeV carbon ion (right panel). For both ions a significant increase in the number of $O_2^{\bullet-}$ can be
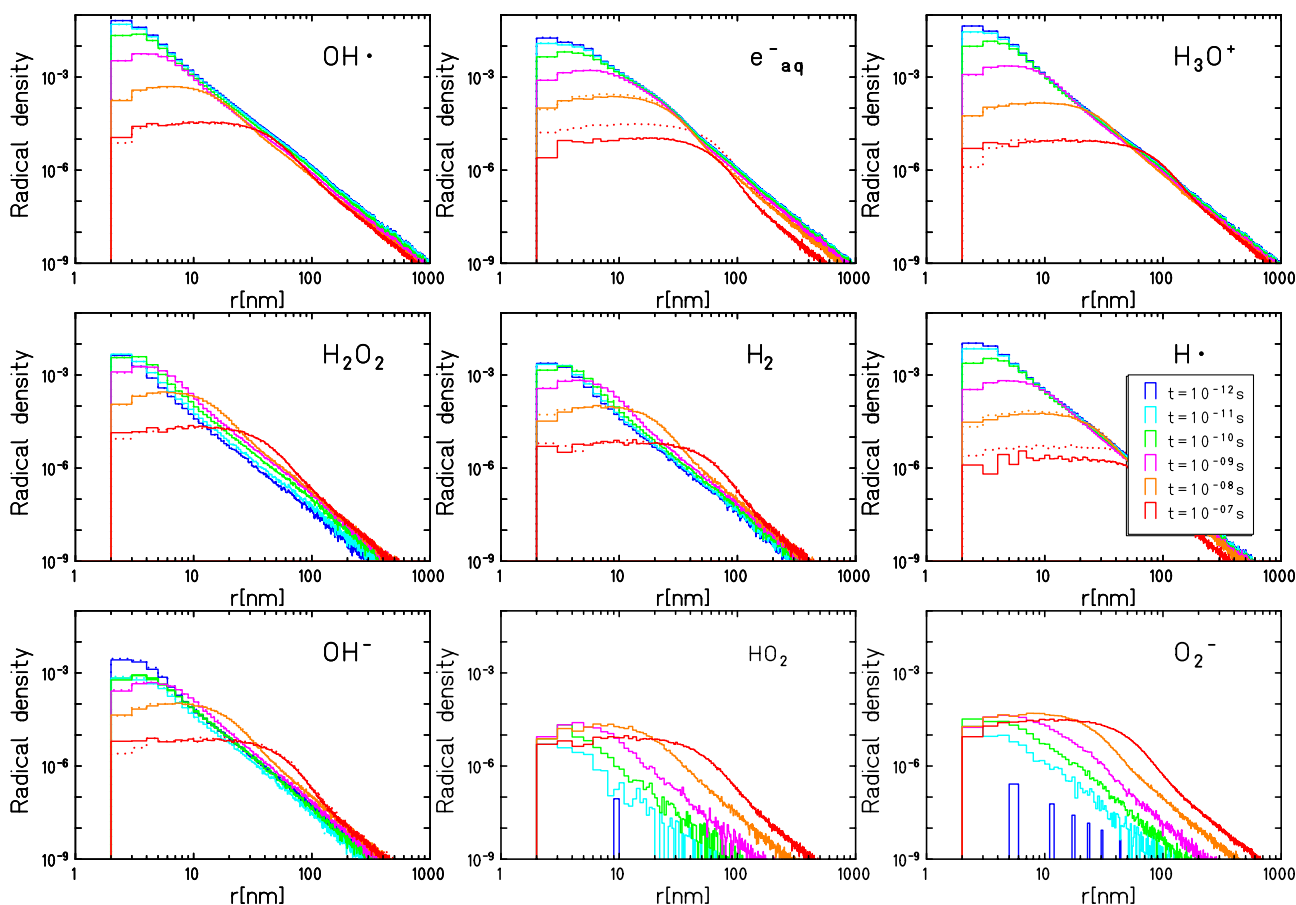
**Figure 5.23.:** Radial density distribution for all the chemical species generated by water radiolysis in the water surrounding a 2 nm AuNP traversed by a carbon ion of 17 MeV/u. Simulation results are presented in the case of hypoxic conditions (dashed line) and for a water sphere in equilibrium with a gas with an oxygen partial pressure of 21% (solid line).

observed at times larger than a nanosecond and it constantly grows during the whole track evolution. In analogy, but less pronounced, an increase of the $HO_2^\bullet$ is also observed.

Figure 5.26 shows a comparison between the species specific radiolysis enhancement factor in hypoxic and oxic conditions. The overall trend of the REF for the majority of the species does not show a significant dependence on the oxygenation level in the water surrounding the nanoparticle. Since the $O_2^{\bullet -}$ and the $HO_2^\bullet$ are not present in the initial stage of the chemical evolution, their REF is calculated from $10^{-11}$ s after the irradiation. Both of these species show a trend in the REF similar to the one of the $e_{aq}^-$ and $H^\bullet$, respectively, which is justified by the direct relation between the number of $e_{aq}^-$ and $H^\bullet$ and the formation of $O_2^{\bullet -}$ and $HO_2^\bullet$.
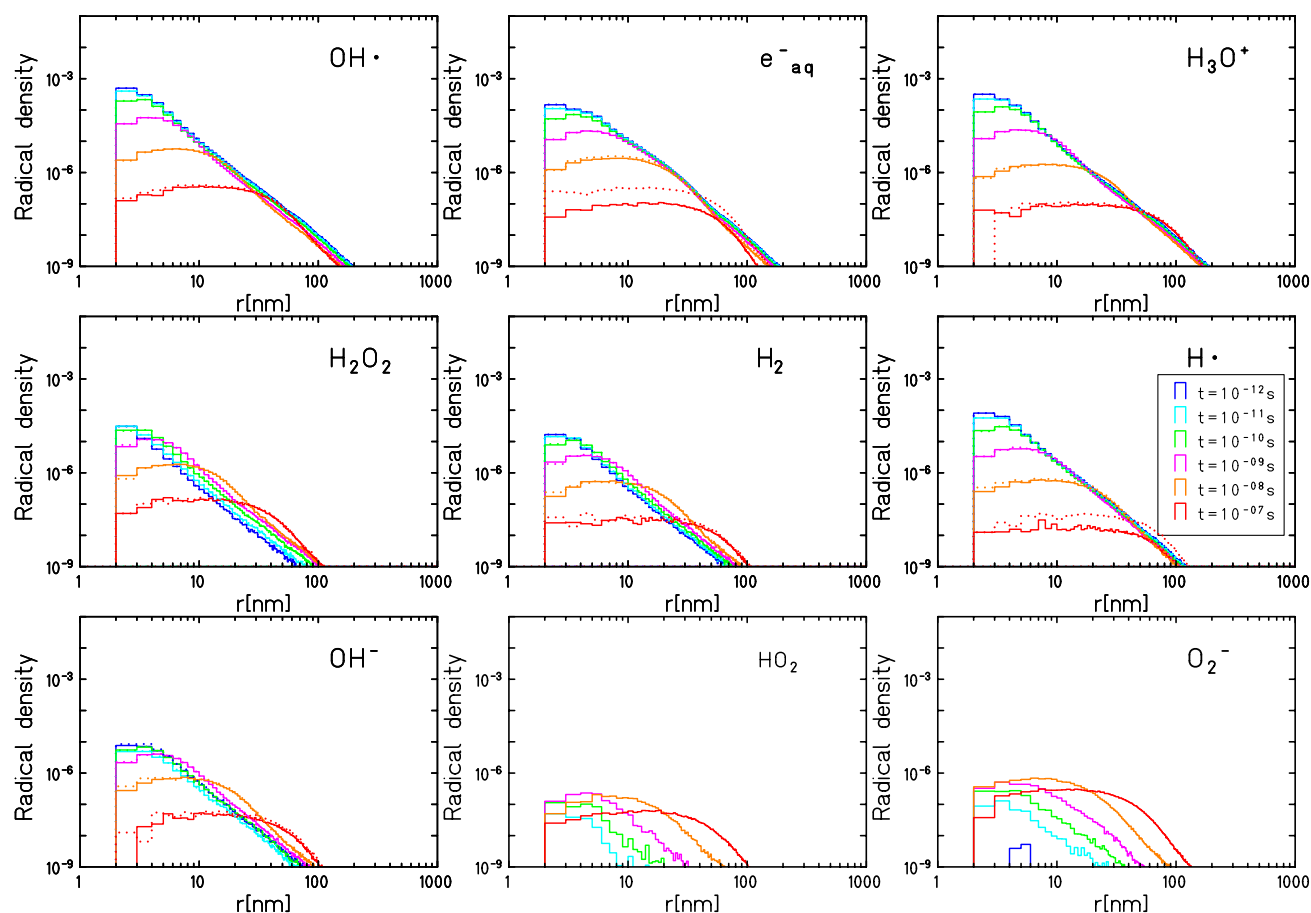
**Figure 5.24.:** Radial density distribution for all the chemical species generated by water radiolysis in the water surrounding a 2 nm AuNP traversed by a proton of 80 MeV/u. Simulation results are presented in the case of hypoxic conditions (dashed line) and for a water sphere in equilibrium with a gas with an oxygen partial pressure of 21% (solid line).

## 5.4 Summary

In this chapter, an extended analysis of the nanoscopic mechanisms involved in the NP sensitization effect has been carried out with the classical version of the TRAX code and with the recently implemented chemical extension, under the assumption of ions traversing the NP in the center.

The radiation dose enhancement effect of AuNPs has been evaluated by comparing the dose deposition of secondary electrons escaping an AuNP and a water nanoparticle (WNP) of the same volume and in the same position. Spherical nanoparticles, of three different sizes, surrounded by a water volume were analyzed for different particle radiations at different energies. The radial dose deposited in the water sphere surrounding the NP was calculated in a spherical geometry: scoring the deposited dose in spherical shells centered in the center of the NP. In all the analyzed cases the dose deposited around the gold nanoparticle results to be between 5 and 20 times larger than in the corresponding water case. The largest effect is observed for the smaller NPs (2 nm radius) at around 100 nm from the NPs' surface where

a maximum in the dose enhancement factor can be observed. For the smaller nanoparticles, indeed, the absorption effects of gold are minimized while in the case of larger NPs, part of the secondary electrons lose a large part of their energy in NP bulk. The nature of the maximum enhancement at 100 nm from the NP is still not entirely justified, however it has been demonstrated that a large contribution can be addressed to Auger electrons. A small and not obvious dependence of the dose enhancement factor has been instead observed for the different radiation quality. However the complex symmetry of dose deposition around the NP, figure 5.5, poses some difficulties for the interpretation of the results.

The enhanced production of water free radical induced by the enhanced production of secondary electrons escaping the NP has been studied as well. Time-dependent radical concentrations in the water volume surrounding a 2 nm NP have been calculated, for the very first time, with the TRAX-CHEM code for different ion traversing the nanoparticle and in different water oxygenation conditions. The enhanced production of radiolytic species in the case of AuNPs results to be up to 20 times larger respect to the case of WNP. In agreement with what was observed for the dose enhancement effect, in the early stages of the chemical evolution (for the first $10^{-10}$ s), it reaches a maximum around 100 nm from the NP surface. However, at larger time scale (from 10 ns to 0.1 $\mu$s) recombination and diffusion effects can be observed and this maximum tends to disappear. Even though the total number of radiolytic products is not significantly affected by the oxygenation level of the scoring volume, a significant decrease in the $e_{aq}^-$ and $H^\bullet$ yield is predicted especially in the last stage of the chemical evolution while a significant increase in the production of $O_2^{\bullet-}$ and $HO_2^\bullet$ can be observed.

Whenever it was possible, the simulation results have been compared with calculations of other simulation tools and a good agreement can be observed. A further validation comes, indirectly, from the validation of the implemented cross section for gold targets. However, presently unavailable experimental data on the basic physical and chemical mechanisms involved in the NP radiosensitization are needed in order to validate the predictive capability of these simulation tools.
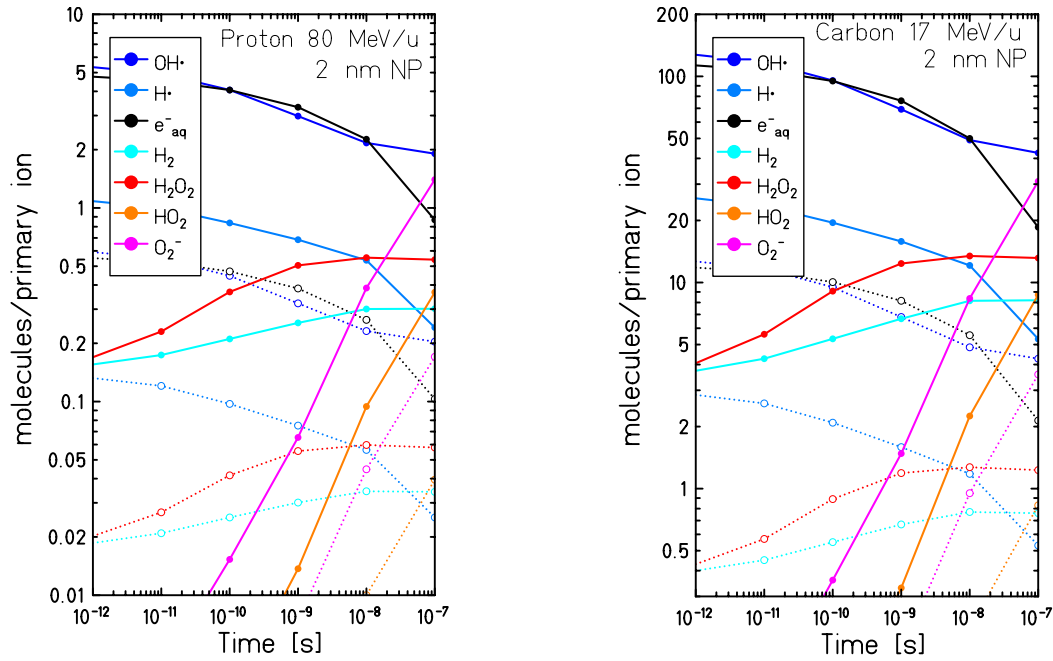
**Figure 5.25.:** Total yield as a function of the time of $e_{aq}^-$, $OH^\bullet$, $H^\bullet$ and $H_2O_2$ around a AuNP (solid lines) and a WNP (dashed line) in the water hallow surrounding the NP. The scoring volume is supposed to be in equilibrium with a gas with an oxygen partial pressure of the 21%. Left panel: calculation results for a 80 MeV proton traversing the NP. Right panel: calculation results for a 17 MeV/u carbon ion traversing the NP.
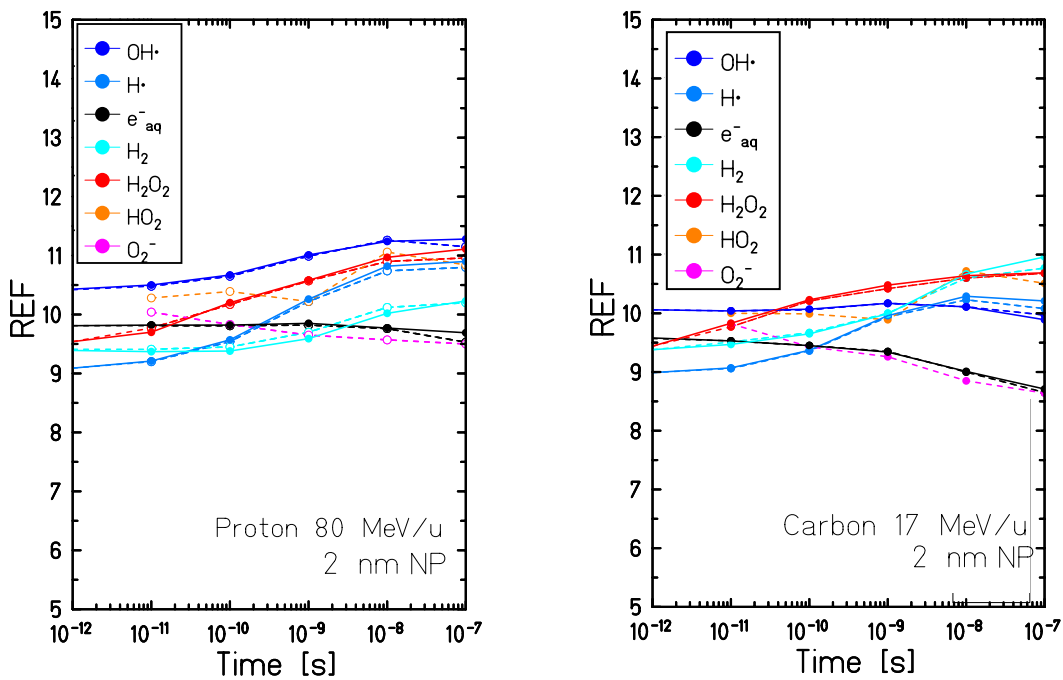


**Figure 5.26.:** Time evolution of the REF for the total number $e_{aq}^-$, $OH^\bullet$, $H^\bullet$, $H_2O_2$, $HO_2^\bullet$ and $O_2^{\bullet-}$, in an oxygenated volume (dashed lines) and in a hypoxic volume (solid line).

# Conclusion and Outlook

The radiation effect on biological media is only partially induced by the direct effect of radiation (ionization and excitation). For low LET radiation, up to 70% of the radiation damage is, indeed, induced by the indirect effect of radiation mediated by the action of reactive chemical species generated by radiolysis processes. For ion radiation, the contribution of the indirect damage is less important but, nevertheless, essential to describe and understand the nanoscopic mechanisms of radiation damage on biological media (Ito et al., 2006).

To better investigate the chemical processes taking place along an ion track, and to be able to tackle problems where the chemical pathway seems unavoidable, the Monte Carlo particle track structure code TRAX has been extended to the pre-chemical and chemical stage of the radiation effect in water targets. Thanks to this new implementation, the production, diffusion, and reaction of radiolytic species can be evaluated with a step by step approach in the time interval between $10^{-12}$ and $10^{-6}$ s after the irradiation. According to the standard paradigm of radiation effect, track evolution is treated as a three stage process: the physical, the pre-chemical and the chemical stage. The physical stage, covered by the classical version of the code, consists in the description of the direct effect of radiation and it is supposed to be concluded within $10^{-15}$ s after the irradiation. The pre-chemical stage (from $10^{-15}$ s to $10^{-12}$ s after the irradiation) consists of the formation of the radiolytic species by dissociation processes of ionized and excited water molecules and in their thermalization. During the chemical stage, the newly produced chemical species diffuse and react among themselves and with the solvent until reaching the equilibrium at $\sim 10^{-6}$ s after the irradiation.

The validity of the chemical model implemented has been verified by comparing the calculated production yields for the most abundant radiolytic species ($e^-_{aq}$, $OH^\bullet$, $H^\bullet$, $H_3O^+$, $H_2$, $OH^-$ and $H_2O_2$ ) for different particle radiation and different energies, with both experimental data and other simulation approaches. A good agreement in the time-dependent radical yield has been found for 1 MeV electron irradiation and 3 MeV proton irradiation. Molecular yields at the end of the chemical stage have been also calculated as a function of the LET, showing a good agreement with experimental data and theoretically predicted values in the low and medium LET region. In the high LET region, instead, some refinements in the model are still required. However, considering the large uncertainties, especially in modeling the pre-chemical stage of radiation effect, this represents also a motivation for the basic research in molecular physics, for further studies on the molecular dissociation and thermalization processes in liquid water. Since the chemical implementation of the TRAX code relies on external tabulated data, the chemical models can be easily adopted and updated when more accurate information on the basic processes of water radiolysis will be available.

Additionally, to stress the importance of the choice of the pre-chemical models on the time evolution of the radical species a thorough sensitivity analysis on the impact of the sub-excitation electron thermalization model on the time-dependent and LET-dependent yields of all the radiolytic species is shown.

The chemical composition and the presence of dissolved material in the target medium can have an impact on the track chemical evolution and on the yield of the different chemical species. The TRAX-CHEM code has been, then, further extended in order to be able to handle the presence of molecules in solution in the water target. In this case, to limit the computational costs of the simulation, the dissolved molecules are assumed to be uniformly distributed in the target material and are treated as a continuum. In particular, the effect of dissolved molecular oxygen ($O_2$) on the track chemical evolution has been studied. This choice was motivated by the intention of better understanding the nanoscopic mechanisms involved in the oxygenation effect. Time-dependent and LET-dependent yield of all the considered radiolytic species at different oxygenation levels have, then, been studied for different ion radiation and different energies. The range of $O_2$ concentration investigated was selected in order to simulate water targets in realistic conditions: from completely anoxic condition ($pO_2=0\%$) to water target in equilibrium with air ($pO_2=21\%$). In oxygenated condition, a large production of two highly toxic species ($O_2^{\bullet-}$ and $HO_2^{\bullet}$ ), which are not produced in hypoxic conditions, has been predicted, especially for low LET radiation. These species are generated as reaction products, from the interaction of respectively $e_{aq}^-$ and $H^{\bullet}$ with the dissolved molecular oxygen. As a consequence, a decrease in the final yield of the $e_{aq}^-$ and $H^{\bullet}$ can be observed for poorly oxygenated targets and a complete consumption is observed for oxygen concentrations at the water surface larger than 10%. Little impact of the dissolved molecular oxygen has been, instead, predicted on the yield of production of the other radiolytic species. Consistently with the LET dependence of the oxygen effect on the macroscopic level, a strong decrease in the yield of production of $O_2^{\bullet-}$ and $HO_2^{\bullet}$ is observed with the increase of the LET. This suggests a possible direct or indirect involvement of $O_2^{\bullet-}$ and $HO_2^{\bullet}$ on the oxygen sensitization effect. This hypothesis is supported by both theoretical and experimental studies, (Colliaux, 2009). An additional confirmation comes from preliminary measurements of nucleic DNA repair assay (Ferruz et al., 2016). As shown in Figure 5.27, in this experiment, indeed, a larger number DSBs produced by radiation in oxic conditions respect to anoxic conditions, for short time after the irradiation, has been measured. Considering the low reactivity of $O_2^{\bullet-}$ with DNA, a possible explanation for this observation is an increased production of $OH^{\bullet}$ and reactive nitrogen species (RNS), induced by the large production of $O_2^{\bullet-}$. These two species are particularly deleterious for DNA, and both can be produced by $O_2^{\bullet-}$ in living organisms through the Haber-Weiss reaction (catalyzed by the presence of transitions metals) and the interaction with nitrogen monoxide ($NO^{\bullet}$) respectively. In order to further investigate this aspect, an additional extension of the code including the interaction with biologically relevant compounds might be considered. Thanks to their capability to enhance the radiation effect, high atomic number (Z) nanoparticles (NPs) are considered to be one of the most promising tools for improving tumor targeting and radiation therapy efficacy. The increased effectiveness of a combined treatment of X-ray radiation and nanoparticle has been already extensively investigated and clinical trials have been already initiated (Lacombe et al., 2017; Kuncic and Lacombe, 2018). For particle therapy, instead, several studies demonstrating the feasibility of a joint use of NP exist, however, a consistent picture of the physical and chemical processes underlying this effect is still missing. In this work nanoscale processes initiated by the interaction of radiation with gold nanoparticles (AuNPs) have been investigated with the aim to evaluate an optimal combination between the irradiation conditions and the NPs sensitization effect. The studies presented here, have been carried out in parallel to a series of in-vitro experiment, performed at HIT (Heidelberg, Germany) in collabora-
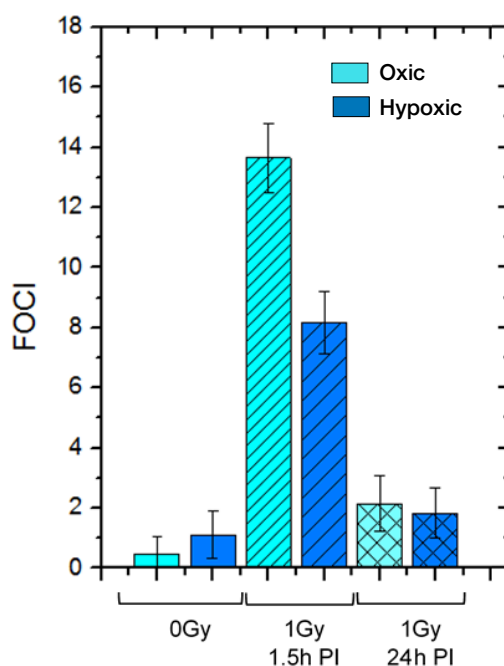
**Figure 5.27.:** Preliminary results of nucleic DNA repair assay for HeLa cells, in oxic and hypoxic conditions, at 1.5 and 24 hours after being irradiated by 1 Gy carbon ion radiation with a dose average LET of 100 keV/$\mu$m. A larger number of double strand break at 1.5 is shown in oxic condition. Courtesy of Dr. B. Jakob (Ferruz et al., 2016).

tion with the group of Prof. Lacombe (Université Paris-Saclay, France) and are presented in the Ph.D. thesis of Dr. Bolsa-Ferruz (Bolsa Ferruz, 2017).

In the context of this thesis work, an extended analysis of the nanoscopic mechanisms involved in the NP sensitization effect has been carried out with the classical version of the TRAX code for different ion radiation and nanoparticle of different sizes, under the assumption of ion traversing the NP. In addition, for the very first time, the radiolysis enhancement effect of 2 nm NPs traversed by different ion radiations and in different oxygenation conditions has been simulated, with the newly implemented chemical extension of the TRAX code. A significant increase in the dose deposition and in the production of radiolytic species has been observed in both oxic and hypoxic conditions, which can lead to an enhancement of the radiation effect. Additionally, in presence of molecular oxygen, a significant increase of $O_2^{\bullet-}$ and $HO_2^{\bullet}$ (the two highly toxic species considered to be responsible for a part of the oxygen effect) has been observed. However, the assumption of ion traversing the NP, which results to necessary for characterizing the effect of the NP, is highly unprobable (in a standard proton treatment it has been estimated to be between $10^{-3}$ and $10^{-4}$), significantly reducing the overall enhancement effect. Additionally, surface effects, such as surface plasmon excitation, are still not accounted in TRAX and additional catalytic processes responsible for an increased radical production might be considered as well. Unfortunately, very little experimental data able to validate these theoretical models exists, especially on the basic physical and chemical mechanisms involved in the NP radiosensitization. In this direction, a proposal for measuring the radical enhancement effect of AuNP in water solutions under ion irradiation has been submitted and approved for the GSI beam-time of 2018 and 2019 in collaboration

with the group of Prof. Currell (Queen University, Belfast), who already performed a similar experiment with X-ray (Sicard-Roselli et al., 2014), revealing new interesting pathways for the radioenhancement effect.

# A Appendix

## A.1 Brownian motion and diffusion

The brownian motion is the motion resulting from the collision of molecules or particles suspended in a fluid medium.

It is convenient to describe this motion trough the probability density of finding a suspended molecule as a function of the time, Guadagnini (2014). In order to define this probability it is convenient to start from some general considerations on the random walk.

### Random walk

For simplicity we assume a unidimensional system where the objects can move along the x axis with a random step of length $l$. The probability make a step forward is the same of the one make a step backward.

In the case of independent processes, after $N$ steps the probability of having a specific sequence of $n_1$ step forward and $n_2$ step in the other direction will be $(1/2)^{n_1} \times (1/2)^{n_2} = (1/2)^N$.

The probability of having $n_1$ step forward over a total of $fN$ steps, $P_N(n_1)$, can be obtained by multiplying this probability for the number of possible sequences (Chandrasekhar, 1943):

$$P_N(n_1) = \left(\frac{1}{2}\right)^N \frac{N!}{n_1!(N-n_1)!}. \tag{A.1}$$

For $N \to \infty$ and adopting the approximation $n! \simeq n^n e^{-n}$, the probability distribution Equation A.1 can be approximated as

$$P_N(n_1) = \frac{1}{\sqrt{2\pi N}} exp\left(-2(N/2 - n - 1)^2/N\right). \tag{A.2}$$

The effective distance made in the forward direction, in units of steps is given by $p = n_1 - n_2 = 2n_1 - N$. Substituting, than, $n_1 = (p + N)/2$ in Equation A.2 and renormalizing we obtain the probability distribution of making a total distance $p$ in a forwarded direction

$$P_N(p) = \frac{1}{\sqrt{2\pi N}} exp\left(-p^2/2N\right). \tag{A.3}$$

Since each step length is $I$, the total distance made by the considered object will be $x = pl$. The probability of making a distance x in $N$ steps ( with $N \to \infty$), will then be given by

$$P_N(x) = \frac{1}{\sqrt{2\pi N l^2}} exp\left(-x^2/2Nl^2\right). \tag{A.4}$$

## Diffusion distribution

If a particle suspended in a solution makes $\bar{n}$ steps in a unit of time, after a time $t$ the number of steps will be $N = \bar{n}t$. If the particle makes a random walk in the suspension the density probability distribution for a distance $x$ in a time $t$ can be derived from Equation A.4

$$P(x,t) = \frac{1}{2\sqrt{\pi Dt}} exp\left(-x^2/4Dt\right), \tag{A.5}$$

where $D = \frac{1}{2}\bar{n}l^2$.

In a three dimensional system, $P(\vec{x}, t)$ can be derived from Equation A.6

$$P(\vec{x},t) = \frac{1}{8(\pi Dt)^{-\frac{3}{2}}} exp\left(-|x|^2/4Dt\right). \tag{A.6}$$

It is possible to demonstrate that $P(\vec{x}, t)$ satisfy the diffusion equation for a system with diffusion coefficient $D$. Considering, indeed the two relations

$$\frac{\partial P(\vec{x},t)}{\partial t} = \left(-\frac{3}{2t} + \frac{|x|^2}{4Dt^2}\right)P(\vec{x},t)$$

$$\nabla^2 P(\vec{x},t) = \left(-\frac{3}{2Dt} + \frac{|x|^2}{4D^2t^2}\right)P(\vec{x},t)$$

the Fick diffusion equation can be obtained

$$\frac{\partial P(\vec{x},t)}{\partial t} = D\nabla^2 P(\vec{x},t).$$

The root mean square of the distance travelled by the particle in a time $t$, can then be finally derived from applying

$$<|\vec{x}|^2> = 6Dt. \tag{A.7}$$

# Bibliography

Agostinelli, S., Allison, J., Amako, K. a., Apostolakis, J., Araujo, H., Arce, P., Asai, M., Axen, D., Banerjee, S., Barrand, G. ., et al. (2003). Geant4—a simulation toolkit. *Nuclear Instruments and Methods in physics research section A: Accelerators, Spectrometers, Detectors and Associated Equipment*, 506(3):250–303.

Ahmad, R., Royle, G., Lourenco, A., Schwarz, M., Fracchiolla, F., and Ricketts, K. (2016). Investigation into the effects of high-Z nano materials in proton therapy. *Physics in Medicine & Biology*, 61(12):4537.

Aikens, J. (1991). Perhydroxyl radical ($HO_2^\bullet$) initiated lipid peroxidation. the role of fatty acid hydroperoxides. *The Journal of Biological Chemistry*, 266(23):15091–8.

Alper, T. (1956). The modification of damage caused by primary ionization of biological targets. *Radiation Research*, 5(6):573–586.

Appleby, A. and Schwarz, H. A. (1969). Radical and molecular yields in water irradiated by $\gamma$-rays and heavy ions. *The Journal of Physical Chemistry*, 73(6):1937–1941.

Balagopalakrishna, C., Manoharan, P. T., Abugo, O. O., and Rifkind, J. M. (1996). Production of superoxide from hemoglobin-bound oxygen under hypoxic conditions. *Biochemistry*, 35(20):6393–6398.

Ballarini, F., Biaggi, M., Merzagora, M., Ottolenghi, A., Dingfelder, M., Friedland, W., Jacob, P., and Paretzke, H. G. (2000). Stochastic aspects and uncertainties in the prechemical and chemical stages of electron tracks in liquid water: a quantitative analysis based on Monte Carlo simulations. *Radiation and Environmental Biophysics*, 39(3):179–188.

Barkas, W. H. (1963). *Nuclear Research Emulsions*, volume 1. Academic Press.

Barnett, R. and Landman, U. (1995). Pathways and Dynamics of Dissociation of Ionized $(H_2O)_2$. *The Journal of Physical Chemistry*, 99(48):17305–17310.

Baro, J., Sempau, J., Fernández-Varea, J., and Salvat, F. (1995). PENELOPE: an algorithm for Monte Carlo simulation of the penetration and energy loss of electrons and positrons in matter. *Nuclear Instruments and Methods in Physics Research Section B: Beam Interactions with Materials and Atoms*, 100(1):31–46.

Bartels, D. M., Cook, A. R., Mudaliar, M., and Jonah, C. D. (2000). Spur decay of the solvated electron in picosecond radiolysis measured with time-correlated absorption spectroscopy. *The Journal of Physical Chemistry A*, 104(8):1686–1691.

Baverstock, K. and Burns, W. (1981). Oxygen as a product of water radiolysis in high-LET tracks. II. Radiobiological implications. *Radiation Research*, 86(1):20–33.

Belloni, J., Billiau, F., Delaire, J., Delcourt, M., and Marignier, J. (1983). Ionizing radiation-liquid interactions: A comparative study of polar liquids. *Radiation Physics and Chemistry (1977)*, 21(1):177 – 183.

Berg, H. C. (1993). *Random walks in biology*. Princeton University Press.

Berger, M. J. et al. (1963). Monte Carlo calculation of the penetration and diffusion of fast charged particles. *Methods in Computational Physics*, 1:135–215.

Beuve, M., Moreau, J.-M., Rodriguez, C., and Testa, E. (2015). Biological systems: from water radiolysis to carbon ion radiotherapy. *Journal of Physics: Conference Series*, 629(1):012004.

Bisby, R. H., Cundall, R. B., Sims, H. E., and Burns, W. G. (1977). Linear energy transfer (LET) effects in the radiation-induced inactivation of papain. *Faraday Discussions of the Chemical Society.*, 63:237–247.

Bolsa Ferruz, M. (2017). *Oxygen effect in medical ion beam radiation combined with nanoparticles*. PhD thesis, Paris Saclay.

Boscolo, D., Krämer, M., Durante, M., Fuss, M., and Scifoni, E. (2018). Trax-chem: A pre-chemical and chemical stage extension of the particle track structure code trax in water targets. *Chemical Physics Letters*, 698:11–18.

Boudaïffa, B., Cloutier, P., Hunting, D., Huels, M. A., and Sanche, L. (2000). Resonant formation of DNA strand breaks by low-energy (3 to 20 eV) electrons. *Science*, 287(5458):1658–1660.

Boyle, J. W., Ghormley, J. A., Hochanadel, C. J., and Riley, J. F. (1969). Production of hydrated electrons by flash photolysis of liquid water with light in the first continuum. *The Journal of Physical Chemistry*, 73(9):2886–2890.

Buetler, T. M., Krauskopf, A., and Ruegg, U. T. (2004). Role of superoxide as a signaling molecule. *Physiology*, 19(3):120–123.

Burns, W. G., May, R., Buxton, G. V., and Wilkinson-Tough, G. S. (1981). Nanosecond proton pulse radiolysis of aqueous solutions. Part 2.-Improved measurements and isotope effects. *Journal of the Chemical Society, Faraday Transactions 1*, 77:1543–1551.

Burns, W. G. and Sims, H. E. (1981). Effect of radiation type in water radiolysis. *Journal of the Chemical Society, Faraday Transactions 1*, 77:2803–2813.

Butterworth, K. T., McMahon, S. J., Currell, F. J., and Prise, K. M. (2012). Physical basis and biological mechanisms of gold nanoparticle radiosensitization. *Nanoscale*, 4:4830–4838.

Buxton, G. V. (1972). Nanosecond pulse radiolysis of aqueous solutions containing proton and hydroxyl radical scavengers. *Proceedings of the Royal Society of London A: Mathematical, Physical and Engineering Sciences*, 328(1572):9–21.

Carlson, D. J., Stewart, R. D., and Semenenko, V. A. (2006). Effects of oxygen on intrinsic radiation sensitivity: A test of the relationship between aerobic and hypoxic linear-quadratic (LQ) model parameters. *Medical Physics*, 33(9):3105–3115.

Carter, J. D., Cheng, N. N., Qu, Y., Suarez, G. D., and Guo, T. (2007). Nanoscale energy deposition by X-ray absorbing nanostructures. *The Journal of Physical Chemistry B.*, 111.

Champion, C., Incerti, S., Aouchiche, H., and Oubaziz, D. (2009). A free-parameter theoretical model for describing the electron elastic scattering in water in the Geant4 toolkit. *Radiation Physics and Chemistry*, 78(9):745–750.

Chandrasekhar, S. (1943). Stochastic problems in physics and astronomy. *Reviews of modern physics*, 15(1):1.

Chen, Y., Azad, M., and Gibson, S. (2009). Superoxide is the major reactive oxygen species regulating autophagy. *Cell Death and Differentiation*, 16(7):1040.

Cho, J., Gonzalez-Lepera, C., Manohar, N., Kerr, M., Krishnan, S., and Cho, S. H. (2016). Quantitative investigation of physical factors contributing to gold nanoparticle-mediated proton dose enhancement. *Physics in Medicine & Biology*, 61(6):2562.

Christman, E. A. and Appleby, A. (1981). Radiation chemistry of high-energy carbon, neon, and argon ions: integral yields from ferrous sulfate solutions. *Radiation Research*, 85(3):443–457.

Clifford, P., Green, N. J., and Pilling, M. J. (1985). Stochastic models of scavenging in radiation-induced spurs. *The Journal of Physical Chemistry*, 89(6):925–930.

Clifford, P., Green, N. J. B., Oldfield, M. J., Pilling, M. J., and Pimblott, S. M. (1986). Stochastic models of multi-species kinetics in radiation-induced spurs. *Journal of the Chemical Society, Faraday Transactions 1*, 82:2673–2689.

Cobut, V., Frongillo, Y., Patau, J. P., Goulet, T., Fraiser, M., and Jay-Gerin, J. (1998). Monte Carlo Simulation of fast electron and proton tracks in liquid water I. Physical and physicochemical aspects. *Radiation Physics and Chemistry*, 51(3):229 – 243.

Colliaux, A. (2009). Implication de l'oxygène et des anti-oxydants dans le processus de radiolyse de l'eau induit par l'irradiation aux ions de haute énergie. *PhD thesis*.

Colliaux, A., Gervais, B., Rodriguez-Lafrasse, C., and Beuve, M. (2011). $O_2$ and glutathione effects on water radiolysis: a simulation study. *Journal of Physics: Conference Series*, 261(1):012007.

Combs, S. E., Ganswindt, U., Foote, R. L., Kondziolka, D., and Tonn, J.-C. (2012). State-of-the-art treatment alternatives for base of skull meningiomas: complementing and controversial indications for neurosurgery, stereotactic and robotic based radiosurgery or modern fractionated radiation techniques. *Radiation Oncology*, 7(1):226.

Conde, J., Tian, F., Baptista, P. V., and Jesús, M. (2014). Multifunctional Gold Nanocarriers for Cancer Theranostics: From Bench to Bedside and Back Again? In *Nano-Oncologicals*, pages 295–328. Springer.

de Grey., A. D. (2004). HO$_2^*$: The forgotten radical. *DNA and Cell Biology*, 21(4):251–257.

Deslattes, R., Kessler Jr, E., Indelicato, P., De Billy, L., Lindroth, E., Anton, J., Coursey, J., Schwab, D., Chang, C., Sukumar, R., et al. (2005). X-ray transition energies (version 1.2).[online] available: http://physics. nist. gov/xraytrans [2009, october 20]. National Institute of Standards and Technology, NIST. *Gaithersburg, MD*.

Dingfelder, M., Hantke, D., Inokuti, M., and Paretzke, H. G. (1999). Electron inelastic-scattering cross sections in liquid water. *Radiation Physics and Chemistry*, 53(1):1–18.

Dingfelder, M., Inokuti, M., and Paretzke, H. G. (2000). Inelastic-collision cross sections of liquid water for interactions of energetic protons. *Radiation Physics and Chemistry*, 59(3):255–275.

Dingfelder, M., Ritchie, R., Turner, J., Friedland, W., Paretzke, H., and Hamm, R. (2008). Comparisons of calculations with PARTRAC and NOREC: transport of electrons in liquid water. *Radiation Research*, 169(5):584–594.

Draganić, Z. and Draganić, I. (1975). Formation of primary reducing yields (G(e$_{aq}^-$)and G(H$_2$)) in the radiolysis of aqueous solutions of some positive ions. *International Journal for Radiation Physics and Chemistry*, 7(2):381 – 386.

Durante, M. and Paganetti, H. (2016). Nuclear physics in particle therapy: a review. *Reports on Progress in Physics*, 79(9):096702.

Eigen, M. and de Maeyer, L. (1958). Self-dissociation and protonic charge transport in water and ice. *Proceedings of the Royal Society of London A: Mathematical, Physical and Engineering Sciences*, 247(1251):505–533.

El Omar, A. K., Schmidhammer, U., Jeunesse, P., Larbre, J.-P., Lin, M., Muroya, Y., Katsumura, Y., Pernot, P., and Mostafavi, M. (2011). Time-dependent radiolytic yield of OH$^*$ radical studied by picosecond pulse radiolysis. *The Journal of Physical Chemistry A*, 115(44):12212–12216. PMID: 21970432.

Elliot, A. J., Chenier, M. P., and Ouellette, D. C. (1993). Temperature dependence of g values for H$_2$O and D$_2$O irradiated with low linear energy transfer radiation. *Journal of the Chemical Society, Faraday Transactions*, 89:1193–1197.

Emfietzoglou, D., Cucinotta, F. A., and Nikjoo, H. (2005). A complete dielectric response model for liquid water: a solution of the Bethe Ridge problem. *Radiation Research*, 164(2):202–211.

Ferradini, C. and Jay-Gerin, J.-P. (1999). La radiolyse de l'eau et des solutions aqueuses : historique et actualité. *Canadian Journal of Chemistry*, 77(9):1542–1575.

Ferruz, M. B., Boscolo, D., Porcel, E., Lacombe, Sokol, O., Wiedemann, J., Scifoni, E., Tinganelli, W., Jakob, B., Roux, S., Jimenez, G., Durante, M., and Krämer, M. (2016). Nanoparticles radio-enhancement of ion beams at different oxygenation conditions. *GSI Scientific Report*.

Ferruz, M. B., Ivošev, V., Haume, K., Ellis-Gibbings, L., Traore, A., Thakare, V., Rosa, S., de Vera, P., Tran, V.-L., Mika, A., et al. (2017). New research in ionizing radiation and nanoparticles: the ARGENT project. In *Nanoscale Insights into Ion-Beam Cancer Therapy*, pages 379–434. Springer.

Francis, Z., Incerti, S., Capra, R., Mascialino, B., Montarou, G., Stepan, V., and Villagrasa, C. (2011). Molecular scale track structure simulations in liquid water using the Geant4-DNA Monte-Carlo processes. *Applied Radiation and Isotopes*, 69(1):220–226.

Fridovich, I. (1997). Superoxide anion radical ($O_2^{\bullet}$), superoxide dismutases, and related matters. *Journal of Biological Chemistry*, 272(30):18515–18517.

Friedrich, T., Scholz, U., ElsäSser, T., Durante, M., and Scholz, M. (2012). Systematic analysis of RBE and related quantities using a database of cell survival experiments with ion beam irradiation. *Journal of Radiation Research*, 54(3):494–514.

Frongillo, Y., Goulet, T., Fraiser, M., Cobut, V., Patau, J. P., and Jay-Gerin, J. (1998). Monte Carlo simulation of fast electron and proton tracks in liquid water II. Nonhomogeneous chemistry. *Radiation Physics and Chemistry*, 51:245–254.

Fyles, A., Milosevic, M., Hedley, D., Pintilie, M., Levin, W., Manchul, L., and Hill, R. (2002). Tumor hypoxia has independent predictor impact only in patients with node-negative cervix cancer. *Journal of Clinical Oncology*, 20(3):680–687.

Gao, J. and Zheng, Y. (2014). Monte Carlo study of secondary electron production from gold nanoparticle in proton beam irradiation. *International Journal of Cancer Therapy and Oncology*, 2(2).

Gervais, B., Beuve, M., Olivera, G., and Galassi, M. (2006). Numerical simulation of multiple ionization and high LET effects in liquid water radiolysis. *Radiation Physics and Chemistry*, 75(4):493 – 513.

Gervais, B., Beuve, M., Olivera, G., Galassi, M., and Rivarola, R. (2005). Production of $HO_2$ and $O_2$ by multiple ionization in water radiolysis by swift carbon ions. *Chemical physics letters*, 410(4-6):330–334.

Goldstein, S. and Czapski, G. (1995). The reaction of $NO^{\bullet}$ with $O_2^{\bullet-}$ and $HO_2^{\bullet-}$: A pulse radiolysis study. *Free Radical Biology and Medicine*, 19(4):505 – 510.

Gray, L. H., Conger, A., Ebert, M., Hornsey, S., and Scott, O. (1953). The concentration of oxygen dissolved in tissues at the time of irradiation as a factor in radiotherapy. *The British Journal of Radiology*, 26(312):638–648.

Green, A. and Stolarski, R. (1972). Analytic models of electron impact excitation cross sections. *Journal of Atmospheric and Terrestrial Physics*, 34(10):1703–1717.

Green, N. J. B., Pilling, M. J., Pimblott, S. M., and Clifford, P. (1990). Stochastic modeling of fast kinetics in a radiation track. *The Journal of Physical Chemistry*, 94(1):251–258.

Grosswendt, B. and Waibel, E. (1978). Transport of low energy electrons in nitrogen and air. *Nuclear Instruments and Methods*, 155(1-2):145–156.

Guadagnini, E. (2014). *Primo corso di fisica statistica*. Pisa University Press.

Haber, F. and Weiss, J. (1932). Über die katalyse des hydroperoxydes. *Naturwissenschaften*, 20(51):948–950.

Hainfeld, J. F., Dilmanian, F. A., Slatkin, D. N., and Smilowitz, H. M. (2008). Radiotherapy enhancement with gold nanoparticles. *Journal of Pharmacy and Pharmacology*, 60(8):977–985.

Hainfeld, J. F., Slatkin, D. N., and Smilowitz, H. M. (2004). The use of gold nanoparticles to enhance radiotherapy in mice. *Physics in Medicine & Biology*, 49.

Hall, C. N. and Garthwaite, J. (2009). What is the real physiological NO concentration in vivo? *Nitric Oxide*, 21(2):92–103.

Han, P. and Bartels, D. M. (1990). Hydrogen/deuterium isotope effects in water radiolysis. 2. Dissociation of electronically excited water. *The Journal of Physical Chemistry*, 94(15):5824–5833.

Haume, K., Rosa, S., Grellet, S., Śmiałek, M. A., Butterworth, K. T., Solov'yov, A. V., Prise, K. M., Golding, J., and Mason, N. J. (2016). Gold nanoparticles for cancer radiotherapy: a review. *Cancer Nanotechnology*, 7(1):8.

Hawkins, R. B. (2003). A microsimetric-kinetic model for the effect of non-Poisson distribution of lethal lesions on the variation of RBE with LET. *Radiation Research*, 160(1):61–69.

Hespeels, F., Heuskin, A., Scifoni, E., Kraemer, M., and Lucas, S. (2017). Backscattered electron emission after proton impact on carbon and gold films: Experiments and simulations. *Nuclear Instruments and Methods in Physics Research Section B: Beam Interactions with Materials and Atoms*, 401:8–17.

Hill, M. and Smith, F. (1994). Calculation of initial and primary yields in the radiolysis of water. *Radiation Physics and Chemistry*, 43(3):265 – 280.

Hirayama, R., Ito, A., Noguchi, M., Matsumoto, Y., Uzawa, A., Kobashi, G., Okayasu, R., and Furusawa, Y. (2013). OH radicals from the indirect actions of X-rays induce cell lethality and mediate the majority of the oxygen enhancement effect. *Radiation Research*, 180(5):514–523.

Hirayama, R., Ito, A., Tomita, M., Tsukada, T., Yatagai, F., Noguchi, M., Matsumoto, Y., Kase, Y., Ando, K., Okayasu, R., et al. (2009). Contributions of direct and indirect actions in cell killing by high-LET radiations. *Radiation Research*, 171(2):212–218.

Holthusen, H. (1921). Beiträge zur Biologie der Strahlenwirkung. *Pflüger's Archiv für die gesamte Physiologie des Menschen und der Tiere*, 187(1):1–24.

International Commission on Radiation Units and measurements, ICRU (1998). Fundamental quantities and units for ionizing radiation. Technical report.

Ito, A., Nakano, H., Kusano, Y., Hirayama, R., Furusawa, Y., Murayama, C., Mori, T., Katsumura, Y., and Shinohara, K. (2006). Contribution of indirect action to radiation-induced mammalian cell inactivation: dependence on photon energy and heavy-ion LET. *Radiation Research*, 165(6):703–712.

Jay-Gerin, J.-P. and Ferradini, C. (2000). A new estimate of the OH$^\bullet$ radical yield at early times in the radiolysis of liquid water. *Chemical Physics Letters*, 317(3):388 – 391.

Johansen, I. and Howard-Flanders, P. (1965). Macromolecular repair and free radical scavenging in the protection of bacteria against X-rays. *Radiation Research*, 24(1):184–200.

Jonah, C. D. and Miller, J. R. (1977). Yield and decay of the hydroxyl radical from 200 ps to 3 ns. *The Journal of Physical Chemistry*, 81(21):1974–1976.

Kaplan, I., Miterev, A., and Sukhonosov, V. (1990). Simulation of the primary stage of liquid water radiolysis. *International Journal of Radiation Applications and Instrumentation. Part C. Radiation Physics and Chemistry*, 36(3):493 – 498.

Karamitros, M., Mantero, A., Incerti, S., Friedland, W., Baldacchino, G., Barberet, P., Bernal, M., Capra, R., Champion, C., Bitar, Z., et al. (2011). Modeling radiation chemistry in the Geant4 toolkit. *Progress in Nuclear Science and Technology*, 2:503–508.

Katz, R. (1970). RBE, LET, and Z/$\beta^\alpha$.

Kawazumi, H. and Ogawa, T. (1987). Dissociation of water by controlled electron impact: rotational and translational energies of OH (X 2Πi) fragment. *Chemical Physics*, 114(1):149 – 155.

Keyer, K., Gort, A. S., and Imlay, J. A. (1995). Superoxide and the production of oxidative DNA damage. *Journal of Bacteriology*, 177(23):6782–6790.

Kim, J.-K., Seo, S.-J., Kim, H.-T., Kim, K.-H., Chung, M.-H., Kim, K.-R., and Ye, S.-J. (2012). Enhanced proton treatment in mouse tumors through proton irradiated nanoradiator effects on metallic nanoparticles. *Physics in Medicine & Biology*, 57(24):8309.

Kim, J.-K., Seo, S.-J., Kim, K.-H., Kim, T.-J., Chung, M.-H., Kim, K.-R., and Yang, T.-K. (2010). Therapeutic application of metallic nanoparticles combined with particle-induced X-ray emission effect. *Nanotechnology*, 21(42):425102.

Kim, Y.-K. and Rudd, M. E. (1994). Binary-encounter-dipole model for electron-impact ionization. *Physical Review A*, 50:3954–3967.

Kim, Y.-K., Santos, J. P., and Parente, F. (2000). Extension of the binary-encounter-dipole model to relativistic incident electrons. *Physical Review A*, 62(5):052710.

Klassen, N. V. and Ross, C. K. (1997). Water calorimetry: The heat defect. *Journal of research of the National Institute of Standards and Technology*, 102(1):63–74.

Kobayashi, K., Usami, N., Porcel, E., Lacombe, S., and Sech, C. (2010). Enhancement of radiation effect by heavy elements. *Reviews in Mutation Research*, 704.

Krämer, M. and Durante, M. (2010). Ion beam transport calculations and treatment plans in particle therapy. *The European Physical Journal D-Atomic, Molecular, Optical and Plasma Physics*, 60(1):195–202.

Krämer, M. and Kraft, G. (1994). Calculations of heavy-ion track structure. *Radiation and Environmental Biophysics*, 33(2):91–109.

Krämer, M., Scifoni, E., Schuy, C., Rovituso, M., Tinganelli, W., Maier, A., Kaderka, R., Kraft-Weyrather, W., Brons, S., Tessonnier, T., et al. (2016). Helium ions for radiotherapy? Physical and biological verifications of a novel treatment modality. *Medical Physics*, 43(4):1995–2004.

Kramida, A., Ralchenko, Y., Reader, J., and Team, N. A. (2013). NIST atomic spectra database. http://physics.nist.gov/asd.

Kreipl, M. S., Friedland, W., and Paretzke, H. G. (2008). Time- and space-resolved Monte Carlo study of water radiolysis for photon, electron and ion irradiation. *Radiation and Environmental Biophysics*, 48(1):11.

Kuncic, Z. and Lacombe, S. (2018). Nanoparticle radio-enhancement: principles, progress and application to cancer treatment. *Physics in Medicine & Biology*, 63(2):02TR01.

Kuninaka, S., Ichinose, Y., Koja, K., and Toh, Y. (2000). Suppression of manganese superoxide dismutase augments sensitivity to radiation, hyperthermia and doxorubicin in colon cancer cell lines by inducing apoptosis. *British Journal of Cancer*, 83(7):928.

Kurawaki, J., Ueki, K., Higo, M., and Ogawa, T. (1983). Translational energy distribution and production mechanism of H$^*$ and D$^*$ produced by controlled electron impact on water and heavy water. *The Journal of Chemical Physics*, 78(6):3071–3077.

Kwatra, D., Venugopal, A., and Anant, S. (2013). Nanoparticles in radiation therapy: a summary of various approaches to enhance radiosensitization in cancer. *Translational Cancer Research*, 2(4).

Lacombe, S., Porcel, E., and Scifoni, E. (2017). Particle therapy and nanomedicine: state of art and research perspectives. *Cancer Nanotechnology*, 8(1):9.

Larsen, E. W. and Tolar, D. R. (2001). *A "Transport" Condensed History Method*. Springer, Berlin, Heidelberg.

LaVerne, J. A. (2000). OH Radicals and Oxidizing Products in the Gamma Radiolysis of Water. *Radiation Research*, 153(2):196–200.

LaVerne, J. A. and Pimblott, S. M. (1991). Scavenger and time dependences of radicals and molecular products in the electron radiolysis of water: examination of experiments and models. *The Journal of Physical Chemistry*, 95(8):3196–3206.

LaVerne, J. A., Štefanić, I., and Pimblott, S. M. (2005). Hydrated electron yields in the heavy ion radiolysis of water. *The Journal of Physical Chemistry A*, 109(42):9393–9401. PMID: 16866387.

Li, S., Penninckx, S., Karmani, L., Heuskin, A.-C., Watillon, K., Marega, R., Zola, J., Corvaglia, V., Genard, G., Gallez, B., et al. (2016). LET-dependent radiosensitization effects of gold nanoparticles for proton irradiation. *Nanotechnology*, 27(45):455101.

Lin, Y., McMahon, S. J., Paganetti, H., and Schuemann, J. (2015). Biological modeling of gold nanoparticle enhanced radiotherapy for proton therapy. *Physics in Medicine & Biology*, 60(10):4149.

Liu, C., Lin, Q., and Yun, Z. (2015a). Cellular and molecular mechanisms underlying oxygen-dependent radiosensitivity. *Radiation Research*, 183(5):487–496.

Liu, Y., Liu, X., Jin, X., He, P., Zheng, X., Dai, Z., Ye, F., Zhao, T., Chen, W., and Li, Q. (2015b). The dependence of radiation enhancement effect on the concentration of gold nanoparticles exposed to low-and high-LET radiations. *Physica Medica: European Journal of Medical Physics*, 31(3):210–218.

Liu, Y., Liu, X., Jin, X., He, P., Zheng, X., Ye, F., Chen, W., and Li, Q. (2016). The Radiation Enhancement of 15 nm Citrate-Capped Gold Nanoparticles Exposed to 70 keV/$\mu$m Carbon Ions. *Journal of Nanoscience and Nanotechnology*, 16(3):2365–2370.

Maslov, M., Brunger, M. J., Teubner, P. J. O., Zatsarinny, O., Bartschat, K., Fursa, D., Bray, I., and McEachran, R. P. (2008). Electron-impact excitation of the $(5d^{10}6s)^2S_{1/2} \rightarrow (5d^{10}6p)^2P_{1/2,3/2}$ resonance transitions in gold atoms. *Physical Review A*, 77:062711.

McMahon, S. J., Hyland, W. B., Muir, M. F., Coulter, J. A., Jain, S., Butterworth, K. T., Schettino, G., Dickson, G. R., Hounsell, A. R., O'Sullivan, J. M., Prise, K. M., Hirst, D. G., and Currell, F. J. (2011). Nanodosimetric effects of gold nanoparticles in megavoltage radiation therapy. *Radiotherapy and Oncology*, 100.

Meesungnoen, J., Filali-Mouhim, A., Ayudhya, N. S. N., Mankhetkorn, S., and Jay-Gerin, J.-P. (2003). Multiple ionization effects on the yields of $HO_2/O_2^-$ and $H_2O_2$ produced in the radiolysis of liquid water with high-LET $^{12}C^{6+}$ ions: a Monte-Carlo simulation study. *Chemical Physics Letters*, 377(3):419 – 425.

Meesungnoen, J. and Jay-Gerin, J.-P. (2005). High-LET radiolysis of liquid water with $^1H^+$, $^4He^{2+}$, $^{12}C^{6+}$, and $^{20}Ne^{9+}$ ions: effects of multiple ionization. *The Journal of Physical Chemistry A*, 109(29):6406–6419. PMID: 16833985.

Meesungnoen, J. and Jay-Gerin, J.-P. (2009). High-LET ion radiolysis of water: oxygen production in tracks. *Radiation Research*, 171(3):379–86.

Meesungnoen, J., Jay-Gerin, J.-P., Filali-Mouhim, A., and Mankhetkorn, S. (2002). Low-energy electron penetration range in liquid water. *Radiation Research*, 158(5):657–660.

Michael, B. (1996). A multiple-radical model for radiation action on DNA and the dependence of OER on LET. *International Journal of Radiation Biology*, 69(3):351–358.

Michaud, M., Wen, A., and Sanche, L. (2003). Cross sections for low-energy (1-100 eV) electron elastic and inelastic scattering in amorphous ice. *Radiation Research*, 159(1):3–22.

Mikkelsen, R. and Wardman, P. (2003). Biological chemistry of reactive oxygen and nitrogen and radiation-induced signal transduction mechanisms. *Oncogene*, 22(37):5734–54.

Miller, J. and Green, A. (1973). Proton energy degradation in water vapor. *Radiation Research*, 54(3):343–363.

Monchick, L. (1956). Note on the theory of diffusion controlled reactions: application to photodissociation in solution. *The Journal of Chemical Physics*, 24(2):381–385.

Muddineti, O. S., Ghosh, B., and Biswas, S. (2015). Current trends in using polymer coated gold nanoparticles for cancer therapy. *International Journal of Pharmaceutics*, 484.

Muroya, Y., Lin, M., Wu, G., Iijima, H., Yoshii, K., Ueda, T., Kudo, H., and Katsumura, Y. (2005). A re-evaluation of the initial yield of the hydrated electron in the picosecond time range. *Radiation Physics and Chemistry*, 72(2):169 – 172. Christiane Ferradini Memorial Issue.

Naleway, C. A., Sauer, M. C., Jonah, C. D., and Schmidt, K. H. (1979). Theoretical analysis of the LET dependence of transient yields observed in pulse radiolysis with ion beams. *Radiation Research*, 77(1):47–61.

Neary, G. (1965). Chromosome aberrations and the theory of RBE: 1. General considerations. *International Journal of Radiation Biology and Related Studies in Physics, Chemistry and Medicine*, 9(5):477–502.

Nikjoo, H., Emfietzoglou, D., Liamsuwan, T., Taleei, R., Liljequist, D., and Uehara, S. (2016). Radiation track, DNA damage and response—a review. *Reports on Progress in Physics*, 79(11):116601.

Nikjoo, H., Uehara, S., and Emfietzoglou, D. (2012). *Interaction of rdadiation with matter*. CRC Press.

Nikjoo, H., Uehara, S., Emfietzoglou, D., and Cucinotta, F. (2006). Track-structure codes in radiation research. *Radiation Measurements*, 41(9):1052 – 1074. Space Radiation Transport, Shielding, and Risk Assessment Models.

Noyes, R. M. (1961). Effects of diffusion rates on chemical kinetics. *Progress in Reaction kinetics and Mechanism*, 1:129–160.

Paretzke, H. G. (1988). *Simulation von Elektronenspuren im Energiebereich 0, 01-10 keV in Wasserdampf*. Gesellschaft für Strahlen-und Umweltforschung mbH München.

Pastina, B. and LaVerne, J. A. (1999). Hydrogen peroxide production in the radiolysis of water with heavy ions. *The Journal of Physical Chemistry A*, 103(11):1592–1597.

Paudel, N., Shvydka, D., and Parsai, E. I. (2015). Comparative study of experimental enhancement in free radical generation against Monte Carlo modeled enhancement in radiation dose deposition due to the presence of high Z materials during irradiation of aqueous media. *International Journal of Medical Physics, Clinical Engineering and Radiation Oncology*, 4(04):300.

Peer, D., Karp, J. M., Hong, S., Farokhzad, O. C., Margalit, R., and Langer, R. (2007). Nanocarriers as an emerging platform for cancer therapy. *Nature nanotechnology*, 2(12):751.

Perkins, S., Cullen, D., Chen, M., Rathkopf, J., Scofield, J., and Hubbell, J. (1991). Tables and graphs of atomic subshell and relaxation data derived from the LLNL Evaluated Atomic Data Library (EADL), Z= 1–100. Technical report, Lawrence Livermore National Lab., CA (United States).

Pimblott, S. M. and LaVerne, J. A. (1994). Diffusion-Kinetic Theories for LET Effects on the Radiolysis of Water. *The Journal of Physical Chemistry*, 98(24):6136–6143.

Pimblott, S. M. and LaVerne, J. A. (1997). Stochastic simulation of the electron radiolysis of water and aqueous solutions. *The Journal of Physical Chemistry A*, 101(33):5828–5838.

Pimblott, S. M. and LaVerne, J. A. (2002). Effects of Track Structure on the Ion Radiolysis of the Fricke Dosimeter. *The Journal of Physical Chemistry A*, 106(41):9420–9427.

Pimblott, S. M., LaVerne, J. A., Bartels, D. M., and Jonah, C. D. (1996). Reconciliation of transient absorption and chemically scavenged yields of the hydrated electron in radiolysis. *The Journal of Physical Chemistry*, 100(22):9412–9415.

Pimblott, S. M., Pilling, M. J., and Green, N. J. (1991). Stochastic models of spur kinetics in water. *International Journal of Radiation Applications and Instrumentation. Part C. Radiation Physics and Chemistry*, 37(3):377 – 388.

Plante, I. (2011a). A Monte–Carlo step-by-step simulation code of the non-homogeneous chemistry of the radiolysis of water and aqueous solutions. Part I: theoretical framework and implementation. *Radiation and Environmental Biophysics*, 50(3):389–403.

Plante, I. (2011b). A Monte-Carlo step-by-step simulation code of the non-homogeneous chemistry of the radiolysis of water and aqueous solutions—Part II: calculation of radiolytic yields under different conditions of LET, pH, and temperature. *Radiation and Environmental Biophysics*, 50(3):405–415.

Plante, I. and Devroye, L. (2017). Considerations for the independent reaction times and step-by-step methods for radiation chemistry simulations. *Radiation Physics and Chemistry*, 139(Supplement C):157 – 172.

Polf, J. C., Bronk, L. F., Driessen, W. H. P., Arap, W., Pasqualini, R., and Gillin, M. (2011). Enhanced relative biological effectiveness of proton radiotherapy in tumor cells with internalized gold nanoparticles. *Applied Physics Letters*, 98.

Porcel, E., Li, S., Usami, N., Remita, H., Furusawa, Y., Kobayashi, K., Sech, C. L., and Lacombe, S. (2012). Nano-sensitization under gamma rays and fast ion radiation. *Journal of Physics: Conference Series*, 373(1):012006.

Porcel, E., Liehn, S., Remita, H., Usami, N., Kobayashi, K., Furusawa, Y., Sech, C., and Lacombe, S. (2010). Platinum nanoparticles: a promising material for future cancer therapy? *Nanotechnology*, 21.

Porcel, E., Tillement, O., Lux, F., Mowat, P., Usami, N., Kobayashi, K., Furusawa, Y., Le Sech, C., Li, S., and Lacombe, S. (2014). Gadolinium-based nanoparticles to improve the hadrontherapy performances. *Nanomedicine: Nanotechnology, Biology and Medicine*, 10(8):1601–1608.

PTCOG (2016a). Particle therapy facilities in operation (last update: July 2017). `https://www.ptcog.ch/index.php/facilities-in-operation`.

PTCOG (2016b). Particle therapy facilities under construction (last update: June 2017). `https://www.ptcog.ch/index.php/facilities-under-construction`.

Reczek, C. R. and Chandel, N. S. (2017). The two faces of reactive oxygen species in cancer. *Annual Review of Cancer Biology,*, 1(1):79–98.

Reiter, R. J., Melchiorri, D., Sewerynek, E., Poeggeler, B., Barlow-Walden, L., Chuang, J., Ortiz, G. G., and AcuñaCastroviejo, D. (1995). A review of the evidence supporting melatonin's role as an antioxidant. *Journal of Pineal Research*, 18(1):1–11.

Repetto, M., Semprine, J., and Boveris, A. (2012). Lipid peroxidation: chemical mechanism, biological implications and analytical determination. In *Lipid peroxidation*. InTech.

Rice, S. A., Playford, V. J., Burns, W. G., and Buxton, G. V. (1982). Nanosecond proton pulse radiolysis. *Journal of Physics E: Scientific Instruments*, 15(11):1240.

Salvat, F., Fernández-Varea, J. M., and Sempau, J. (2006). PENELOPE-2006: A code system for Monte Carlo simulation of electron and photon transport. In *Workshop proceedings*, volume 4.

Sauer Jr, M. C., Schmidt, K. H., Hart, E. J., Naleway, C. A., and Jonah, C. D. (1977). LET dependence of transient yields in the pulse radiolysis of aqueous systems with deuterons and $\alpha$ particles. *Radiation Research*, 70(1):91–106.

Sauer Jr, M. C., Schmidt, K. H., Jonah, C. D., Naleway, C. A., and Hart, E. J. (1978). High-LET Pulse Radiolysis: and Oxygen Production in Tracks. *Radiation Research*, 75(3):519–528.

Schardt, D., Elsässer, T., and Schulz-Ertner, D. (2010). Heavy-ion tumor therapy: physical and radiobiological benefits. *Reviews of Modern Physics*, 82(1):383.

Schlathölter, T., Eustache, P., Porcel, E., Salado, D., Stefancikova, L., Tillement, O., Lux, F., Mowat, P., Biegun, A. K., Van Goethem, M.-J., et al. (2016). Improving proton therapy by metal-containing nanoparticles: nanoscale insights. *International Journal of Nanomedicine*, 11:1549.

Scholz, M. (2003). Effects of ion radiation on cells and tissues. In *Radiation effects on polymers for biological use*, pages 95–155. Springer.

Scholz, M. and Kraft, G. (1996). Track structure and the calculation of biological effects of heavy charged particles. *Adv. Space Res.*, 18:5–14.

Scholz, M. and Kraft, G. (2004). The Physical and Radiobiological Basis of the Local Effect Model:A Response to the Commentary by R. Katz. *Radiation Research*, 161(5):612–620.

Schwarz, H. A. (1969). Applications of the spur diffusion model to the radiation chemistry of aqueous solutions. *The Journal of Physical Chemistry*, 73(6):1928–1937.

Scifoni, E. (2015). Radiation biophysical aspects of charged particles: From the nanoscale to therapy. *Modern Physics Letters A*, 30(17):1540019.

Scifoni, E., Surdutovich, E., and Solov'yov, A. (2010a). Radial dose distribution from carbon ion incident on liquid water. *The European Physical Journal D-Atomic, Molecular, Optical and Plasma Physics*, 60(1):115–119.

Scifoni, E., Surdutovich, E., and Solov'yov, A. V. (2010b). Spectra of secondary electrons generated in water by energetic ions. *Physical Review E*, 81(2):021903.

Scifoni, E., Tinganelli, W., Weyrather, W., Durante, M., Maier, A., and Krämer, M. (2013). Including oxygen enhancement ratio in ion beam treatment planning: model implementation and experimental verification. *Physics in Medicine & Biology*, 58(11):3871.

Shiraishi, H., Katsumura, Y., Hiroishi, D., Ishigure, K., and Washio, M. (1988). Pulse-radiolysis study on the yield of hydrated electron at elevated temperatures. *The Journal of Physical Chemistry*, 92(10):3011–3017.

Sicard-Roselli, C., Brun, E., Gilles, M., Baldacchino, G., Kelsey, C., McQuaid, H., Polin, C., Wardlow, N., and Currell, F. (2014). A new mechanism for hydroxyl radical production in irradiated nanoparticle solutions. *Small*, 10(16):3338–3346.

Siegbahn, H., Asplund, L., and Kelfve, P. (1975). The auger electron spectrum of water vapour. *Chemical Physics Letters*, 35(3):330–335.

SIES, H. (1993). Strategies of antioxidant defense. *European Journal of Biochemistry*, 215(2):213–219.

Sokol, O., Scifoni, E., Tinganelli, W., Kraft-Weyrather, W., Wiedemann, J., Maier, A., Boscolo, D., Friedrich, T., Brons, S., Durante, M., et al. (2017). Oxygen beams for therapy: advanced biological treatment planning and experimental verification. *Physics in Medicine & Biology*, 62(19):7798.

Sonntag, C. (1987). *The Chemical Basis of Radiation Biology*. Taylor & Francis.

Stuglik, Z. (1995). On the "oxygen in heavy-ion tracks" hypothesis. *Radiation Research*, 143(3):343–8.

Surdutovich, E. and Solov'yov, A. V. (2014). Multiscale approach to the physics of radiation damage with ions. *The European Physical Journal D*, 68(11):353.

Takashi, S. and Meiseki, K. (1982). The yield of hydrated electrons at 30 picoseconds. *Chemistry Letters*, 11(12):1887–1890.

Terrissol, M. and Beaudré, A. (1990). Simulation of space and time evolution of radiolytic species induced by electrons in water. *Radiation Protection Dosimetry*, 31(1-4):175–177.

Thomas, D. (1997). *www.chembio.uoguelph.ca/educmat/atomdata/bindener/elecbind.htm*.

Thomas, J. K. and Bensasson, R. V. (1967). Direct observation of regions of high ion and radical concentration in the radiolysis of water and ethanol. *The Journal of Chemical Physics*, 46(10):4147–4148.

Thomsen, C. L., Madsen, D., Keiding, S. R., Thøgersen, J., and Christiansen, O. (1999). Two-photon dissociation and ionization of liquid water studied by femtosecond transient absorption spectroscopy. *The Journal of Chemical Physics*, 110(7):3453–3462.

Tinganelli, W., Durante, M., Hirayama, R., Krämer, M., Maier, A., Kraft-Weyrather, W., Furusawa, Y., Friedrich, T., and Scifoni, E. (2015). Kill-painting of hypoxic tumours in charged particle therapy. *Scientific Reports*, 5.

Tomita, H., Kai, M., Kusama, T., and Ito, A. (1997). Monte Carlo simulation of physicochemical processes of liquid water radiolysis. *Radiation and Environmental Biophysics*, 36(2):105–116.

Trajmar, S., Register, D. F., and Chutjian, A. (1983). Electron scattering by molecules II. Experimental methods and data. *Physics Reports*, 97(5):219–356.

Tran, H. N., Karamitros, M., Ivanchenko, V. N., Guatelli, S., McKinnon, S., Murakami, K., Sasaki, T., Okada, S., Bordage, M. C., Francis, Z., El Bitar, Z., Bernal, M. A., Shin, J. I., Lee, S. B., Barberet, P., Tran, T. T., Brown, J. M. C., Nhan Hao, T. V., and Incerti, S. (2016). Geant4 Monte Carlo simulation of absorbed dose and radiolysis yields enhancement from a gold nanoparticle under MeV proton irradiation. *Nuclear Instruments and Methods in Physics Research Section B: Beam Interactions with Materials and Atoms*, 373:126–139.

Trumbore, C. N., Short, D. R., Fanning, J. E., and Olson, J. H. (1978). Effects of pulse dose on hydrated electron decay kinetics in the pulse radiolysis of water. a computer modeling study. *The Journal of Physical Chemistry*, 82(26):2762–2767.

Turner, J., Hamm, R., Wright, H., Ritchie, R., Magee, J., Chatterjee, A., and Bolch, W. E. (1988). Studies to link the basic radiation physics and chemistry of liquid water. *International Journal of Radiation Applications and Instrumentation. Part C. Radiation Physics and Chemistry*, 32(3):503 – 510.

Turner, J. E., Magee, J. L., Wright, H. A., Chatterjee, A., Hamm, R. N., and Ritchie, R. H. (1983). Physical and chemical development of electron tracks in liquid water. *Radiation Research*, 96(3):437–449.

Uehara, S. and Nikjoo, H. (2006). Monte Carlo simulation of water radiolysis for low-energy charged particles. *Journal of Radiation Research*, 47(1):69–81.

Uehara, S., Nikjoo, H., and Goodhead, D. (1993). Cross-sections for water vapour for the Monte Carlo electron track structure code from 10 eV to the MeV region. *Physics in Medicine & Biology*, 38(12):1841.

Usami, N., Furusawa, Y., Kobayashi, K., Frohlich, H., Lacombe, S., and Sech, C. L. (2005). Fast $He^{2+}$ ion irradiation of DNA loaded with platinum-containing molecules. *International Journal of Radiation Biology*, 81(7):515–522.

Usami, N., Furusawa, Y., Kobayashi, K., Lacombe, S., Reynaud-Angelin, A., Sage, E., Wu, T.-D., Croisy, A., Guerquin-Kern, J., and Le Sech, C. (2008). Mammalian cells loaded with platinum-containing molecules are sensitized to fast atomic ions. *International Journal of Radiation Biology*, 84(7):603–611.

Usami, N., Kobayashi, K., Furusawa, Y., Frohlich, H., Lacombe, S., and Le Sech, C. (2007). Irradiation of DNA loaded with platinum containing molecules by fast atomic ions $C^{6+}$ and $Fe^{26+}$. *International Journal of Radiation Biology*, 83(9):569–576.

van Elmpt, W., Zegers, C. M., Das, M., and Ruysscher, D. D. (2013). Imaging techniques for tumour delineation and heterogeneity quantification of lung cancer: overview of current possibilities. *Journal of Thoracic Disease*, 6(4).

Verkhovtsev, A. V., Korol, A. V., and Solov'yov, A. V. (2015a). Electron production by sensitizing gold nanoparticles irradiated by fast ions. *The Journal of Physical Chemistry C*, 119.

Verkhovtsev, A. V., Korol, A. V., and Solov'yov, A. V. (2015b). Revealing the mechanism of the low-energy electron yield enhancement from sensitizing nanoparticles. *Physical Review Letters*, 114.

Wälzlein, C., Krämer, M., Scifoni, E., and Durante, M. (2014a). Advancing the modeling in particle therapy: from track structure to treatment planning. *Applied Radiation and Isotopes*, 83:171–176.

Wälzlein, C., Krämer, M., Scifoni, E., and Durante, M. (2014b). Low-energy electron transport in non-uniform media. *Nuclear Instruments and Methods in Physics Research Section B: Beam Interactions with Materials and Atoms*, 320:75–82.

Wälzlein, C., Scifoni, E., Krämer, M., and Durante, M. (2014). Simulations of dose enhancement for heavy atom nanoparticles irradiated by protons. *Physics in Medicine & Biology*, 59(6):1441.

Wälzlein, C. G. (2013). *Nanometer scale description of electron transport and damage in condensed media using the TRAX Monte Carlo Code*. PhD thesis, Technische Universität, Darmstadt.

Ward, J. (1994). The complexity of DNA damage: relevance to biological consequences. *International Journal of Radiation Biology*, 66(5):427–432.

Wasselin-Trupin, V., Baldacchino, G., Bouffard, S., and Hickel, B. (2002). Hydrogen peroxide yields in water radiolysis by high-energy ion beams at constant LET. *Radiation Physics and Chemistry*, 65(1):53 – 61.

Watanabe, R. and Saito, K. (2001). Monte Carlo simulation of water radiolysis in oxygenated condition for monoenergetic electrons from 100 eV to 1 MeV. *Radiation Physics and Chemistry*, 62(2):217 – 228.

Williams, G. (2000). *userweb.jlab.org/gwyn/ebindene.html*.

Williart, A., Muñoz, A., Boscolo, D., Scifoni, E., Krämer, M., and G, G. (2018). Study on tl-204 simultaneous electron and photon emission spectra and their interaction with gold absorbers. experimental results and monte carlo simulations. *Nuclear Instruments and Methods in physics research section A: Accelerators, Spectrometers, Detectors and Associated Equipment*, Submitted.

Winter, M. (2012). *https://www.webelements.com*.

Winterbourn, C. C. (2008). Reconciling the chemistry and biology of reactive oxygen species. *Nature Chemical Biology*, 4(5):278–286.

Wolff, R. K., Bronskill, M. J., Aldrich, J. E., and Hunt, J. W. (1973). Picosecond pulse radiolysis. IV. Yield of the solvated electron at 30 picoseconds. *The Journal of Physical Chemistry*, 77(11):1350–1355.

Zaider, M., Vracko, M., Fung, A., and Fry, J. (1994). Electron transport in condensed water. *Radiation Protection Dosimetry*, 52(1-4):139–146.

Zatsarinny, O., Bartschat, K., Maslov, M., Brunger, M. J., and Teubner, P. (2008). Electron-impact excitation of the $(5d^{10}6s)^2S_{1/2} \rightarrow (5d^96s^2)^2D_{5/2,3/2}$ transitions in gold atoms. *Physical Review A*, 78(4):042713.

Zhang, S., Li, J., Lykotrafitis, G., Bao, G., and Suresh, S. (2009). Size-dependent endocytosis of nanoparticles. *Advanced Materials*, 21.

# Acknowledgment

It seems that I am at the end of this long trip, which suddenly became incredibly short, and I am happy to thank all of the people who made it possible.

Firstly, I would like to express my sincere gratitude to my advisor Prof. Marco Durante for giving me the opportunity to perform my Ph.D in the Biophysics group in GSI, you have been a tremendous mentor and a source of inspiration for me. I would also like to thank Prof. Regine von Klitzing for taking on the co-reference of this work, and Prof. Bengt Friman and Prof. Michael Vogel for accepting to take part of my committee.

One of the most important thank you goes to Emanuele Scifoni, and Michael Krämer, you definitely have one the most important contribution to this thesis. Both of you gave me all the instruments and motivations I needed for carrying on this project. A special thank goes also to Martina Fuss, even if she is the "last new entry" of the group, her suggestions and her guidance in the last year was really precious to reach this goal. Emanuele, Michael, and Martina, you supported, motivated, encouraged and guided me with a lot of patience during the whole project and for this I really thank you.

I need to acknowledge the financial support received from the European Union Seventh Framework Programme (PEOPLE-2013-ITN-ARGENT Marie Curie project), under grant agreement no. 608163. This project not only founded my studies but also allowed me to travel all over Europe working in a close collaboration with an exciting interdisciplinary and international community. A special thank goes to the project coordinator Prof. Sandrine Lacombe, who made it possible, and to all of the other ESRs for the very nice time we had together. Lily, Arek, Sophie, Soraia, Ali, Alexei, Pablo, Vu-Long, Kaspar Vladimir, Marta, Vivek I am really happy to have met you.

I would like to thank Corinna Kausch for the coordination and organization work for the department and for the help she gave me with the administrative work. Thanks to Lucilla Croce Ferri for taking care of all the financial and bureaucratic aspects of my contract. Thanks also to Maria for her friendship for being always supportive and helpful.

I would like to thank Prof. Gustavo Garcia (CSIC, Madrid Spain) for hosting me for a month in his laboratory, I really enjoyed this experience. Thanks to Prof. Fred Currell (Queen University, Belfast) for letting me participate in some of his radiation chemistry experiments at the Diamond Light Source Facility (Didcot, Oxfordshire, UK ), I learned a lot during these days. Many thanks to the people of IBA Trento, TIFPA (Trento Institute for Fundamentals Physics Applications) and of the proton therapy center in Trento letting me stay with them for an unforgettable month.

I would like to thank my historical officemate, Olga, with whom I shared all the most important moments of this long way. Thank you also to Martin, for the help you gave me with some python scripts and to Rebecca and Christoph, with whom I shared the office for a long time. Thanks also to all the colleague/ friends which are not in GSI anymore but left a big part of themselves here: thanks to Marta, Francesco N., Palmina, Walter, Francesco Anna, Alex, Giorgia, and Francesco.

Last but not least I would like to thank my family and friends, my life during these three years was much nicer thanks to the contribution of all of you!

# Curriculum Vitae Daria Boscolo

## Personal information

| | |
|---:|:---|
| Name | Daria Boscolo |
| Date-of-birth | 16 April 1987 |
| Place of birth | Cecina, Livorno, Italy |
| Nationality | Italian |

## University education

| | |
|---:|:---|
| from 09/2014 | **Technische Universität Darmstadt** |
| | Ph.D. candidate in Biophysics (carried on in the Biophysics department at GSI) |
| | Nanoscale insights on hypoxia radiosensitization with ion beams. |
| | Supervisor: Prof. M. Durante |
| 2011 - 2014 | **University of Pisa, Pisa, Italy** |
| | Master of Science in Physics |
| | TLD efficiency calculations for heavy ions. |
| | Supervisors: Prof. V. Rosso and Prof. M. Durante |
| 2013-2014 | GSI Helmholtzzentrum für Schwerionenforschung, Biophysics department |
| | Erasmus Placement |
| 2006 - 2011 | **University of Pisa, Pisa, Italy** |
| | Bachelor studies in Physics |

## School education

| | |
|---:|:---|
| 2001 - 2006 | **Liceo scientifico E.Fermi** |
| | Cecina, Livorno, Italy |
| | High School Degree |

# Erklärung zur Dissertation

Hiermit versichere ich, die vorliegende Dissertation ohne Hilfe Dritter nur mit den angegebenen Quellen und Hilfsmitteln angefertigt zu haben. Alle Stellen, die aus Quellen entnommen wurden, sind als solche kenntlich gemacht. Diese Arbeit hat in gleicher oder ähnlicher Form noch keiner Prüfungsbehörde vorgelegen.

Darmstadt, den April 10, 2018

_____

(Daria Boscolo)